Micro- and Nano-Structure of Polymers and Molecular Materials

By Abdullah Mohammed M. Alswieleh

DEPARTMENT OF CHEMISTRY

UNIVERSITY OF SHEFFIELD

A Thesis Submitted to the University of Sheffield for the Degree of

Doctor of Philosophy

July 2014

Declaration

This thesis is submitted in fulfillment of the requirements of the degree of Doctor of Philosophy at the University of Sheffield. The work described in this thesis was undertaken between January 2011 and July 2014 under the supervision of Professor Graham Leggett and Professor Steven Armes. Unless otherwise stated, it is the work of the author and has not been submitted in whole or in part for any other degree at this or any other university or institution.

July 2014

Signed: ……..

Abdullah Mohammed Alswieleh

Department of Chemistry,

Dainton Bulding,

University of Sheffield,

Brook Hill,

Sheffield, UK.

S3 7HF

Acknowledgements

For the duration of my PhD I have been fortunate enough to work with some truly talented, inspirational and friendly people. I would like to take this opportunity to say thank you to them:

- I would like to thank Professor Graham Leggett and Professor Steven Armes, for giving me the unique opportunity of working in their research groups and for their advice and guidance throughout this project.

- I would like to thank the University of Sheffield and everybody in chemistry department. I would like to thank GJL and SPA group members past and present, especially Alexander Johnson, Andrew Morse, Anna Tsargorodska, Ehtsham ul Haq, Irene Canton, Maria Cardellach, Mark Moxey, Mat Pringle, Nan Cheng, Omed Qadir, Osama El-Zubir, Paul Chapman, Peng Fan, Robert Ducker, Samson Patole, Sijing Xia, Vicki Cunningham, Vincent Ladmiral, Xuan Xue and Zhenyu Zhang.

- I would like to thank all at the Kroto Research Institute, especially Claire Hurley.

- I would like to thank King Saud University (KSU) in Riyadh for financial support for my PhD research.

- Finally, I would like to thank all my family, my father, my mother and my brothers and sisters I couldn't have done this without their support. Also, I do not forget my wife, I would not have been able to do this work without her.

Publications

1- Alswieleh AM, Cheng N, Leggett GJ & Armes SP. Spatial control over crosslinking dictates the pH-responsive behavior of poly(2-(tert-butylamino)ethyl methacrylate) brushes. *Langmuir*, **2014**, 30 (5), 1391–1400.

2- Alswieleh AM, Cheng N, Canton I, Ustbas B, Xue X, Ladmiral V, Xia S, Ducker RE, El Zubir O, Cartron ML, Hunter CN, Leggett GJ and Armes SP. Zwitterionic poly(amino acid methacrylate) brushes. *J. Am. Chem. Soc*, **2014**, 136 (26), pp 9404–9413

3- Cunningham V, Alswieleh AM, Thompson K, Williams M, Leggett GJ, Armes SP, Musa O. Poly(glycerol monomethacrylate)-poly(benzyl methacrylate) diblock copolymer nanoparticles via RAFT emulsion polymerization: synthesis, characterization and interfacial activity. *Macromolecules* **2014**, 47 (16), pp 5613–5623.

4- Blakeston AC, Alswieleh AM, Heath GR, Roth J, Bao P, Cheng N, Armes SP, Leggett GJ, Bushby RJ, Evans SD. A new poly(amino acid methacrylate) brush supports the formation of well-defined lipid membranes. In preparation.

5- ‘‘Spatial control over crosslinking affects the pH-responsive behavior of poly(2-(tert-butylamino)ethyl methacrylate) brushes’’ AM Alswieleh, SP Armes and GJ Leggett, Poster presentation at Soft Matter, Freiburg Institute of Advanced Studies, Germany, October 2013.

6- ‘‘Spatial control over crosslinking affects the pH-responsive behavior of poly(2-(tert-butylamino)ethyl methacrylate) brushes’’ AM Alswieleh, SP Armes and GJ Leggett, Poster presentation at 3rd Annual Postgraduate Symposium on Nanotechnology, the University of Birmingham, UK, December 2013.

Contents

Abbreviations

AFM	Atomic force microscope
AHT	6-Amino-1-hexanethiol hydrochloride
APTES	3-Aminopropyltriethoxysilane
ATRP	Atom transfer radial polymerization
BE	Binding energy
BIBB	2-Bromoisobutyryl bromide
BIBB-APTES	2-Bromo-2-methyl-N-(3-triethoxysilyl-propyl)-propionamide
Bipy	2, 2'Bipyridine
BSA	Bovine serum albumin
CRP	Controlled/living radical polymerization
DCM	Dichloromethane
DHPC C6	1,2-Hexyanoylsn-glycero-3-phosphocholine
DMF	Dimethyl formamide
DMSO	Dimethyl sulfoxide
DMT	Derjagun-Muller-Toporov
DMPP	Dimethylphenylphosphine
DOPE	1,2-Dioleoyl-sn-glycero-3-phosphoethanolamine
DOPG	1,2-Dioleoyl-sn-glycero-3-phospho-rac-(1-glycerol) sodium salt
DOTAP	N-[1-(2,3-Dioleoyloxy)propyl]-N,N,N-trimethylammonium chloride
DPN	Dip-pen nanolithography
DVB	Divinylbenzene
EBL	Electron beam lithography
EGDMA	Ethylene glycol dimethacrylate
EPR	Electron paramagnetic resonance
EUV	Extreme ultraviolet
F_F	Frictional force
FFM	Friction force microscopy
F_N	Normal force
FTIR	Fourier transform infrared spectroscopy
FRAP	Fluorescence recovery after photobleaching
FWHM	Full width at half maximum
GFP	Green fluorescence protein
GPC	Gel Permeation Chromatography
HDF	Human Dermal Fibroblasts
HMTETA	1,1,4,7,10,10-Hexamethyltriethylenetetramine
HPLC	High performance liquid chromatography
IL	Interferometric lithography
IPA	Isopropyl alcohol
JKR	Johnson-Kendall-Roberts
KE	Kinetic energies
MA	Methacrylate
MEA	Mercaptoethylamine

NHS	Normal human serum
NMP	Nitroxide-mediated polymerization
NMR	Nuclear magnetic resonance
NPPOC	2-(2-Nitrophenyl)propoxycarbonyl
ODT	Octadecyl thiol
OEG	Oligo (ethylene glycol)
OTMS	Octadecyltrimethoxysilane
OTS	Octadecyltrichlorosilane
PAA	Poly(acrylic acid)
PAAm	Polyacrylamide
PBS	Phosphate buffered saline
PCBMA	Poly(carboxybetaine methacrylate)
PCDMA	Poly(cadmium dimethacrylate)
PCysMA	Poly(amino acid methacrylate)
PDHPA	Poly(N-[(2,3-dihydroxypropyl)acrylamide])
PDEAEMA	Poly(N,N (diethylamino)ethyl methacrylate
PDMAEMA	Poly(N,N (dimethylamino)ethyl methacrylate)
PDMS	Polydimethylsiloxane
PEG	Polyethylene glycol
PEGMA	Poly(ethylene glycol) methacrylate
PEO	Poly(ethylene oxide)
PGMA	Polyglycidyl methacrylate
pKa	Acid dissociation constant
PKSPMA	Poly(3-sulfopropyl methacrylate potassium salt)
PHEMA	Poly(2-hydroxyethyl methacrylate)
PHPMA	Poly(hydroxypropyl methacrylate)
PIBMA	Poly(isobutyl methacrylate)
PMA	Poly(methyl acrylate)
PMETAC	Poly(2-(methacryloyloxy)ethyltrimethylammonium chloride)
PMMA	Polymethyl methacrrylate
PMPC	Poly(2-methacryloyloxyethyl phosphorylcholine)
POPC	1-Palmitoyl-2-oleoylphosphatidylcholine
PNIPAAM	Poly(N-isopropylacrylamide)
PNIPPAM	Poly(N-isopropylacrylamide)
PNPMA	Poly(neopentyl methacrylate)
POEGMA	Poly(oligo(ethylene glycol)) methacrylate
PPG-TDI	Tolylene 2, 4-diisocyanate-terminated poly propylene glycol
PSBMA	Poly(sulfobetaine methacrylate)
PSerMA	poly(serine methacrylate)
PSty	Poly(styrene)
PTBAEMA	Poly(2-(tert-butylamino) ethyl methacrylate)
PTFEMA	Poly(2,2,2-trifluoroethyl methacrylate)
PVD	Physical vapor deposition
RAFT	Reversible addition-fragmentation chain transfer

RCA	Radio Cooperative America method
RMS	Root Mean Square
RMSE	Root mean square error
ROP	Living ring-opening polymerization
SAMs	Self-assembled monolayers
SET-LRP	Single electron transfer living radical polymerization
SI-ATRP	Surface-initiated atom transfer radical polymerization
SI-PIMP	Surface-initiated photoiniferter-mediated polymerization
SNOM	Scanning near-field optical microscope
SNP	Scanning near-field photolithography
SPL	Scanning probe lithography
SPM	Scanning probe microscope
STM	Scanning tunnelling microscopy
T_c	Threshold temperature
TEA	Triethylamine
THF	Tetrahydrofuran
TPMA	Tris(2-pyridylmethyl)amine
TFEA	2-Amino-1,1,1-trifluoroethane
UHV	Ultra high vacuum
UV	Ultraviolet
XPS	X-ray photoelectron spectroscopy
μCP	Micro-contact printing

List of Figures

List of Tables

List of Schemes

Abstract

Surface-initiated atom transfer radical polymerization (SI-ATRP) was used to grow a variety of polyelectrolyte polymer brushes from hydroxlated surfaces functionalised with a brominated initiator. The kinetics of brush formation were investigated and conditions required to control the brush growth were identified. These films have been characterized by contact angle measurement, ellipsometry, atomic force microscopy (AFM), surface zeta potential measurements, and X-ray photoelectron spectroscopy (XPS). Photolithographic techniques were used to pattern the surface on both micrometer and nanometer length scale using, respectively, mask based and interferometric techniques. Friction force microscopy (FFM) and AFM were used to characterize the patterned surfaces. Protein attachment was examined by confocal microscopy and AFM.

Poly(2-(tert-butylamino)ethyl methacrylate) (PTBAEMA) brushes showed stimulus-responsive behaviour, resulting from the formation of charges on the secondary amino groups. These pH-responsive weak polybase brushes can be crosslinked via their secondary amine groups using a commercially available polymeric diisocyanate crosslinker. If this reaction is conducted in a good solvent (THF), then relatively uniform crosslinking is achieved throughout the brush layer. On the other hand, if crosslinking is conducted using a bad solvent (n-hexane), then it is confined to the upper surface of the brush layer. The spatial location of the crosslinking profoundly affects the pH-responsive behaviour of the PTBAEMA brush layer when immersed in acidic solution.

A novel zwitterionic monomer, cysteine methacrylate (CysMA) was synthesised via thia-selective thia-Michael addition reaction, and used to grow brushes by ATRP. PCysMA brushes showed stimulus-responsive behaviour, resulting from the formation of charges at either the carboxylic acid or the amino groups at below pH 2 or above pH 9.5, respectively. No pH responsive behaviour was observed when both groups are charged at intermediate pH. PCysMA brushes expanded in the presence of added salt at pH 6; however, at either pH 9.8 or pH 1.5 the brushes collapse being observed. AFM topographical imaging indicated significant mass loss from the brush layer during UV irradiation, while XPS studies confirm that aldehyde groups were generated which can be derivatized with amines. Both micro- and nano-structured PCysMA brushes were used to immobilize green fluorescent protein (GFP) via surface aldehyde groups generated during their photodegradation.

Four different polymeric systems, including poly[2-(methacryloyloxy)ethylphosphorylcholine] (PMPC), poly(3-sulfopropylmethacrylate potassium salt) (PKSPMA), poly(2-methacrylato)ethyl trimethylammonium chloride) (PMETAC), and PCysMA brushes were prepared to be used as supported lipids bilayers. No lipids were formed on PMPC brushes when using positive and negative vesicles. However, the addition of short chain lipids (C6) in the positive charge lipids can form islands of lipid bilayers on PMPC brushes, with diffusion coefficient of 0.4 $\mu m^2\ s^{-1}$. Moreover, a homogeneous bilayer was formed on PMPC surface with diffusion coefficient of ca. 0.1 $\mu m^2\ s^{-1}$, when using spin-coating approach. The PKSPMA brushes showed significant vesicle absorbed on the surface, and a fluid bilayer underneath with diffusion coefficient ca.0.5 $\mu m^2/s$. A fluid lipid layer was formed on PMETAC surface, with very slow diffusion coefficient ca. 0.02 $\mu m^2\ s^{-1}$. The vesicles slowly fused and required several days to form a fluid bilayer on the PCysMA brushes. A homogeneous lipid layer was formed on the PCysMA surface, after 48 h incubation time when used 25% mol DOTAP vesicles. The diffusion coefficient of lipids on PCysMA was ca. 1.0 $\mu m^2\ s^{-1}$.

Thin films of gold have been prepared on titanium and chromium as adhesive layers. ODT SAMs were fully photo-oxidized at ca. 30 $J.cm^{-2}$, as judged by contact angle measurements. ODT monolayers on gold surface have been patterned by exposing the samples at ca. 35 $J.cm^{-2}$ through a mask and at ca. 25 $J.cm^{-2}$ by a Lloyd's mirror two-beam interferometer. Gold micro-structures were obtained after immersion of the samples into etching solution for 20 min, and gold nano-structures were obtained after 15 min etching time. XPS suggested that not all gold had been removed from the surface at these etching conditions. Silane films derivatised with a ATRP initiator (BIBB-APTES) have been formed on both titania and chromia surfaces, after the gold film had been etched, as confirmed by contact angle measurements and XPS. PCysMA brushes have been grown from BIBB-APTES functionalised Ti and Cr surfaces. The AFM height images showed the growth of PCysMA brushes from the oxide regions to yield patterned binary gold/PCysMA brush structures at both mico- and nanometre length scales.

Chapter 1: Introduction

1.1 Self-Assembled Monolayers (SAMs)

The term self-assembled monolayers (SAMs) refers to an organized assembly of organic molecules formed spontaneously on the surface of a substrate, in the solution or the gas phase.[1-4] SAMs molecules have a head group with a specific and high affinity for the substrate, terminal functional groups oriented toward outside the surface and backbone chain that attach the head and the terminal functional groups (Figure 1.1). There are several types of head groups the can bind to specific substrates, such as metals, metal oxides, and semiconductors.[1-2] Alkanethiols are extensively used to form SAMs on gold, silver, palladium and platinum.[4-5] Alkylsiloxanes have been widely used to form SAMs on a wide range of substrates, including silicon oxide, glass, aluminum oxides and titanium oxides.[1-2]

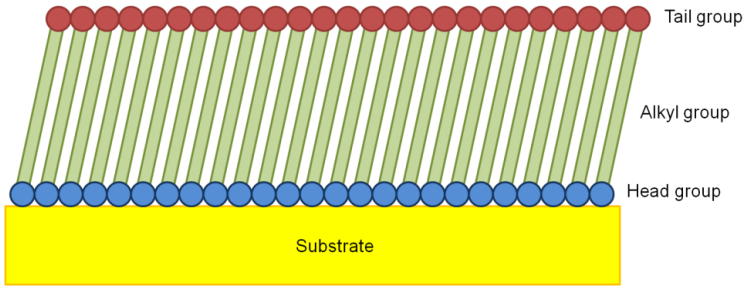

Figure 1.1. Schematic illustrating the main components of SAMs film

The field of SAMs has been developed since Nuzzo and Allara stated in 1983, the preparation SAMs of alkanethiolates on gold from dilute solutions of di-n-alkyl disulfides.[6] The properties of SAMs have made the powerful tool in the surface studies.[1] They are frequently used as model surfaces in a range of applications, including electrode modification,[7] adhesion,[8-9] corrosion protection of metals,[10] wetting,[11] and preparation of biocompatible materials.[9,12] They may be patterned on both micrometer and nanometer scales,[13-15] making them suitable for further modifications. SAMs offer a wide variety of possibilities for functionalization of a surface which has revolutionized the study of molecular interfaces particularly in electronics and biological applications.[14]

1.1.1 SAMs of organosulfur derivatives

Silicon wafers, glass and mica are the most common planar substrates used to support thin films of metals for alkanethiol SAMs, including gold,[5,16] silver,[5,17] copper,[5,18] palladium,[19] platinum,[20] and nickel.[21] These surfaces can be prepared via several methods such physical vapor deposition (PVD) and electrodeposition.[1,22] A few nanometers of an adhesion layer of titanium, chromium, or nickel is followed by deposition a layer of the metal of interest. The adhesion layer is important for metals that do not form oxides readily, such as gold.[1] Metal films are polycrystalline with grains of metal in size of 10 to 1000 nm, depending on the conditions.[2,23]

The formation of monolayers by adsorption of alkanethiols and dialkyl disulfides on gold has been widely studied,[1-2,5,16,24] since it was first reported by Nuzzo and Allara.[6] The driving force for monolayer formation is a combination of the strong interaction between gold and sulfur atoms and the lateral dispersion forces between adjacent alkyl chains . The reaction is an oxidative addition of the alkanethiol to the gold surface, followed by the reductive elimination of hydrogen, in the absence of oxygen, as shown: [2]

$$R - S - H + Au_n^0 \rightarrow R - S^- Au^+ . Au_n^0 + \frac{1}{2} H_2$$

In the case of dialkyl disulfides follow: [4]

$$R - S - S - R + Au_n^0 \rightarrow 2R - S^- Au^+ . Au_n^0$$

where R represents the hydrocarbon chain. The thiol hydrogen might also react to form water in the presence of oxygen in the reaction medium.[1]

SAMs of organosulfur derivatives (thiols, disulfides, sulfides) can be prepared by either in the solution or the vapor phase.[1] However, assembly from solution is convenient and is widely used for SAMs formation. There are a number of factors that can affect the structure and formation rate of the resulting SAMs, including: solvents; the concentration of oxygen in the solution and the cleanliness of the substrate; the concentration of the adsorbate; the temperature and the immersion time.[1] The presence of solvent can affect the formation of SAMs because of the possibility of interaction between solvent and adsorbate molecules and/or between solvent and substrate molecules. The solvent-substrate interaction may hinder

the adsorption of the adsorbate from the solution, so the adsorbate molecules must displace the solvent molecules from the surface.[1,25] SAMs of alkanethiols have been prepared using a variety of solvents, including tetrahydrofuran, dimethylformamide, acetonitrile, cyclooctane, toluene and ethanol.[24-25] However, ethanol is the most widely used for preparing SAMs, due to the solvation a variety of alkanethiols, its low cost, its available in high purity and its low toxicity.[24] In previous studies, the rates of formation SAMs of alkanethiols in non-polar solvents such dodecane and hexadecane were comparable to those of SAMs formed from ethanol.[26] However, surface characterization suggests that SAMs formed from ethanol solution are more organized than formed in non-polar solvents.[27,24]

The presence of oxygen in the solution can oxidize the thiol molecules to sulfonates and other oxygenated species. Reducing the concentration of oxygen is highly recommended for preparing SAMs of thiols on palladium, silver, copper, and platinum surfaces, due to the oxidation of the sulfur moieties in SAMs with 1-7 days at the ambient atmosphere.[5,19] Deoxygenation the solvent with an inert gas before preparing the solution and maintaining the solution under inert gas during the SAMs formation, can improve the rate of the formation and the structure of the SAMs.[5,19] The contaminants and impurities can also affect the quality of the SAMs. The adsorbate must displace the contaminants and impurities from the surface before the adsorption on the surface, which affect the formation of the SAMs. The surface should be cleaned with strongly oxidizing chemicals (70% concentrated sulfuric acid and 30% of hydrogen peroxide (30%)) or oxygen plasmas prior to immersion in a solution of thiols.[1]

SAMs of thiols are typically made by immersion of a clean substrate into a dilute ethanolic solution of the adsorbate of choice (1-10 mM) for ca.18 h at 20 ^{o}C.[1,24] The thiol concentrations and immersion time are inversely related: a low concentration of thiol requires long immersion time to form a closed packed, ordered SAM.[24,28] SAM formation is quite fast (ca. 1 min) even at diluted solution (>5μM) and produces well-ordered and densely packed SAMs, but it requires times in order to maximize the adsorbate density and minimize the defects of the SAM.[28] The physical properties of the film at concentration below 1 μM are not the same as those for films formed from more concentrated solutions.[24] Although elevated temperature can improve the rate of SAM formation and decrease the defects in the film, it can also increase the desorption rate of the contamination and solvent molecules on the surface.[27,29] Uosaki and co-workers suggested that the formation of SAMs can be affected by the temperature in particular during the first few minutes of the SAMs.[27]

1.1.2 SAMs of organosilicon derivatives

SAMs of alkylsiloxanes and alkylchlorosilanes requires a hydroxlated surface for their formation. [2,30] Most of the widely alkylsiloxanes consist of one Si atom connected to three hydrolysable substituents that can react with surface hydroxyl groups, and an organic functional groups.[30] The silane-surface reaction consists of four steps. Initially, hydrolysis of the three hydrolysable groups occurs to form silanol. In this step, water may come from the atmosphere, or may be present on the surface or added to the solution. Condensation of silanols is followed to form oligomers. Then, the oligomers bind to OH groups of the substrate via hydrogen bonds. Finally, a covalent linkage of siloxane (Si-O-Si) bonds is formed between the oligomers and the substrate after elimination of water, during drying typically between 50 and 120 ^{o}C (Figure 1.2).[30-33] The reaction time to form silane monolayers spontaneously varies in the range from one hour to a few days, depending on the reactivity of the head group.[32-33] The organic functional group (R) remains available for chemical reaction (covalent bond) or physical interaction with other molecules.[30]

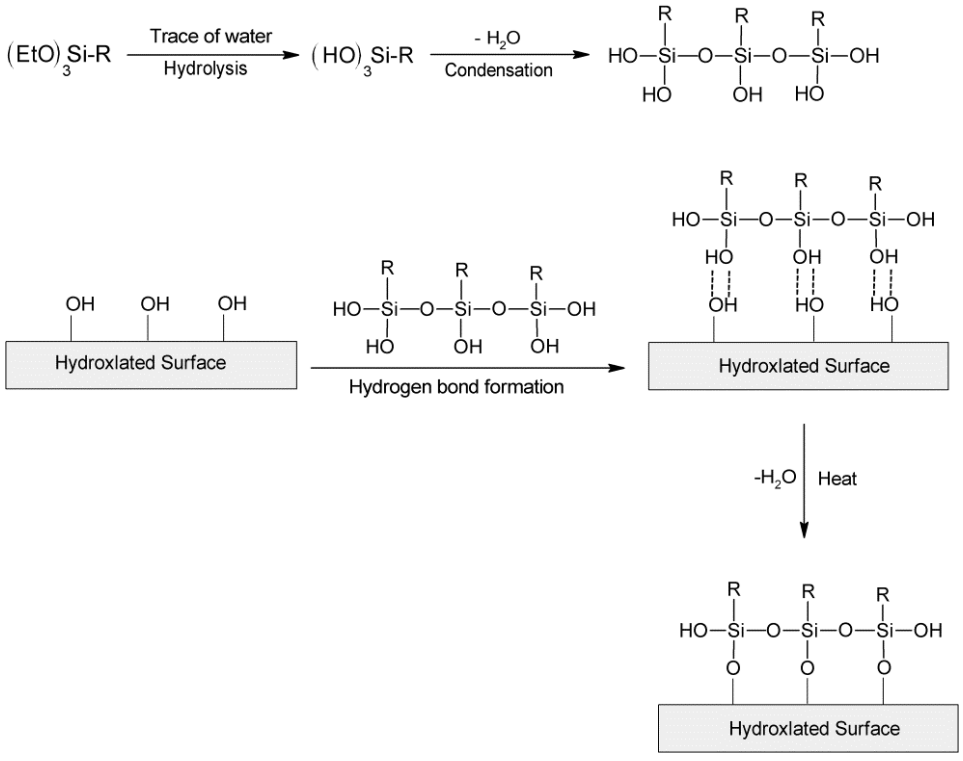

Figure 1.2. Schematic representation of the mechanism of the silanation reaction.

SAMs of silanes have been used to modify a substrate either via vapor phase or solution phase deposition techniques.[2] An ultra-high vacuum chamber has been used for deposition SAMs in vapor phase.[26,34] This technique provides an ultra clean environment which is reflected in the quality of the SAMs.[26] In solution phase deposition, a clean substrate is exposed to a solution containing surface active molecules to form SAMs, followed by rinsing. This technique is more popular, comparing to vapor phase because it is easy for preparation and the low cost of the solvents.[2,26]

There are a number of factors that influence the formation of silane films on a hydroxylated surface, including the concentration of hydroxyl groups at the surface, the amount of water and the temperature.[2,35] Several methods have been used to prepare clean surfaces prior to SAMs and to maximize the number of hydroxyl groups on the surface.[36] In silicon for example, silanol groups are essential for the formation of siloxane bonds so it is known that submerging silicon wafers in piranha solution and subsequent rinsing in water can maximize the silanol groups on silicon wafers.[37-38]

The quality of silane SAMs is determined by the amount of water in solution. In the absence of water, incomplete silane monolayers may be formed, while excess water may produce polysiloxane in solution and deposite on the surface. The thickness of polysiloxane adsorbed on the surface depends on the concentration of the siloxane solution; if it is too large, multilayer adsorption results.[2,35] Many groups have studied the importance of water content on the substrate surface.[35,39] The formation of closely packed monolayers of octadecyltrichlorosilane (OTS) was achieved from a fully hydrated oxidized silicon wafer, as observed by Le Grange et al.[40] However, it is not necessary to have a fully hydrated surface for formation of homogenous OTS SAMs.[32,40] McGovern et al. reported the adsorption of OTS SMAs in the surface.[41] The authors concluded that the optimum condition for formation homogeneous monolayers was a moisture quantity of 0.15 mg/100 mL of solvent. Rozlosnik et al. Reported that high density coverage of OTS was obtained in the addition of water to the solvents.[42] They observed that the thickness of resulting silane SAMs increased in the addition of water in dodecane, forming multilayers. A homogenous OTS SAMs with high surface coverage was achieved when used solvent of intermediate water solubility (between toluene and dodecane), heptanes.[42] Wang and Lieberman suggested that presence of water during OTS SAM depostion could affect the film quality.[32] However, the growth of OTS SAM under dry condition could form ultra-smooth film with roughness (rms) of ca. 1 A^{o}.

Temperature and the length of alkyl chain were found to be important factors for the formation of silane monolayers. It was found that the threshold temperature for formation of silane monolayers was dependent on the chain length.[2] Rondelez and co-workers studied the influence of temperature on the quality of films formed by the adsorption of several n-alkyltrichlorosilanes (n = 10 -22) on silicon oxide wafer.[43] They found that the highest packing density was found, if the silanization was carried out at temperature below the threshold temperature (Tc). The threshold temperature of these monolayers was 28°C for short-chain silanes and there was an increase in the threshold temperature after increasing the length of the alkyl chain. The performance of SAMs formation increased, as the temperature decreased. The length of the alkyl chains influences the packing of the resulting monolayers. Ohtake et al. studied the effect of the alkyl chain length on the SAMs order. They suggested that ordered layers resulted from the adsorption of molecules with more than 8 carbon atoms in their alkyl chains, while disordered SAMs were observed following adsorption of molecules with less than 8 carbon atoms in their alkyl chains.[44]

3-Aminopropylalkoxysilane SAMs have been used for the formation of amine-terminated surfaces via the formation of siloxane bond, Si-O-Si, and is ideal for further derivatization. It has been used for many applications such as immobilization biological and other materials.[45-46] The structures of films formed by adsorption of 3-aminopropylalkoxysilane on silica surface depend on the density of molecules, the binding between molecules and the nature of the surface (Figure 1.3).[47-49] The aminosilane molecule can be linear when the molecule is covalently attached to the surface via a siloxane bond, or it can be tilted when the terminal amine interacts with the proton on the silanol (Figure 1.3A and 1.3B).[34,48] The aminosilane molecules can be physisorbed to the surface via hydrogen bonding, in which case they may be removed by rinsing with water (Figure 1.3C and 1.3D).[48] In addition, the aminosilane molecules are capable to from dense multilayers by cross-linking through polymerization vertically and horizontally (Figure 1.3E and 1.3F).[34,50]

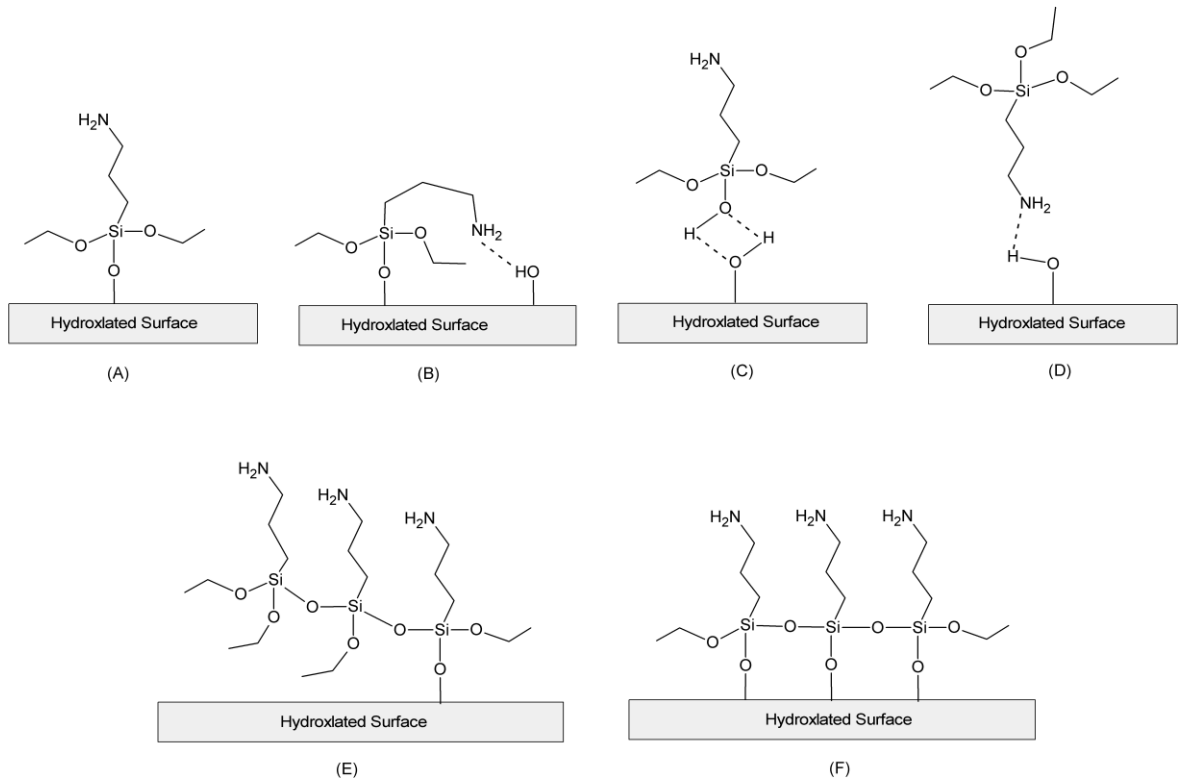

Figure 1.3. Schematic representation of possible conformations of 3-aminopropyltriethoxysilane (APTES) on silicon surface. (A) Aminosilane attached covalently to the surface, (B) aminosilane attached to the surface and the terminal amine with the silanol, (C and D) physisorption of the aminosilane molecules on the surface, and (E and F) the aminosilane molecules vertically and horizontally cross-linked.

The reactivity of the amine groups in the surface was studied by Zang et al. and Asenath et al., who also examined how it might be improved.[38,48] It has been reported that curing aminosilane film at a temperature slightly higher than 100 °C can increase the amount of primary amine due to breaking the hydrogen bonds that formed between amine groups and silica surface.[38,48] However, an excessively high curing temperature can reduce the amine groups due to a reaction with carbon dioxide to form carbamate.[38]

A survey of the literature reveals that a very large number of different approaches have been used to the preparation of 3-aminopropyltriethoxysilane (APTES) films. For example, Petri et al. have reported the formation of homogeneous APTES film on flat surface by dipping freshly cleaned Si wafers into a solution of APTES in toluene((1%) w/w) at 60 °C, for 4 min.[51] Zhang et al. reported that an APTES film was prepared by immersion of glass slides

into a APTES dilute solution in methanol at room temperature for 24 h.[52] Heid et al. studied the formation behavior in self assembled films and concluded that aminosilanes form disordered multilayer films.[53] It has been reported that 40-50% of amino groups on the surface are hydrogen-bonded or protonated in the case of gas-phase deposition of aminosilanes.[54-55]

1.2 Polymer brushes

The term "polymer brush" refers to polymer chains that are attached to the surface of a solid substrate via one chain end, and are stretched away from the surface.[56-59] Such polymer brushes can be attached to a polymeric backbone so that every part of the backbone carries a polymer side chain polymer.[56, 60] For polymer chains attached to a surface, there are two regimes depending on the graft density of tethered chains.[56] If the distance between two points of attachment is greater than the size of the tethered polymers, then the chains are isolated from each other.[56] Two possible structures can occur in this case, depending on the strength of interaction of the polymer segments with the surface. Firstly, if the interaction between the polymeric segments and the surface is weak or repulsive, the chains are randomly attached to the surface.[56] This conformation has been termed the "mushroom" conformation (Figure. 1.4A).[56-57] However, if the polymeric segments interact strongly with the surface or if the solvent is a poor solvent for the chains, they may lay on the surface to yield a so-called "pancake" conformation (Figure. 1.4B).[56-57] If the distances between the anchor sites are short (high grafting densities), then the polymer chains stretch away from the surface.[56-57] The stretched polymeric chains are oriented perpendicular to the surface to yield the brush conformation (Figure 1.4C).[56,59]

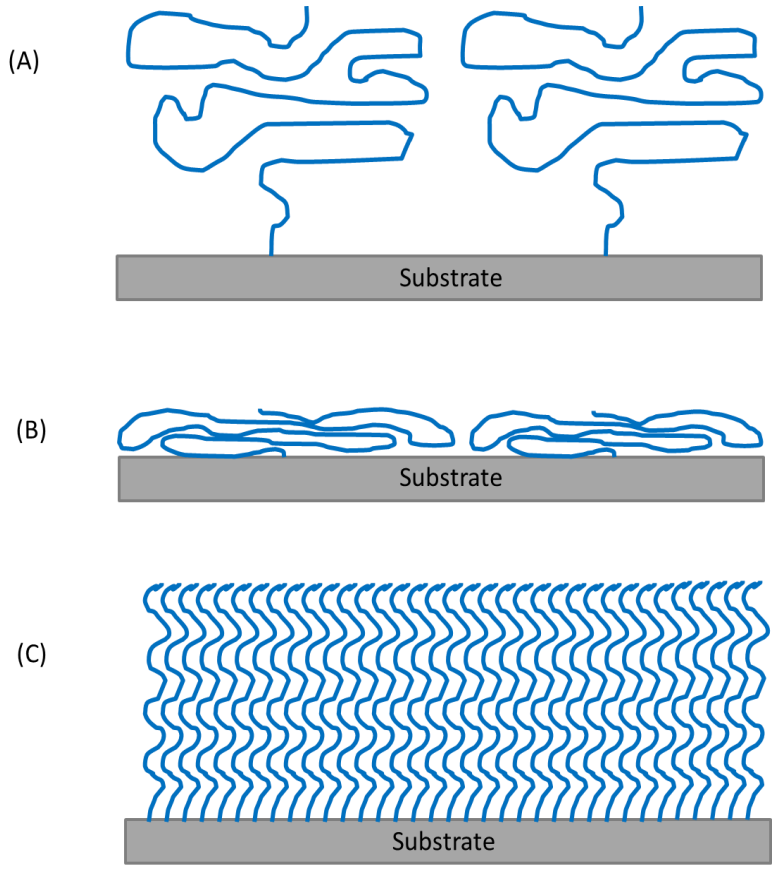

Figure 1.4. (A) "Mushroom" conformation of surface-attached polymer. (B) "Pancake" conformation of surface-attached polymer. (C) "Brush" conformation of surface-attached polymer.

1.2.1 Types of Polymer Brushes

There are two main strategies to prepare polymer brushes covalently attached to a substrate: the grafting to method and the grafting from method. These are discussed in turn below.[58,61-62]

1.2.1.1 Grafting To

This strategy is based on attachment of pre-formed polymers to the substrate via chemisorption .[57-60,63] As shown in Figure 1.5 , end groups of pre-formed polymers can react with suitable functional groups on the surface to form polymer brushes.[64] The pre-formed polymer can be synthesized by controlled/"living" polymerization techniques.[56,64] These techniques enable conversion of the chain ends into many functional groups including hydroxyl, carboxyl, thiol and amino.[56] The surface chemistry is important for attachment of

the polymer layer. Gold, for example, can react with polymer chains containing thiol groups under appropriate conditions to form a tethered polymer.[56] Also, SAMs and other coupling agents can be used to modify these groups to introduce a variety of functionalities to tethered polymer chains.[56,64]

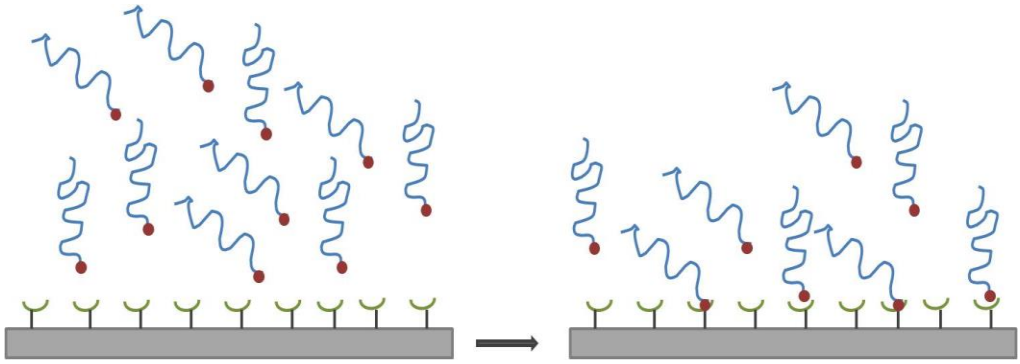

Figure. 1.5. Schematic illustration of the *grafting to* process.

However, this method suffers from some limitations. The amount of immobilized polymer is limited in terms of both a relatively low grafting density and the thickness of the resulting brushes.[57,62] As more polymer chains are attached to the surface, the concentration of polymers becomes higher on the surface than the chain concentration in the bulk. The polymer molecules must diffuse through tethered polymer chains to reach the reactive sites on the surface.[60,63,65] As the surface grafting density increases, the rate of polymer chain attachment decreases due to steric hindrance.[56-57,60]

Many groups have used this approach to prepare thin film of polymers on surfaces.[66-69] For example, the immobilization of pre-formed poly(sodium 4-styrenesulfonate), poly((*ar*-vinylbenzyl) trimethylammonium chloride) and poly(*N*,*N*-dimethylacrylamide) onto gold films using the *grafting to* technique was reported by Sumerlin and co-workers.[67] Tran and Auroy reported the formation of dense poly(styrene sulfonate) terminated silane on silicon wafer using this technique.[66] Poly(ethylene glycol) terminated silanes (PEG silanes) have been grafted onto silicon surface, yielding ultrathin film with an extreme low roughness.[68]

1.2.1.2 Grafting From

In this approach, the polymer chains are grown from a surface, as shown in Figure 1.6. The surface functionalized with initiators is exposed to a solution containing monomer, catalyst

and solvent etc. Polymer chains grow only from initiator sites without any reaction occurring in the solution.[70] When the monomers approach to the surface, they either start to react with the initiator sites, or they add to a growing polymer molecule. Polymer brushes with very high grafting densities can be accomplished without steric hindrance, due to the formation of very short chains in the initial step and the continuous addition of monomer to the growing chains.[58,60,63] This method allows very dense, uniform and thick polymer brushes are produced. Grafting from is widely used to prepared polymer brushes in order to overcome the limitations of the grafting to technique.[58-60,63,70]

The main part of the *grafting from* approach is to functionalize the surface with an initiator to grow polymers.[57-58,63,71] This functionalization can achieved using a film deposited onto the surface via Langmuir-Blodgett techniques or, more commonly, by formation of an initiator-containing SAM.[56] The choice of the initiator depends on the polymerization chemistry.[56] In principle, almost any polymerization technique can be applied to grow polymers from a variety of surfaces in a well-defined manner.[71-73] Controlled/"living" polymerisation strategies have been extensively investigated to control the film thickness and density and the properties of the surface-confined polymer chains. Moreover, this controlled/"living" polymerisation strategy allows the production of block copolymer brushes.[59,72,74] Many controlled/"living" polymerization techniques, including living anionic/cationic polymerizations, living ring-opening polymerisation (ROP), nitroxide-mediated polymerization (NMP) and reversible addition-fragmentation chain transfer (RAFT) polymerization, have been utilized for chain growth reactions.[75-79] Surface-initiated controlled radical polymerization (SI-ATRP) is probably the most widely used technique for production of polymer brushes due to the less stringent requirements for the experimental conditions, compared to other techniques.[57] ATRP is discussed in more detail in the following sections.

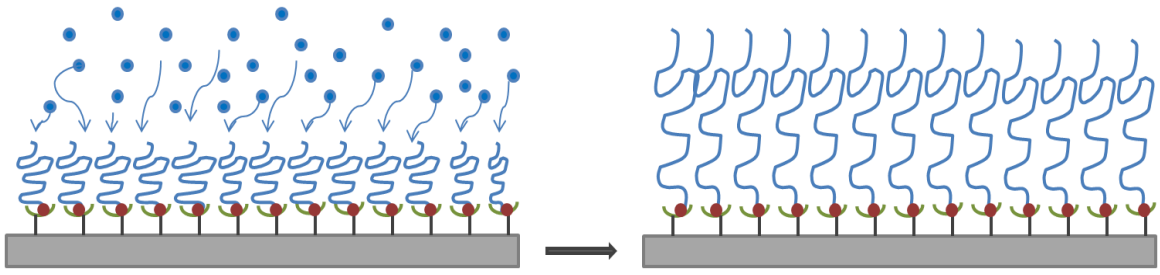

Figure. 1.6. Schematic illustration of the *grafting from* process

1.2.2 Atom transfer radical polymerization (ATRP)

In 1995, atom transfer radical polymerization (ATRP) was first reported by Matyaszewski.[80] ATRP allows the regular controlled growth of polymer chains.[81] Interest in ATRP has been increasing rapidly since the technique was discovered because of its suitability for polymerization of a wide range of monomers to yield well-defined polymers.[82-83] ATRP is a valuable synthetic tool among the controlled/living radical polymerization (CRP) techniques [82] and is widely used in polymer synthesis for preparing polystyrene, poly(acrylates) and poly(methacrylates).[81,84] Such polymers are well-defined, with predetermined molecular weights,[85] very low polydispersities (polydispersity = Mw/Mn) and good tolerance of functionalities.[86] A vast array of polymers with controlled compositions, topologies and functionalities can be synthesised using ATRP.[82] Furthermore, ATRP has allowed many polymers to be produced in the form of regular nano-structured morphologies.[83]

The basic mechanism of ATRP involves cleavage of an alkyl halide bond (R-X) by a transition metal complex (Mt^nL_m) to generate a metal halide complex with a higher oxidation state ($Mt^{n+1}L_mX$) and an alkyl radical ($R^{\cdot}$) which can add to a monomer (M).[84] An equilibrium exists between active and dormant chains that activates and deactivates the propagating radicals from the initiator or the end of the polymer chain, adding radical to monomer, and termination by either coupling or disproportionation (see Figure 1.7).[87-88] The equilibrium between the active and the dormant chains lies to the left and hence ensures a low concentration of propagating radicals and reduces the possibility of termination.[88-89]

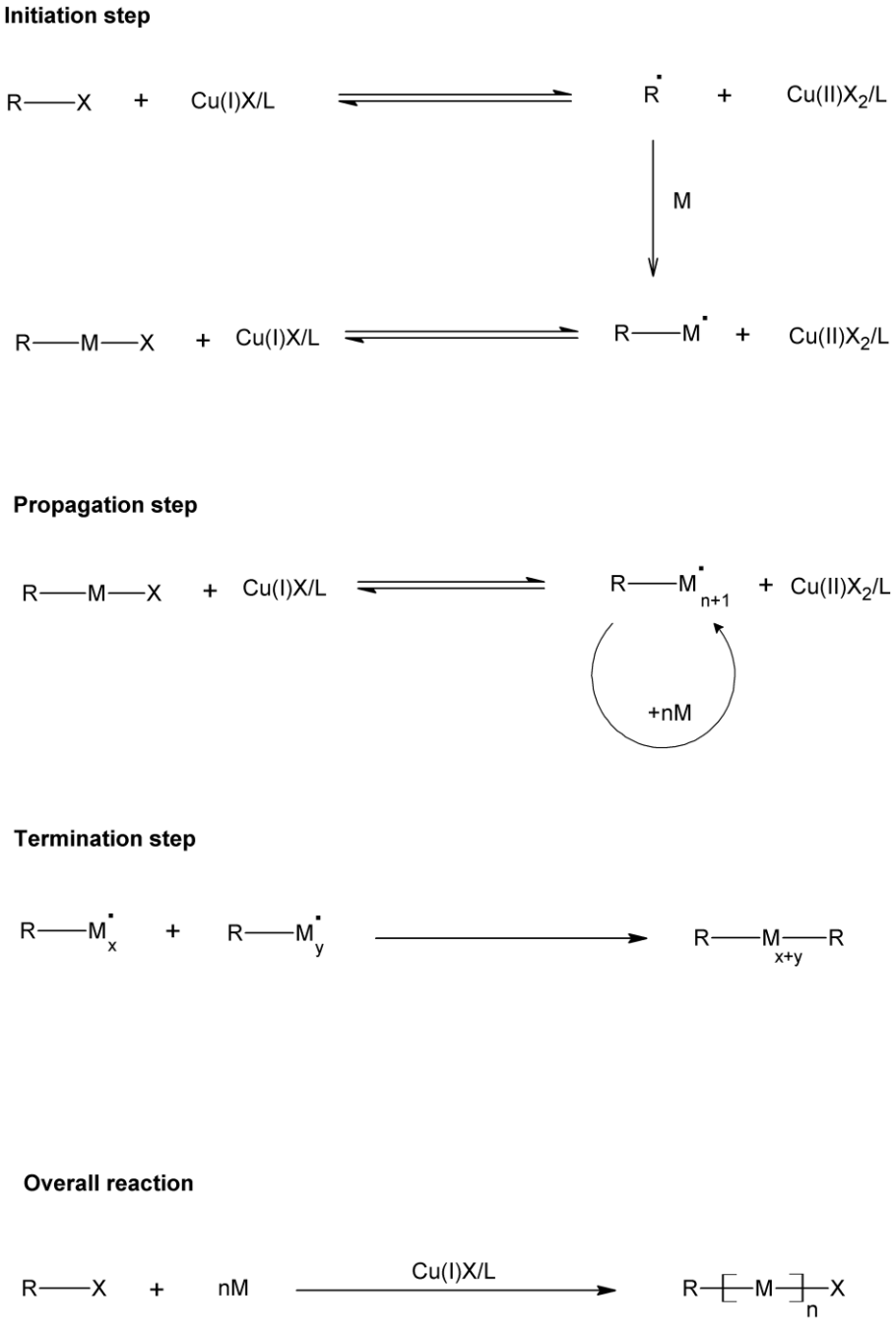

Figure 1.7. The mechanism of ATRP according to Matyjaszewski et.al.[8]

In ATRP, just 5% or less of the total growing polymer chains are prematurely terminated during the early stages of the polymerization reaction. Successful ATRP will have only a small fraction of terminated chains. All other polymer chains grow uniformly, achieved through the use of fast initiation step and rapid reversible deactivation.[81] ATRP is sensitive to oxygen but sometimes polymerization can occur in the presence of small amounts of oxygen. The catalyst concentration is much higher than that of the polymerizing radicals, so the

catalyst can scavenge oxygen atom in the media. However, oxidation of the metal complex reduces its concentration and increases that of the deactivator; as a result the polymerization rate reduces.[90] The lability of the halogen end- groups on the polymer chains can be considered as an advantage of the ATRP formulation. In principle, this terminal halogen atom can be replaced by $–N_3$, -OH $–NH_2$ or –CN by post-polymerisation modification.[86]

ATRP can be affected by several factors including the choice of monomer, initiators, temperature and time, solvent and combined ligands with the transition metals.[85] ATRP has been successfully used to polymerize a wide range of vinyl monomers.[90] Styrene, (meth)acrylates, (meth)acrylamides and acrylonitrile all contain substituents that can stabilize the propagating radicals, so are well-suited for ATRP.[81] Each type of monomer requires specific conditions for ATRP, since each monomer has a unique atom transfer equilibrium constant for both the active and deactivated species, even under the same conditions and using the same catalyst.[81,90] For low equilibrium constants, ATRP cannot occur or only occurs very slowly; however, a very high equilibrium constant leads to a high concentration of radicals and, as a result, a large amount of termination. This problem can be solved by employing a large amount of deactivated species (higher oxidation state metal complex); in consequence, the equilibrium shifts toward the dormant species, but this leads to slower polymerizations.[81,85,90] Each monomer has a particular characteristic propagation rate constant. Thus, the concentration of propagating radicals and the rate of radical deactivation need to be adjusted for each monomer to control the polymerization.[81] The overall position of the equilibrium can also be adjusted by the amount and reactivity of the catalyst.[81,87,90]

The initiator determines the number of growing polymeric chains.[90] The number of growing polymer chains is equal to the initial concentration of the initiators.[81] The molecular weight of the polymer increases with the initial concentration of initiator ($Mw \propto [initiator]^{-1}$).[90] In principle, the mean degree of polymerization (DP) is given by (1.1):

$$DP = [monomer] / [initiator] \qquad (1.1)$$

Alkyl halides (R-X) are typically utilized as ATRP as initiators.[81,87-89] Well-defined polymers with narrow molecular weight distributions can be obtained by using a appropriate halide (X), which must rapidly migrate between the growing chains and the transition metal complex, so bromine and chlorine are the most suitable halides to control the molecular weight of the polymer.[90] Iodine can work well in copper-mediated ATRP to polymerize acrylate. It can also be used with rhenium or ruthenium catalysts to prepare polystyrene.[81] The C-F bond is too

strong to undergo homolytic cleavage so that fluorine cannot be used in ATRP.[81] Ideally, the structure of the alkyl (R) group of the initiator should be similar to the structure of the dormant polymers. Thus, 1-phenylethyl halides are appropriate for the synthesis of polystyrene and α-halopropionitriles are useful for acrylonitrile chain ends.[81,90] The isobutyrate group is widely used to polymerize methacrylates.[90] Generally, ATRP initiators can be any alkyl halide with activating substituents on the α-carbon such as aryl, carbonyl or allyl groups [86]. ATRP initiators can also be polyhalogenated compounds (e.g. CCl_4 and $CHCl_3$) and compounds with a weak R-X bond, such as N-X, S-X and O-X.[81,90]

The most important component of an ATRP formulation is the catalyst, because it determines the position of the atom transfer equilibrium, i.e. the exchange between the dormant and active species.[81] ATRP catalysis typically involves a transition metal and ligands.[82-84,86] The polymerization rate depends on the concentration of the catalyst. However, the catalyst concentration does not affect the molecular weight of the polymer.[86] Several factors need to be considered for an efficient transition metal catalyst. Firstly, the transition metal must have at least two accessible oxidation states separated by one electron. Secondly, the metal centre should form bonds with halogen atoms. Thirdly, the coordination sphere around the metal centre should be expandable upon oxidation to accommodate the halogen atom. Fourthly, the metal-ligand bonds must be relatively strong.[81-82,84] Finally, the metal centre in the catalyst complex must not be a strong Lewis acid.[90] A variety of transition metal complexes can be used as ATRP catalysts such the complexes of Mo, Re, Ru, Fe, Rh, Ni, Pd, Co, Os, Ti, Zr, Hf, Rf and Cu metals.[82,84,91] Copper halides have proven to be the most efficient catalysts.[86] Ligands are very important components and often the key to solubilisation of the catalyst, as well as tuning the redox potential in the Mt^n/Mt^{n+1} cycle.[86] In general, electron-donating ligands stabilize the higher oxidation state of the metal centre and increase the polymerization rate.[90] Ligands often contain nitrogen atom and are widely utilized in conjunction with Cu, including derivatives of bidentate bipyridine (bpy), phenanthroline (phen), terpyridine(tpy), tridentate diethylenetriamine (DETA) and other multidentate ligands.[84] Generally, CuCl or CuBr is used in ATRP reaction as a catalyst and 2, 2'bipyridine is often used as a ligand.[85]

Polymerization media are usually non-polar solvents such as diphenyl ether, p-dimethyoxy benzene or p-xylene but various other solvents have been successfully used. These include polar solvents for different monomers such as toluene, ethyl acetate, acetone, dimethyl formamide (DMF), ethylene carbonate, alcohol, water and many others.[90] Polar solvents may be preferred for ATRP in order to achieve faster rates of polymerization. There are several

factors that affect the solvent choice. First, polymer chain transfer to solvent should be low and the interaction between the catalyst complex and solvent should be considered.[81] Second, catalyst poisoning by solvent and solvent-assisted side reactions should be minimized.[90] Third, in some cases the catalyst structure may change in certain solvents which negatively affect the ATRP reaction.[81] Finally, side reactions may occur in presence of certain solvent, such the end groups of the polystyryl halides can sometimes eliminate HX at 110 to 130 ^{o}C in some polar solvents.[90]

1.2.3 Surface initiated atom transfer radical polymerization (SI-ATRP)

ATRP has become the most popular strategy among controlled radical polymerization (CRP) techniques for the preparation of well-defined polymers with low polydispersities because of its compatibility with a wide range of functional monomers and less demanding experimental conditions.[72,74,92-93] Nano-objects of precise dimension and functionality have also been achieved by ATRP of various monomers [74,93].

Surface initiated atom transfer radical polymerization (SI-ATRP) has become one of the most popular methods for the growth of polymer brushes, because of its tolerance to a wide range of functionalized monomers, the ability of the end groups to be used as macroinitiator for the preparation of di- and triblock copolymers, and experimentally, it does not require rigorously dry conditions such as the living anionic and cationic polymerizations.[70,74] The chain length and film density can be controlled with this technique.[94] SI-ATRP can be employed on various surfaces including both planar and colloidal ones, e.g. inorganic particles.[92] Many polymers have been grown from macroscopic wafers or microscopic particles using this technique and many reports illustrate its ability to control polymer architectures.[56-57,74,95] The polymer chain length, the surface density of the polymer chains and their configuration (e.g., mushroom, pancake, brush) are mainly controlled by variation of reaction parameters such as initiator density on the surface, polymerization time and the polymer architecture (e.g. weather a linear polymer or a comb polymer).[94]

Weather flat or curved, both organic and inorganic surfaces have been successfully coated with ATRP initiator groups.[85] The most convenient and appropriate initiator for the monomer can be employed in SI-ATRP.[73] The initiator groups are usually placed on surfaces with a relatively low geometric surface area.[74] The presence of a uniform monolayer of initiators on the surface is necessary to prepare polymer brushes.[92] Techniques have been developed to immobilize ATRP initiators on a wide range of substrates, including inorganic substrates

such as silicon, silica, titanium, gold and chromium (Figure 1.8), and polymeric / organic substrates such as cellulose and Nylon.[92] Initiators for ATRP are rarely attached directly to inorganic substrate.[73] The silicon wafer is modified with silane SAMs film to yield initiator groups. Bromomethyl- and chloromethyl-terminated silanes were immobilized as ATRP initiators.[92] Silicon surface modified with an initiator film composed of 2-bromoisobutyrate fragments has been widely utilized.[96-99] Alternatively, silicon wafers are reacted with 3-aminopropyltriethoxysilane (APTES) to form uniform SAMs; followed by treatment with 2-bromoisobutyryl bromide (BIBB) and triethylamine (TEA) to give an amide-based initiator.[73,100-102] Titanium surfaces can be modified with an initiator layer using silane SAMs,[103] bromomethyl-terminated biomimetic catechol,[92] or bromomethyl-terminated phosphonic acid.[104] Immobilization of ATRP initiator on chromium can be achieved by treating the surface with piranha solution to create a film of chromium(III) oxide followed by deposition of initiator silane film.[105] The ATRP initiator on gold surfaces can be prepared directly by immobilizing bromomethyl-terminated thiol agents, or immobilizing amino- or hydroxyl-terminated thiol, followed by treatment with BIBB and TEA.[106-108]

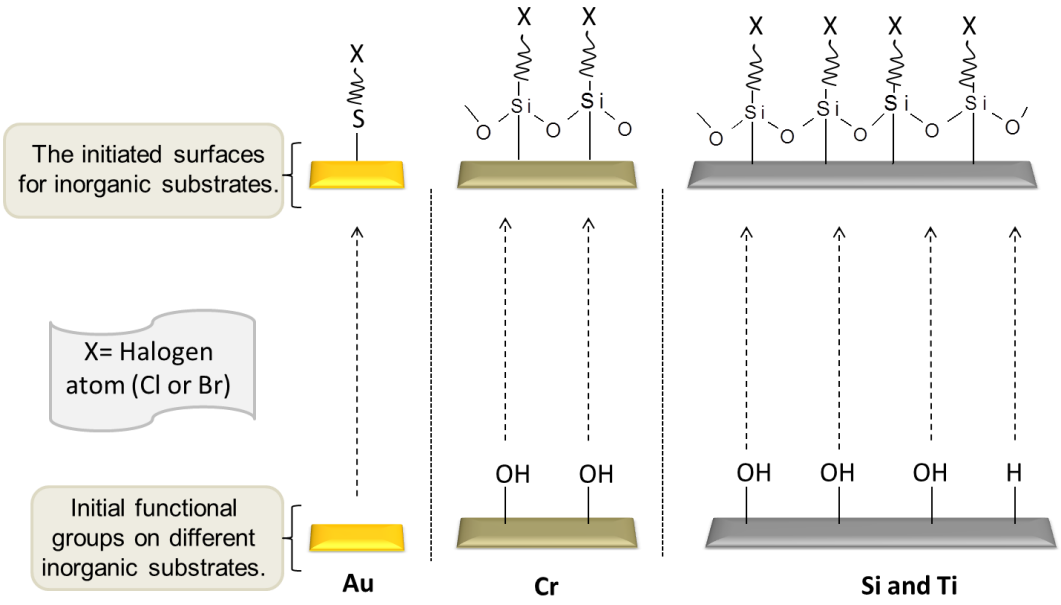

Figure. 1.8. Methods for immobilizing ATRP initiators on various inorganic and organic substrates for the preparation of functional polymer brushes by surface-initiated ATRP, including (gold, chromium, titanium and silicon).

One advantage of SI-ATRP is that initiation can normally occur at room temperature.[85] The synthesis of surface-bound initiators for SI-ATRP (such thiol and silane derivatised) is easier than initiator for free radical and NMP polymerizations.[70] Initiators with α-haloester groups are the most commonly used for ATRP technique (Figure 1.9A).[81,109] Generally, initiating radicals produced from α-haloisobutyrates are faster than those produced from others, such α-halopropionates; because the generated radicals have better stabilization after initiation step.[81] Amide-based initiators have been successfully used to prepare polymers (Figure 1.9B).[101,109-112] In general, amide-based initiators are less efficient than ester-based initiators in solution;[100-101,113-116] because of the leadency to lose bromine end groups during the early stages of polymerisation by intramolecular reactions with the lone pair in the amide groups, leading to poor control in ATRP.[101,113] Polymers prepared using amidic initiators have low monomer conversions and produce high polydispersities polymers.[114-116] In surfaces, Brown et al. investigated the effect of initiator structure on growth of POEGMA brush.[117] They found that POEGMA brush formed from amide- and ester based initiators were roughly the same under similar conditions.

Figure 1.9. illustration the structure of: (A) Ester- and (B) Amide-based ATRP initiators.

SI-ATRP polymerisation is carried out after immobilization of ATRP initiator on the target surface and in the presence of a transition metal halide / nitrogen-based ligand catalyst system and a suitable monomer. Methacrylate (MA) monomers are the most widely used monomer for the growth of polymer brushes via SI-ATRP.[70]

Ejaz et al. was reported the immobilization of ATRP initiator onto a silicon surface to give a well-ordered layer of initiator sites, from which PMMA was grown.[118] The authors studied the effect of the addition of free initiator to the polymerisation. They found that the polymer brush thickness was dependent on the concentration of the added free initiator; thicker brushes were obtained at lower concentration of the free initiator. Matyjaszewski et al. studied the polymerizations of styrene and acrylates from silicon surfaces modified with

ATRP initiator.[96] They found that controlled radical polymerizations can be achieved in the presence of the proper ratio of Cu^{I} and Cu^{II} species, without adding free initiator.

The concentration of deactivator after the halogen atom transfer to the catalyst may be too low to reversibly cap the propagating radicals which can result in uncontrolled polymer chain growth. Thus, the concentration of the deactivated complex has to be sufficiently high at the beginning of the ATRP reaction to quickly establish equilibrium between the active and dormant chains.[92] At the beginning of the SI-ATRP reaction, the addition of the radical-deactivating complex facilitates exchange between halogen-capped dormant chains active polymer radicals.[73] The use of ATRP to polymerize styrene or methyl acrylate in the presence of excess deactivator on a planar surface results in an increase in the brush thickness with time.[73]

SI-ARTP in polar and, in particular, aqueous solutions can introduce fast with controlled polymer brush growth at low temperature,[119-122] even for water-insoluble polymers such as polymethyl methacrylate (PMMA) and polyglycidyl methacrylate (PGMA).[123] Surface polymerization at low temperature is very important for substrates that are sensitive to elevated temperature, such as thiol SAMs on gold. Moreover, polymerization at low temperature reduces the possibility of spontaneous thermal polymerization and other side reactions (e.g. transesterification, elimination).[70] Growing very thick polymer brushes in short polymerization times can be achieved in aqueous media by ATRP. Baker and co-workers reported the growth of very thick brushes of poly(2-hydroxyethyl methacrylate) (PHEMA) on gold surfaces.[124] Surface polymerization occurred rapidly in aqueous media to form 700 nm thick PHEMA brushes in just 12 h, at 20 ^{o}C. Control experiments using neat monomer, catalyst and ligand yielded polymer brushes of only 6 nm in an equivalent polymerization time.[124] Jones and Huck reported growth of thick films of PMMA and PGMA brushes in aqueous media at room temperature using SI-ARTP.[123] 30 nm thick PMMA brushes were synthesised in aqueous solution in only 35 min, compared to 37 nm in 12 hours as previously reported by Kim et al.[125] PGMA brushes a thickness of 125nm were also obtained in just 90 min polymerization time.[123] Moreover, the authors illustrated the growth of PHEMA brush from silicon surface using water and water/methanol mixture as solvents. The thickness of PHEMA films grown in water reached 100 nm in 2 h, whereas when water/methanol mixture used, the thickness at the same time was ca. 65 nm.[123] Zhu and co-workers studied the effect of solvents on the growth of poly(oligo glycol) methacrylate (POEGMA) from silicon wafer.[126] The thickness of POEGMA brushes depended on the polarity of the solvent: as the

solvent polarity decreased in the order water, water/methanol mixture, pure methanol, ethanol, and 2-propanol, the brush thickness decreased.

Purification of the final polymer chains prepared by SI-ATRP is easier than for conventional solution ATRP, because the catalyst complex can be easily removed from the polymer brushes by simply removing the planar substrate (e.g. a glass slide) from the polymerizing solution, followed by rinsing/washing with pure solvent.[92]

The grafting density of polymer brushes (i.e., the number of chains per unit area) can be calculated using the following equation (1.2): [126-128]

$$\sigma = \frac{h\rho N_A}{M_n} \qquad (1.2)$$

where σ is the graft density (chains.nm^{-2}), h is the brush thickness, ρ is the density of the polymer film, N_A is Avogadro's number, and M_n is the number-average molecular weight of the polymer chains on the surface, assumed to be the same as that in free polymer produced in solution using via free initiators.[126-128] It should be pointed out that the M_n of chains in both surface and solution polymerized samples under the same condition were similar, as reported by several studies.[79,129] The polymer grafting density depends on the initiator density at the surface.[117,130-131] The polymer density can dictate whether the regime is brush or mushroom. The effect of the initiator density on the conformation of polyacrylamide (PAAm) brush was reported by Genzer and coworkers.[130] A gradient density of initiator was formed on silicon wafer, followed by growing PAAm. The film thickness decreased gradually, as the initiator density decreased. Therefore, the conformation changed from brush regime to mushroom regime.[130]

1.2.4 Stimulus-responsive polymer brushes

Surfaces coated with thin polymer films are widely used to modify surface properties and are used in studies of wettability, biocompatibility, friction and corrosion resistance applications.[60] There is interest in using these polymers for smart or responsive surfaces that yield a change in their physical properties when an external stimulus is applied such as a temperature switch or a change in pH or solvent.[57,59,62-63,65,71,93]

1.2.4.1 Solvent-responsive polymer brushes

The structure of a polymer brush depends on the nature of the polymer-solvent interaction, or "solvent quality". Polymer brushes will swell to maximise the polymer/solvent interactions in the presence of a good solvent.[57] On the other hand, the chains collapse in a poor solvent in order to minimize the interaction between the polymer and solvent.[57,71,132] The size difference for the brushes between good and poor solvents is larger than is observed for the polymers in solution.[65] For a homopolymer, the change can be affected by the grafting density of the brushes.[65] For example, the response for low grafting density (e.g. mushroom) brushes is similar to that of a coiled polymer in solution while the response for high density brushes in a poor solvent is weak because of the very crowded chains.[63,65] Copolymer brushes can be more complex than homo-polymers in terms of their response.[57] For instance, a solvent may be a good solvent for one co-monomer but a poor solvent for the other, depending on the nature of each component.[57]

The solvent response of PMMA brushes grafted from silicon wafers was studied by Chen et al.[133] The behaviour of PMMA brushes in a good solvent (THF) and a poor solvent (water) was studied using ellipsometry and atomic force microscopy (AFM). The layer thickness and surface roughness were both reduced after immersion in water. The investigation of the dynamics of swelling of PMMA brushes with different grafting densities in good and poor solvents was reported by Aoki et al.[134] It was observed that the polymer thickness was about a factor of two higher in a good solvent (benzene) than in a poor solvent (acetonitrile). Furthermore, the influence of the brush density on the swelling was studied. It was observed that the brush conformation could be easily changed and the response to solvent exchange was fast for low density brushes, whereas the no response to solvent-exchange was observed in high density brushes.[134]

The solvent responsive behaviour of copolymers brushes has also been studied.[135-136] Rowe et al. studied the behaviour of different diblock copolymer brushes (poly(styrene) (PSty)-*b*-PSty, PSty-*b*-poly(acrylic acid) (PAA), PSty-*b*-poly(N-isopropylacrylamide) (PNIPAAm), and poly(methyl acrylate) (PMA)-*b*-poly(N,N (dimethylamino)ethyl acrylate)) (PDMAEA) in different solvents.[135] N,N-dimethylformamide, cyclohexane, toluene and dichloromethane were used as either good or poor solvents. The diblock copolymer brushes were immersed into a good solvent (for both blocks), and then immersed into a good solvent for the inner block and a poor solvent for the outer block. After the second step, contact angle and X-ray

photoelectron spectroscopy (XPS) measurements confirmed that strong collapse of the outer block and swelling of the inner block.[135] The solvent response of PS-*b*-(PMMA-*co*-poly(cadmium dimethacrylate) (PCDMA) copolymer brushes was also studied by Yu et al. and they observed similar behaviour.[137]

1.2.4.2 pH- and ion-sensitive polymer brushes

Polymer brushes can be classified as either charged (polyelectrolyte) or neutral.[58,60,71] Polyelectrolyte brushes containing charged repeat units can be used as pH- or ion-responsive materials.[57,138] There are two types of polyelectrolyte depending on the ionisable group: strong (e.g. strong acids or bases) or weak (e.g. weak acids or bases) polyelectrolyte brushes.[57,65,138] For strong polyelectrolytes, the brush charge density is fixed, so pH or ions do not influence the brush behaviour unless the ionic strength of the salt in solution is similar to that inside the brushes.[57,65] Weak polyelectrolyte brushes exhibit more interesting responsive behaviour since they are sensitive to changes in both pH and ionic strength.[57,59] Polymer chains comprising weakly basic groups become stretched at low pH, whereas polymer chains carrying acidic groups become collapsed under the same conditions.[63,65,71] The chain stretching is due to repulsive interactions between charged groups.[63,139] The addition of salt to cationic/anionic polyelectrolyte brushes reduces the electrostatic interaction between the polyelectrolyte chains, resulting in collapse of the brush conformation.[57,62-63,140]

Various monomers have been used to prepare stimuli responsive brushes such PAA, poly(methacrylic acid) (PMAA) and PDMAEMA.[63,141-142] Brittain et al. studied the pH-responsive behaviour of PAA brushes by in the pH range 2 to 10.[143] They observed a linear increase in brush thickness with pH from 16 to 26 nm up to pH 8. The effect of grafting density on the pH-induced conformational changes of PAA brushes has been investigated by Wu et al.[144] They found that the degree of swelling of PAA brush was affected by the grafting density at pH 4 and 5.8, whereas at pH 10 the degree of swelling was independent of the grafting density. The pH response of PDMAEMA brush has been studied by several groups.[142,145-147] For example, Sanjuan et al. studied the selling behaviour of PDMAEMA at pH 2, 7 and 10.[142] They observed that the PDMAEMA brush became less expanded as the solution became more basic. Geoghegan et al. reported that PDMAEMA brush swollen at lower pH when the grafting density increased, causing a shift in pK_a of the brush.[147]

Brittain and co-workers investigated the effect of salt on the behaviour of PAA brush.[95,141] The brush height decreased with increasing the concentration of mono- and divalent salts. Xu

et al. reported the effect of monovalent salt on the quaternized PMAEMA (PMETAI).[148] They found that the PMETAI brush collapsed at high salt concentrations. Biesalski et al. reported that for positively charged poly-4-vinyl[N-methyl-pyridinium] (MePVP) brushes, the height did not change at low concentrations of KI.[149] However, the brush height decreased at higher concentrations [KI] > 0.1M. Similar behaviour was observed by Huck and co-workers for investigation the effect of ions on the conformation of the poly(2-(methacryloyloxy)ethyltrimethylammonium chloride) (PMETAC) brushes.[150-151]

Polyzwitterionic polymers contain both cationic and anionic groups, compared to poly acid or polybase.[152-153] The polyzwitterions may be classified into four classes, depending on the responses to change in the pH.[152] First, polyzwitterions that contain permanent charges on both the anionic and the cationic groups, which may be insensitive to changing the pH (Figure 1.10A).[154] Second, polyzwitterions that contain neutralized anionic species, while the cationic groups are insensitive to the pH (Figure 1.10B).[153] Third, polymers in which the cationic groups are neutralized, and the anionic groups are insensitive to changes in the pH (Figure 1.10C).[152] Finally, polyzwitterions that contain both anionic and cationic groups that are neutralized, and in which both groups are sensitive to changes the pH (Figure 1.10D).[155] Addition of salt to zwitterionic polymers leads to chain expansion, due to reduction in the attractive inter-chain interaction.[63]

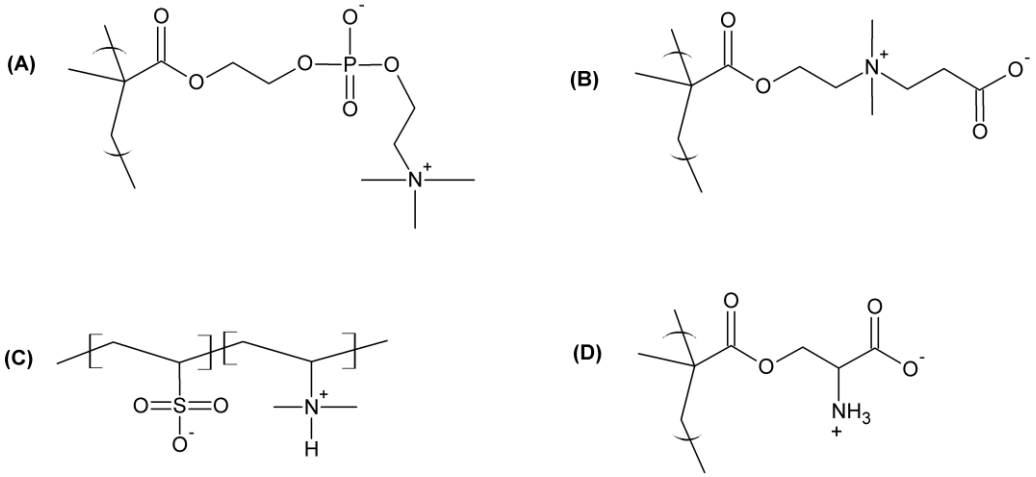

Figure 1.10. Structure of the four different classes of polyzwitterionic polymers. (A) Polymers containing permanent charges on both the anionic and the cationic groups, (B) polymer containing neutralized anionic groups and permanent positive charge on cationic species, (C) polymer containing permanent negative charge on anionic groups and neutralized cationic groups, (D) polymers containing neutralized anionic and cationic groups.

Various monomers have been used to prepare zwitterionic polymer brushes, including 2-methacryloyloxyethyl phosphorylcholine (MPC),[156-157] sulfobetaine methacrylate (SBMA)[158-160] and carboxybetaine methacrylate (CBMA).[160-162] Poly(2-methacryloyloxyethyl phosphorylcholine) (PMPC) has been widely studied.[163-165] Edmondon et al. reported the swelling of PMPC brushes in water and alcohol/water mixtures. They found that the ellipsometric thickness in water increased from 32.5 nm in the dry state to ca.153 nm under pure water.[165] Takahara and co-workers reported PMPC brush swelling in aqueous NaCl solutions of various NaCl concentrations, using AFM.[166] They observed that the thickness of the PMPC brush, independent of the salt concentration and the PMPC brush thickness, increased from ca.25 nm in dry state to almost 150 nm in solution.

1.3 Patterned SAMs and Polymer Brushes

The ability to control structure on the nm length scale may open up new possibilities in many fields ranging from molecular electronics to medical diagnostics to catalysis.[167] A wide variety of techniques can be used to generate nano-scale structure. Generally, these can be classified under two main headings.[168-170] Top-down approaches involve the physical modification of materials in order to impose spatial organisation.[170-171] In this case, lithographic techniques are used to pattern surfaces.[170-171] In contrast, bottom-up approaches are based upon the use of chemical methods to join molecules and atoms together to form larger structures.[168-169]

1.3.1 Microcontact printing (µCP)

Microcontact printing (µCP) was first introduced in 1993 by Kumar and Whitesides.[172] The µCP technique can be successfully applied to pattern large areas with resolution in the submicrometre range.[173] An elastomeric stamp with bas-relief features is utilized to transfer the ink to the target substrate (Figur. 1.11).[174] The surface of the stamp is coated with ink and brought into physical contact with the substrate, leading to transfer of the ink. Binding between the ink and the new surface must be more energetically favourable than that between the ink and the stamp to ensure efficient transfer of the material onto the substrate.[174-175] µCP was originally used to deposit SAMs on gold surfaces,[176] but it has been developed to enable the patterning of proteins, metals and polymers.[175,177] To achieve the best resolution,

conditions must be optimized to avoid the lateral diffusion of the ink, the deformation of the stamp and contamination of the patterns.[173]

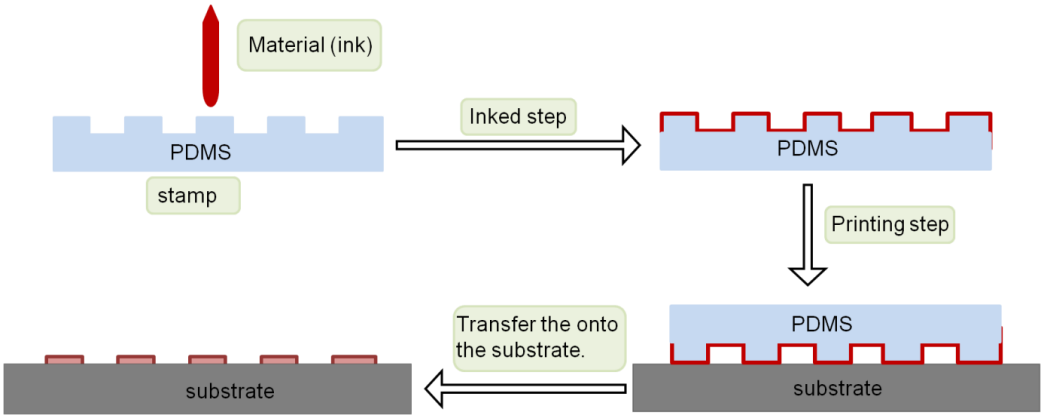

Figure 1.11. Schematic representation of the principle of microcontact printing of molecules (ink) onto a planar substrate.

μCP stamps are usually made of a silicone elastomer, typically polydimethylsiloxane (PDMS). The surface energy of a PDMS stamp is very low, which allows the inked material to be easily transferred from the stamp to the substrate. Furthermore, PDMS does not react with most chemicals, but it can sometimes become swollen in certain organic solvents.[174]

μCP is a simple and efficient patterning technique. However, it has some problems.[174,178-180] Stamps often swell by absorption of the ink during the printing process, which increases the mean feature size. In addition, an excess of ink can deform the patterns by increasing diffusion of the imprinted molecules on the patterned substrate. PDMS is a highly hydrophobic material, and this causes problems when patterning polar inks.[178-179] Deformation of elastomeric stamps is a problem which can easily distort surface patterns. Pattern deformation is more likely when the size of the pattern is on the submicron length scale.[174] Another disadvantage of using elastomeric stamps is that the patterns can be sometimes contaminated with low molecular weight siloxane impurities leaching from the stamp.[178] This problem can be overcome by washing the stamps with heptane or by treating the stamps with UV/ozone.[178]

Microcontact printing has been successfully employed to directly or indirectly pattern surfaces with monolayers and polymers.[181] In direct μCP, the material (ink) is directly transferred from the stamp to the surface. However, with this method, it is not easy to achieve

high resolution patterning of macromolecules.[173] In indirect μCP, a pre-patterned surface is prepared, for example by selectively depositing a SAM of initiators, followed by surface-initiated ARTP.[181]

Alkanethiolate SAMs on gold have been patterned using μCP.[176,179] Patterned SAMs have been used for as resists for chemical etching.[179] SAMs of alkanethiolates have been used to pattern gold surfaces with specific functional groups to enable growth of polymer microstructure by selective deposition of polyion multilayers.[182] Protein patterning has been reported using μCP to pattern oligoethyleneglycol (OEG)-thiols on a gold surface, followed by immobilization of mixed SAMs consisting of 1-mercaptoundecanol and biotinylated thiols on the remaining bare gold regions of the sample.[183] Labelled streptavidin was then specifically immoblized by attachment to biotinylated thiols.

Polymer brush patterning has been achieved by μCP by forming a pattern of a nonreactive SAMs of alkylthiolates, followed by immersion of the sample into a solution of a thiol with initiator at the tail end. A polymer (e.g. poly(caprolactone)) can be grown from these sites.[184] A polymer brush based on poly(N-[(2,3-dihydroxypropyl)acrylamide]) (PDHPA) with latent aldehyde functionality for use as a template for protein micropatterning was reported by Kizhakkedathu and co-workers.[185] This synthesis was carried out via SI-ATRP on a silicon substrate to yield high-density brush. Micropatterning of single proteins and multiple proteins were successfully accomplished using this substrate. Zhou et al. reported a general preparation route to form multicomponent polymer brushes on gold surface.[181] They found that multicomponent brushes could be prepared by repeating the patterning using μCP technique of initiator-terminated thiols without backfilling the remaining bare gold surface with inert thiols during brush growth.

1.3.2 Photolithography

The basic principle of photolithographic methods is to expose a substrate to electromagnetic radiation in order to change the molecular structures of the substrate [14]. Photolithography techniques are widely used on industry to pattern surfaces. Many researchers have been working in developing photolithographic techniques to provide structural resolution below 100 nm.[171] Photolithographic patterns are obtained by illuminating the surface using a mask or aperture, or interference methods.[14]

Photolithography is a suitable technique for patterning large flat surfaces with good alignment, controlled topography and a broad range of features. However, photolithography is not suitable to pattern curved surfaces directly.[173] Micrometre and sub-micrometre patterns are achieved using this technique.[14] The photolithographic resolution increases on reducing the wavelength of the light used for exposure.[169]

The two challenges in patterning polymers using photolithography are (i) to combine patterning at low cost and high resolution and (ii) to pattern functional polymers without changing their properties. For example, in the presence of weak bonds in π-conjugated polymers, direct photoirradiation causes polymer degradation and destroys the desirable electronic and optical properties of these materials.[173]

1.3.2.1 Micro-scale UV lithography

Surface modification on the micron-scale can be conveniently achieved by UV lithography. The photoresist mask is placed on the wafer surface (e.g. coated monolayers or polymer film) then the light is passed through the mask to modify the macromolecule. Consequently, positive tone resists are degraded by exposure or negative tone resists are cross-linked after their development (Figure 1.12).[186] For example, photolithography methods have been used to modify SAMs of nitro groups to obtain amines which, were subsequently functionalized with acid anhydrides.[171]

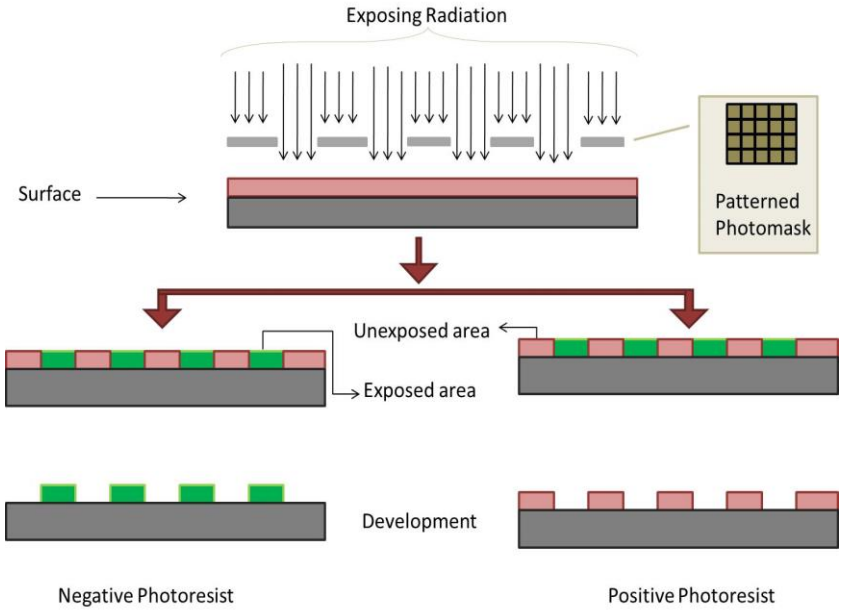

Figure 1.12. Diagram illustration the process of photolithography using a mask.

Leggett et al. reported that SAMs of thiolates on gold surface could be oxidized to weakly bound sulfonates by exposing the sample to deep UV light.[187] Patterned samples were prepared by exposure through a mask and immersion of the sample into a solution of a contrasting alkanethiol to replace the oxidised species. Friction force microscopy (FFM) was used to confirm the conversions. Ducker et al., demonstrated the etching of structures into gold surface with good resolution and low defect density by etching it after exposure in a mixture of mercaptoethylamine (MEA) and ammonia hydroxide.[188] Leggett and co-workers studied the photodeprotection of N-NPPOC 3-aminopropyltriethoxysilane, using UV light with 325 and 364 nm.[189] Micropattering was achieved by exposing the sample to UV light through a mask, to yield an amine-functionalized surface.

Patterned polymer brushes can be produced by UV irradiation using several methods. One approach is to pattern the surface-bound initiator, and then subsequently grow the polymer. ATRP initiator-functionalized substrates can be patterned using UV light, to remove initiator so that polymer brush will only grow from masked areas. Kamitani et al. reported that UV irradiation could be used to pattern APTES SAMs, and the remaining amino groups on the surface (non-exposed area) could be modified to produce ATRP initiators.[190] Finally, polymer brush was grown from immobilized initiators to create carbohydrate arrays. UV light with a wavelength of 244 nm was used to selectively remove the halogens from films of chloromethylphenyltrichlorosilane and 3-(2-bromoisobutyramido)propyl-triethoxysilane on silicon dioxide.[191] Micropatterning was accomplished by illuminating the organic films through a mask, then POEGMA brushes were grown from the intact halogenated regions using SI-ATRP to form micro-structured brushes. UV radiation can also be used to degrade (pattern) polymer films. This strategy have been used by Zhou et al. to pattern PMMA brushes by exposing a sample to UV light through a mask.[192] Ahmed et al. reported UV-induced photodegradation of protein-resistant POEGMA brushes.[193] UV light with a wavelength of 244 nm was utilized to pattern the brush at the micrometer scale by exposing the film through a photomask.

1.3.2.2 Interferometric lithography

Interference lithography (IL) is an optical method for fabricating patterns over large areas of the surface.[61,169,194] It is based around the use of interference patterns formed by the interference of two or more coherent laser beams to modify a sample surface.[61,170,195] It provides to fabricate periodic nano-structures over large areas, and the fact that it is a mask-

less method meaning that much simpler apparatus is needed than is the case for other lithographic methods.[61,170] The basic idea process is shown schematically demonstrated in Figure.1.13.[170,194]

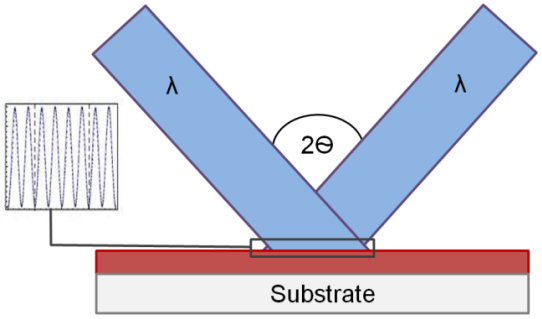

Figure 1.13 Schematic representation of a dual-beam interferometer.

The period (peak-to-peak distance between maxima) is given by equation (1.3):[170]

$$p = \frac{\lambda}{2 \sin \theta} \qquad (1.3)$$

where p is the period, λ is the wavelength and θ is the angle between the beams and the sample. The ultimate resolution of IL is dependent on the illumination wavelength (λ).[196] Smaller features can be achieved when a shorter wavelength is used.[194] UV and deep ultraviolet radiation are commonly used in IL to obtain nanostructured features.[170] The pattern size is also affected by the angle (θ) between two the beams and the sample.[195] For example, UV light with 257 nm wavelength at an incident angle 80^{o} produce lines and spaces with a period (p) of 130 nm.[170]

Figure 1.14 shows the configurations of two types of dual-beam interferometer. In a Lloyd's mirror interferometer a mirror is fixed at an angle 2θ to the sample (Figure 1.14A). Half of the beam is directed onto the sample, and the other half is pointed directly onto the mirror, from where it is reflected onto the sample surface where it interferes with the first half of the beam to fabricate a sinusoidal interference pattern.[197-198] The apparatus is simple and inexpensive and has been used to fabricate a high-resolution nanostructure with a pitch of ca. 38 nm by EUV on PMMA.[199] In the apparatus in figure 1.14B the laser beam is split into half and folded into itself to maintain contrast (Figure 1.14).[197-198] This setup is more complicated because there a number of reflections and the path length difference between the splitter and the sample must be within the longitudinal coherence distance.

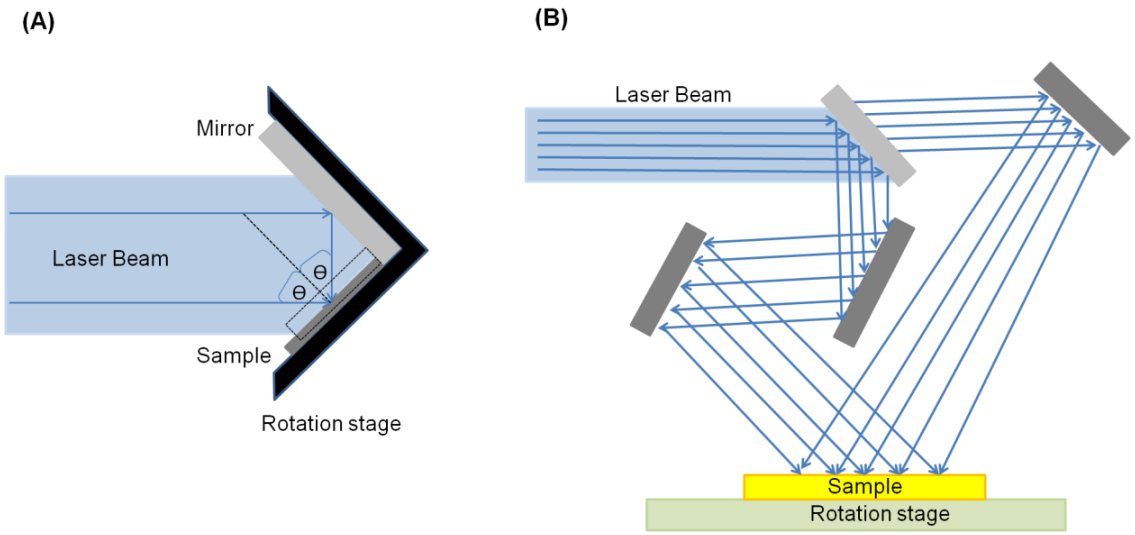

Figure 1.14. A schematic representation of two experimental setups for interferometric lithography.

IL provides a simple method for patterning SAMs. Patterning SAMs of alkylthiolate using deep UV with 193 nm wavelength was reported by Freibel et al.[200] Alkylthiolate SAMs were patterned over a large area with a period of 532 nm and then used as a template to deposit $CaCO_3$, $Zn(OH)_2$, and polymers. Extreme-UV interference lithography (EUV-IL) was used to create nanopatterns in SAMs of 4′-nitro-1,1′-biphenyl-4-thiol (NBPT) on gold.[201] Patterns with periods ranging between 2000 and 60 nm were achieved. Alkylphosphonates on Ti were patterned using a Lloyd's mirror interferometer.[202] The exposed molecules were replaced by a contrasting alkylphosphonate, yielding lines with a width of 46 nm. Subsequently , the patterned SAMs were used as a resist for wet etching of Ti and produced feature sizes in the range 46-126 nm, depending on exposure time.

Solak et al. used EUV with 13.4 nm wavelength to pattern Si wafers coated with 40nm PMMA films, using interference lithography.[203] The period of lines and space patterns produced by IL was ca. 45 nm. Schuh et al. used IL to generate gradients of PMMA brush density.[204] The feature size of PMMA grown from photoinitiator SAM was as small as 100 nm. Nano-patterned POEGMA brushes grown from pre-fabricated initiators using ATRP have been achieved by Leggett and co-workers.[191] UV light with a wavelength of 244 nm was used to selectively remove the halogen atoms of ATRP initiator. Nano-structured POEGMA was achieved and such brushes exhibited a full width at half maximum height of 78 nm with a period of 225 nm.

1.3.3 Electron beam lithography

Electron beam lithography (EBL) offers ultra-high resolution fabrication of patterns in SAMs.[205-206] Organic thin film have shown to be sensitive for exposure to electrons.[207] There are some drawbacks of using this technique. EBL operates in a clean room facility, and it requires ultra-high vacuum. Also, nanofabrication over large areas is time consuming. EBL has been used to fabricate SAMs of octadecylphosphonic acid (ODPA) on aluminium to produce nanolines and spaces of ca.100 nm.[208] Octadecylsiloxane SAMs have also been patterned using this technique to generate high resolution patterns of ca.10 nm.[209]

Ober and co-workers reported direct patterning of PMMA, poly(2-hydroxyethyl methacrylate) (PHEMA), poly(isobutyl methacrylate) (PIBMA), poly(neopentyl methacrylate)(PNPMA), and poly(2,2,2-trifluoroethyl methacrylate) (PTFEMA) brushes grown on silicon, in a single step by electron beam lithography to obtain nanopatterned polymer brush surfaces. Using this technique, nanostructured polymer brush patterns with high resolution (down to 50 nm lines) were obtained.[210] Paik et al. have also directly fabricated complex PHEMA and PMMA brushes structures with nano-scale features by means of electron beam lithography.[211] In addition, the authors fabricated sub-surface polymer brush channels with nano-scale features.[211] With the chains tethered to a surface, a diblock copolymer brush with a negative tone upper layer (polystyrene) and a positive tone underlayer (either PMMA or PHEMA) were patterned in order to create channels.

1.3.4 Scanning probe lithography (SPL)

Surface characterization techniques have been developed in order to identify the small size of patterned features.[171] Scanning tunnelling microscopy (STM), atomic force microscopy (AFM) and near-field scanning optical microscopy (NSOM) are designed to image surfaces.[14] Scanning probe methods allow identification of the structure of surfaces and adsorbates at molecular or even atomic resolution.[212] The basic principle of scanning probe methods is that a sharp tip (< 50 nm) scans in proximity to the sample surface. These techniques can be applied to both inorganic and organic substrates, as well to determine the interaction forces between proteins and receptors in bio-based applications.[171]

Scanning probe-based lithography (SPL) was developed after the invention of STM.[212] Currently, SPL methods have become widely used in the fabrication of surface nanostructures because of their low cost and in view of the high resolution that can be

achieved.[213] In SPL techniques, the position and direction of the probe can be controlled during patterning.[214] Moreover, patterning large areas has become possible using highly developed multi-probe systems and automated scanning probe equipment. Furthermore, patterns and chemical modifications on surfaces are useful for both the top-down and the bottom-up approaches.[213] Recently, several methods have been developed based on the SPL technique in order to increase its productivity. Most SPL methods rely on either elimination or modification of the surfaces.[167]

1.3.4.1 Scanning near-field optical microscopy (SNOM)

The concept of scanning near-field microscopy at optical wavelengths first appeared in the late 1980's, after the invention of the STM. The most important part of a SNOM is its probe.[214] Generally, a SNOM probe consists of three parts: the wave guide to deliver the radiation to or from the SNOM tip, a tapered intermediate region to link the wave guide to the SNOM tip, and a sub-wavelength size aperture to limit the interaction of the radiation with the target surface. Al-coated quartz tips were used initially, but tapered fibres are now widely used as standard SNOM probes.[214] The preparation of fibre probes is achieved by either etching the fibre in HF or by heating in a laser and pulling to yield a sharp tip. To prevent leakage of the electric field through the probe, the fibre must be coated with a metal such as aluminium or gold.[186] There are two kinds of SNOM probe that can use optical apertures. The first probe is based on a bent optical fibre. The second one utilizes a cantilever-style probe (such as that used in atomic force microscopy) which has a small aperture at its apex. This type of SNOM probe is effective but not as commonly used as the optical fibre probe.[186,215]

SNOM instruments have been used to carry out lithography on surfaces (Figure.1.15). Many surfaces, including thin films and oxide substrates, have been patterned using this technique.[187,189,193,216-217] Self-assembled monolayers of alkanethiols on gold have been patterned using near-field optical methods.[216-217] SAMs were exposed using UV light with a wavelength 244nm to convert the alkanethiols to alkylsulfonate species. Patterns of proteins with nanometre-scale features have been prepared by exposing a film of protein-resistant oligo(ethylene glycol) (OEG)-terminated to UV light so as to photo-oxidize the head groups, then proteins were immobilized on the exposed area.[215]

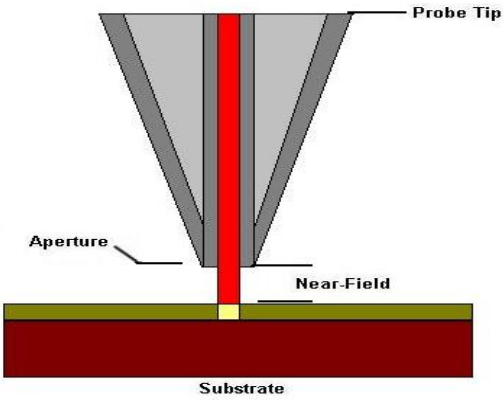

Figure 1.15 Schematic representation of the SNOM probe process used to modify the surface.

Sub-40 nm patterns on gold were achieved using near-field optical lithography.[188] Self-assembled monolayers have been widely applied in the fabrication of sub-micrometre sized structures. A scanning near-field optical microscope coupled to a UV laser (244 nm) was used to form nanometre-scale patterns in SAMs by Sun et al.[216] Well-defined features with sizes of 40 nm, and occasionally 25 nm, were achieved. Moreover, SNOM coupled to a UV laser has been used to fabricate self-assembled monlayers of alkanethiols on gold by Leggett and co-workers.[217] Molecular features widths of 20 nm (smaller than the aperture in the SNOM probe) have been successfully achieved. Ducker et al. reported the fabrication of structures on gold films by etching the gold surface using alkylthiol resist.[188] The exposure of the SAMs to UV light with a wavelength of 244 nm generated alkylsulfonates that were weakly bounded to the surface. After gold etching, nano-structures were formed that exhibited good edge definition with 30 nm full width at half-maximum depth (fwhm).[188] Leggett and co-workers also reported a direct patterning of POEGMA brushes using SNOM coupled to 244 nm radiation.[193] The UV light caused a photodegradation of the polymer and created nanometer scale lines with feature of 200nm width and 9 nm depth.[193]

1.3.4.2 Dip-pen lithography

In 1999, Mirkin's group invented a technique now known as dip-pen nanolithography (DPN).[218] DPN is a constructive technique and relies on transferring material (ink) from an AFM tip to the surface to write the patterns directly with submicrometer resolution (Figure 1.16).[212] The transferred material can be either the constituents of the AFM tip itself (induced

by current or force), or can be physisorbed materials on the AFM tip.[168] The inks in the tip are transferred to the substrate via capillary forces.[218] The ink is adsorbed chemically or physically to the surface.[173] The original DPN technique was used to pattern alkanethiol self-assembled monolayers onto gold substrates with high resolution.[168] Since then, it has been extensively used to transport small organic molecules, proteins and polymers of submicron dimension and a variety of surfaces have also have patterned, including insulating, semiconducting and metallic substrates.[168,218] Dip-pen lithography allows nano-structures to be generated on a surface with more than one ink by using a second tip to functionalize an area next to a previously prepared structure constructed with another ink.[171] The pattern resolution depends on the scanning speed, the surface chemistry, the ambient humidity and temperature.[173]

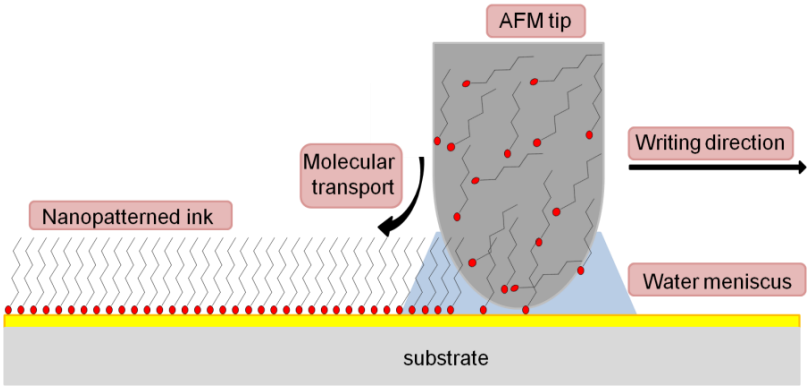

Figure 1.16 Schematic representation of the DPN process. A water meniscus forms between the AFM tip which is coated with transferred materials (ink) and the substrate.

DPN is used to generate patterns of polymer nanostructures and can be accomplished by delivering the polymer molecules directly from either solution or the melt to the target substrate.[173] The DPN method has also been used extensively to immobilize proteins on surfaces. For example, proteins could be successfully positioned on a gold substrate in nanoarrays with diameters of 200 nm.[171] DPN has been used to immobilized initiators on the surface, followed by growing brush.[219-220] For example, Zhou et al. used parallel dip-pen nano-lithography to pattern a surface with initiator over millimetre length scales.[220] They achieved high defined 3D polymer structure after the brush had been grown. The DPN technique has been successfully applied in the patterning of molten polymers. Patterns of poly(3-dodecylthiophene) have been obtained using an AFM tip integrated with a heater. The

generated patterns were multilayers of poly(3-dodecylthiophene) with the allyl groups oriented perpendicular to the surface. To transfer the polymers from the tip, the temperature of the tip must exceed the melting temperature of the polymer.[173]

1.3.4.3 Local oxidation patterning

In 1993, lithography by local oxidation was successfully transferred from STM to AFM.[221] The oxidation process has been applied to pattern many different substrates including Si, Ti, SAMs and organic resists.[222] In 1995, AFM lithography was first applied to a Si substrate coated with a thin film of a siloxane, in order to demonstrate probe lithography with 40 nm resolution. The oxidation of the terminal organic end groups can be obtained by applying a bias voltage between a conductive AFM tip (e.g. boron-doped tungsten carbide or copper- and silver-coated silicon nitride) and a sample.[171]

A conductive AFM tip has been employed to generate patterns of chemically-active groups on OTS SAMs on silicon by converting $–CH_3$ groups of the base monolayer to –COOH sites.[223] Nanolines of MoO_3 were fabricated by local-probe oxidation.[224] Mo was evaporated to form a layer on the top of PMMA film supported by Si. The Mo film was locally oxidized by local-probe oxidation to produce a pattern of MoO_3 features of 35 nm width. Zhang and co-workers used AFM tips coated with Pt to pattern 1-hexadecanethiol monolayer on Au by oxidizing the methyl groups of the monolayer.[225] Micro- and nanopatterning oligo(ethylene glycol) (OEG)-terminated alkyl monolayers on silicon substrates were reported by Qin et al.[226] They suggested that carboxylic acid and aldehyde groups on the surface were generated when OEG film is oxidized. Avidin was then immobilized onto the oxidized regions.

1.3.4.4 Mechanical surface patterning

The aim in AFM is to image without damaging the surface. However, imaging soft materials (organic materials) in contact mode (with relatively hard tips and stiff cantilevers) can easily damage the surface.[171] Similar effects may occur during STM imaging of poorly conducting substrates or highly superconducting substrates when low or high current conditions reduce the tunnelling gap sufficiently to cause contact between the tip and the sample. The concept behind mechanical surface patterning using AFM tips is that forces larger than those used for AFM imaging loaded onto the tip should leave an indentation in the surface.[227] In this technique, either diamond tips or diamond-coated tips have been used to prevent excessive deformation during patterning of surfaces.[171]

Several metallic surfaces and films of soft materials can be successfully patterned by using a mechanical patterning technique (force lithography). Several pattern structures, including thin lines and pits, have been fabricated.[171] There has been strong interest in the patterning of polymers using AFM mechanical patterning. El Zubir et al. have used this technique to generate nanopattern of octadecylphosphonate SAMs at aluminium oxide surfaces.[228] Aminobutylphosphonate was then adsorbed to yield features as small as 39 nm. Films of PMMA and poly(ethylene oxide) (PEO) were successfully patterned using force lithography.[222] Kaholek et al. demonstrated the preparation of nanopatterned poly(N-isopropylacrylamide) (PNIPAAM) on gold surface.[229] AFM tip was used as manomechanical tool to remove methyl-terminated 1-octadecanethiol (ODT) from the surface. Then ATRP initiator was immobilized, followed by SI-ATRP of PNIPAAM to yield nanopattern polymer brush.

1.4 Objectives and outline of the thesis

This thesis introduces the synthesis of polymer brushes via SI-ATRP, and the use of photolithographic techniques to pattern these surfaces. Very little work investigating the pH-responsive behaviour of well-defined *secondary* amine methacrylates, *zwitterionic* polymer brushes containing amino acid as side-chains, and binary patterned gold/polymer brush structures has been reported in the literature. The goal of this work was to expolare the possibility of using ATRP in combination with photolithography to produce biologically functional, stimulus-responsive polymer nanostructures. A long-term goal is the integration of such structures with supported lipid bilayers containing integral membrane protiens. This thesis describes the development of enabling methodologies designed to facilitate this goal. The relevant surface analysis techniques in chapter 2, and the results are presented in chapters 3 to 6. Chapter 3 focuses on the synthesis and pH-responsive behavior of poly(2-*tert*-butylaminoethyl methacrylate) (PTBAEMA) brushes. Chapter 4 describes the synthesis and nanometer-scale patterning of stimulus-responsive, biofouling-resistant zwitterionic poly(amino acid methacrylate) brushes. The development of new polymeric system supported lipid bilyers was presented in chapter 5. Chapter 6 describes the preparation of binary-patterned gold/ poly(amino acid methacrylate) brushes. The final chapter presents the conclusion and future work for this study.

Chapter 2: Experimental

2.1 Materials

Silicon wafers ([100] orientation, boron doped, 0-100 Ω cm) were obtained from Compart Technology (Peterborough, UK)). The dopant is present at very low concentration and does not influence the brush density. Glass slides (22 mm x 64 mm and thickness = 1.5 mm) were bought from menzel-glaser. Deionised water was obtained using an Elga Pure Nanopore 18.2 MΩ system. A carousel 12 Reaction Station (Radleys, UK) was used to prepare polymer brush samples under nitrogen.

Chemicals were analytical reagent grade and were used as received from the manufacturer. 3-Aminopropyltriethoxysilane (APTES) (98.0+ %), 2-bromoisobutyryl bromide (BIBB) (98%) and triethylamine (99%) were purchased from Sigma-Aldrich UK (Gillingham, UK), as well as copper (I) bromide (98.0+ %), copper (II) bromide (99.0+ %), copper (II) chloride (99.0+ %) (Cu (II) Cl_2), copper (I) chloride (99.995+ %) (Cu (I) Cl), 2, 2'-bipyridyl (99.0+ %) (BiPy), 2-(tert-butylamino) ethyl methacrylate (97.0 %) (TBAEMA), tolylene 2, 4-diisocyanate-terminated poly propylene glycol (PPG-TDI), 3-sulfopropyl methacrylate potassium salt (98%) (KSPMA), 2-(methacryloyloxy)ethyl trimethylammonium chloride) (80 wt. % in H_2O) (PMETAC), tris(2-pyridylmethyl)amine (98.0%) (TPMA), dimethylphenyl phosphine (99.0%) (DMPP), phosphate buffered saline (PBS), L-cysteine (97%), deuterium oxide (99.9%), 3-(acryloyloxy)-2-hydroxypropyl methacrylate (99%), methoxy-capped oligo(ethylene glycol) methacrylate (480 g mol^{-1}), potassium chloride (>99%), 2-amino-1,1,1-trifluoroethane (98%) (TFEA), chloroform-d (99.8 %), n-octadecanethiol (98.0%), mercaptoethylamine hydrochloride (≥ 98%) and 6-amino-1-hexanethiol hydrochloride. 2-(Methacryloyloxy) ethylphosphorylcholine monomer (MPC, >99% purity) was kindly donated by Biocompatibles Ltd. Glutaraldehyde solution (50.0 % in H_2O) was purchased from Alfa Asear. Aluminium oxide and magnesium sulfate were obtained from Fisher Scientific (Loughborough, UK). METAC and TBAEMA monomers were purified using an aluminium oxide column to remove the inhibitors.

Methanol (99.8%, HPLC grade), 2-propanol (99.5%, HPLC grade), dichloromethane (HPLC grade), and ethyl acetate (HPLC grade) were obtained from Sigma-Aldrich UK (Gillingham, UK). Hydrogen peroxide (30 %), sulfuric acid (95.0 %), ethanol (99.8%, HPLC grade), ethanol (99.8%, analytical grade), ammonium hydroxide (analytical grade) and dichloromethane (HPLC grade), acetone (99.8%, HPLC grade), dichloromethane (HPLC

grade), tetrahydrofuran (99.5 %, HPLC grade) (THF), hexane (HPLC grade) and ethyl acetate (HPLC grade) were obtained from Fisher Scientific (Loughborough, UK).

2.2 Cleaning glassware and substrates

All glassware and substrates were cleaned with piranha solution to minimize the contamination. Piranha solution consists of a mixture of hydrogen peroxide (30%) and concentrated sulfuric acid (70%) in the ratio of 3:7 respectively. (**Caution**: *Piranha solution is an extremely strong oxidizing agent which has been known to detonate spontaneously upon contact with organic material*). Extra care is taken when using piranha as it is potentially very dangerous and it is always used inside a fume hood using a blast shield, thick rubber gloves and goggles. The glassware was first cleaned by acetone, water and then dried. The substrates were placed individually into samples tubes to be fully cleaned. Hydrogen peroxide was first added to the glassware and substrates, and then sulfuric acid was added. The glassware and samples were left in the piranha solution until it was cool. The solution was discarded into dilution tank. Then the substrates and glassware were washed with deionised water for several times then sonicated for 10 min and then rinsed with deionised water.

After piranha solution, the RCA (Radio Corporation of America) method was employed on silicon wafers and glass before a silane formation. The substrates were submerged in a solution of ammonium hydroxide, 30% hydrogen peroxide and deionised water in the ratio of 1:1:5, respectively. The solution was heated to 85 °C for 30 min and left to cool. The samples were washed with deionised water at least 5 times and sonicated for 10 min, and then dried in an oven at 120 ^{o}C in an oven for an hour.[191,230]

2.3 Formation of self-assembled monolayers (SAMs)

2.3.1 Silane initiator

Glassware was cleaned using piranha solution before used. Silane SAMs were prepared by immersion of silicon wafer or glass microscope slides in a solution of 3-aminopropyltriethoxysilane (APTES) 2% (v/v) in ethanol (HPLC grade). After the substrates had been immersed in this solution for 30 min, the samples were rinsed with ethanol, dried under N_2 and then baked for 30 min at 120 ^{o}C.[191,193,230] Aminosilane SAMs were immersed in a solution of bromoisobutyryl bromide (BIBB) (0.37 mL, 3 mmol) and triethylamine (0.41

mL, 3 mmol) in 60 ml of dichloromethane (DCM) for 30 min. Subsequently, the samples were rinsed with ethanol and DCM and dried under nitrogen.[231]

2.3.2 Thiol monolayers

Gold deposition on glass microscope slides was carried out using an Edwards Auto 306 evaporator system (BOC Edwards UK) at a pressure ca. 8.0 x 10^{-7} mbar. Before gold (ca. 20 nm) was deposited on the glass, an adhesion layer of titanium or chromium (ca. 5 nm) was evaporated first. The evaporation rate was ca. 0.1 nm s^{-1} for Ti or Cr, and 0.4 -1 nm s^{-1} for Au. The gold slides were immersed in cleaned sample vials, containing 1mM solution of n-octadecanethiol (ODT) in degassed ethanol, for approximately 24 h at 20 ^{o}C. Then the samples were removed, rinsed with ethanol and dried under N_2.[188]

2.4 Sample handling

Samples were only handled with tweezers to minimize surface contamination. The tweezers were cleaned with acetone and ethanol then dried under nitrogen before use. A diamond scribe and a metal ruler, cleaned with ethanol, were used to cut the samples. The silicon wafers and glass were cut into 1 cm^2 portions, followed by washing with ethanol and dried under steam of N_2.

2.5 Surface characterizations

A variety of surface analysis techniques were used to characterize outermost nm of the samples. These provide detailed information on thin organic layers such as the chemical composition, the chemical structure, the topography and the physical properties.

2.5.1 Contact angle measurements

2.5.1.1 Background

The contact angle of a solid-liquid-vapor syatem is defined as the angle between the liquid–vapor and solid–liquid interfaces.[232-236] The contact angle measurement provides information on the outermost few angstroms surfaces.[232] The contact angle measurement can be carried out in two different manners: advancing contact angle, (θ_A) and receding contact angle (θ_R), as shown in Figure 2.1. The advancing contact angle is assessed in the process of dropping the liquid onto the surface, and the receding contact angle is taken while withdrawing the liquid from the solid surface. [232,234-236]

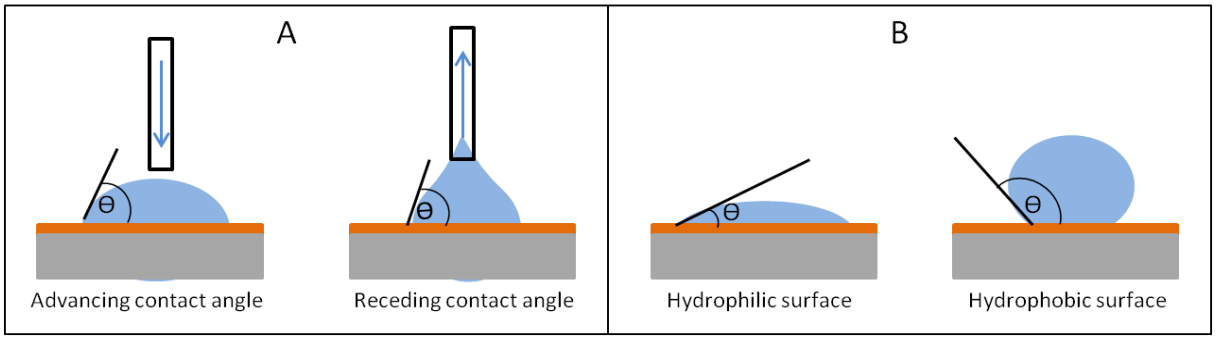

Figure 2.1. Illustration of (A) advancing and receding contact angle measurements. (B) the different in hydrophobicity of surfaces.

The shape of the drop resting on the surface depends on the thermodynamic equilibrium around the perimeter of the drop. The contact angle can be measured directly using a microscope fitted with goniometer scale. Young's equation describes the relationship between the contact angle and the interfacial tension:

$$\gamma_{SL} + \gamma_{LV} cos\theta_o + \gamma_{SL} = \gamma_{SV} \qquad (2.1)$$

where γ_{SL} is the interfacial tensions between the solid and the liquid, γ_{LV} the interfacial tension between gas and vapour, γ_{SV} is the interfacial tensions between the solid and the vapour, and (θ_o) is the contact angle between liquid and the surface.[233-236]

2.5.1.2 Experimental procedure

Advancing sessile drop contact angles were measured using a Rame-Hart model 100-00 goniometer (Netcong, NJ). A microlitre syringe was used to place a 2 µL drop of water onto the surface of the sample. The sample stage was lowered until the water droplet separated from the tip of the syringe. The angle between liquid/vapour and solid/ liquid interface was measured. The contact angle was measured at five different locations on the sample and averaged.

2.5.2 Atomic Force Microscopy (AFM)

2.5.2.1 Introduction to AFM

Binnig, Quate and Gerber invented the atomic force microscope (AFM) in 1986, just after the invention of scanning tunnelling microscope (STM).[237] The STM has been used to investigate the surfaces of conductor materials, however the AFM is used to study the

surfaces of a wide range of materials.[237-238] It can be used in ambient air, liquids or ultra-high vacuum (UHV).[239] In its modern form, the AFM consists of a cantilever with a sharp tip (with a radius at its apex typically in the range 10-100 nm) that is scanned across the sample surface, a sensitive photodetector measuring the deflection of the cantilever, a piezoelectric tube, to control the scan motions, and a feedback system that maintains a constant force between tip and sample. A piezoelectric material is one that contracts or expands in response to a potential difference.

Figure 2.2 shows a schematic diagram of an atomic force microscope. The cantilever is placed parallel to the sample surface and then a laser beam is focused on the back of the cantilever-tip and reflects onto the sensitive photodetector.[240-241] The force between the tip and the sample causes a variation in the deflection of the laser beam and changes the position of the laser spot on the photodetector. When probe is scanned, the tip scans across the sample surface to measure local properties such as topography, friction, electrical, magnetic etc.[238,241-242]

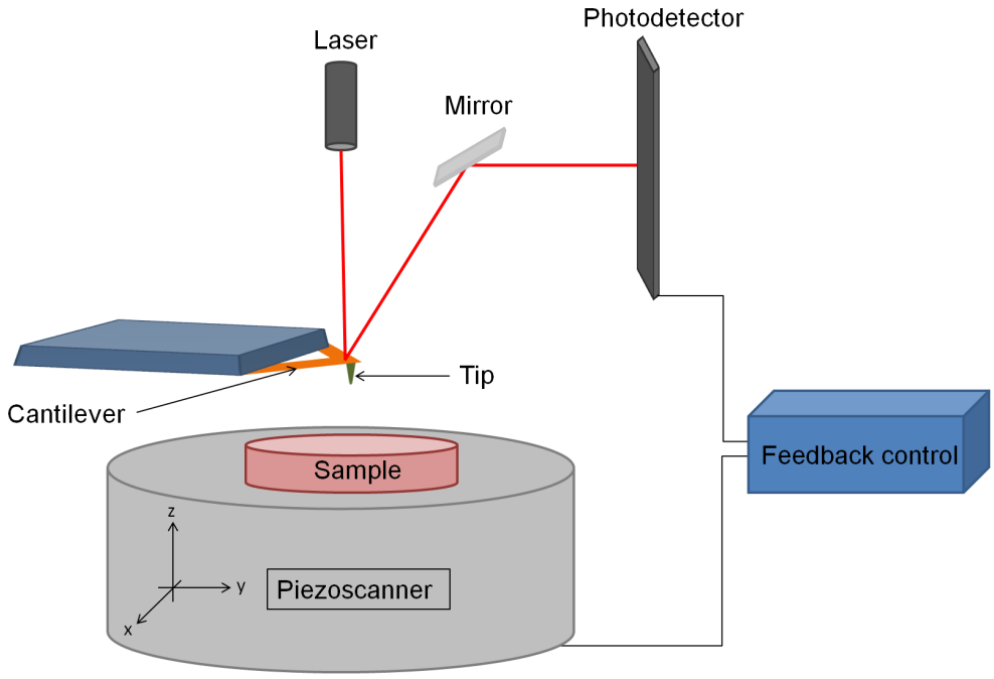

Figure 2.2. Schematic diagram of an atomic force microscope (AFM).

Three modes of operation are available in AFM: contact mode (the most commonly used), non-contact mode and tapping mode. In contact mode the tip is in mechanical contact with

the surface, and the repulsive forces between the tip and sample are measured.[243-244] In ambient conditions, a water meniscus is formed when the tip contacts the surface which can roughly affect the interaction force.[244-245] The effect of water capillary condensation can be minimised by performing the experiment under an organic solvent such as ethanol. Cantilevers made of silicon nitride with a relative low spring constant are used in this mode. Contact mode is the most used for imaging hard materials such as gold; however soft materials, polymers for example, have smaller moduli and are susceptible to probe-induced damage.[246] In non-contact mode, the cantilever oscillates close to the sample and the changes in the interactions between the tip and the surface are measured.[243]

In the tapping mode, which is the most frequent mode of operation after contact mode, the cantilever is oscillated with high resonant frequency (300 kHz) and the tip strikes the surface. The feedback loop can be adjusted to control the tip-sample interaction to keep the set point, which might be created by the amplitude of modified oscillation, at a constant value to produce a topographic image.[244,247] The cantilevers are made from silicon with larger spring constants than those that are used for contact mode. Tapping mode has been developed to reduce the contact and lateral forces between the tip and sample surface so it is useful technique when imaging soft material and biological molecules.[248] Moreover, phase images can be acquired in tapping mode by measuring the oscillation damping of the cantilever when the tip strikes the surface, so the differences in mechanical properties of the surface can be distinguished.[247-248]

2.5.2.2 Friction force microscopy (FFM)

Friction force microscopy (FFM) is a powerful technique to provide information about chemical compositions, molecular organization, and mechanical properties for the surface. In addition FFM provides nano-scale resolution with high sensitivity and can be employed to obtain quantitative data.[242,249-251] FFM is based upon the measurement of the lateral interaction force between the tip and the surface while the tip scans across the sample. The lateral deflections of the cantilever are measured using a laser beam reflected from the backside of the cantilever to a photodetector. [242,249]. Lateral deflections result from the load resolved in the plane of the surface and the frictional interactions between the tip and the sample. The trace and retrace data (scans acquired with opposite directions of the tip motion) is subtracted to remove the topographical effects.[242] In chemical force microscopy the chemical nature of the tip is fixed (e.g. by deposition of a self-assembled monolayer or by

other means) so that changes in the friction force in response to changes in chemical composition may be measured. For examples if the tip interacts strongly with polar regions of the surface more than non-polar regions the cantilever will be deflected further in the lateral direction when traversing polar regions, and a larger lateral signal at the photo-detector will be detected.[249,252] FFM can be used under an appropriate liquid such as ethanol to reduce water capillary that condensate between the tip and surface.[242]

FFM can be employed to obtain quantitative data.[249] The normal force can be calculated if the spring constant of the cantilever and the photodetector signal are known.[238,242,249] The frictional force data can be fitted into contact mechanics models.[242,249] Amontons' Law describes the relationship between the friction force (F_F) and the normal load (F) by:

$$F_F = \mu F \qquad (2.2)$$

where μ is the coefficient of friction. The friction coefficient is represented from the slopes of the F_F vs. F curves. In principle, Amontons' law is based on contacts multiple asperities on the sliding surfaces. It is applied in the situations where there is nonadhesive sliding. It has been suggested that a single asperity would be more accurate in modelling friction data acquired by AFM. The Johnson-Kendall-Roberts (JKR) model is an adaptation of the Hertz model for mechanics that takes account of adhesive force. The JKR model is applied when the adhesion between the surface and the tip is strong.[242,249] The contact area A between a sphere of radius R and a plane can be calculated at zero loads:

$$A = \pi\left(\frac{R}{K}\right)^{\frac{2}{3}}\left(F + 3\pi\gamma R + \sqrt{6\pi\gamma RF + (3\pi\gamma R)^2}\right)^{\frac{2}{3}} \qquad (2.3)$$

Where R is the radius of the probe, γ is the interfacial tension and K is the elastic modulus.

The Derjagun-Muller-Toporov (DMT) model can be applied for when the elastic deformation of the asperity is small. In the DMT model, the adhesion forces between the materials and tip radii is weak.[242,249] The contact area is given by:

$$A = \pi\left(\frac{R}{K}\right)^{\frac{2}{3}}(F + 4\pi\gamma R)^{\frac{2}{3}} \qquad (2.4)$$

2.5.2.3 Experiment

Atomic force microscopy was carried out using a Digital Instruments Nanoscope IV Multimode Atomic Force Microscope (Veeco, Santa Barbara, USA) with a 'J' scanner (0 - 125 µm). Two main modes were used to image the surface, depending on need: contact mode and tapping mode. Each mode has different type of tip; silicon nitride nano-probes (Digital Instruments, Cambridge, UK) containing 4 cantilevers with different force constants (used 0.06 or 0.12 N m^{-1}) and tip radii in the range 20-60 nm were used for contact mode imaging. Silicon probes containing one cantilever with average spring constants between 20 and 80 Nm^{-1} were used for tapping mode.

Samples were washed with ethanol or methanol and dried under dry nitrogen before use. The samples were fitted to metal disc using carbon double-sided adhesive tape. The metal discs were placed on the scanner head. The optical video feed on the microscope was used to position the probe on the sample.

In both contact mode and tapping mode, the tip was mounted in the cantilever holder, then placed over the sample. The laser was aligned on the end of the tip then the horizontal and vertical positions of the photodetector were aligned. The tip was then manually moved towards the surface until it was almost in contact with the surface. In tapping mode the tip was tuned using a routine in the software to find the resonant frequency of the tip. The software was used to drive the tip to be in interaction with the surface so that an image could be acquired.

2.5.2.4 Image Acquisition

In contact mode, height and the friction images were at a scan angle 90^{o}, an acquisition rate of 2 Hz and typical gain settings of 1 and 1.5 for the integral and proportional respectively. The deflection setpoint was determined in each experiment using the software to control the force on the sample. For tapping mode height and the phase images were acquired, in general with a scan angle of 0^{o}, scan rate of 2 Hz and typical gain settings of 0.2 for the integral and 0.3 for the proportional. A liquid cell was used when the sample required imaging in liquid in both contact and tapping mode images. For imaging under liquid, a dry image was taken then the cantilever was brought out from the contact from the surface and then the liquid flushed through the cell. The photodetector was aligned again and the tip was driven towards the surface and then an image was taken.

2.5.3 Ellipsometry

2.5.3.1 Background

Ellipsometry is a non-contact, non-destructive optical measurement technique which can be used to measure the thickness of thin films from less than a nanometer to several microns, roughness and other material properties.[253-256] Ellipsometry utilizes polarized light and measures the change in polarization that occurs upon reflection or transmission from a sample, and then compares it to a model. Ellipsometric measurements must be made on reflective samples. The material properties can be determined from the polarization changes.[253-255]

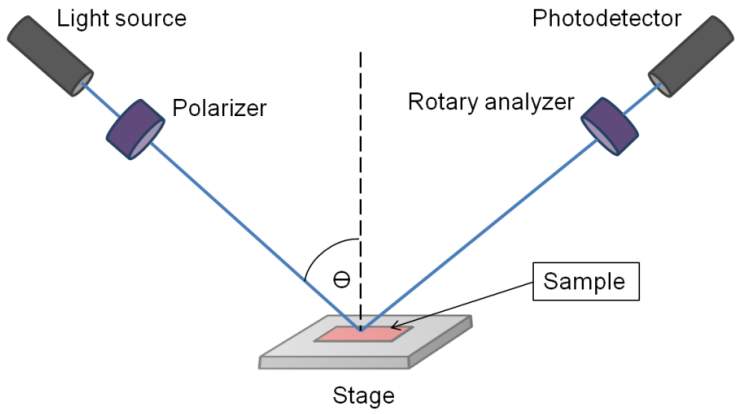

Figure 2.3. Schematic diagram showing the basic principles of ellipsometry.

Figure 2.3 illustrates the basic principles of ellipsometry. An unpolarized light source is used (usually a He-Ne laser with wavelength (λ) = 632.8 nm). This light beam is polarized. The beam hits the sample at a defined angle, penetrates into the layers and reaches the interface between the layer and the substrate, from where it is reflected. The light beam leaves the sample with the same angle as the incidence angle and passes through a rotating analyzer, which enables measurement of the refelctions from all phases, before hitting a photodetector. Finally, the intensity of the incoming light as a function of the angle of the rotating analyzer is measured by a photodetector.[255,257] The recorded data are transferred to a computer for the calculation of material properties (such as film thickness and/or refractive indices).

2.5.3.2 Experimental procedure

Ellipsometric studies were conducted using a Alpha-SE ellipsometer (J. A. Woollam Co., Lincoln, NE, USA) equipped with a He-Ne laser ($\lambda = 633$ nm) at an incident angle (Φ) of 70^{o} from the normal. Ellipsometric thicknesses were calculated from silicon substrate models. Measurements were conducted from 300 to 700 nm and modelling was performed using WVASE software (J. A. Woolam Co., USA). Fit quality was assessed using the root mean square error (RMSE) between the measured and modelled ellipsometric constants Δ and Ψ over all measured wavelengths. The dry films were modelled as a single layer of variable thickness with refractive index given by the Cauchy parameters of An 1.5, Bn 0.005 μm^2.The ellipsometric brush thickness for each sample was determined in at least three different places on the wafer and reported as the mean ± standard error.[258] *In situ* measurements of brush thickness in aqueous solution were conducted using a home-made liquid cell. The sample cell was rinsed several times with deionized water between each measurement. Ellipsometric data were fitted using a single slab model with a refractive index given by a linear effective medium approximation (EMA) between the wet brush and water.[165,259] Again, three measurements were recorded for each brush sample and reported as the mean ± standard error.

Comparison of the ellipsometric and AFM thicknesses (patterned samples) for PMPC, PTBAEMA, PKSPMA, PMETAC and PCysMA brushes revealed that the differences in dry state were relatively small (maximum difference ca. 4 nm) and the maximum difference in wet state was ca.9 nm (see Table 2.1). Generally, AFM tended to give a higher layer thickness than ellipsometry although there is a reasonable agreement between the two methods which suggests that either could give a good estimate of brush thickness.

Table 2.1. Comparison of some polymer brush thicknesses measured by ellipsometry and AFM, in both dry state and under PBS buffer solution.

Samples	**Ellipsometric Brush Thickness / nm**		**AFM Brush Thickness / nm**	
	Dry Brush	*Wet Brush*	*Dry Brush*	*Wet Brush*
PMPC	12.2 ± 0.1	45.8 ± 0.8	10.0 ± 0.5	35 ± 1.2
PTBAEMA	16 ± 0.2	58.5 ± 1.3	14.5 ± 0.8	62 ± 2.5
PKSPMA	33.8 ± 0.4	57.6 ± 0.9	30 ± 1.7	66 ± 3.1
PMETAC	15.4 ± 0.2	28.8 ± 0.4	17 ± 1.2	35 ± 1.9
PCysMA	16.2 ± 0.2	27 ± 0.8	15 ± 1	28.5± 1.7

2.5.4 X-ray Photoelectron Spectroscopy (XPS)

2.5.4.1 Background

X-ray photoelectron spectroscopy (XPS), also known as electron spectroscopy for chemical analysis (ESCA) was developed in 1960s by Kai Siegbahn. This technique is widely used for surface analysis with a wide range of materials, starting from Li to U. XPS can provide information on the surface composition and the chemical environments of the molecules that are bonded to the surface, such as their oxidation states. In XPS the sample is irradiated with X-rays which causing the ejection of electrons from the surface, with sampling depth of 10 nm. Each element produces photoelectrons with a characteristic kinetic energy (KE). The chemical composition of the sample can be directly determined from the relative numbers of these ejected photoelectrons. The KE of the photoelectron is measured by the photoelectron spectrometer.[260-263] The binding energy (BE) of the electron is given by following equation:

$$BE = h\upsilon - KE - \varphi \qquad (2.5)$$

where φ is the electron spectrometer work function and the hυ is the characteristic energy of the X-ray photon. Variations in the binding energies (chemical shifts) as a result of changes in bonding lead to changes in the KE which are recorded by the spectrometer. The photoelectron spectrum is recorded as a function of KE. The relative concentrations of atomic species can be determined directly from the photoelectron intensities.[262-263]

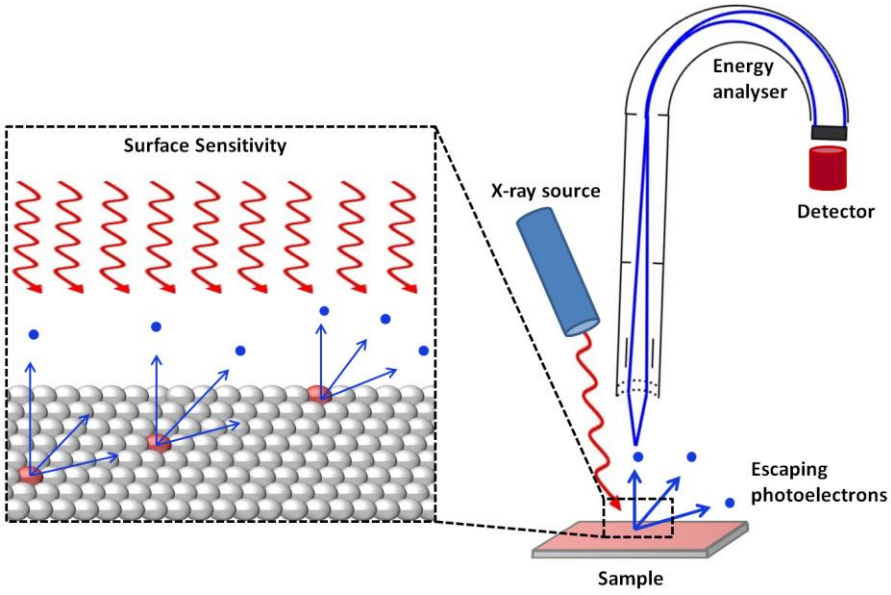

Figure 2.4. Schematic diagram showing the basic principles of photoemission in XPS.

As shown in Figure 2.4, an XPS instrument consists of an X-ray source, an electron energy analyser, a detector, and a vacuum system. Monochromatised Al Kα and Mg Kα X-rays are commonly used in XPS. The electron energy analyser measures the energy distribution of electrons ejected from the surface. A concentric hemispherical analyser (CHA) is commonly used to detect the photoelectrons. It uses electrostatic lenses to focus photoelectrons of different energies. The detector is a single channel electron multiplier. The XPS instrument operates under ultra-high vacuum (UHV) conditions, at pressure of ca. 10^{-10} mbar, to eliminate electron scattering by gas molecules, and to reduce the adsorption of residual gas molecules onto the sample.[260]

2.5.4.2 Experiment and data analysis

X-ray photoelectron spectroscopy was carried out using a Kratos Axis Ultra spectrometer (Kratos Analytical, Manchester, UK) with a monochromatized Al Kα X-ray source operating at a power of 150 W with an emission current of 8 mA and a pressure in the analysis chamber between 10^{-8} to 10^{-10} mbar. Electron energy analyzer pass energies of 160 eV and 20 eV were used to acquire survey (wide) scans and high resolution spectra, respectively. The wide scan provides general information on the sample composition, while the narrow scan provides information on the bonding environment of the molecules at the surface.

The samples were prepared with approximate dimensions ca. 5x5 mm^2 and then rinsed with ethanol and dried under dry N_2 before the experiment was run. High- resolution peaks were fitted and processed using CasaXPS software (Casa, http://www.casaxps.com, U.K.). Changes in the bonding to the surface cause small shifts in the binding energy. A carbon atom in a hydrocarbon gives an unshifted C 1s peak at a BE of 285.0 eV, thus all binding energies were referenced relative to the alkyl chain peak C1s, 285.0 eV. This is because the majority of organic thin film contains C-H bonds. Carbon–heteroatom bond shifts C 1s peak due to the electron density around C atom. A list of common shifts is given in Table 2.2.[260]

Table 2.2. Common C 1s chemical shifts (eV) relative to saturated hydrocarbon.

Functional Group	***Structure***	***Binding Energy (eV)***
Hydrocarbon	C—H	285.00
Amine	C—N	285.94
Ether	C—O	286.45
Carbonyl	C=O	287.90
Carboxylic Acid	COOH	289.26
Perfluoro (CF_3)	C—F	292.69

2.5.5 Laser Scanning Confocal Microscopy

Scanning confocal microscopy was first described and patented by Marvin Minsky in 1961.[264] The basic principles of this technique are shown in Figure 2.5. First, the sample is illuminated by passing a laser beam through a spatial filter and a beam splitter, through objective lens, to yield a diffraction-limited spot at the sample. Then, the emitted fluorescence is reflected through the beam splitter, allowing light from the sample (longer wavelength) reach the detector. The microscope detects only the fluorescence within the focal plane and eliminates out of focus light by using a spatial pinhole.[265-266]

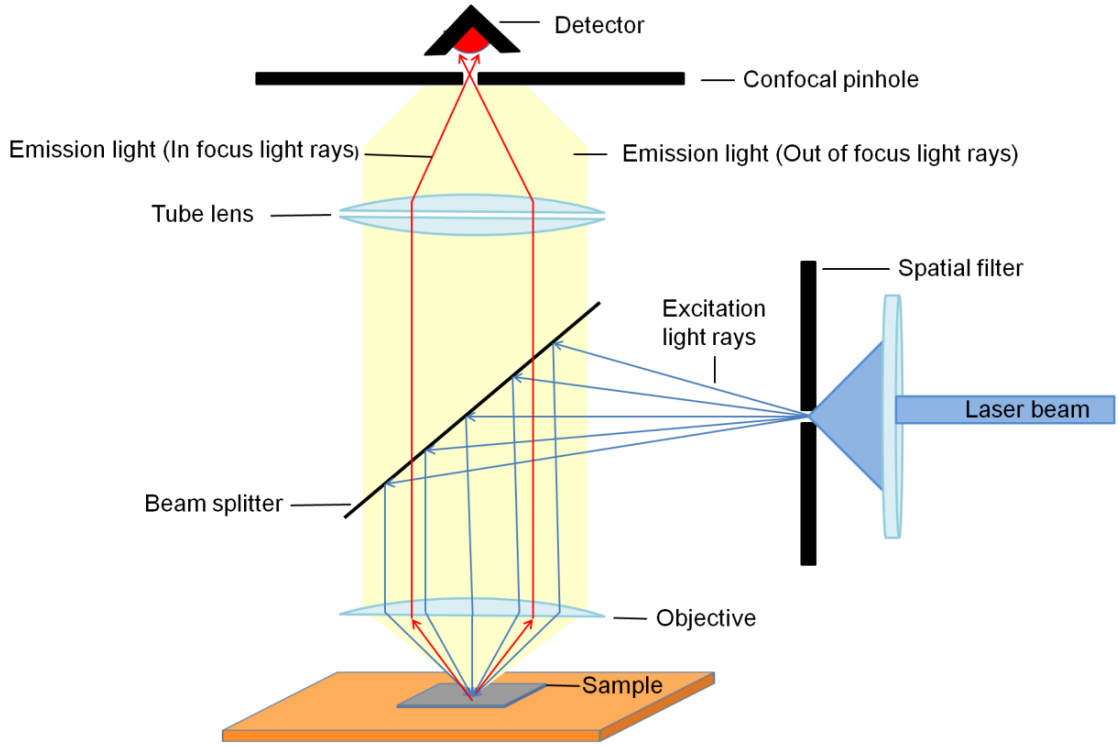

Figure 2.5. Schematic diagram showing the operation of a laser scanning confocal microscopy.

Confocal fluorescence microscopy images were acquired using a LSM 510 meta laser scanning confocal microscope (Carl Zeiss, Welwyn Garden City, UK). The sample was placed on a glass microscope slide. A droplet of Citifluor as an antifade reagent (glycerol-PBS solution, AF1) (Citifluor Ltd., London, United Kingdom) was added to the sample surface and then another glass slide was placed on the top of the sample. A 63x magnification oil immersion lens with numerical aperture 1.40 was used to image the sample. A small drop of immersion oil (Immersol 518 F, Zeiss) was located on the slide, facing the center of the light. The 514 nm band of an Ar laser (1.5 mW) was used to excite fluorescence, and the

fluorescence was recorded at wavelengths above 535 nm. Band filters operating between 535 and 590 nm was used to block the incident light from the detector. The captured images were analyzed by Zeiss LSM image browser software (Zesiss, http://microscopy.zeiss.com, U.K.).

2.5.6 Surface Zeta Potential

2.5.6.1 Introduction to zeta potential

The electrical potential on a surface can dominate many of the important surface properties of polymer.[232] An electrical charge appears at the interface when a charged surface is in contact with a liquid phase.[232,267-268] An interfacial double layer is established at the location of the slip plane.[267-269] The zeta potential is the potential at the double layer, which is the different in the potential between the stationary layer and diffusion layer, as shown in Figure 2.6.[267-268]

Zeta potential measurement is a valuable technique for the acquisition of data on surfaces. Zeta potential measurement is an important technique to characterize the properties of polymer surface such as hydrophilicity, swelling and other physico-chemical properties.[232] Surface isoelectric points in surface ionizable groups can be determined using zeta potential measurements.[267,270-271] Ions adsorptions are determined by the potential and charge distribution on the surface.[232]

The zeta potential can be determined by measuring the electroosmotic mobility, the movements of a spherical particle in an applied E-field or the streaming potential.[268-269,272] The zeta potential can be determined directly from the electroosmotic mobility. The transit time of an optically active or conductive tracer through a microchannel (or capillary) can be measured as a function of the electric field, and the electroosmotic mobility is directly related to the zeta potential. While in the second method, which is commonly used in studies of colloidal suspensions, an electric field is applied across the sample and then the electrophoretic mobility (particles responsive) is measured by the light scattering of the particles.[268-269] The streaming potential is a technique used to determine the charge on fibre surfaces. The solution flows through a pad of fibres from the sample and then a known pressure is applied to push the solution. A potential is measured between electrode probes on either side of the pad and then the resulting voltage is compared to the voltage before

applying pressure. Zeta potential can be estimated from the streaming potential using the factors, including the electrical conductivity, fluid viscosity, and the structure of the fiber pad.[268]

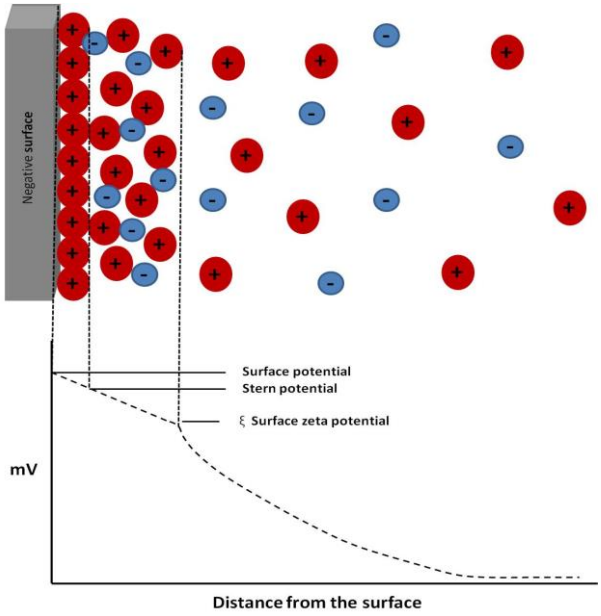

Figure 2.6. illustrates potential difference as a function of distance from particle surface.

2.5.6.2 Surface zeta potential cell theory

In the malvern's streaming potential cell, employed in the present work, the surface zeta potential of planar surfaces can be measured in the presence of tracer particles. The electrophoretic mobility of the particles is measured at varying distances from the surface.

The cell is in a dip cell format and designed with a rotating top attached to a screw thread which allow changing the sample height. The sample is attached to the sample holder and tied to the cell and then dipped into a cuvette a containing a medium and tracer particles. Applying an electric field via the electrodes that will initiate electrophoresis of the particles. Electro-osmosis will be established close to the surface. The mobility of the tracer particles will be different at different distance from the sample: the closer to the surface, the greater the significance of electro-osmosis. The effect of the electro-osmosis will decrease as the distance from the surface increases. The electrophoretic mobility of tracer particles is measured using Malvern Zetasizer NanoZS model ZEN 3600 instrument. The particle electrophoretic mobility will vary as a function of displacement from the sample surface. The

intercept (zero displacement) can be extrapolated by plotting the measured mobility, or zeta-potential, as a function of distance from the surface. The measured intercept is a necessary component to calculate the surface zeta potential because zeta potential always involves a component of the electrophoretic motion. The surface zeta potential can be given by the equation:

$$\xi_{surface} = -\text{intercept} + \xi\,\text{particle} \qquad (2.6)$$

where $\xi_{surface}$ is surface zeta potential, $\xi_{particle}$ is the zeta potential of the tracer and the intercept is extrapolated by plotting the reported mobility (zeta-potential), as a function of displacement from the surface.

2.5.6.3 Experimental procedure

Samples were prepared with dimensions of 5-7 mm, depth 4 mm and thickness 2 mm, rinsed with ethanol and dried under N_2. The sample was attached to the sample holder using cyanoacrylate adhesive. Once the adhesive had been cured, the sample was fitted in between two electrodes in the surface zeta potential cell, and the screw was tightened to secure it in place. By rotating the cell cap, the height of the sample was adjusted using a cell height alignment tube. The cell was placed in a cuvette contained 0.7 mL of the medium to be studied and (0.01%) PMPC-stabilized polystyrene latex particles as tracer. The PMPC-stabilized polystyrene was selected because its hydrophilic, permanently zwitterionic character should ensure no interaction with the brush chains at any solution pH. PMPC-PS nanoparticles were prepared by Prof. Steve Armes group. The cell and the cuvette were placed into a Zeta Nanosizer. The height of the sample was adjusted using the software to find the zero position against the laser. The temperature was set at 25 ^{o}C and four different displacements were used. Five measurements were made with a 50 s gap between measurements for the sample and a 20 s gap between the measurements for tracer. The measurements were performed at 125, 250, 375 and 500 μm from the sample surface. The final measurement was at 1000 μm, to determine the zeta potential of the tracer particles. Finally, the surface zeta potentials were determined by the software.

2.6 Photo-patterning of organic films

2.6.1 Micron-scale patterning

Photo-patterning was performed using a Coherent Innova 300C FreD argon ion laser (Coherent FreD 300C, Coherent U.K., Ely). The fundamental emission wavelength of this laser is 488 nm and the UV wavelengths (244 nm) are obtained after doubling the frequency of using a Brewster-cut beta-barium borate crystal. The (UV) laser was turned on and left for 30 min before use to allow the beam intensity to stabilize. The power output of the argon ion laser was adjusted to be 100 mW.

Samples were cleaned with ethanol and dried with N_2 before exposure to UV light. The micropatterning apparatus consists of a converging lens and a mirror at 45^o to the incident beam, to focus the beam on the samples with a spot size of approximately 0.2 cm^2. A Cu electron microscope grid consisting of a pattern of orthogonal bars (masked) and squares (open) (Agar, Cambridge, UK) was employed as a mask [193]. This mask was placed on the sample and then a clean quartz disc was used to hold it in position during exposure. Once the exposure was complete, the sample was rinsed with ethanol and dried under dry N_2.

2.6.2 Nano-scale lithography

2.6.2.1 Interference lithography (IL)

In the present work a two-beam Lloyd's mirror interferometer was employed. When two coherent beams interfere, a sinusoidal pattern of intensity results. Interferogram consists of alternating bands of constructive and destructive interference.[273] The periodicity p in the sample is given by:

$$p = \frac{\lambda}{2 \sin \theta} \qquad (2.7)$$

Where λ is laser wavelength and θ the angle of incidence.[273]

Figure 2.7 shows a schematic diagram of the apparatus used. The stage holds the mirror and sample at a orientation of 2θ to each other (θ to the beam). The stage can be rotated to control the pattern pitch. The same frequency-doubled Ar ion laser that was used for a micropatterning was also used as a light source for IL. To obtain a coherent beam, the laser

was focused by a lens through a spatial filter with aperture 5 μm . The edge of the coherent beam was cut by using a mask with a suitable aperture. Half of the beam was pointed onto the mirror and the other half was directed onto the sample surface. When the light was reflected from the mirror onto the sample surface, the two beams interfered on the surface, yielding a sinusoidal pattern of intensity. The sample was subsequently rinsed with ethanol or methanol and dried under N_2.

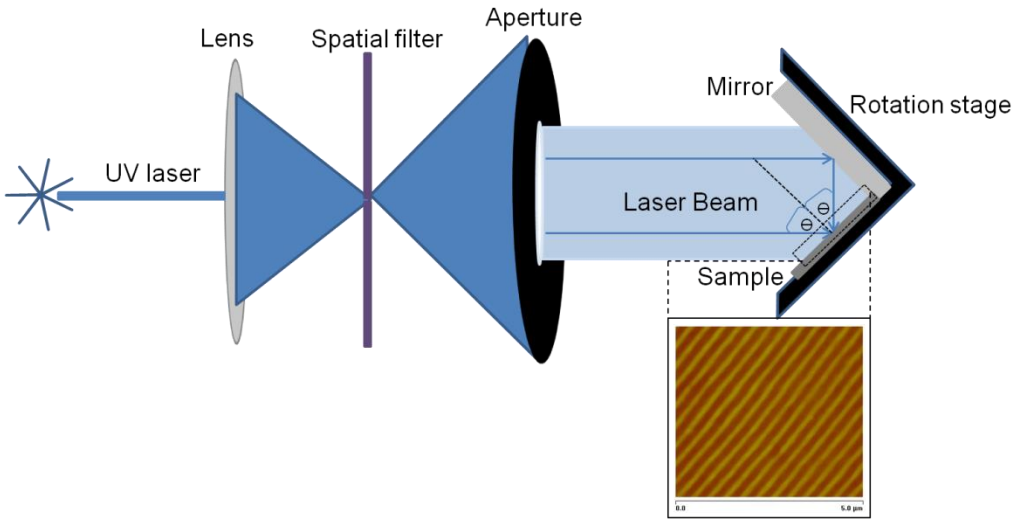

Figure 2.7. Schematic diagram of the apparatus used to carry out two-beam interference lithography.

Three-beam IL has been used to create hole/dot patterns with hexagonal symmetry. A two beam Lloyd's mirror interferometer was modified into a three-beam interferometer by adding second Lloyd's mirror, with the position of the mirrors chosen to guarantee 120° symmetry of exposure, see Figure 2.8. The direct incident light on the sample and the reflections from the two mirrors produced a hexagonal symmetry. This advantage of this setup is to simplify the alignment by fixing the position of the mirrors with respect to the sample. Moreover, only a single exposure is needed to generate hole/dot patterns.[274-275] The periodicity of the patterns is given by:

$$p = \frac{2\,\lambda}{3\sin\theta} \qquad (2.8)$$

Where λ is laser wavelength and θ the angle of incidence.[274]

After the pattern was completed, the sample was washed with ethanol or methanol and then dried under steam of nitrogen.

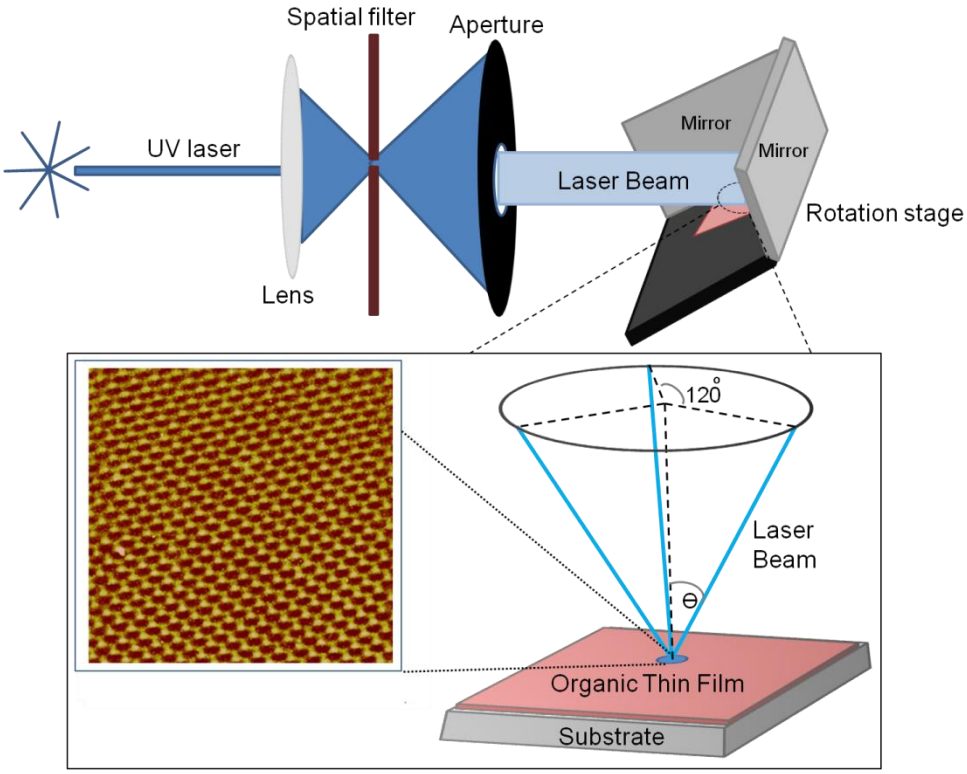

Figure 2.8. Schematic diagram of the three-beam interferometer used in this work.

Chapter 3: Spatial control over crosslinking affects the pH-responsive behaviour of poly(2-(tert-butylamino)ethyl methacrylate) brushes

3.1 Introduction

Polyelectrolyte brushes are commonly known to be responsive to changes in solvent, temperature, pH and ionic strength.[276-277] One of the most studied groups of these stimuli-responsive surfaces is pH-responsive polymer brushes. The ionization of functional groups on the polymers causes chain extension or collapse upon environmental pH changes. Polyacids, such as PAA,[278-280] and PMAA [281-282] and polybases, such as PDMAEMA [283-285]and poly(vinyl pyridine) (PVP),[286-287] have been widely studied.

At low pH, a weak polybase brush swells because of the increasing inter-chain repulsion (coulombic repulsion), which can produce large changes in layer thickness.[145-146,259] Moglianetti el al. reported that at pH lower than 3, PDMAEMA brushes become more swollen due to a greater osmotic pressure that causes stretching of the segments away from the interface.[146] The fraction of protonated segments varies with segment density through the brush layer; outer segments are more protonated than those in the interior of the brush (a high grafting density leads to a low fraction of protonated segments).[288] Jia et al. studied the variation in PDMAEMA brush swelling behavior with grafting density and pH. They found that the degree of swelling depends on the grafting density: a lower grafting density is correlated with a greater degree of swelling.[145]

Cross-linking of polymer brushes is a route to the preparation of materials with better mechanical and chemical stability, compared to linear polymer brushes. Crosslinked thin films can be prepared by polymerizing cross linkable monomers.[289] Huang et al. reported the direct polymerization of ethylene glycol dimethacrylate (EGDMA) from a gold surface to form crosslinked polymer films.[289] They reported that the cross-linked films are very uniform in the range 5-200nm as revealed by FTIR, ellipsometry and AFM. Moreover, crosslinked thin films can be prepared by introducing the crosslinker into a pre-prepared cross-linkable polymer film. Moglianetti et al, have studied the interaction between PDMAEMA segments and sodium dodecyl sulfate (SDS) in both acidic and alkaline midea. They reported a reduction in the swelling of PDMAEMA brushes after the PDMAEMA chains are physically crosslinked vis SDS ions.[290]

However, there has been very little work focused on *secondary* amine methacrylates such as poly(2-*tert*-butylaminoethyl methacrylate) (PTBAEMA) brushes. Morse et al. have synthesized PTBAEMA latex in the presence of divinylbenzene (DVB) cross-linker and poly(ethylene glycol) methacrylate (PEGMA) stabilizer. These Pickering emulsions proved to be pH-responsive and can be used as an effective Pickering emulsifier at pH above 10. [291]Jerome and co-workers have prepared PTBAEMA functionalized polyolefin fibres via two protocols.[292-293] In first study, a polyolefin-PTBAEMA diblock copolymer was synthesized by ATRP and dispersed within low-density polyethylene, which led to bactericidal activity towards *E. coli*. In the second case, primary amine-functionalized PTBAEMA chains were prepared via an azide-functional initiator, which led to chemical grafting of the PTBAEMA to maleic anhydride-grafted polypropylene. Dispersion of this graft copolymer within native polypropylene led to long-lasting antibacterial activity. However, as far as we are aware, there is very little work on the synthesis and pH-responsive behavior of well-defined PTBAEMA brushes in the literature.

In the present work, uniform PTBAEMA brushes are grown from silicon substrates using surface-initiated ATRP. The pH-responsive behaviour of linear brush is studied using ellipsometry and AFM, and then compared to that of crosslinked PTBAEMA brushes. Crosslinking is achieved by a reaction between the secondary amine groups in the TBAEMA residues with isocyanate groups in a commercially available polymeric diisocyanate. Spatial control of the brush crosslinking is achieved by selecting the solvent used for the crosslinking reaction. Using a good solvent for the PTBAEMA brush (e.g. THF) leads the crosslinker to react uniformly throughout the brush layer, while using a poor solvent allows the crosslinker being confined to the upper surface of the collapsed brush (see Scheme 1). It is hypothesised that spatial confinement of crosslinking should affect the pH-responsive behaviour of the brush film. Various surface characterization techniques are used including contact angle goniometry, *in situ* ellipsometry, AFM, XPS and surface zeta potential.

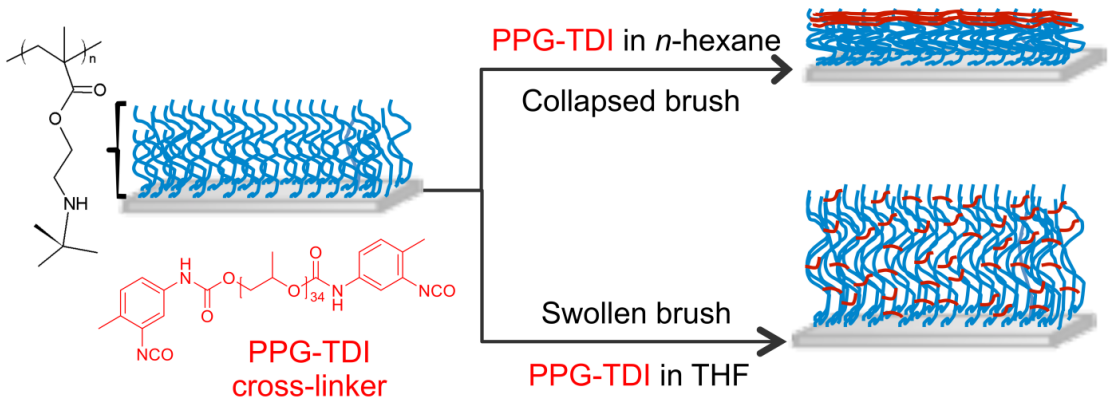

Scheme 3.1. Schematic representation of the nature of the cross-linking produced within a PTBAEMA brush layer when using a PPG-TDI cross-linker in conjunction with a good solvent (THF) or a poor solvent (*n*-hexane). The former solvent results in a *uniformly-crosslinked* brush, whereas the latter results in *a surface-crosslinked* brush.[294]

3.2 Experimental

3.2.1 Preparation of ATRP initiator on silicon wafers

The process of cleaning the silicon wafers with Piranha solution followed by RCA and the formation of bromo initiator on silicon substrates are described in section 2.3.1. The substrates were submerged 2 % solution of APTES in ethanol for 30 min then rinsed with ethanol then dried at 120 ^{o}C. To functionalise the surface with initiator, the samples were immersed in (0.37mL, 3mmol) BIBB and (0.41mL, 3mmol) triethylaminedissolved in 60 mL of DCM for 30 min then the samples were rinsed with ethanol and DCM then dried under N_2 (shown in scheme 3.2).

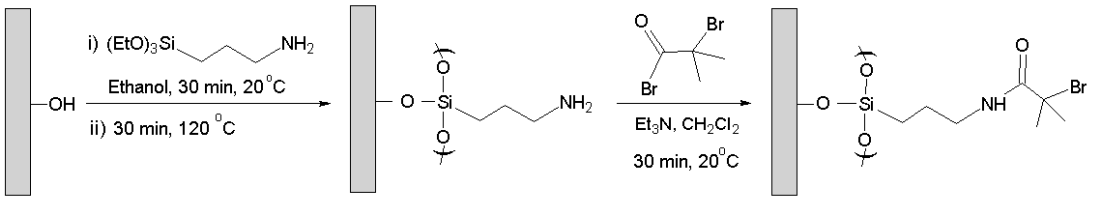

Scheme 3.2. Schematic represents the formation of initiators including the formation of 3-aminopropyltriethoxysilane (APTES), subsequently by the reaction of bromoisobutyryl bromide (BIBB).

3.2.2 UV irradiation of ATRP initiator-functionalized surfaces

UV exposure of BIBB-APTES monolayer was carried out using a frequency-doubled argon ion laser with wavelength of 244 nm as described in section 2.6. The exposure was carried out on samples with a beam size of 0.2 cm^2.

Micro-patterns were obtained by exposing BIBB-APTES film on silicon surface to UV light through a Cu electron microscope grid (2000 mesh) as a mask to remove the bromine from patterned area. IL was conducted using a two-beam interference system at 20^o. Then the samples were cleaned with ethanol and dried under steam of N_2.

3.2.3 ATRP synthesis of PTBAEMA brushes

TBAEMA (5.0 g, 27 mmol) was dissolved in isopropanol (IPA; 5.0 mL) at 20 ^oC, degassed by passing a continuous stream of nitrogen through the solution for 30 min while stirring the solution. TPMA (58.8 mg, 0.203 mmol), and Cu(II)Br_2 (15.0 mg, 0.068 mmol) were added to the solution and degassed for 20 min. Cu(I)Br (19.0 mg, 0.135 mmol) was added and the mixture was degassed for a further 10 min. Initiator-functionalised wafers were sealed in Schlenk tubes and degassed via three vacuum/nitrogen cycles. The monomer/catalyst mixture (2 mL) was added by syringe into each tube under a nitrogen atmosphere and the surface polymerization of TBAEMA was allowed to proceed at 20 ^oC (scheme 3.3). The samples were removed after various polymerization times, followed by washing with IPA and ethanol several times. The same protocol was used for the synthesis of patterned PTBAEMA brushes.

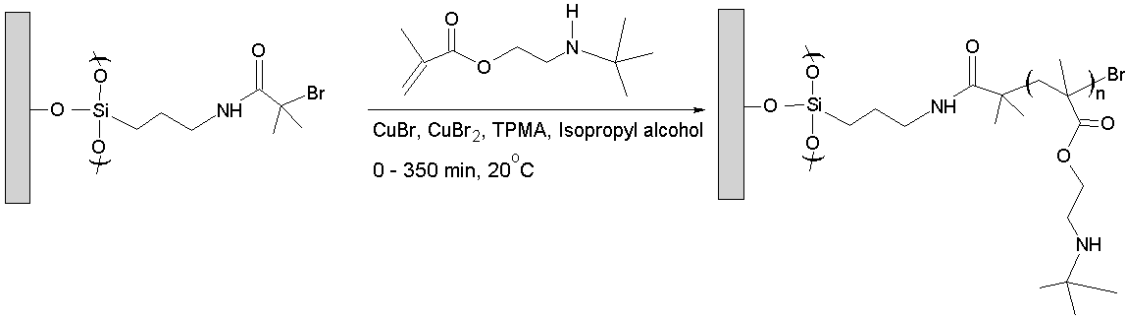

Scheme 3.3. Synthesis of a linear PTBAEMA brush from an initiator-functionalized planar surface using Atom Transfer Radical Polymerization (ATRP) in isopropyl alcohol (IPA).

3.2.4 Preparation of PTBAEMA homopolymer

TBAEMA (5.0 g, 27 mmol) was dissolved in isopropanol (IPA; 5.0 mL) at 20 ^{o}C, degassed for 30 min. TPMA (58.8 mg, 0.203 mmol), and Cu(II)Br_2 (15.0 mg, 0.068 mmol) were added to the solution and degassed for 20 min. Cu(I)Br (19.0 mg, 0.135 mmol) was added and the mixture was deoxygenated for a further 10 min. In a separate Schlenk tube, which was vacuum/backfilled three times, BIBB-APTES functionalized Si surface and 2-(dimethylamino)ethyl-2-bromoisobutyrylamide initiator (3.0 mg, 0.013 mmol**)** as the sacrificial initiator were added. The sacrificial initiator was used to control the polymer chain length under the assumption that the chains grown from the Si surface and in solution have similar molecular weights. The polymerization solution was syringed into Schlenk tube and allowed to proceed at 20 ^{o}C. After 90 min the catalyst was deactivated by exposing the polymerization solution to air. The substrate was washed with IPA and ethanol, then the dry ellipsometric thickness was measured to be 10 nm. The crude polymer was purified by equilibrium dialysis to remove the catalyst and unreacted monomers. The purified polymer was freeze-dried. The mean molecular weight of PTBAEMA was judged by GPC analysis in THF, indicate a *Mn* of 12700 using poly(methyl methacrylate) as a standard.

3.2.5 Preparation of crosslinked PTBAEMA brushes

Uniformly-crosslinked PTBAEMA brushes (with dry brush thicknesses ranging from 4 to 15 nm) were prepared by immersing the linear PTBAEMA brush-coated wafers in 1 mL of a 1 mg/L stock solution of 2, 4-diisocyanate-terminated poly(propylene glycol) (PPG-TDI) in dry THF at 20 ^{o}C. It has been published a method to calculate the grafting density of a polymer brush directly from the dry brush thickness (h_{dry}).[126,145] The chain grafting density (σ) was described by equation $\sigma = h_{dry}\ \rho N_A/Mn$, where *Mn* is the mean degree of polymerization, ρ is the bulk density of the polymer and N_A is Avogadro's number. For a PTBAEMA brush of 10 nm dry thickness grown from a 1 cm^2 silicon wafer substrate and the mean degree of polymerization of 12700, the grafting density was calculated to be 0.55 chains nm^{-2} (using a calculation described in the literature and the density of 1.10 g cm^{-3} for the PTBAEMA brush).[295] Thus for the crosslinking conditions used in the present work, we calculate that there are approximately 21.5 secondary amine units (due to PTBAEMA) per isocyanate unit (due to PPG-TDI). This ensures that the brush layer is not over-crosslinked, so that it retains some degree of stimulus-responsive behavior. After 10 min, the wafer was rinsed copiously with THF to remove any unreacted PPG-TDI crosslinker and dried under a

stream of nitrogen gas. The same protocol was utilized to prepare *surface-crosslinked* PTBAEMA brushes, except that *n*-hexane was used instead of THF.

3.2.6 Surface characterization

The formation of silane films functionalised with the bromo-initiator, PTBAEMA brushes and further surface modification were characterized by contact angle, ellipsometry, AFM and XPS. Advancing sessile drop contact angles were measured using a Rame-Hart model 100-00 goniometer (Netcong, NJ) as described in section 2.5.1. Ellipsometric measurements were carried out on a Jobin Yvon UVISEL spectroscopic ellipsometer. The data were fitted to a model consisting of a polymer brush layer of variable thickness on a silicon substrate as described in section 2.5.3. AFM was carried out using digital instruments Nano-scope IV Multimode Atomic Force Microscope (Veeco, Santa Barbara, USA) with a 'J' scanner (0 - 125 µm) as described in section 2.5.2. Silicon nitride nano-probes (Digital Instruments, Cambridge, UK) with nominal force constants of 0.06 or 0.12 N m^{-1} and tip radii between 20 to 60 nm were used for contact mode imaging, and silicon probes with nominal spring constants between 20 and 80 Nm^{-1} were used for tapping mode. XPS was carried out using a Kratos Axis Ultra spectrometer (Kratos Analytical, Manchester, UK) with a monochromatized Al Kα X-ray source operating at a power of 150 W with emission current at 8 mA and with pressure between 10^{-8} to 10^{-10} mbar was utilize to analyze the surface as described in section 2.5.4. High- resolution peaks were fitted and processed using CasaXPS software and all binding energies were referenced relative to the main hydrocarbon peak C1s which was 285 eV.

3.3 Results and discussion

3.3.1 Characterization of BIBB-APTES film

APTES surface functional groups on silicon wafers were reacted with BIBB in the presence of triethylamine as a base to generate BIBAPTES. The base reacts with HBr that results from the coupling reaction. BIBB-APTES film exhibited a contact angle 67 ± 2^{o}, compared to 47 ± 2^{o} for the initial APTES monolayer. The topography of BIBB-APTES films was acquired using contact mode AFM, (Figure 3.1). The root mean square (rms) of three samples was found to be between 0.5 and 0.7 nm. The smooth surfaces of these samples indicated the formation of high quality formation films. The chemical composition of the BIBB-APTES film was assessed using high resolution XPS spectra of C1s, Br3d and N1s (Figure 3.2). The C1s spectrum was fitted with three components with binding energies of 285.0, 286.4 and 288.4 eV, which were attributed to C-C, C-Br/C-N and O=C, respectively. The experimental ratios were 4.5 : 2.1 : 1, which is in good agreement with the theoretical 4 : 2 : 1 ratio. The Br3d high resolution spectrum was fitted with two components with relative intensities of 1.4:1, corresponding to $Br3d_{5/2}$ and $Br3d_{3/2}$ with binding energies of ~70.3 and ~71.3 eV, respectively resulting from spin-orbit coupling.[191,296] The Br/N atomic ratio suggested that 80-90% of surface amine groups had reacted with 2-bromoisobutyryl bromide, generating the desired BIBB-APTES.

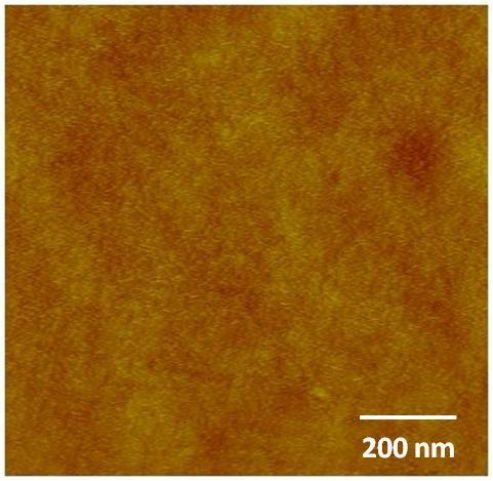

Figure 3.1. Height image of a 3-(2-Bromoisobutyramido)propyl(triethoxy) silane (BIBB-APTES) film, 1.0 × 1.0 μm^2, z-range 0 – 10 nm dark to bright.

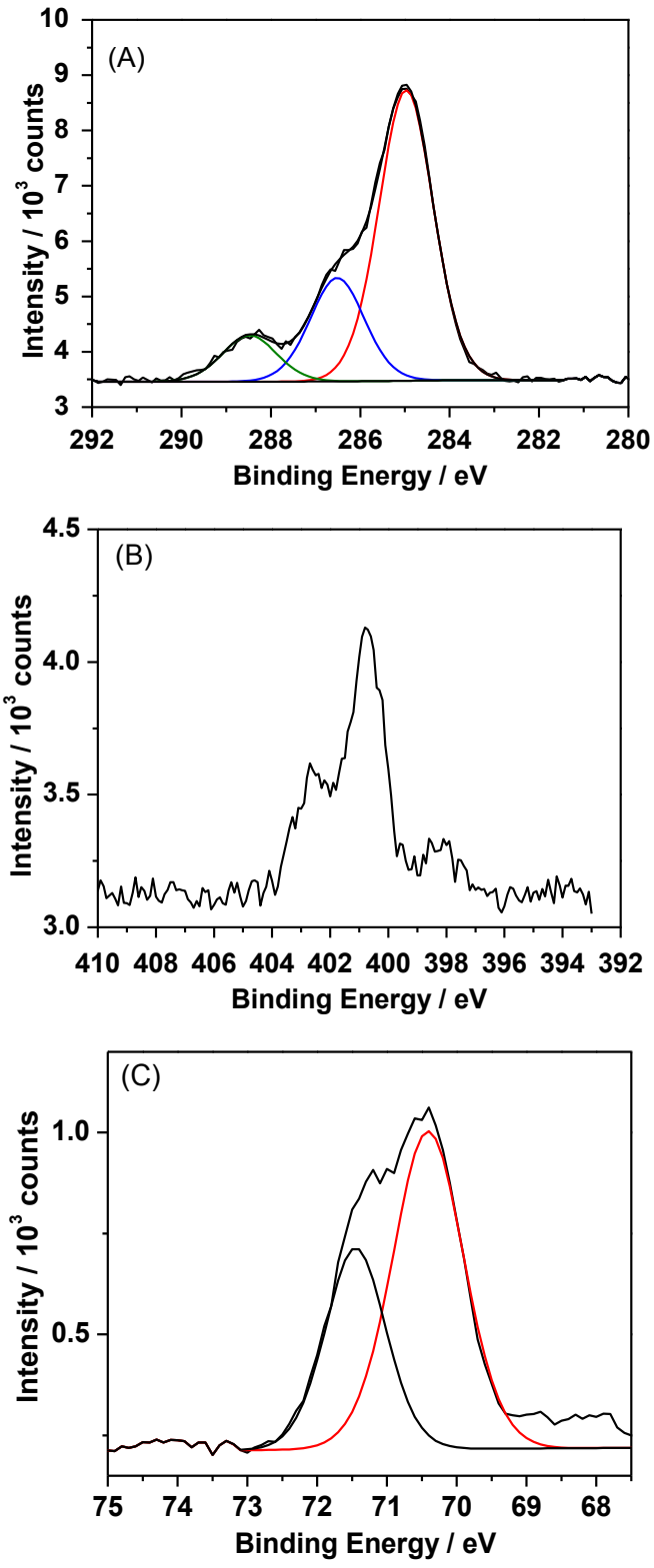

Figure 3.2. Curve-fitted X-ray photoelectron spectra recorded for BIBBAPTES initiator-functionalized planar wafers: (A) C1s core-line spectrum; (B) N1s core-line spectrum; and (C) Br3d core-line spectrum.

Surface zeta potential vs. pH curves were constructed for both APTES- and BIBB-APTES-functionalized silicon wafers (Figure 3.3). The former substrate is cationic between pH 2 and pH 7 (with zeta potentials of 35 ± 10 mV) owing to protonation of the surface primary amine groups. Anionic character was observed in alkaline media, with an isoelectric point at around pH 8-9; these observations are consistent with previous studies.[297-299] The BIBB-APTES silicon wafer exhibits rather lower surface zeta potentials (8 ± 5 mV) at low pH, and negative values above pH 9. This is consistent with our XPS observations, which indicated that a minor fraction of surface primary amine groups had not reacted with 2-bromoisobutyryl bromide.

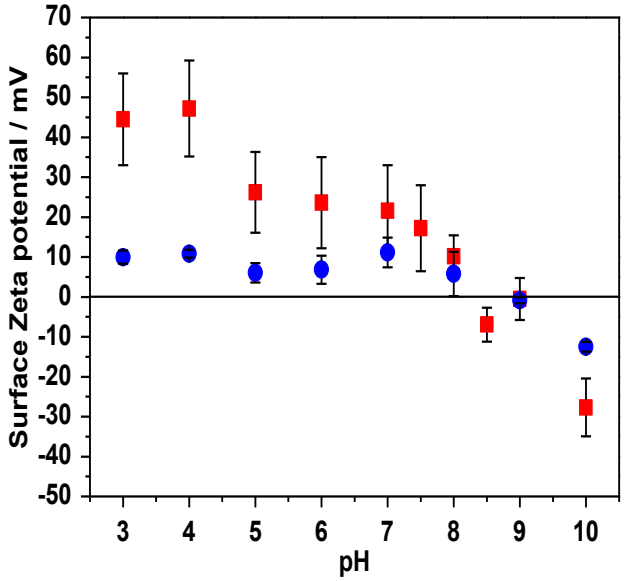

Figure 3.3. The surface zeta potential of APTES and BIBB-APTES functionalized Si wafers immersed in aqueous solution as a function of solution pH. (■) APTES film. (●) BIBB-APTES film.

3.3.2 UV modification of initiator films

Ahmed et al. has reported the UV modification of such BIBAPTES layers.[191] In agreement with their work, it was found that the water contact angle gradually decreased with increasing of UV exposure (Figure 3.4). It can be seen that the contact angle remained at 58±0.5^{o} after an exposure of 1.7 J cm^{-2}. XPS studies confirmed the photodegradation process: the intensity of the Br3d signal was progressively attenuated with increasing exposure time and became undetectable after 2.2 J cm^{-2}, indicating complete removal of Br as shown in Figure 3.5.

Micro-patterning was achieved by exposing BIBAPTES-functionalized silicon wafers through 2000 mesh electron microscope grid to 2.2 J cm^{-2} to ensure full removal of Br. Friction force microscopy was utilized to image the resulting patterns and there was a clear contrast between the masked area (bar) and exposed regions (squares) (Figure 3.6A). The brightest contrast illustrates the more polar exposed regions, which possess a higher frictional coefficient with respect to the AFM probe.

Nano-scale patterning was carried out using IL technique to photolytically pattern BIBAPTES film on the silicon wafer. A dual beam interference set-up was used to fabricate the surface. A coherent UV laser beam was directed towards a mirror and sample placed at angular separation of 2θ. Half of this laser beam falls on the mirror, from where it is reflected onto the sample to interfere with the other half of the beam, forming a sinusoidal intensity pattern with a period of $\lambda/2\sin\theta$, where λ is the laser wavelength. In this experiment, BIBAPTES film was exposed to 0.7 J cm^{-2} at 20^{o}. FFM was used to image fabricated BIBAPTES film (Figure 3.6B). The bright bands correspond to areas of extensive modification with widths of 160 ± 7 nm, whereas the dark bands indicate regions of low modification with widths of 140 ± 6 nm. The contrast between the dark regions and light regions revealed by FFM is because of the more polar nature of the laser-exposed regions, which possess a higher frictional coefficient with respect to the AFM probe. Topographical image, acquired with the FFM image, revealed that there was no height contrast in the image indicating no removal of material had occurred.

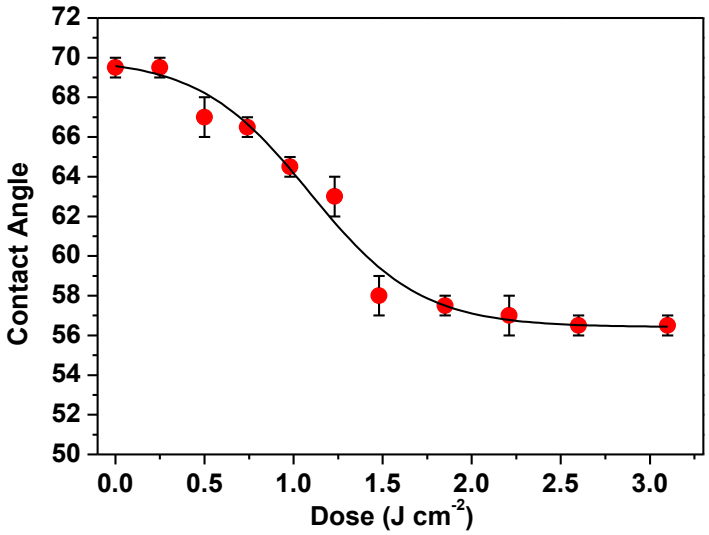

Figure 3.4. Variation in the advancing water contact angle with UV exposure dose (J cm^{-2})

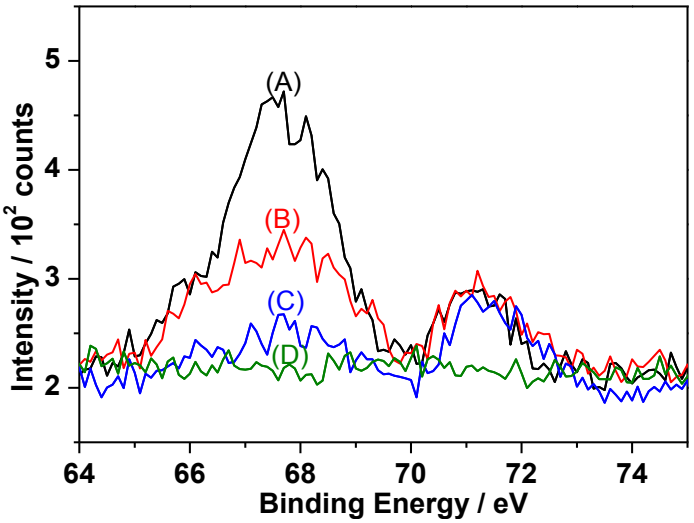

Figure 3.5. Observed changes in the Br3d core-line spectrum of the BIBBAPTES initiator-functionalized wafers measured by XPS following exposure to UV laser radiation (λ = 244 nm): (A) original pristine surface; (B) after exposure for 0.75 J cm^{-2}; (C) after exposure for 1.5 J cm^{-2}; (D) after exposure for 2.25 J cm^{-2}.

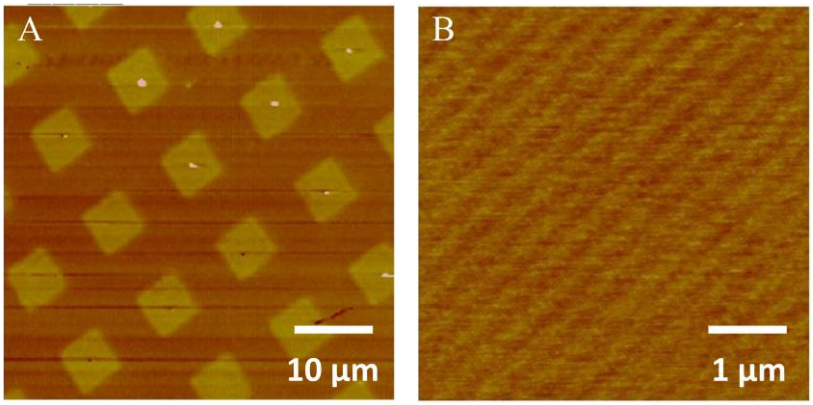

Figure 3.6. Friction force microscopy (FFM) images of patterned BIBBAPTES-functionalized silicon wafers obtained using AFM. (A) Micro-patterned substrate following an exposure of 2.2 J cm^{-2}, 50 × 50 μm^2, z-range 0 – 3 V dark to bright. (B) Nano-patterned substrate formed by IL with an angle of 20 ^{o} between the mirror and the sample, after an exposure of 0.7 J cm^{-2} , 5 × 5 μm^2, z-range 0 – 3 V dark to bright.

3.3.3 The growth of PTBAEMA brushes from Si surface

PTBAEMA brushes were prepared by surface-initiated ATRP. This living radical polymerization technique has been widely used to grow polymer brushes.[300-302] A slow growth of PTBAEMA brushes from a planar silicon substrate via living radical polymerization was reported by Ding et al. They used two techniques: SI-ATRP involving using a $CuCl/CuCl_2$/HMTETA catalyst at 90 ^oC in the bulk, and a single electron transfer living radical polymerization (SET-LRP) technique employing Cu(0) in DMSO at 75 ^oC.[303] SI-ATRP gave a relatively smooth brush of approximately 20 nm dry thickness after 72 h, whereas SET-LRP produced a less uniform brush of around 17 nm after 96 h. However, no detailed information regarding the kinetics of PTBAEMA brush growth was reported, and the pH-responsive PTBAEMA brush was not investigated.

In the present work, several modifications were attempted including changing in the ligand, catalyst, solvents and temperature in order to prepare thicker layer of PTBAEMA brushes, enable control of brush growth and reduce the polymerization time. Table 3.1 shows the comparison of different experimental conditions in SI-ATRP technique to control the growth of PMATBAE brushes. When HMTETA and bipy were used as ligands, the film thickness of PMATBAE brushes was found to be less than 4 nm over a period of 24 h. However, using TPMA ligand showed an increase in brush thickness up to 44 nm in 24 h at 60 ^oC. The best catalyst system for polymerisation of TBAEMA was Cu(I)Br, $Cu(II)Br_2$ combined with a TPMA ligand. The molar ratio of [TBAEMA]:[CuBr]:[$CuBr_2$]:[TPMA] was 200:1:0.5:1.5 respectively and the surface polymerization was conducted in IPA as a solvent. The polymerization was performed at room temperature (20 ^oC) and the dry thickness of the brushes, as measured by ellipsometry, reached 28±3 nm after polymerization for 350 min. Figure 3.7 shows the variation in PTBAEMA brush thickness with the polymerization time. Under the stated reaction conditions, the evolution in brush thickness was almost linear with time, with 22 nm brushes being achieved within 3 h. Subsequently, the brush layer grew more slowly, attaining 28 nm within 350 min. This non-linear growth suggests a gradual loss of living character.

Table 3.1. Reaction conditions and average dry polymer brush thicknesses of poly(2-(tert-butylamino)ethyl methacrylate) (PTBAEMA) brushes from Si-initiated substrates using SI-ATRP methods.

No.	Dry polymer brush thickness (nm)	Catalyst(s)	Ligand	Solvent	Temperature (^{o}C)	Reaction Time (h)
1	1.2 ± 0.4	CuBr	HMTETA	Bulk	20	24
2	1.5 ± 0.6	CuBr	HMTETA	Bulk	90	24
3	4.2 ± 0.9	CuBr	HMTETA	Toluene	90	24
4	2.2 ± 0.3	CuBr	Bipy	IPA/H_2O	60	24
5	2.1 ± 0.5	CuBr	TPMA	Bulk	90	24
6	44 ± 2	CuBr	TPMA	IPA/H_2O	60	24
7	22 ± 0.5	CuBr	TPMA	IPA/H_2O	20	24
8	24 ± 1	CuBr/$CuBr_2$	TPMA	IPA/H_2O	60	4

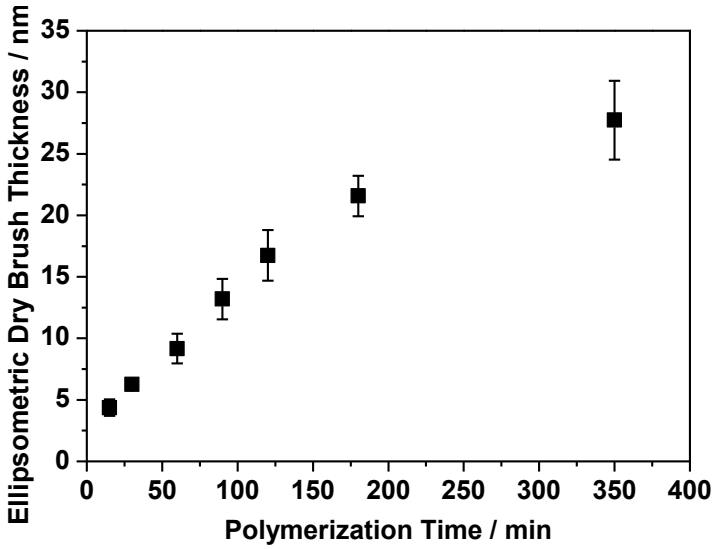

Figure 3.7. Evolution of ellipsometric dry PTBAEMA brush thickness versus polymerization time via SI-ATRP in isopropyl alcohol (IPA) at 20 ^{o}C. Conditions: [TBAEMA]: [CuBr]: [$CuBr_2$]: [TPMA] molar ratio = 200: 1.0 : 0.5 : 1.5.

Polymerization of PTBAEMA was then carried out on the patterned BIBB-APTES functionalized silicon wafers, to test the feasibility of growing polymer brushes from micro- and nano-structured photopatterned surface. AFM studies indicate that the micro-patterned initiator surface does not exhibit any height contrast between exposed and non-exposed areas. However, after polymerization, AFM reveals a difference in height between irradiated areas

(squares) and non-irradiated areas (bars) (Figure 3.8A) . The masked region exhibits greater height contrast than the exposed region. This indicates polymer brush growth from the non-irradiated regions, as expected. Height differences between the PTBAEMA brushes and the irradiated areas were assessed in order to estimate the mean brush height.

Nano-structured PTBAEMA brushes were obtained by growing brushes from nanopatterned ATRP initiators. The AFM height image obtained for such PTBAEMA brushes showed that the dark contrast indicates the regions exposed to UV light which causes debromination (and hence no brush formation), whereas the bright lines correspond to the PTBAEMA brushes. Kaholek et al reported that the height of polymer brushes decreases with decreasing feature size of the pattern [304]. These workers hypothesized that "at constant grafting density a polymer brush in good solvent adopts a vertically less ordered and laterally more extended conformation, induced by the lack of lateral restraint the brush experiences at its boundaries, leading to less chain crowding and thus less chain stretching." Polymer structures grown from finer patterns are also likely to be more relaxed (less brush like) near the edges of the pattern, resulting in thinner polymer brushes even in the dry state. It was observed that brushes grown from such nanopatterns were significantly thinner than brushes grown from micropatterns under the same conditions. The topographical image shows nanopatterned PTBAEMA brushes with a line-width (full width at half maximum, FWHM) of 160 ± 7 nm, whereas the dark region was 145 ± 6 nm, and heights of 4.2 ± 5 nm, whereas the height in micropattern feature, under the same conditions, was 14.0 nm (Figure 3.8B).

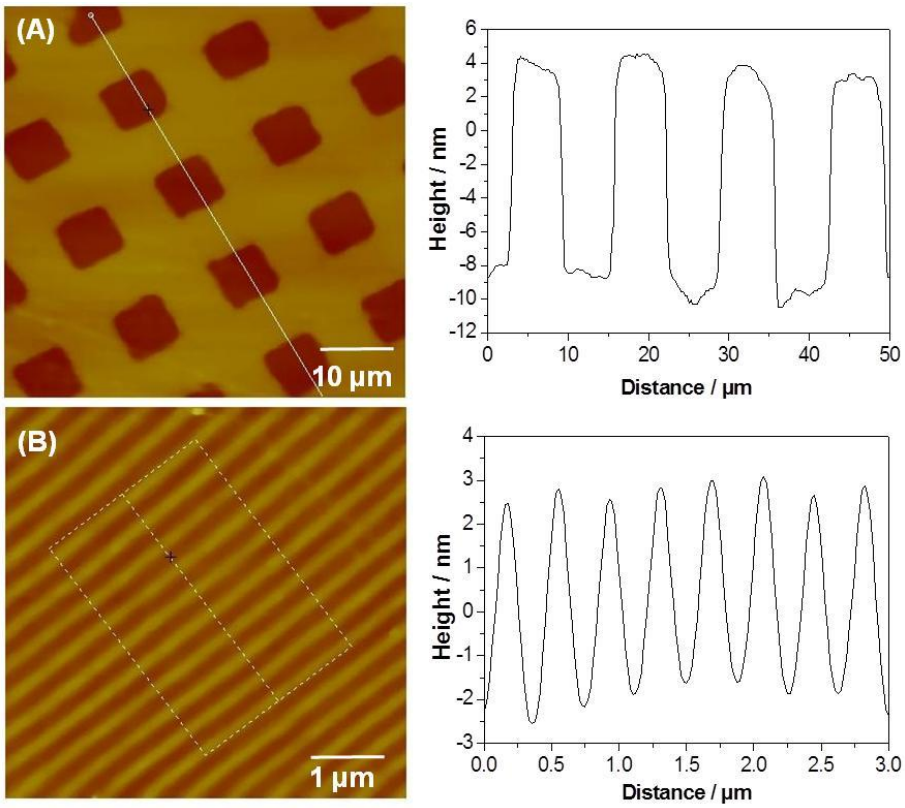

Figure 3.8. (A) AFM tapping mode height image of a micro-patterned *linear* PTBAEMA brush: topographical image (left), cross-section analysis (right). Image size: 50 × 50 µm. (B) AFM tapping mode height image of a nano-patterned *linear* PTBAEMA brush: topographical image (left), cross-section analysis (right). Image size: 5 × 5 μm^2. Conditions: [TBAEMA]: [CuBr]: [$CuBr_2$]: [TPMA] molar ratio = 200: 1.0 : 0.5 : 1.5, at 20 ^oC for 90 min.

3.3.4 Cross linking PTBAEMA brushes

Secondary amine groups on the PTBAEMA repeats units are cross-linkable.[305] Tolylene 2, 4-diisocyanate-terminated poly(propylene glycol) (PPG-TDI) was selected because it has two terminal isocyanate groups which can form robust urea bonds. PPG-TDI has an average molecular weight (Mn) of ~2,300 (degree of polymerization ~34). Thompson and Armes reported that cross-linking of the hydroxyl groups of the poly(glycerol monomethacrylate) (PGMA) stabilized polystyrene latex adsorbed onto oil droplets using PPG-TDI as a cross-linker.[306] The primary and/or secondary amine groups on the poly(ethylene imine) (PEI) stabilized polystyrene latex particles were successfully cross-linked using (PPG TDI).[305]

The mechanism of this reaction is shown in scheme 3.4. Secondary amine on the PTBAEMA chain attacks the carbon of the isocyanate end group in (PPG-TDI), and the bond between the nitrogen and carbon in isocyanate is broken. A bond between the carbon and nitrogen in PTBAEMA chains is formed and the nitrogen then steals a hydrogen from the secondary amine is transferred into the nitrogen in PPG-TDI.

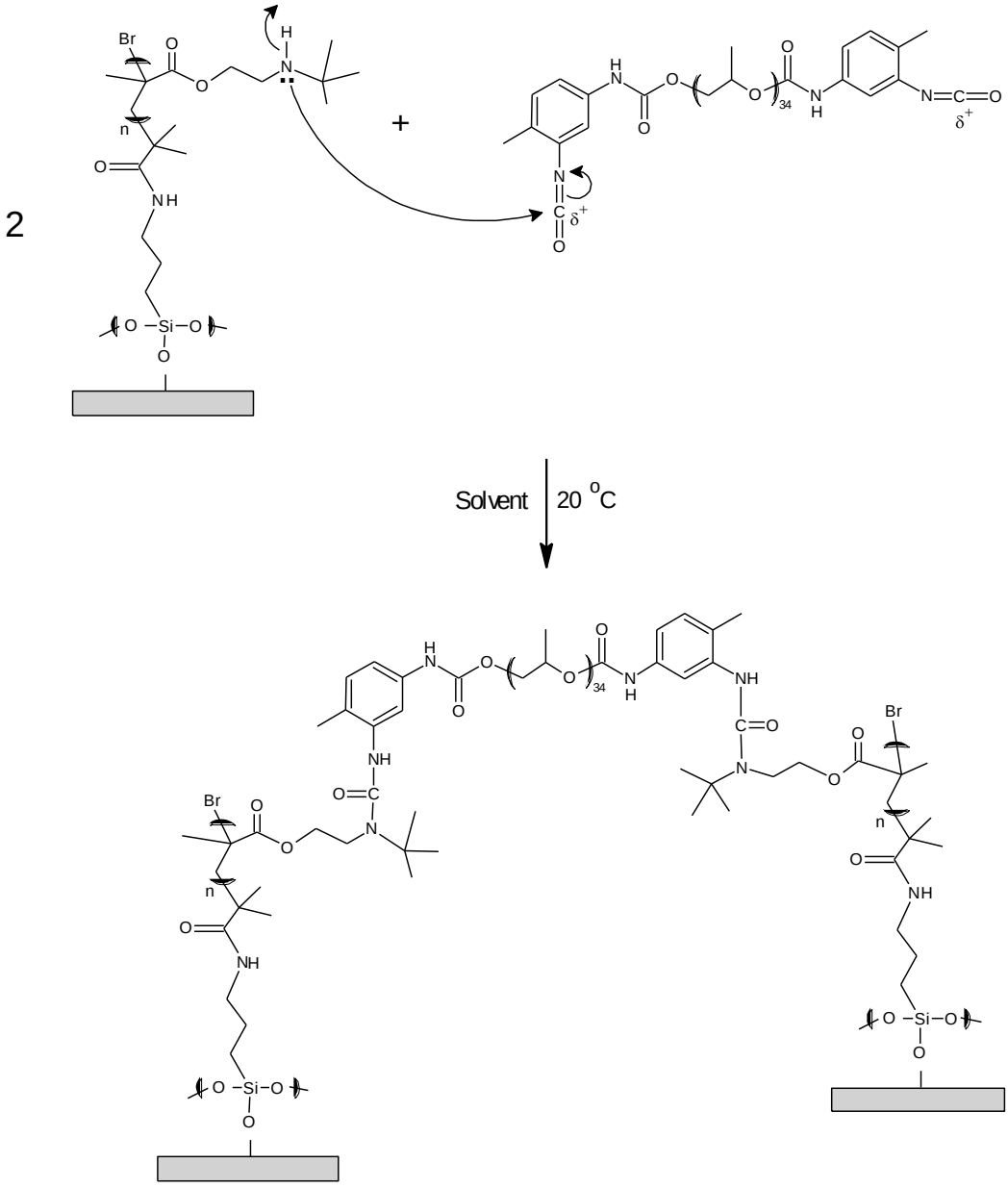

Scheme 3.4. The mechanism of cross-linking reaction between the polymer chains and isocyanate groups in crosslinker (PPG-TDI).

THF is a good solvent for PTBAEMA so the brushes will be highly swollen and the PPG-TDI cross linker will react with secondary amine groups through the brush layer. On other hand if the poor solvent for PTBAEMA brushes, *n*-hexane, is selected for cross-linking, then the brush layer will be collapsed and the cross linker will only react with the upper surface.

3.3.4 Surface characterization

X-ray photoelectron spectroscopy XPS is a surface-specific analysis technique with a sampling depth of around 2-5 nm. The wide scan survey spectrum was acquired to determine the elemental compositions of the surfaces. Table 3.2 determines the elemental compositions of the PPG-TDI crosslinker, *linear*, *uniformly-crosslinked* and *surface-crosslinked* PTBAEMA brushes (the dry brush thickness 18 nm). The elemental compositions of the crosslinker (C, N, O) as shown in Table 3.1, are close to the calculated elemental composition C=73.6%, N=2.5% and O=23.9%. In *linear* PTBAEMA brushes, the elemental compositions (C, N, O) are similar to the calculated values (C=77.0%, N=7.6% and O=15.3%). After crosslinking, the O/N atomic ratio increases due to the incorporation of O atoms in the PPG-TDI crosslinker. The atomic ratio of O/N increases in the *surface-crosslinked* PTBAEMA brushes, implying that there is a significantly higher degree of cross-linking at the surface of this brush. These observations are consistent with the hypothesis that PPG-TDI crosslinking conducted using a poor solvent (*n*-hexane) yields crosslinking that is predominantly confined to the upper surface of the brush layer. There is an increase in O/N atomic ratio for *uniformly-crosslinked* brushes prepared in THF, comparing to linear brush.

Table 3.2. XPS Data Summarizing the Elemental Compositions of the PPG-TDI crosslinker *Linear* PTBAEMA brush, *surface-crosslinked* PTBAEMA brush and *uniformly-crosslinked* PTBAEMA brush.

XPS sample description	**% C**	**% N**	**% O**
PPG-TDI crosslinker	77.43	2.01	20.56
Linear PTBAEMA brush	79.52	6.99	13.49
PTBAEMA brush *surface-crosslinked* in *n*-hexane	76.49	3.94	19.57
PTBAEMA brush *uniformly-crosslinked* in THF	78.63	6.12	15.24

High resolution C1s XPS spectra were acquired for the cross linker and for both non-crosslinked and crosslinked PTBAEMA brushes. XPS C1s spectra of the PPG-TDI cross-linker (which contains 34 polymerized propylene glycol units per crosslink) were fitted using three components at binding energies of 285.0, 286.3 and 288.5 eV, attributable to the C−C−C, C−O/C−N and O=C−N, respectively (Figure 3.9). The ratios of C−C−C, C−O/C−N and O=C−N obtained from the C1s spectrum was 12.7 : 21 : 1 which is consistent with the predicted ratio (11: 21 : 1). We expected that after crosslinking reactions, there will be an increase in −C−O/−C−N region.

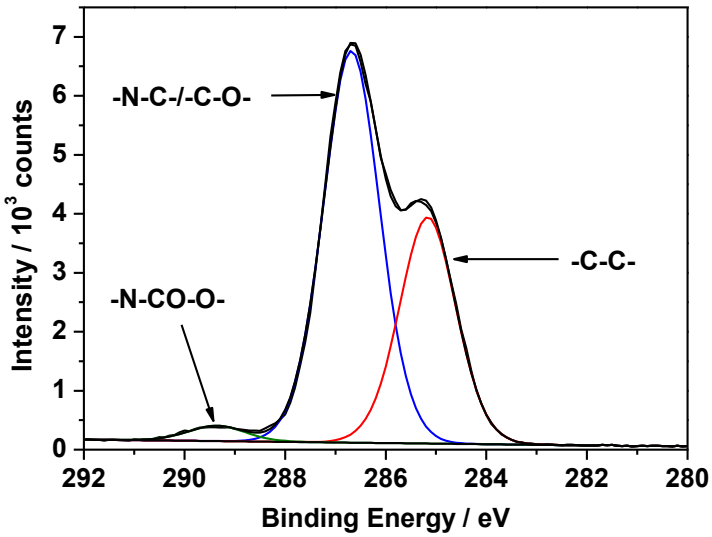

Figure 3.9. X-ray photoelectron core-line spectra recorded for PPG-TDI cross-linker.

To confirm the success of the cross-linking reaction, XPS is a well-established surface analytical technique with the sampling depth depending on the electrons take-off angles. In principle, it can provide useful spectroscopic information on the extent of the crosslinking reaction within the PTBAEMA brush layer. Figure 3.10 shows the C1s spectra for (A) *linear* (B) *surface-crosslinked* and (C) *uniformly-crosslinked* PTBAEMA brushes (18 nm dry brush thickness in each case). For *linear* brushes, the C1s envelope can be fitted using three components, which correspond to the hydrocarbon -C-C-C- signal at 285.0 eV, the -C-C-NH- and -C -C-O- signal at 286.4 eV and the ester carbonyl signal at 288.9 eV. The respective relative peak areas are 5.7 : 2.41 : 1, which are in reasonable agreement with the calculated theoretical ratio of 6 : 3 : 1 (see Figure 3.10A).

Figure 3.10B shows the C1s spectra after crosslinking the PTBAEMA brush in *n*-hexane. The intensity of the –C–C–NH and -C -C-O- components at 286.4 eV is increased in size, since the additional C-O bonds contributed by the PPG-TDI crosslinker (which confers 34 polymerized propylene glycol units per crosslink). The actual degree of crosslinking cannot easily be determined, since the PPG-TDI reagent may also react with two N-H bonds on the same PTBAEMA chain to form an *intramolecular* cycle, rather than forming an *intermolecular* crosslink.

Cross-linking the PTBAEMA brush in THF (Figure 3.10C) leads to an increase in intensity for the –C–C–O component. In contrast to the surface cross-linked brushes, there is a modest increase in the intensity of the C–C–O component. Given that the XPS sampling depth is no more than 10 nm, these data are consistent with the hypothesis that using PPG-TDI in combination with a good solvent (THF) yields more extensive uniform crosslinking within the brush layer (and hence a somewhat lower extent of surface crosslinking).

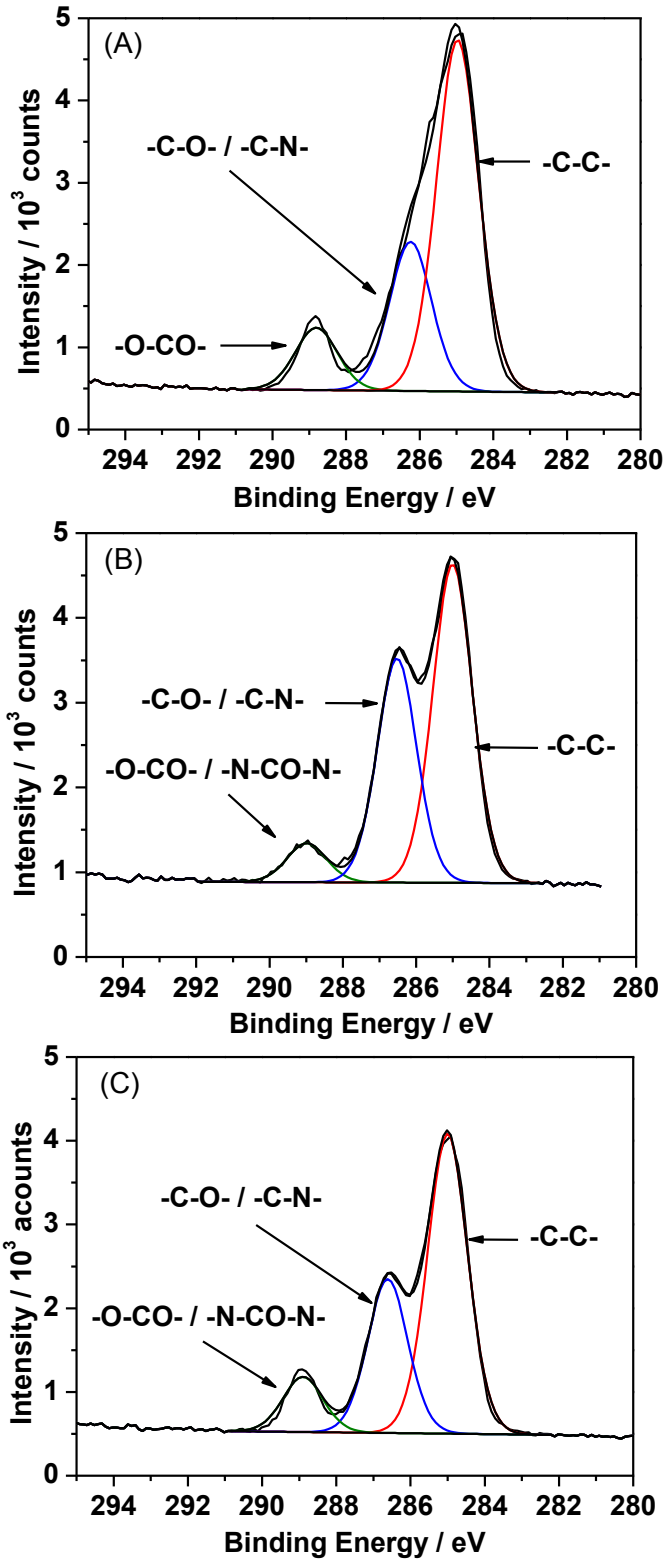

Figure 3.10. X-ray photoelectron core-line spectra recorded for a series of PTBAEMA brushes (each of 18 nm dry thickness).(A) C1s spectrum obtained for a *linear* PTBAEMA brush. (B) C1s spectrum obtained for the same *surface-crosslinked* PTBAEMA brush prepared using PPG-TDI in *n*-hexane. (C) C1s spectrum obtained for the same *uniformly-crosslinked* PTBAEMA brush prepared using PPG-TDI in THF.

AFM The height images of *linear* and *crosslinked* PTBAEMA brushes grafted on Si (~ 15 nm) were acquired by AFM (Figure 3.11). Table 3.3 shows the root mean square (rms) of *linear* and *uniformly/surface crosslinked* PTBAEMA brushes in dry and in aqueous solution at pH 7. The roughness of PTBAEMA brushes was higher for both *uniformly-crosslinked* and *surface-crosslinked* brushes compared to the non-cross linked polymer.

The topography of dry and wet *linear* PTBAEMA was smooth and uniform as shown in Figure 3.11 with rms of less than 0.4 nm. The *uniformly-crosslinked* PTBAEMA brush exhibits a relative smooth morphology (rms < 0.5nm) which is similar to *linear* brushes in both cases which indicates successful crosslinking between the PPG-TDI reagent and the N-H groups within the PTBAEMA brushes (an intermolecular crosslink). It is clear that, the roughness of *surface-crosslinked* PTBAEMA brushes increased to ca. 0.9 nm in both dry and wet state. The high roughness caused by the high density of the cross-linker on the surface and/or may be a reaction between PPG-TDI crosslinker with two N-H bonds on the same PTBAEMA chain to form an intramolecular cycle.

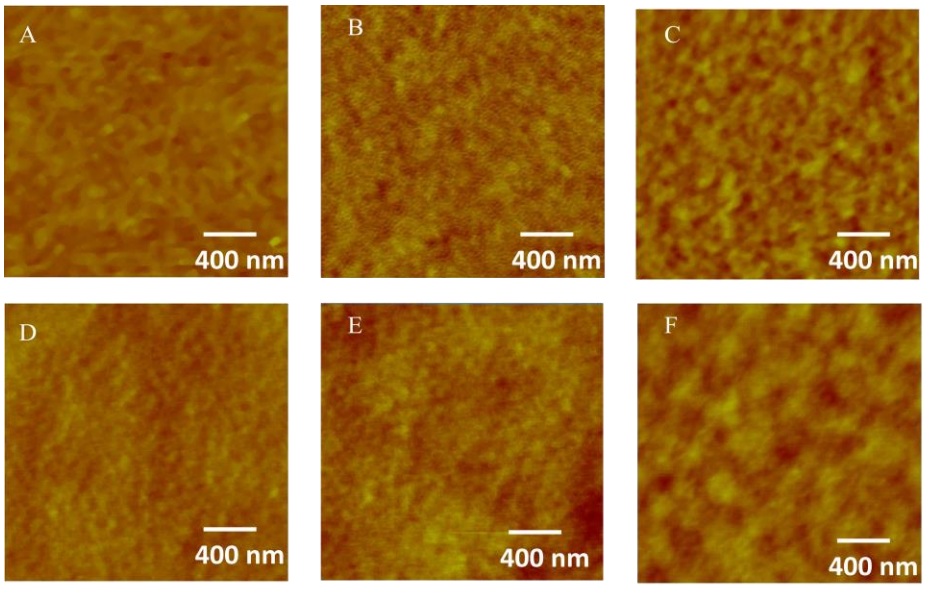

Figure 3.11. AFM height images of a series of PTBAEMA brushes (each of 15 nm dry thickness). (A) Dry *linear* PTBAEMA brush. (B) Dry *uniformly-crosslinked* PTBAEMA brush prepared using PPG-TDI in THF. (C) Dry *surface-crosslinked* PTBAEMA brush prepared using PPG-TDI in *n*-hexane. (D) Wet *linear* PTBAEMA brush. (E) Wet *uniformly-crosslinked* PTBAEMA brush prepared using PPG-TDI in THF. (F) Wet *surface-crosslinked* PTBAEMA brush prepared using PPG-TDI in *n*-hexane. Image size: 2 μm × 2 μm. The z-range is 0-10 nm dark to bright in each case.

Table 3.3. The root mean square (rms) of two samples in dry and aqueous solution at pH 5.5 of *linear* PTBAEMA brush, *uniformly-crosslinked* PTBAEMA brush prepared using PPG-TDI in THF and *surface-crosslinked* PTBAEMA brush prepared using PPG-TDI in *n*-hexane.

	rms of Dry Brushes (nm)	rms of Wet Brushes (nm)
None Cross-linked PTBAEMA	0.4 ± 0.2	0.3 ± 0.1
THF Cross-linked PTBAEMA	0.5 ± 0.2	0.4 ± 0.2
***n*-hexane Cross-linked PTBAEMA**	0.6 ± 0.3	0.6 ± 0.2

3.3.5 pH-dependence of the structure of PTBAEMA brushes

The secondary amine groups presented in the weakly basic PTBAEMA brushes are readily protonated when immersed in acidic solution. The resulting cationic brushes become highly swollen, stretching away from the surface due to the strong lateral electrostatic repulsive forces between adjacent chains. The pH-responsive behaviour of PTBAEMA brushes grown from silicon wafers was investigated by immersion in aqueous solutions ranging from pH 2 to pH 12. In acidic aqueous solution, the brushes become fully protonated and attain their maximum swollen thickness. In alkaline media, PTBAEMA brushes gradually become deprotonated and hence adopt their collapsed conformation. The pH-modulated brush thickness for crosslinked and non-crosslinked PTBAEMA brushes was studied using both ellipsometry (see Figure 3.12) and AFM (see Figure 3.13).

As shown in Figure 3.12, the mean PTBAEMA brush thickness increased from about 16 nm (in its dry state) up to 58 nm below pH 7. Above pH 8, the PTBAEMA chains become deprotonated and collapse to give an 18 nm brush layer, which is close to its dry thickness. Thus the linear swelling factor (the ratio of the thickness of the swollen brush to that of the collapsed film) is ca. 3.3. The mean thickness of a uniformly crosslinked PTBAEMA brush (prepared using PPG-TDI in THF) increases from 17 nm in alkaline media up to 43 nm in acidic solution, corresponding to a linear swelling factor of ca. 2.5. Thus *uniform crosslinking* throughout the brush layer imposes a significant constraint on its pH-responsive behavior, as expected. This is attributed to the multiple crosslinks between the PTBAEMA chains, which restrict the chain mobility. In contrast, for the *surface-crosslinked* PTBAEMA brush prepared

using PPG-TDI in *n*-hexane, the brush thickness varies from around 17 nm when immersed in alkaline media up to approximately 50 nm in acidic solution, which corresponds to a linear swelling factor of 3.0. Thus the *surface-crosslinked* PTBAEMA brushes exhibit very similar pH-responsive behaviour to the *linear* PTBAEMA brushes. This is because the PPG-TDI crosslinker barely penetrates the collapsed brush layer, and hence can only react with the secondary amine groups present in its outer surface. An extensive crosslink network is not created within the brush layer under these conditions, hence this *surface-confined* crosslinking has relatively little effect on the swelling/collapse behaviour of the brush.

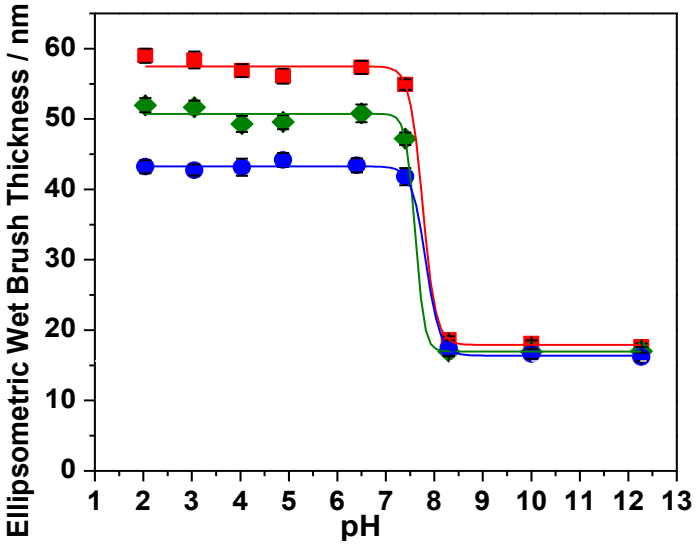

Figure 3.12. *In situ* ellipsometric thickness of PTBAEMA brushes immersed in aqueous solution as a function of solution pH. (■) Linear PTBAEMA brush (original dry thickness = 16 nm). (●) Same PTBAEMA brush *uniformly-crosslinked* in THF using PPG-TDI at 20^{o}C. (♦) Same PTBAEMA brush *surface-crosslinked* in *n*-hexane using PPG-TDI at 20^{o}C.

In order to study the pH-responsive behaviour of PTBAEMA brushes, micro- and nano-patterned PTBAEMA brushes were prepared as stated previously in order to monitor changes in brush height via AFM. Comparing the brush heights for the bright bar regions and dark square enables the mean brush thickness to be determined. The same approach was utilized when immersing the patterned brushes in various pH solutions. These patterned brushes were also crosslinked using PPG-TDI dissolved in either THF or *n*-hexane respectively, followed by AFM studies of their pH-responsive behaviour. The molar ratio of secondary amine (from PTBAEMA brushes) to isocyanate (from PPG-TDI) used was approximately 21.5 : 1. This

ensures that the brush layer is not over-crosslinked, so that it retains some degree of stimulus-responsive behaviour after crosslinking.

AFM studies of the micro-patterned *linear*, *uniformly-crosslinked* and *surface-crosslinked* PTBAEMA brushes were conducted (see Figure 3.13 and Figure 3.14). As expected, the *linear* PTBAEMA brushes exhibit the strongest pH-responsive behaviour: the mean brush height difference increased from 18 nm for the collapsed state (above pH 8) to 64 nm for the fully stretched brush (below pH 7). This indicates a linear swelling ratio of approximately 3.5. In contrast, the *uniformly-crosslinked* PTBAEMA brushes swell from 15 nm (above pH 8) up to 37 nm (below pH 7). Again, the *surface-crosslinked* PTBAEMA brushes exhibited intermediate behaviour, with a swollen brush height of 50 nm and a collapsed brush height of 17 nm indicating a linear swelling ratio of 3.0. These data are in good agreement with the ellipsometric data discussed above, thus confirming that the pH-responsive behaviour of PTBAEMA brushes can be modulated by conducting crosslinking in either a good or a bad solvent. The resulting 3D (or 2D) crosslink networks dictate the observed pH-responsive brush behaviour with greater crosslinking restricting the pH-response, as expected.

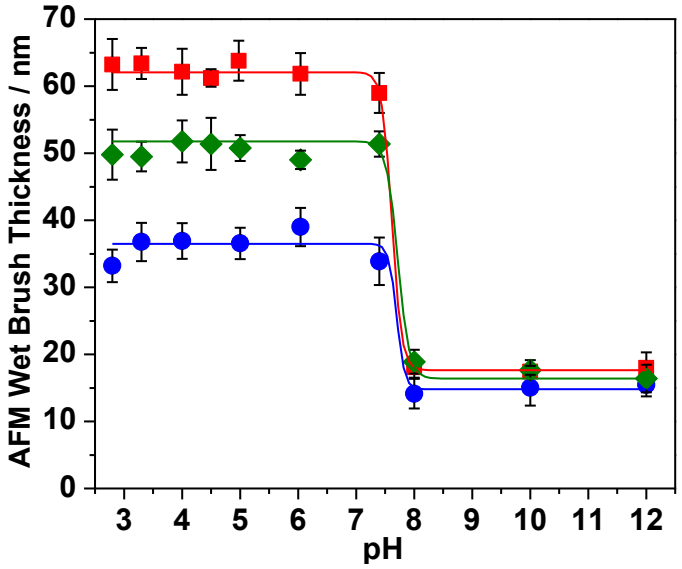

Figure 3.13. *In situ* brush height determined by AFM as a function of solution pH for micro-patterned PTBAEMA brushes: (■) *linear* PTBAEMA brush (original dry brush thickness = 15 nm); (●) *uniformly-crosslinked* PTBAEMA brush prepared using PPG-TDI in THF; (♦) *surface-crosslinked* PTBAEMA brush prepared using PPG-TDI in *n*-hexane.

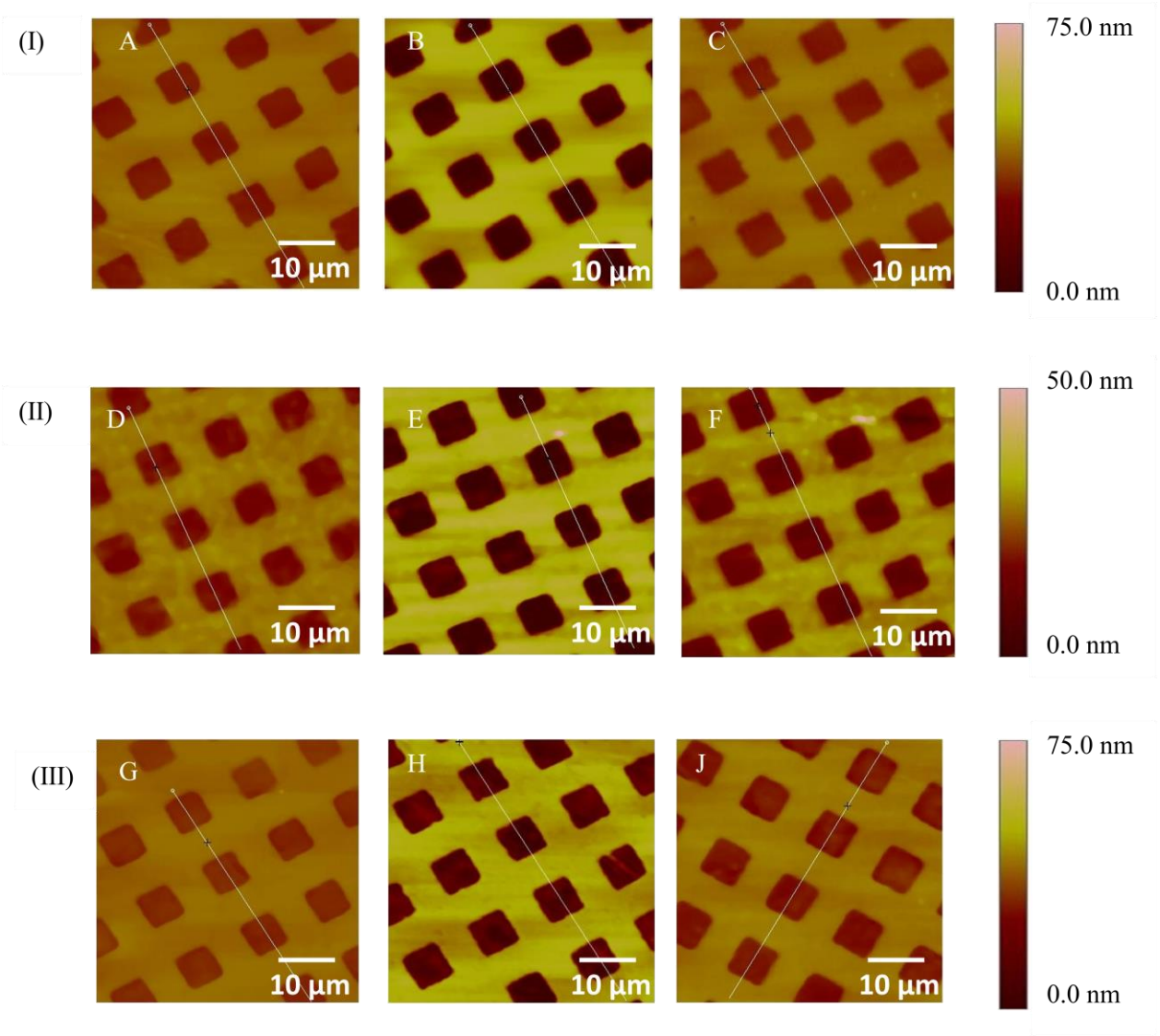

Figure 3.14. AFM height images (50 × 50 µm^2) recorded for micro-patterned samples. (I) *Linear* PTBAEMA brushes: (A) dry brush in air, (B) same brush immersed a solution at pH 7.0 and (C) same brush immersed in alkaline solution at pH 8.0. (II) *Uniformly-crosslinked* PTBAEMA brush prepared using PPG-TDI in THF: (D) dry brush in air, (E) same brush immersed in a solution at pH 7.0 and (F) same brush immersed in alkaline solution at pH 8.0. (III) *Surface-crosslinked* PTBAEMA brush prepared using PPG-TDI in *n*-hexane: (G) dry brush in air, (H) same brush immersed in a solution at pH 7.0 and (J) same brush immersed in alkaline solution at pH 8.0.

The effect of spatially-confined crosslinking was also studied for nano-patterned brushes. The same AFM experiments were conducted on nano-patterned *linear*, *uniformly-crosslinked* and *surface-crosslinked* PTBAEMA brushes (see Figure 3.15 and Figure 3.16). Very similar pH-reponsive behaviour was observed for the three brush types compared to the micro-patterned brushes discussed above, except that the pH-response is somewhat weaker for the nano-patterned brushes. This is probably because, for such small features, the brush chains are more likely to deform at the periphery of the patterned feature, hence brush-like chain stretching normal to the surface is likely to be attenuated

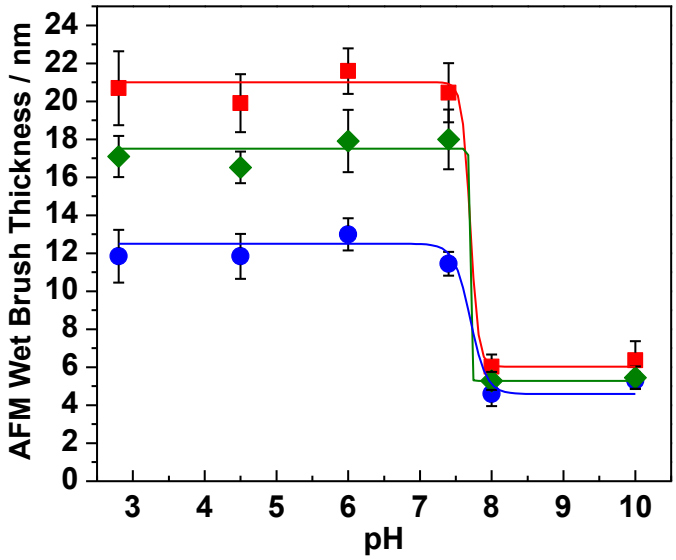

Figure 3.15. *In situ* AFM brush height determined as a function of solution pH for nano-patterned PTBAEMA brushes immersed in aqueous solution: (■) *linear* PTBAEMA brush (original dry brush thickness = 4.5 ± 0.5 nm); (●) *uniformly-crosslinked* PTBAEMA brush prepared using PPG-TDI in THF; (♦) *surface-crosslinked* PTBAEMA brush prepared using PPG-TDI in *n*-hexane

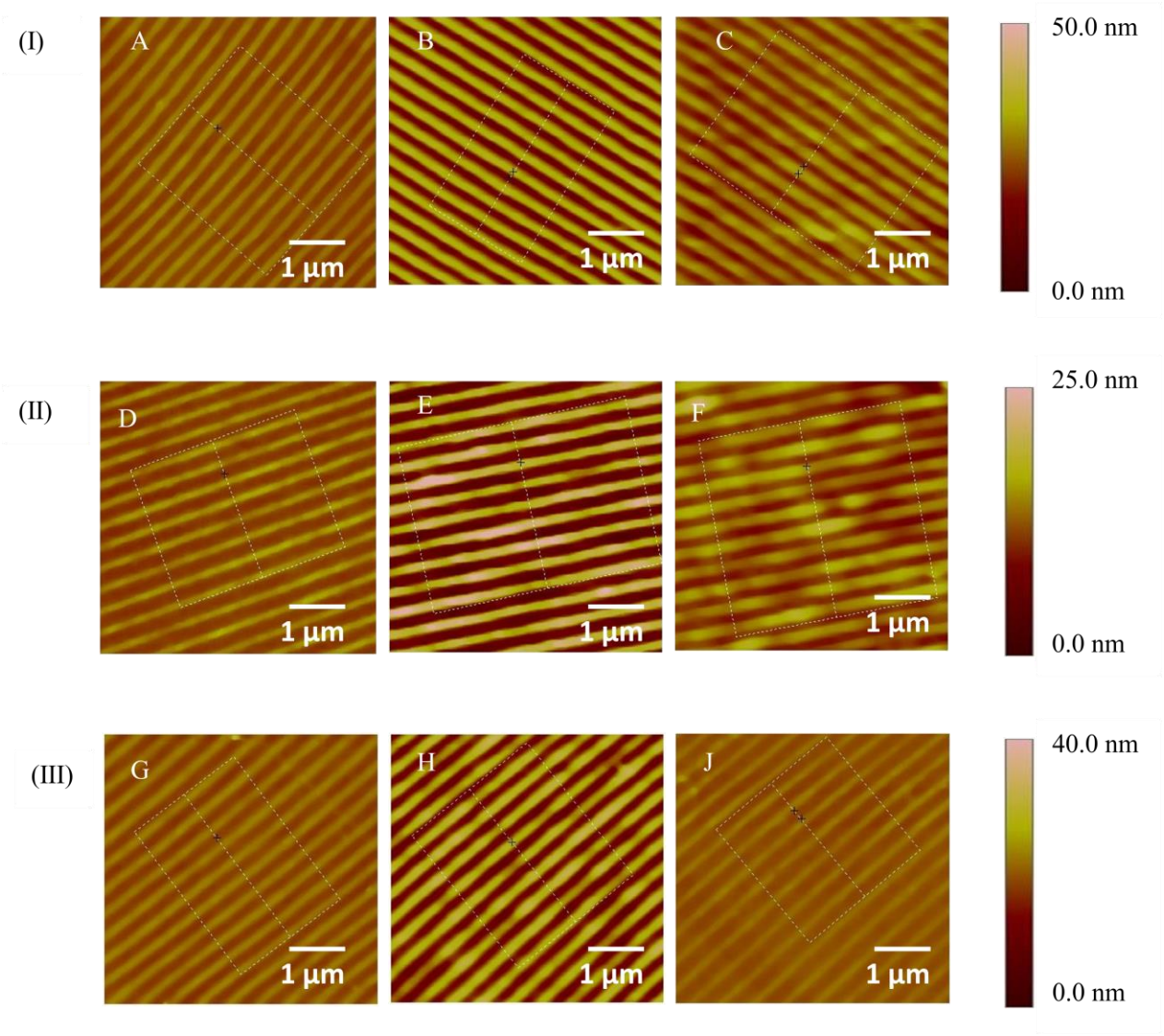

Figure 3.16. AFM height images (5 × 5 µm^2) recorded for nanopatterned samples. (I) *Linear* PTBAEMA brushes: (A) dry brush in air, (B) same brush immersed in acidic solution at pH 2.8 and (C) same brush immersed in alkaline solution at pH 10.0. (II) *Uniformly-crosslinked* PTBAEMA brush prepared using PPG-TDI in THF: (D) dry brush in air, (E) same brush immersed in acidic solution at pH 2.8 and (F) same brush immersed in alkaline solution at pH 10.0. (III) *Surface-crosslinked* PTBAEMA brush prepared using PPG-TDI in *n*-hexane: (G) dry brush in air, (H) same brush immersed in acidic solution at pH 2.8 and (J) same brush immersed in alkaline solution at pH 10.0.

It is worth noting that, the critical pH for the brush collapse/swelling transition in all of these experiments was observed at pH between 7 and 8. Systematic studies within a relatively narrow window at pH between 7 and 8 were carried out. Figure 3.17 suggests that the brush collapse/swelling transition occurred at a pH between 7.6 and 7.8, which is lower than the pK_a of approximately 8.0 recently reported by Morse and co-workers for linear PTBAEMA homopolymer in aqueous solution.[291] At different degree of crosslinking, about 5 % of amino groups on PTBAEMA chains had been reacted with PPG-TDI. The maximum volume fractions of protonated amino groups for PDMAEMA brushes have been reported with range of 0.26-0.42.[146,307] Consequently, just 5 % of ca. 64 % non-protonated amino groups have been replaced with neutral urea linkage; so the different degree of cross-linking does not affect the pKa value of PTBAEMA brushes.

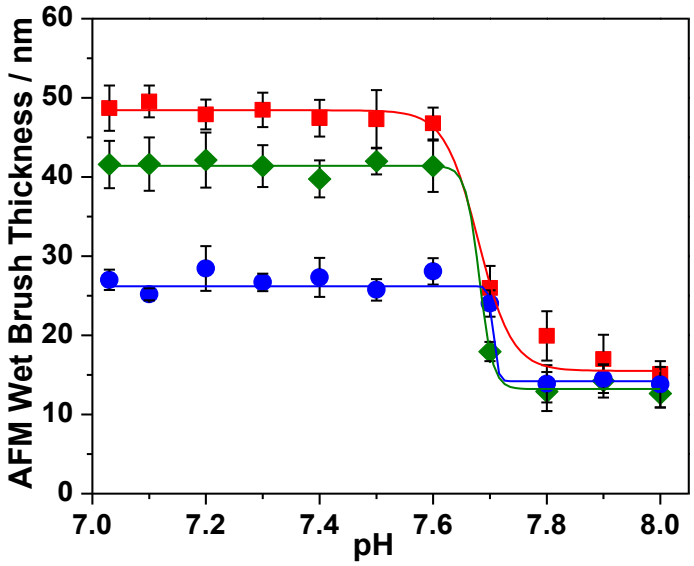

Figure 3.17. *In situ* AFM brush height determined over a relatively narrow pH window for micro-patterned PTBAEMA brushes immersed in aqueous solution: (■) *linear* PTBAEMA brush (original dry brush thickness = 12.5 nm); (●) *uniformly-crosslinked* PTBAEMA brush prepared using PPG-TDI in THF (original dry brush thickness = 11.5 nm); (♦) *surface-crosslinked* PTBAEMA brush prepared using PPG-TDI in *n*-hexane (original dry brush thickness = 12.3 nm) .

3.3.6 Surface zeta potential

The surface zeta potential of linear and cross-linked PTBAEMA brushes was measured over the pH range of 3-10 (Figure 3.18). As expected, the surface zeta of linear PTBAEMA brushes was positive value 45±5 mV at pH ≤ 7, then the surface charge decrease at higher pH. We expected that, after brush cross-linking reaction the surface charge decreases due to the reduction in amino groups in the surface. As expected, the surface zeta potential of surface-crosslinked PTBAEMA brush is lower positive charge than uniformly-crosslinked PTBAEMA brush.

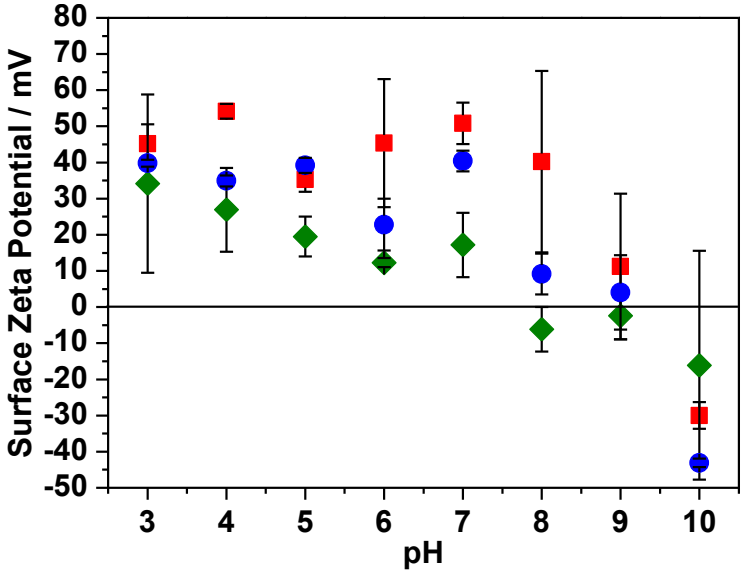

Figure 3.18 Surface zeta potential of PTBAEMA brushes (each of them 18 nm dry thickness). immersed in aqueous solution as a function of solution pH. (■) *Linear* PTBAEMA brush. (●) Same PTBAEMA brush *uniformly-crosslinked* in THF using PPG-TDI at 20 ^{o}C. (♦) Same PTBAEMA brush *surface-crosslinked* in *n*-hexane using PPG-TDI at 25 ^{o}C.

3.4 Conclusions

Linear PTBAEMA brushes of up to 28 nm dry thickness have been prepared via SI-ATRP at 20 ^{o}C. Ellipsometric studies confirm that such brushes exhibit pH-responsive behaviour, as expected. Highly swollen cationic protonated brushes are produced at low pH, with collapsed neutral deprotonated brushes being obtained above a critical pH of approximately pH 7.7. PTBAEMA brushes can be readily crosslinked via their secondary amine groups using a commercially available polymeric diisocyanate (PPG-TDI) to produce robust urea bonds. XPS studies confirm the presence of the reacted PPG-TDI crosslinker within the brush layers. Moreover, the choice of solvent determines the *spatial location* of this crosslinking reaction. Using THF, which is a good solvent for PTBAEMA, leads to relatively *uniform cross-linking* throughout the swollen brush layer. On the other hand, conducting the same crosslinking reaction in *n*-hexane, which is a poor solvent for PTBAEMA, leads to *surface crosslinking* of the collapsed brush layer. This spatial confinement profoundly affects the subsequent pH-responsive behavior of the latter brush layer, which becomes significantly more swollen when immersed in acidic solution than the former uniformly crosslinked brush layer, as judged by ellipsometry and AFM studies. However, brush swelling occurs at approximately pH 7.7 regardless of the spatial location of the crosslinking reaction, which is essentially the same critical pH as that found for the linear brush. This critical pH is slightly lower than the pK_a of around 8.0 reported for linear PTBAEMA chains.[291]

Chapter 4: Synthesis and nanometer-scale patterning of stimulus-responsive, biofouling-resistant zwitterionic poly(amino acid methacrylate) brushes

4.1 Introduction

There is considerable academic and commercial interest in the design of biocompatible non-fouling surfaces for complex biological fluids, particularly blood plasma and serum.[308-310] Protein fouling can damage various types of biomedical devices, including coronary stents,[311] ear grommets [312] and guidewires.[313] Poly(ethylene glycol) (PEG)-based surface coatings are known to offer high resistance towards non-specific protein adsorption and cell adhesion.[314-316] However, PEG-based materials can be oxidized under physiological conditions,[317-318] which can lead to activation of complement responses.[319] Over the last decade or so, much research activity has been focused on the design of an alternative non-fouling biomaterial, which has led to considerable advances in the design of novel biocompatible materials. Various new surface coatings, such as SAMs,[320] grafted polymer layers,[321] and polymer brushes,[3,153,322] have been proposed that substantially reduce protein absorption.

Zwitterionic-based polymers have been used for a wide range of biomedical and engineering applications.[318] Such surface coatings are highly resistant to non-specific protein adsorption, bacterial adhesion, and biofilm formation.[160,323] Jiang et al. has demonstrated the superlow fouling properties of glass slides grafted with two zwitterionic polymers, poly(sulfobetaine methacrylate) (PSBMA) and poly(carboxybetaine methacrylate) (PCBMA). They have shown that these surfaces reduced fibrinogen adsorption to a level comparable with that of adsorption on poly(ethylene glycol)-like films.[161] In some cases the zwitterionic character is insensitive to the solution pH (e.g. PSBMA,[324] and PMPC [325]), whereas in other cases some pH-sensitivity can be observed (e.g. PCBMA [326]).

Particular attention has been paid to *stimulus-responsive* polymer brushes based on either polyacids or polybases.[97,146,259,327-328] These polyelectrolytic brushes are typically responsive to changes in pH or ionic strength.[276-277,328-330] For example, the stimulus-responsive behaviour of PAA brushes has been studied by Ayres et al.[95] Collapsed brushes were observed below the pK_a of the brush, whereas highly anionic swollen brushes were formed above this critical value.[95] The pH-responsive behaviour of PMAA brushes, which enable switching between collapsed and stretched brush conformations at different pH, has been

investigated using ellipsometry and AFM.[331-332] Complementary behaviour has been reported for various weak polybase brushes based on either PDEAEMA,[97] or PDMAEMA).[258-259,333]

As far as we are aware, relatively little work has focused on zwitterionic polymers containing amino acid motifs as side-chains. Such polymers would contain both carboxyl groups (−COOH) and amine groups ($-NH_2$) on α carbons, and a side chain.[155,334-337] Phosphatidylserine (PS) was found to bind copper (II) ions with high affinity at pH 5-8, depending on the PS concentration.[335] Rosen et al. reported that cysteine-functionalized silica nanoparticles resist protein fouling in the presence of either lysozyme or bovine serum albumin (BSA).[334] Azzaroni and co-workers reported the growth of zwitterionic poly(methacryloyl-L-lysine) brushes from mesoporous silica using surface-initiated radical polymerisation with the aim of modulating ionic transport via pH variation.[336-337] Liu et al. prepared zwitterionic poly(serine methacrylate) (PSerMA) brushes grafted onto a planar gold substrate via surface-initiated photoiniferter-mediated polymerization (SI-PIMP) for evaluation as a potential anti-biofouling material.[155]

Herein a new zwitterionic monomer, cysteine methacrylate (CysMA), has been conveniently synthesized on a multi-gram scale in aqueous solution via thia-Michael addition of cysteine to a commercial methacrylate-acrylate precursor. SI-ATRP was then used to grow PCysMA brushes from planar silicon wafers. The stimulus-responsive behavior of PCysMA with respect to changes in pH and ionic strength was also investigated using ellipsometry, AFM and surface zeta potential measurements (Scheme 4.1). The stability of PCysMA brushes in alkaline media was examined. The UV-induced photodegradation of PCysMA brushes was also studied using XPS and AFM. Micro- and nano-structured PCysMA brushes were prepared using a photomask and IL, respectively. Fluorescence microscopy and AFM were utilized to characterize the selective adsorption of fluorescently proteins onto these model surfaces. Complement depletion assays were used to compare the anti-biofouling performance of PCysMA brushes to other well-known biocompatible PMPC and POEGMA brushes.

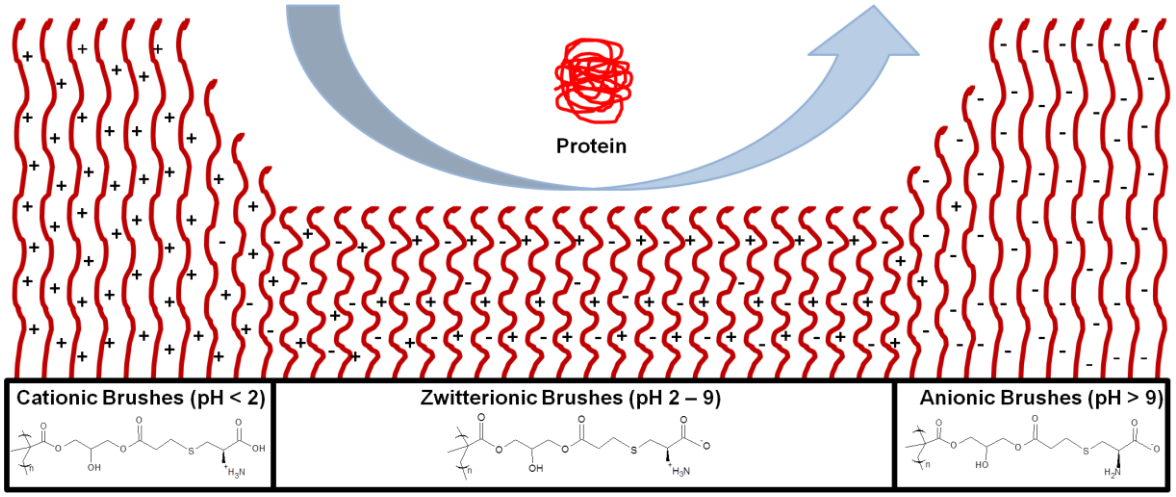

Scheme 4.1 Schematic representation of the nature of PCysMA brush at different pH environments and the resistance of PCysMA brush to non-specific protein adsorption.[338]

4.2 Experimental Section

4.2.1 Synthesis of Cysteine Methacrylate (CysMA)

In a 250 mL round-bottom flask, L-cysteine (15.13 g, 124.88 mmol) was dissolved in deionized water (100 mL). 3-(Acryloyloxy)-2-hydroxypropyl methacrylate (29.43 g, 137.36 mmol) was added to this stirred aqueous cysteine solution, then dimethylphenyl phosphine (20 µL, 1.47 x 10^{-1} mmol) was added and the aqueous reaction mixture was stirred for 2 h at 20^{o}C. The reaction solution was washed twice with ethyl acetate (50 mL) and dichloromethane (2 x 50 mL) and the final CySMA monomer product was isolated as a pure white solid (39.6 g, 94% yield) by freeze-drying the concentrated aqueous solution overnight, (shown in scheme 4.2).

^{1}H NMR (400.13 MHz, D_2O, 298 K) δ (ppm): 1.89 (s, 3H, -CH_3); 2.68-3.17 (m, 6H, -S-CH_2-CH_2-COO-, -S-CH_2-CH(COO$^-$)NH_3^+); 3.79 (m, 1H, CHOH); 3.90 (m, 1H, -CH(COO-)NH_3^+), 4.20-4.30 (m, 4H, -CH_2-CHOH-CH_2-); 5.70 (s, 1H, vinyl), 6.13 (s, 1H, vinyl).

^{13}C NMR (400.13 MHz, D_2O, 298 K) δ (ppm): 17.31 (-CH_3); 26.28 (-S-CH_2-CH_2-); 32.04 (-S-CH_2-); 33.85 (-S-CH_2-CH_2-); 53.47 (-CH_2-CHOH-CH_2-); 65.17, 65.26 (2C, -CH_2-CHOH-CH_2-); 66.81 (-CH(COO-)NH_3^+); 127.39, 135.57 (2C, vinyl); 169.38, 172.70, 174.07 (3C, carbonyls).

($M+H^+$): Calculated: 336.1117. Found: 336.0

Elemental microanalysis: Calculated: C: 46.56 %; H: 6.31 %; N: 4.18 %; S: 9.56 %. Found: C: 46.31 %; H: 6.33 %; N: 4.30 %; S: 9.58 %

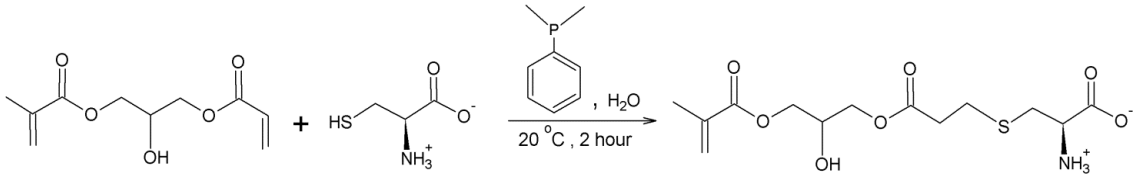

Scheme 4.2 Synthesis of the cysteine methacrylate monomer (CysMA) used in this work.

4.2.2 Preparation and UV modification of of bromo initiators

The preparation of BIBB-APTES film on silicon wafers was prepared as described in section 2.3.1. BIBB-APTES on a silicon wafer was exposed to 2 $J.cm^{-2}$ through an electron microscope Cu grid mask, as described in chapter 3, then the samples were and washed with ethanol, and dried under N_2.

4.2.3 Preparation of poly(cysteine methacrylate) (PCysMA) brushes

Initiator-functionalized silicon wafers were placed in Schlenk tubes within a Carousel 12 Reaction Station (Radleys, UK), degassed via three vacuum/refill cycles, then filled with dry N_2. CysMA (5.0 g, 15.0 mmol) was dissolved in deionized water (12.0 mL) at 20^{o}C and degassed for 30 min. Bipy (234 mg, 1.50 mmol), Cu(I)Br (71.4 mg, 0.50 mmol) and Cu(II)Br_2 (55.6 mg, 0.25 mmol) were added to this aqueous solution. This reaction mixture was degassed for 10 min, and then briefly sonicated. To commence the surface ATRP of the CysMA, an aliquot of this reaction solution (2.0 mL) was transferred into each Schlenk tube. At specific desired reaction times, the substrates were removed from each Schlenk tube, sonicated in water and rinsed with ethanol to remove unreacted monomer, and then dried using a dry N_2 purge, (see Scheme 4.3).

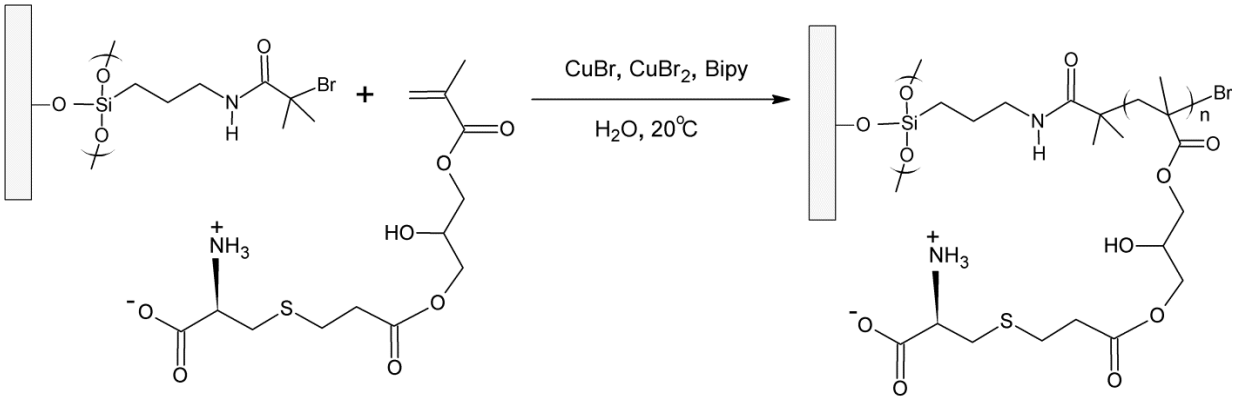

Scheme 4.3 Schematic representation of the synthesis of a PCysMA brush from this initiator-functionalized planar surface via SI-ATRP in deionized water at 20 ^{o}C using a copper-based catalyst.

4.2.4 UV degradation and photopatterning of PCysMA brush

A Coherent Innova 300C FreD argon ion laser with an emission wavelength of 244 nm was used for the UV photodegradation experiments, as described in chapter 2. Micro-patterned brushes were obtained by irradiating uniform polymer brush layers on silicon wafer using an electron microscopy copper grid (2000).[191] For nano-patterned brushes, IL was conducted using either a two-beam interference system (Lloyd's mirror), or a three-beam interference system (Lloyd's mirror).

4.2.5 Surface derivatization

The surface aldehyde groups generated via UV irradiation were derivatized by reaction with 2-amino-1,1,1-trifluoroethane (TFEA). The UV-irradiated PCysMA-coated silicon wafer was immersed in a 1.0 mM ethanolic solution of TFEA for 24 h, after which the wafer was removed, rinsed with ethanol and dried using a stream of dry N_2.

4.2.6 Protein patterning

The protein resistance of UV-irradiated PCysMA brushes was studied using green fluorescent protein (GFP). PCysMA brush-coated silicon wafers were irradiated with UV light (λ = 244 nm, 13.2 J cm^{-2}) using either a photomask to prepare micropatterns or using IL to generate nano-patterned surfaces, as reported in the literature.[193] Unpatterned and patterned PCysMA brush-coated silicon wafers were immersed in an aqueous solution

containing 10.0 mg dm^{-3} of either GFP or YFP in PBS for 12 h at 4 ^{o}C. Then the wafers were thoroughly rinsed with copious amounts of aqueous PBS solution and deionized water, gently dried using a dry N_2 purge.

4.2.7 Preparation of poly[2-(methacryloyloxy)ethyl phosphorylcholine] (PMPC) brushes

2-(Methacryloyloxy)ethyl phosphorylcholine monomer (MPC) (6.0 g, 20 mmol) was placed in a flask under a nitrogen atmosphere after four pump/refill cycles. Water and methanol were degassed separately by a stream of nitrogen (for at least 60 min). Water (5 mL) and methanol (5 mL) were added to the MPC by syringe at room temperature. CuBr (48.4 mg, 0.338 mmol), $CuBr_2$ (36.8 mg, 0.165 mmol), and 2,2'-bipyridine (157.5 mg, 1.014 mmol) were added, then the mixture was stirred under nitrogen for 10 min and then briefly immersed in an ultrasonic bath to aid catalyst dissolution. Initiator-functionalized surfaces were sealed in Schlenk tubes, degassed, then filled with nitrogen. The polymerization solution (2 mL) was added to each tube from a syringe. After various times, individual tubes were opened and washed with water and methanol. The PMPC brush-coated wafers were briefly sonicated removed and then rinsed thoroughly with water and methanol, and dried under a nitrogen stream. The mean dry brush thickness of each PMPC brush layer on Si wafer was measured by ellipsometry.[165,339] The contact angle θ_{AW} for the resulting PMPC brush was measured to be less than 7^{o}.

4.2.8 Preparation of poly(oligo(ethylene glycol)methyl ether methacrylate) brushes

Poly oligo (ethylene glycol) methyl ether methacrylate (480 MW) (5g, 10 mmol) was dissolved in water (5 mL), and degassed by passing a stream of nitrogen through the solution for 30 min. Then, Bipy (0.07g, 0.454 mmol), CuBr (0.023g, 0.16 mmol) and $CuBr_2$ (0.011g, 0.047 mmol) were added to the solution. The monomer/catalyst mixture was degassed with a stream of nitrogen for 10 min. Initiator functionalised samples were sealed in Schlenk tubes and degassed (vacuum/refill cycles). The monomer/catalyst solution (2 mL) was added to each Schlenk tube from a syringe. The samples were removed, washed with water and ethanol, and dried under a steam of N_2. The contact angle was measured to be θ_{AW}: 43^{o}±2.

4.2.9 Surface characterization techniques

Contact angle, ellipsometry, AFM, surface zeta potential measurements and XPS were utilized to characterize polymer brushes, as described in chapter 2. Contact angles were measured and averaged from three water droplets, across the surface. The kinetics of brush growth on was studied by ellipsometry. The Change in the PCysMA brush thickness in solutions of varying pH and NaCl concentration was investigated by ellipsometry and AFM. Wide scan and high resolution XPS spectra were used to determine the surface structures of the polymer brushes, and of the PCysMA after photodegradation. The surface charge was determined at a range of pH. Fluorescence images were obtained for protein patterns on PCysMA using a LSM510 meta laser scanning confocal microscope, as described in chapter 2.

4.2.10 Cell adhesion test and complement depletion assay

Cell adhesion test and complement depletion assay were carried out by Dr. Irene Canton, Department of Biomedical Science, Sheffield University. The complement depletion assay shows whether protein could attach to surfaces. The complement works in a very complex cascade of proteins (e.g. protein one attaches first, then a second one only attaches if protein one is in). There are several cascades happening at the same time and it is very difficult to predict which one will act in the surfaces. Hence, if one only protein is take as a test (in the example of the bovine seroalbumin) it might be underestimating the fouling reaction.

In these experiments, human serum was used which contains all the proteins from the complement in humans. Activated red blood cells were used which they can be fouled by the complement in the human serum. If the complement attach to them, they will break and release haemoglobin which can easily be detected in a plate reader. The red blood cells in the wells compete for the complement proteins with brush surfaces. It is known that all the red blood cells can be lysed with water, so it is 100% lysis. However, when no complement is present, no red blood cells will lyse, so it is assumed to be 0% lysis. By measuring the amount of serum (in percentage) indicate that the brushes are depleting from the well. The more the brushes are depleting (fouling), the less the red blood cells will lyse.

MTT Assay

Samples were disinfected in a sterile environment using ice-cold 70% ethanol for 10 minutes and then washed three times using sterile PBS solution. Afterwards, cell viabilities were assessed via MTT assay (MTT = 3-(4,5-dimethylthiazol-2-yl)-2,5 diphenyl tetrazolium bromide; Sigma-Aldrich, St Louis, MO). Briefly, each brush-coated surface was removed, cells were washed with PBS and then incubated with MTT solution (0.50 g dm^{-3} MTT in PBS, 1.0 ml per well in a 24-well plate) for 45 min at 37°C in a humidified incubator (5% CO_2, 95% air). In healthy viable cells, MTT is reduced to a purple colored formazan salt by the activity of the mitochondrial enzyme, succinyl dehydrogenase. After 45 min, the solution was aspirated and the insoluble intracellular formazan product was solubilized and released from cells by adding acidified 2-propanol (0.50 ml per well in a 24-well plate or 1 mL per cm^2 of cultured tissue) and incubated for 10 min. The optical absorbance at 540 nm was then measured using a UV/Vis spectrophotometer equipped with a plate reader and a 630 nm reference filter.

Mean cell viability data and SEM were normalized relative to a negative control (planar glass surfaces containing no polymer brush, 100% cell viability) and expressed as a percentage viability ± SEM. Experiments were performed in triplicate well samples with n = 3 independent experiments. For statistical analysis, a student's paired t-test was used for the raw data to assess the significance of differences between the various treatments and the control group.

Cell adhesion test

Polymer brushes were grown from identical 13 mm diameter circular glass slides to evaluate cellular adhesion, with uncoated glass slides being used as a control. Both polymer-coated and uncoated glass slides were disinfected using ice-cold ethanol as described above and placed at the bottom of 24-well plates. Then HDF cells were added to the surface (1×10^5 cells per well and surface). Cells were incubated for 24 h to allow sufficient time for possible cell adhesion onto the brush surface. The cell viability MTT test was used to assess the extent of cell adhesion. HDFs cells are adherent cells, and it is well recognized that surface attachment is a requirement for such cells viability.[340] Therefore lack of viability (low MTT values) after cell contact with the brush coated and uncoated surfaces reflected poor adhesion.

Complement depletion assay

Complement activation was assessed as the lytic capacity of a normal human serum (NHS) (Sigma-Aldrich, UK) towards antibody-sensitized sheep erythrocytes after exposure to polymer brush surfaces (scheme 4.4). The methodology was adapted from traditional CH50 tests[341] for use on polymer brushes. Sheep erythrocytes (Oxoid, UK) were sensitized by rabbit anti-sheep erythrocytes antibodies (Abcam, UK) and diluted by the veronal-buffered saline (VBS++) at a final concentration of 2 x 10^9 cells per mL. Veronal-buffered saline containing 0.15 mM Ca^{2+} and 0.5 mM Mg^{2+} (VBS++) were purchased from Lonza, UK. Aliquots of NHS (100 µl) were incubated with 13 mm diameter glass surfaces with polymer brushes of varying thickness (small 4-7 nm, medium 13-16 and long 24-28 nm). Afterwards, NHS supernatants were removed and mixed with fresh antibody-sensitized erythrocytes.

After incubation for 45 min at 37 °C, the reaction mixture was lightly centrifuged at 1000 rcf for 10 min. The absorbance of the carefully decanted supernatant was determined at a fixed wavelength of 415 nm using a microplate reader (Biotek, UK) and compared to the results obtained using control serum in order to evaluate the extent of hemolyzed erythrocytes. Positive and negative controls were prepared for each series of experiments in order to account for any difference in the hemoglobin response for a given erythrocyte preparation. When using diluted serum, a control for the serum lysis capacity was performed, whereby aliquots of the diluted serum were compared to the 100% lysis water control. In order to eliminate false positives, only dilutions that correlated with the 100% lysis control were used for this study. Furthermore, corrections for background noise and spontaneous erythrocyte hemolysis were estimated from UV/VIS spectra recorded for blanks containing only brushes in buffered solution and only erythrocytes, respectively.

For clarity, mean data and SEM were normalized to the 100% serum lysis control (also 0% depletion control) and expressed as a percentage of depletion ± SEM. Experiments were performed in duplicate well samples with n = 3 independent experiments. The Student's paired t-test was used to analyze the raw data to assess the significance of differences between the various treatments and the control group

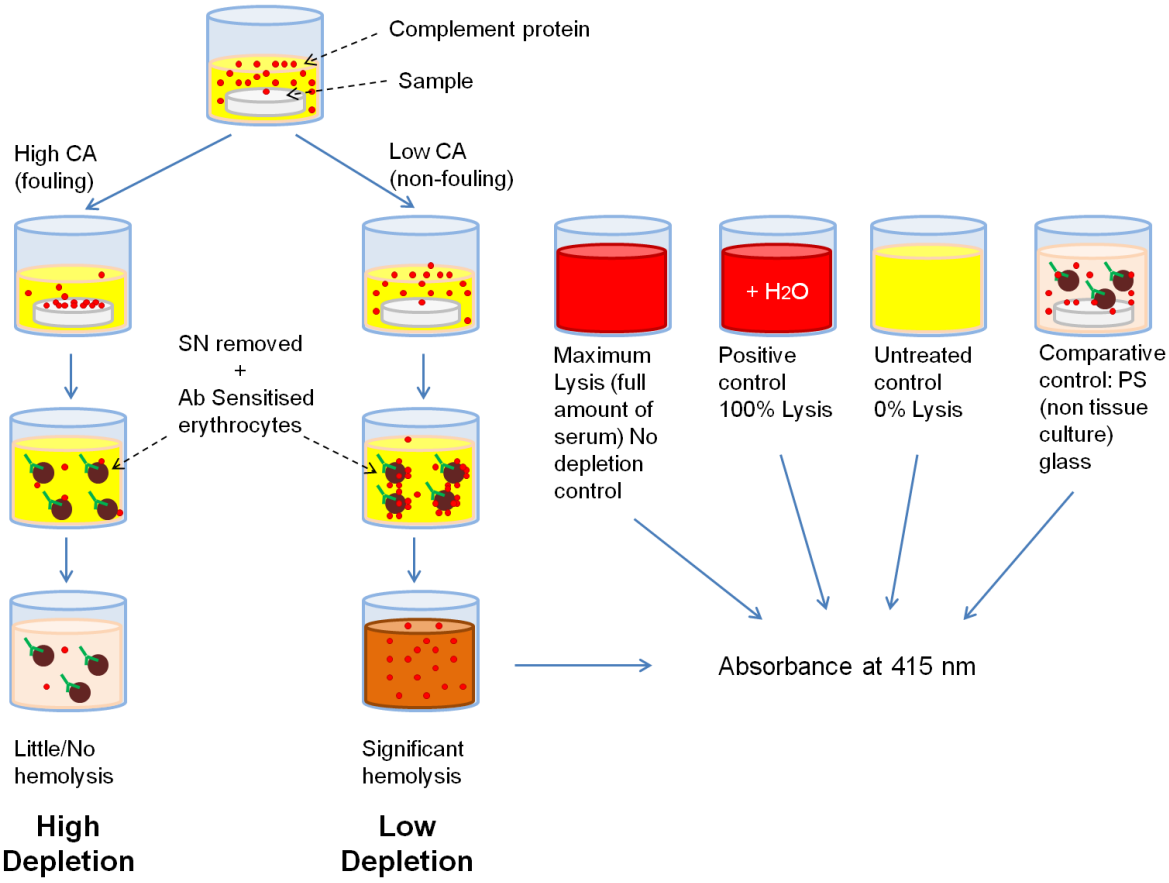

Scheme 4.4. representing the methodology of the complement consumption/depletion assays. Briefly, 13-mm diameter glass surfaces with different thickness polymer brushes were incubated with 100 µl of human serum. Afterwards, the supernatants (SN) were removed and mixed with fresh antibody sensitized erythrocytes. Complement proteins will bind the erythrocytes, and produce lysis. If the surfaces promote complement adhesion (CA), these proteins will be depleted from the serum and in contact with sensitized erythrocytes they will produce low hemolysis. No depletion will result in high hemolysis. Quantification can be done via reading absorbance at 415 nm. Comparative controls are included in the test to normalize the data.

4.3 Results and Discussion

4.3.1 Preparation of CysMA monomer

Cysteine methacrylate (CysMA) monomer was conveniently synthesized in high yield at 20°C in aqueous solution by a selective thia-Michael addition.[342] A natural amino acid, L-cysteine, was reacted with 3-(acryloyloxy)-2-hydroxypropyl methacrylate in the presence of a nucleophile catalyst (dimethylphenylphosphine (DMPP)), see Scheme 4.5. The reaction was relatively fast (2 h), and the overall yield was approximately 94%. The chemical structure of the monomer was confirmed by ^{1}H and ^{13}C NMR, mass spectroscopy and elemental microanalyses.

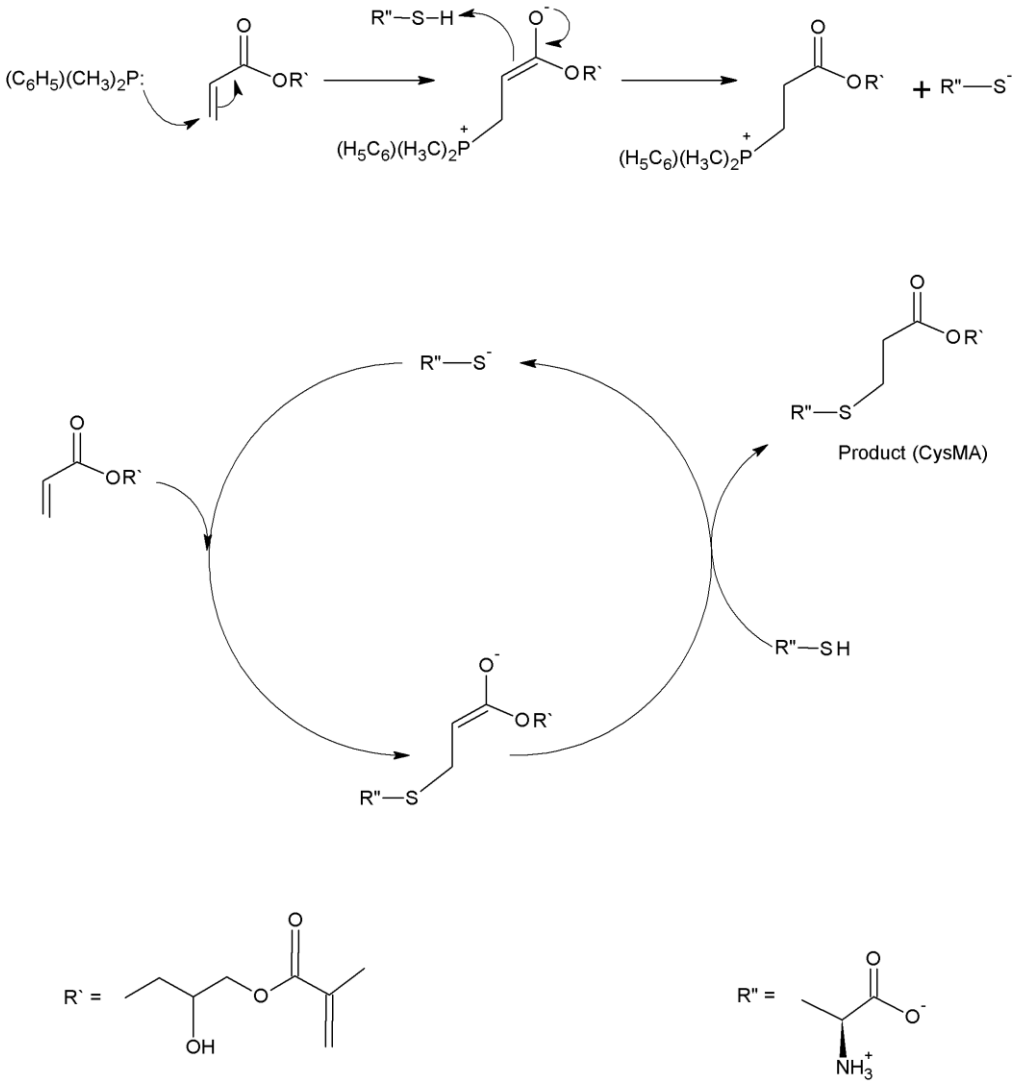

Scheme 4.5 Shows the mechanism of preparing the cysteine methacrylate monomer (CysMA) by a selective thia-Michael addition.

4.3.2 Growth of PCysMA brushes

PCysMA brushes were grown from BIBB-APTES-functionalized silicon wafers via SI-ATRP, which is known to be an effective and convenient technique for the synthesis of dense uniform polymer brushes with controlled thickness. The [CysMA]/[Cu(I)] molar ratio, solvent type and CysMA/catalyst molar ratio in the aqueous ATRP formulation were varied so as to optimize the brush growth conditions. Figure 4.1 shows the evolution of PCysMA brush thickness over time at 20 ^{o}C using [CysMA]/[Cu(I)Br] molar ratios of 30, 100 and 150. Ellipsometric dry brush thicknesses of up to 27 ± 3 nm were achieved after 270 min. The rate of polymerization is very fast for the first 15 minutes, followed by slower, approximately linear brush growth thereafter. Higher [CysMA]/[Cu(I)Br] molar ratios led to thicker PCysMA brushes, as expected.

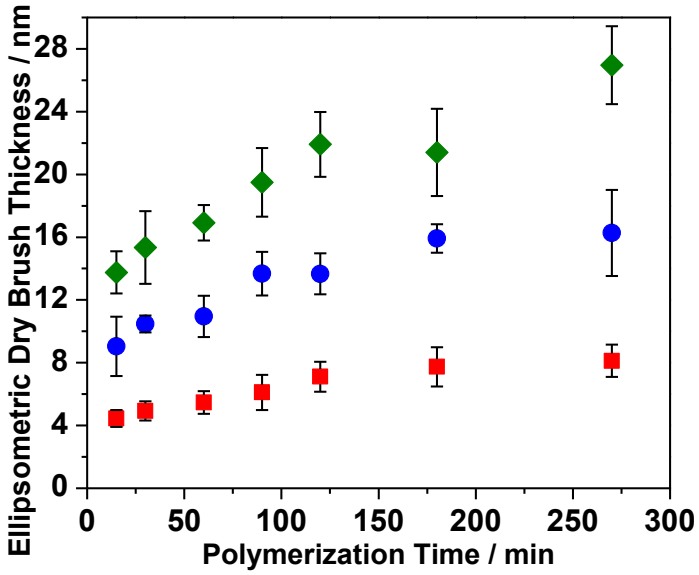

Figure 4.1 Evolution of ellipsometric dry PCysMA brush thickness with polymerization time for the synthesis of PCysMA brushes via SI-ATRP in deionized water at 20 ^{o}C. Conditions: (■) [CysMA]: [CuBr]: [$CuBr_2$]: [Bipy] molar ratio = 30: 1.0 : 0.5 : 3. (●) [CysMA]: [CuBr]: [$CuBr_2$]: [Bipy] molar ratio = 100: 1.0 : 0.5 : 3. (♦) [CysMA]: [CuBr]: [$CuBr_2$]: [Bipy] molar ratio = 150: 1.0 : 0.5 : 3.

Polymerization of CysMA was then conducted using photopatterned BIBB-APTES-functionalized silicon wafers. According to AFM studies, this micro-patterned substrate does not exhibit any height contrast between the UV-exposed and unexposed areas (Figure 4.2).

After polymerization, AFM topographical imaging confirms significant height differences between irradiated areas (squares) and non-irradiated areas (bars), as expected. These height differences were quantified to determine the mean PCysMA brush thickness.

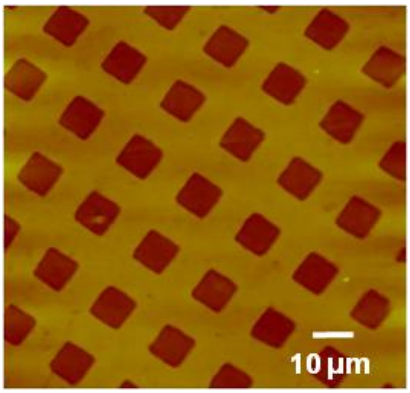

Figure 4.2 AFM topographical image of the periodic brush height recorded for a micro-patterned PCysMA brush. Image size: 75 × 75 µm. The *z*-range: 0- 50 nm dark to bright.

4.3.3 PCysMA surface characterization

AFM topographical images were acquired for non-patterned PCysMA brushes in order to study their surface roughness, both in the dry state and also immersed in PBS (see Figure 4.3). The root mean square (rms) surface roughness averaged across the entire image area was 0.5 ± 0.2 nm in the dry state. However, the PCysMA brush became somewhat smoother when immersed in PBS solution, with an rms of approximately 0.3 ± 0.1 nm.

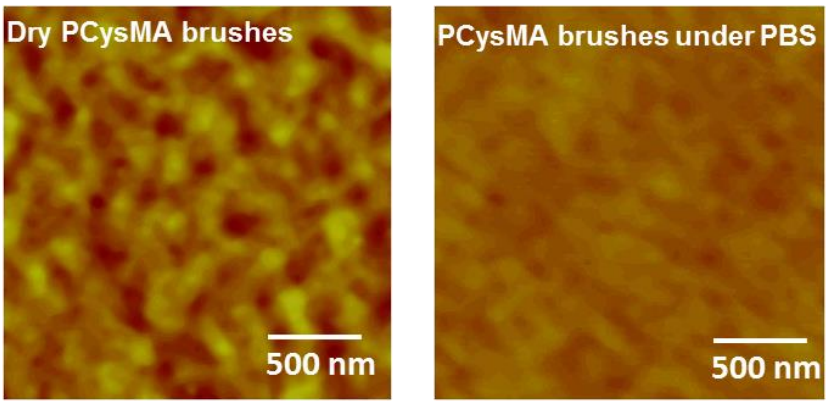

Figure 4.3 Height images of PCysMA brushes grown by SI-ATRP on Si. Image size: 2.0 × 2.0 μm^2. The *z*-range is 0- 5 nm dark to bright in both images.

XPS wide scans were used to estimate the elemental compositions of the PCysMA brushes which are presented in Figure 4.4. The elemental compositions (C, N, O, S) of brushes with a 12 nm dry thickness were close to the calculated values (C = 59.1%, N = 4.5% , O = 31.8% and S = 4.5 %). High resolution C1s, N1s and S2p XPS spectra were acquired for PCysMA dry brushes in order to confirm their chemical structure (see Figure 4.5). XPS C1s spectra were fitted using three components with binding energies of 285.0, 286.3 and 288.5 eV, which correspond to C−C, C−O/C−N and O=C−O, respectively. The C−C, C−O/C−N and O=C−O atomic ratios calculated from the fitted C1s spectrum were 2 : 1.5 : 1 which is close to the theoretical ratio of 2 : 1.3 : 1. The N1s core-line spectrum recorded for the PCysMA brush (dried at pH 6) was fitted using two binding energy components of 399.0 eV and 401.5 eV, which correspond to C-NH_2 and C-NH_3^+ species.[343-344] It is estimated that ca. 80 % of the surface primary amine groups are protonated. The S2p high resolution spectrum was fitted with two $S2p_{3/2}$ and $S2p_{1/2}$ components with binding energies of 163.5 and 164.5 eV, respectively. The relative intensities of these components are in the ratio 1.9 : 1, as expected for 2J + 1 spin-orbit coupling.[343-344]

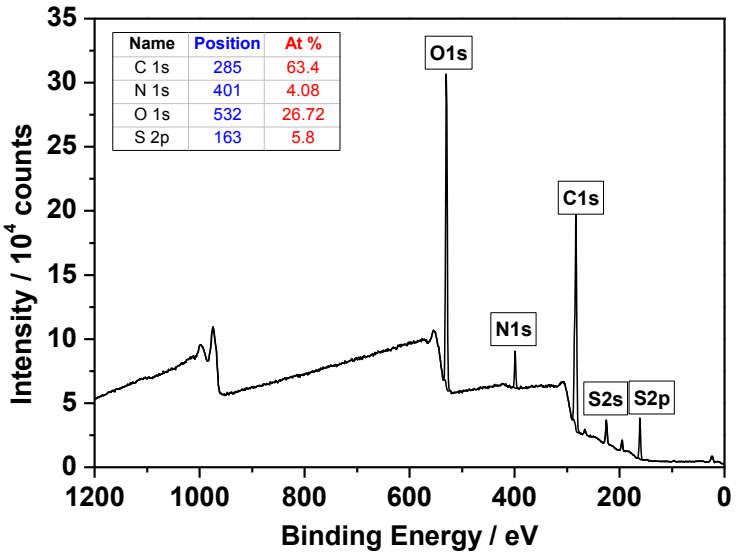

Figure 4.4 Wide scan XPS spectra recorded for 12 nm PCysMA brush.

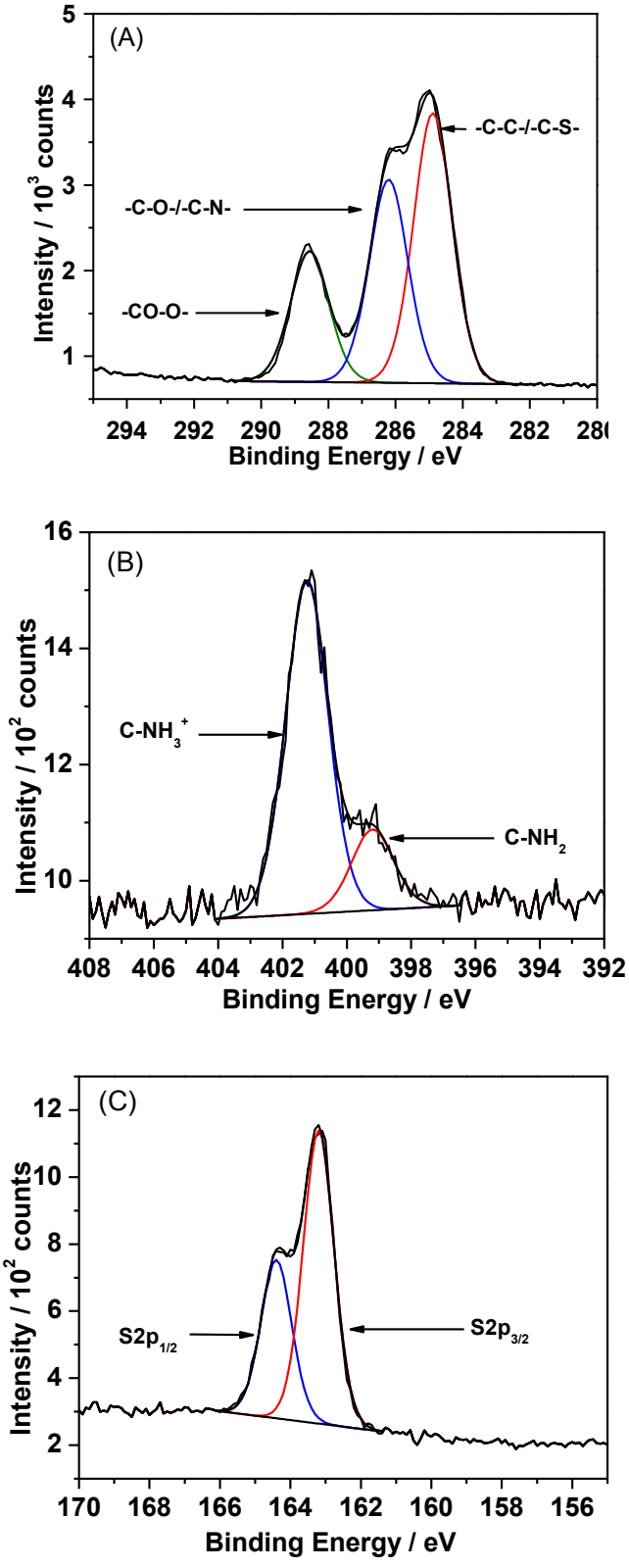

Figure 4.5. X-ray photoelectron core-line spectra recorded for a PCysMA brush of 12 nm dry thickness. (A) C1s spectrum. (B) N1s spectrum. (C) S2p spectrum.

4.3.4 pH-responsive behaviour of PCysMA brushes

The carboxylic acid and amine groups in each CysMA residue confer pH-responsive behaviour on the PCysMA brushes. In this sense these weak acid/weak base brushes differ significantly from permanently zwitterionic betaine-based brushes such as PMPC or PSBMA, or indeed PCBMA (which only possesses weak acid character). Below its pK_a, the carboxylic acid group becomes neutral while all the amine groups remain protonated. Thus the brush layer stretches away from the surface because of the strong electrostatic repulsion between adjacent cationic chains. In contrast, the amine groups become deprotonated above their pK_a while the carboxylic acid groups remain ionized, hence the brushes become anionic and highly swollen. At intermediate pH values (i.e. $pK_a^{COOH} < pH < pK_a^{NH_2}$), the PCysMA brushes exhibit zwitterionic character and are somewhat less swollen than their polyelectrolytic forms. This complex pH-sensitive behavior was studied using both ellipsometry and AFM (see Figure 4.6 and Figure 4.7).

The pH-modulated dimensions of a PCysMA brush (dry brush thickness = 15 nm) immersed in aqueous solution was investigated by varying the solution pH over a wide range. The ellipsometric data (see Figure 4.6) indicates that the PCysMA brushes become protonated below approximately pH 2.0 and attain their maximum swollen thickness at around pH 1.5. Conversely, the brushes are fully deprotonated above pH 9.8 and acquire anionic character. The mean brush thickness increased from 15 nm (dry state) up to approximately 36 nm (at pH ~ 1.5). This corresponds to an increase of about three times between the fully swollen and dry brush thicknesses. Between pH 1.6 and 2.0, there is a gradual reduction in brush thickness from 36 nm to 28 nm because of the higher degree of ionization of the carboxylic acid groups. The mean PCysMA brush thickness then remains constant at approximately 26 nm between pH 2.0 and pH 9.5; this corresponds to the zwitterionic brush regime. Finally, the brush thickness increases gradually from 28 nm up to approximately 34-35 nm between pH 9.5 and pH 9.8 as the amine groups become deprotonated and the brush chains acquire anionic character.

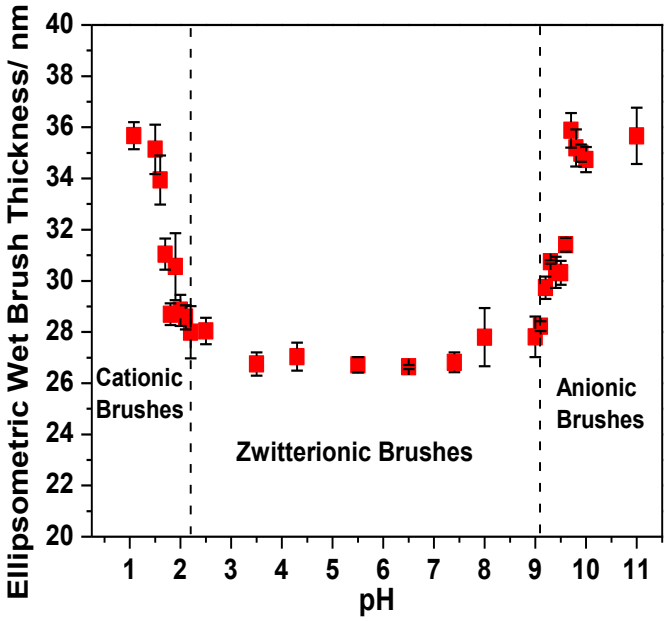

Figure 4.6 Variation of *in situ* ellipsometric dry brush thickness with solution pH for a PCysMA (15 nm dry thickness) brush immersed in aqueous solution. The error bars represent the standard deviation of three measurements in the brush sample.

AFM studies of a micro-patterned PCysMA brush immersed in aqueous solutions of varying pH were also conducted (Figure 4.7 and Figure 4.8). These AFM observations are in generally good agreement with the ellipsometric data, with minor differences most likely arising because of uncertainties in the refractive index of 1.50 estimated for the PCysMA brush when modelling the ellipsometric data (this parameter is also likely to vary with the solution pH). Figure 3b shows the change in brush height for a micro-patterned PCysMA brush as a function of pH. The brush height increases from about 15 nm in the dry state up to 44 nm when immersed in an acidic solution (pH < 1.5). The brush height is gradually reduced between pH 1.6 and 2.0, and then remains constant at approximately 28 nm between pH 2.0 and 9.5. Finally, there is a gradual increase in brush height between pH 9.5 and 9.7 and a maximum brush thickness of 40 nm is observed above pH 10. The pK_a of the carboxylic acid groups in the PCysMA brush is estimated to be approximately 1.7, compared to a pK_a of 2.0 for the carboxylic group of L-cysteine. Similarly, the amine pK_a of the PCysMA brushes is estimated to be 9.6, whereas for L-cysteine it is reported to be 10.2.[345] These differences are attributed to the well-known polyelectrolyte effect: the pH response of polyacids and polybases is always weaker than the corresponding small molecules since polymer chains can resist the build-up of local charge density.[332,346]

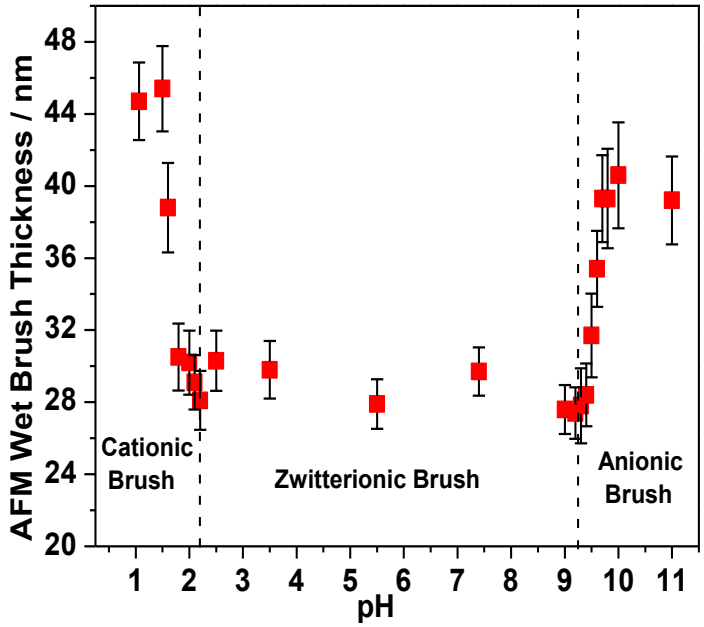

Figure 4.7 Variation of *in situ* brush thickness with solution pH for a PCysMA (15 nm dry thickness) brush immersed in aqueous solution measured by tapping mode AFM. The error bars represent the standard deviation of 10 cross-section lines in the brush sample.

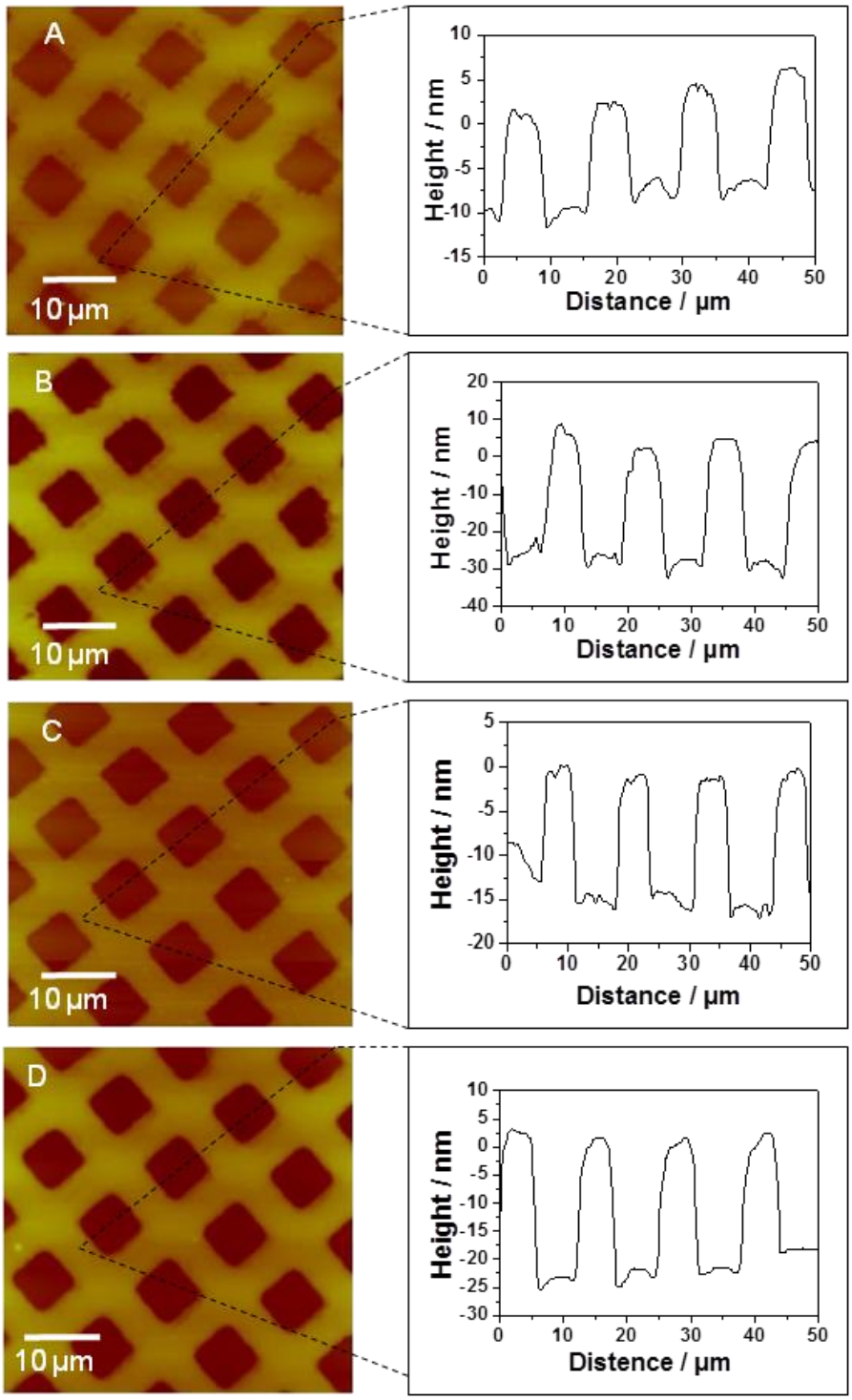

Figure 4.8 AFM height images (50 × 50 µm^2) recorded for micro-patterned of PCysMA brushes: (A) dry brush in air, (B) same brush immersed a solution at pH 1.5, (C) same brush immersed in buffer solution at pH 7.0 and (D) same brush immersed in alkaline solution at pH 10.5. z-contrast range: 0-100 nm dark to bright. A representative cross section through the height image is shown for each image.

4.3.5 Surface zeta potential

Surface zeta potentials were determined for PCysMA brushes over a wide range of solution pH, see Figure 4.9. Positive surface zeta potentials of +15 ± 5 mV were observed below pH 2 for protonated PCysMA brushes. Between pH 2.5 and 9.0, the PCysMA brush exhibited weakly negative surface zeta potentials (-5 to -10 mV). In principle, the brush layer should be in its zwitterionic form over this pH range, so zero surface zeta potentials might be expected. The observed weakly anionic character may indicate preferential adsorption of Cl^- and/or OH^- from the bulk solution. Above pH 9, the surface zeta potential becomes much more negative (- 40 ± 8 mV), indicating deprotonation of the amine groups within the PCysMA brush. Overall, these surface zeta potential data are in good agreement with the changes in brush thickness observed using ellipsometry and AFM discussed above and support our interpretation of the complex pH-modulated behaviour exhibited by this doubly pH-responsive brush in aqueous solution.

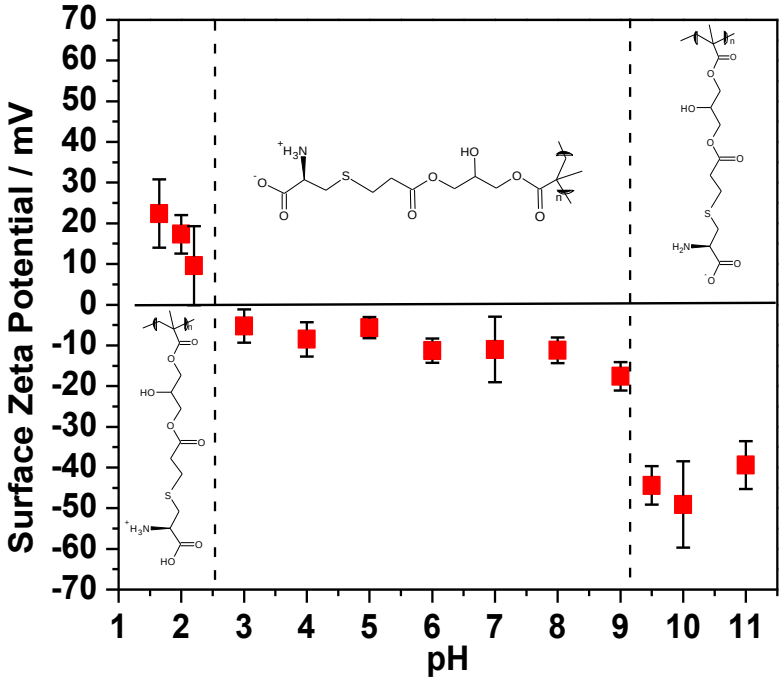

Figure 4.9. Surface zeta potential vs pH curves obtained for PCysMA brushes using a Malvern dip cell. PCysMA brush (original dry brush thickness = 22 nm) immersed in (1 mM KCl) aqueous solutions of varying pH.

4.3.6 Salt-responsive behaviour

The effect of ionic strength on the PCyMA brush dimensions was also investigated by adding salt (NaCl). According to the literature, polybetaines such as PCysMA are expected to expand on addition of salt. Such behaviour is well known for various polybetaines and is known as the so-called 'anti-polyelectrolyte' effect.[63] Figure 4.10 shows the change in PCysMA brush thickness with added salt at pH 6, as judged by ellipsometry. The mean brush thickness increased monotonically from 28.0 nm to 30.5 nm when immersed in 0.3 to 1.5 M NaCl. The added salt screens the inter-chain *attractive* electrostatic interactions, which allows modest brush expansion. In contrast, the addition of salt to polyelectrolytes screens the *repulsive* electrostatic interactions between adjacent chains, which causes their collapse (see Figure 4.10). There was a gradual decrease in the wet brush thickness, from 43 nm to 35 nm with addition of salt at pH 1.5. When the concentration of NaCl in solution is increased at pH 9.8, the brush is observed to swell until reaching a maximum brush swelling at 100 mM. This might be due to the proton concentration inside the brush is higher than that in the solution. Addition of salt could replace the protons by salt counterions, as a result the ionization degree of the polymer chains increases.[347-349] At added salt concentrations >100 mM, it was observed that the thickness of the PCysMA brush decreases gradually decreased from 48 nm to 35 nm at 1M of NaCl.

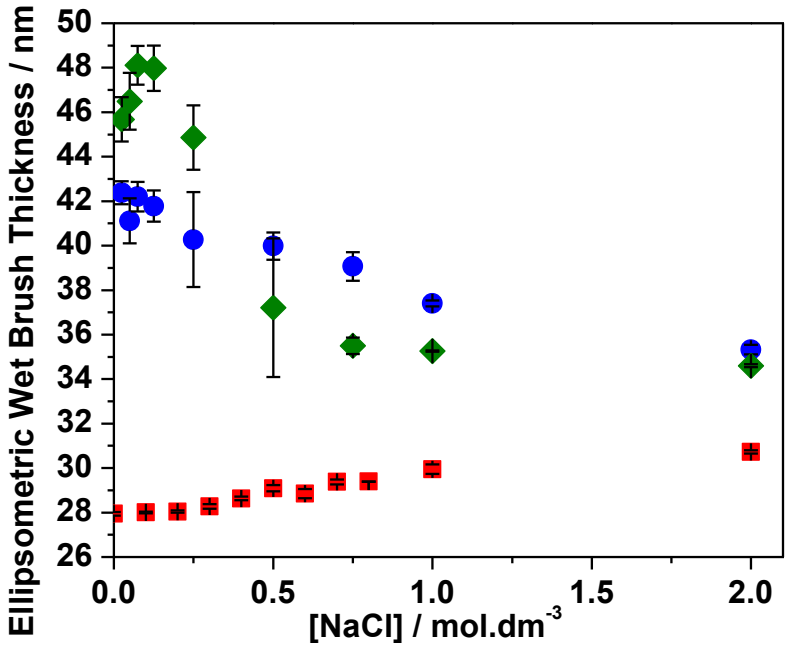

Figure 4.10 *In situ* ellipsometric wet thickness of PCysMA brushes as a function of added at 20°C. (■) immersed in aqueous solution at pH 6 (original dry thickness = 15 nm). (●) immersed in aqueous solution at pH 1.5 (original dry thickness = 18 nm). (♦) immersed in aqueous solution at pH 9.8 (original dry thickness = 18 nm).

4.3.7 Chemical degradation of PCysMA brushes

PCysMA brushes exhibit good chemical stability in either acidic or neutral aqueous solution. However, chemical degradation occurs in alkaline solution since the deprotonated primary amine groups can attack the two ester groups in the CysMA repeat units. Similar observations have been reported for poly(2-aminoethyl methacrylate) in dilute aqueous solution.[350] This phenomenon occurs at ambient temperature at a rate that is strongly pH-dependent. Herein the chemical degradation of PCysMA brushes was studied at pH 8, 9, 10 and 11, with the primary amine groups being either partly or fully deprotonated under these conditions. There are at least four possible degradation pathways, as shown in scheme 4.6. A primary amine could react intramolecularly with an ester carbonyl group that is located either on the same CysMA residue or on an adjacent repeat unit to form an amide. If the primary amine group reacts with an ester carbonyl on a neighboring PCysMA chain, a cross-link could be formed. At higher pH, base-catalyzed ester hydrolysis may also occur. No changes

in the ellipsometric brush thickness after 10 days at pH 8. Ellipsometric studies indicate a gradual reduction in brush thickness from 10 nm to 7 nm at pH 9 (see Figure 4.11). At pH 10, the mean brush thickness decreased from 10 nm to 3 nm within 48 h. Finally, a brush thickness of just 1.5 nm was observed within 24 h, at pH 11.

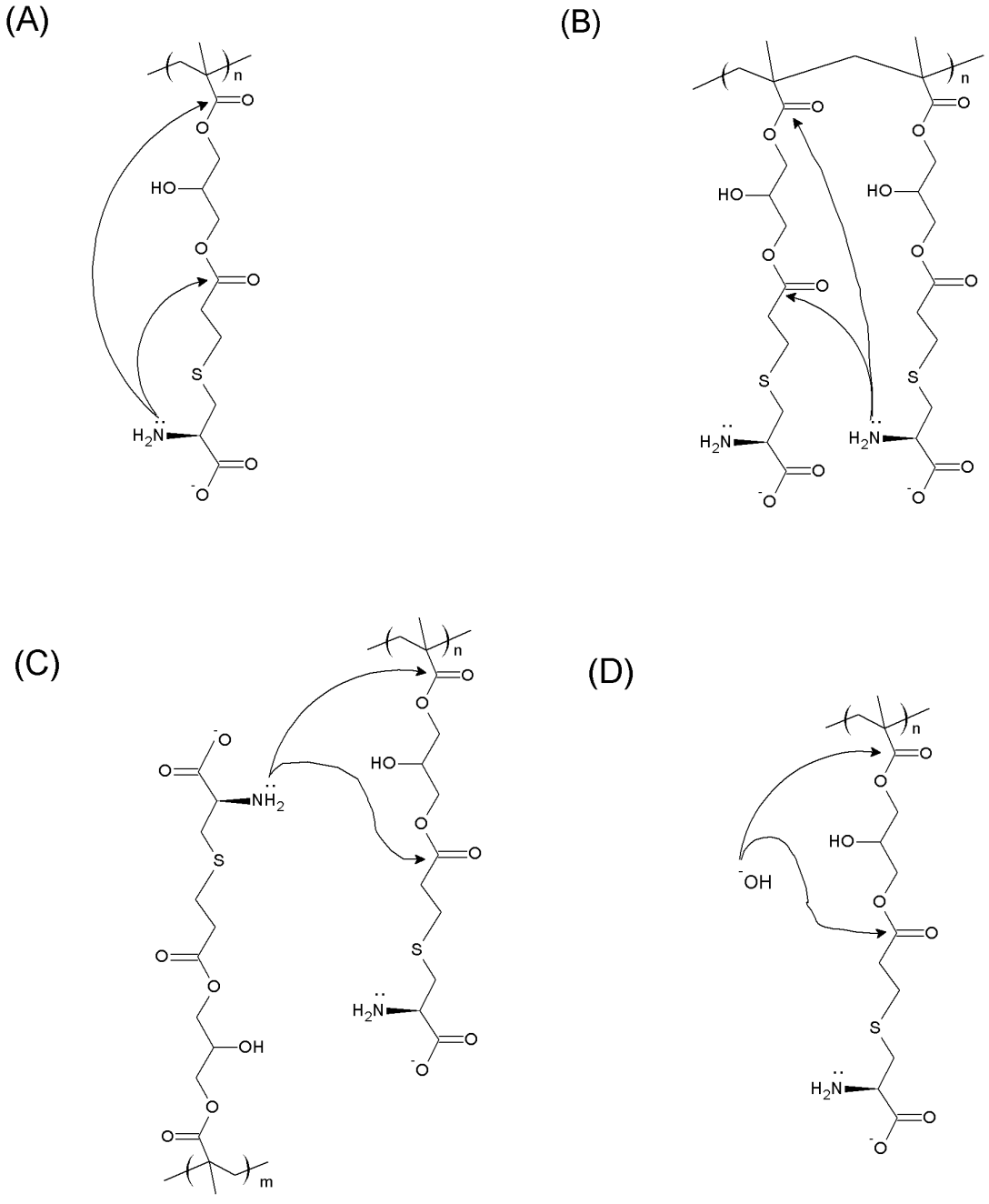

Scheme 4.6 Illustrates the four possible degradation pathways of PCysMA at pH above 8. (A and B) intramolecular amidation, (C) intermolecular amidation and (D) ester hydrolysis.

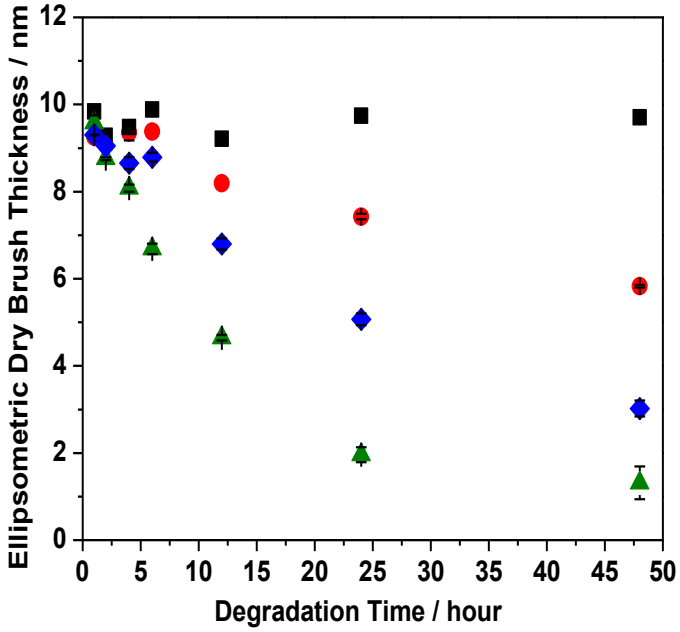

Figure 4.11 *In situ* ellipsometric dry thickness of PCysMA brushes as a function of immersion time at 20°C (original dry thickness = 10 nm). (■) immersed in aqueous solution at pH 8. (●) immersed in aqueous solution at pH 9. (♦) immersed in aqueous solution at pH 10. (▲) immersed in aqueous solution at pH 11.

No changes are observed in the XPS spectra recorded for PCysMA brushes after their immersion in an aqueous solution at pH 8 for 48 h. However, exposing PCysMA brushes to alkaline media (pH > 9), led to spectroscopic changes being observed (Figure 4.12). A significant reduction in the C1s intensity was observed, which indicates substantial mass loss and implies chemical degradation. The S2p and N1s signals both become attenuated over time, indicating loss of sulfur and nitrogen atoms (and hence the cysteine fragment) from the brush layer. However, it is emphasized that no evidence for chemical degradation was observed at neutral pH, which indicates that this new zwitterionic PCysMA brush has potential applications as a surface coating under physiological conditions.

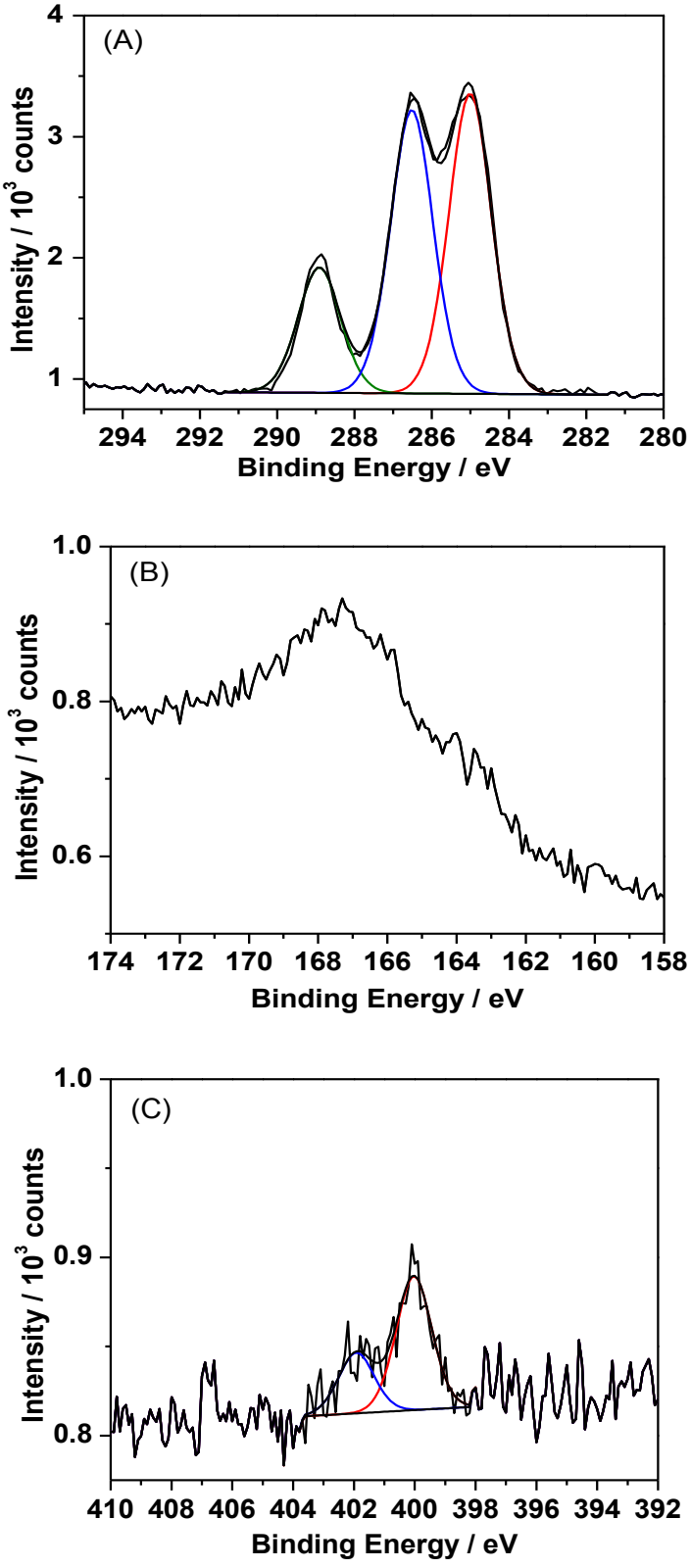

Figure 4.12. X-ray photoelectron core-line spectra recorded for PCysMA brush after pH degradation (3 nm dry thickness). (A) C1s spectrum obtained for PCysMA brush. (B) S2p spectrum obtained for the same PCysMA brush. (C) N1s spectrum obtained for the same PCyMA brush.

4.3.8 Photodegradation of PCysMA brushes

PCysMA brushes grown from silicon wafers were subjected to various doses of UV radiation at 244 nm. XPS studies confirmed the changes occurred in the C1s core-line spectra during this UV irradiation. There was a systematic reduction in the C1s signal intensity with longer exposure times, which suggests that the brush thickness is reduced with increasing UV exposure (Figure 4.13A). Moreover, a new component was observed at ~ 288 eV which was assigned to the formation of surface aldehyde groups (Figure 4.13B).

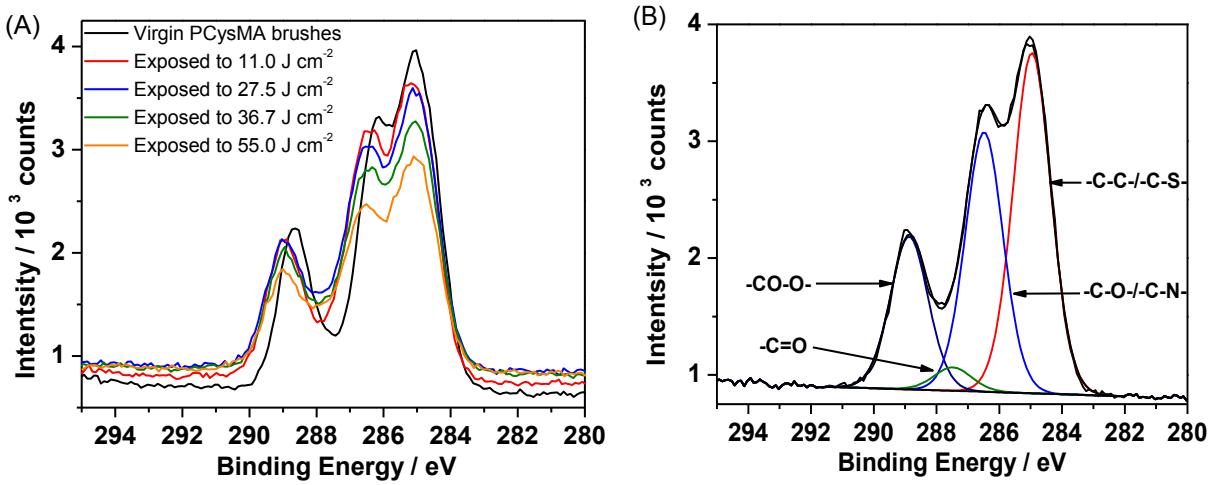

Figure 4.13 (A) Observed changes in the C1s core-line spectrum of PCysMA brushes measured by XPS following exposure to UV laser radiation (λ = 244 nm). (B) C1s spectrum of PCysMA brush after exposure to 10.4 J.cm^{-2} showing peak fits, including the aldehyde component at 288 eV.

Photodegradation was also attempted using an HeCd laser emitting at 325 nm. There was no photodegradation of PCysMA film, was observed which suggested that the photodegradation process is dependent on photo wavelength. Photons with 325 nm wavelength may not have sufficient energy to break bonds on PCysMA brushes.

These surface aldehyde groups were reacted with a perfluorinated primary amine, which is a well-known assay that has the advantage of enhancing the XPS sensitivity. Figure 4.14 shows the C1s and F1s spectra recorded for a PCysMA brush exposed to a 14 J cm^{-2} dose of UV radiation (λ = 244 nm), before and after subsequent exposure to an ethanolic solution of trifluoroethylamine. XPS studies confirm that there was no detectable fluorine prior to

exposure to the trifluoroethylamine solution. After exposure, a strong F1s peak was observed at 688.5 eV, and a new signal appeared in the C1s spectrum at ca. 293 eV, which was assigned to the $\underline{C}F_3$ unit in the trifluoroethylamine reagent.

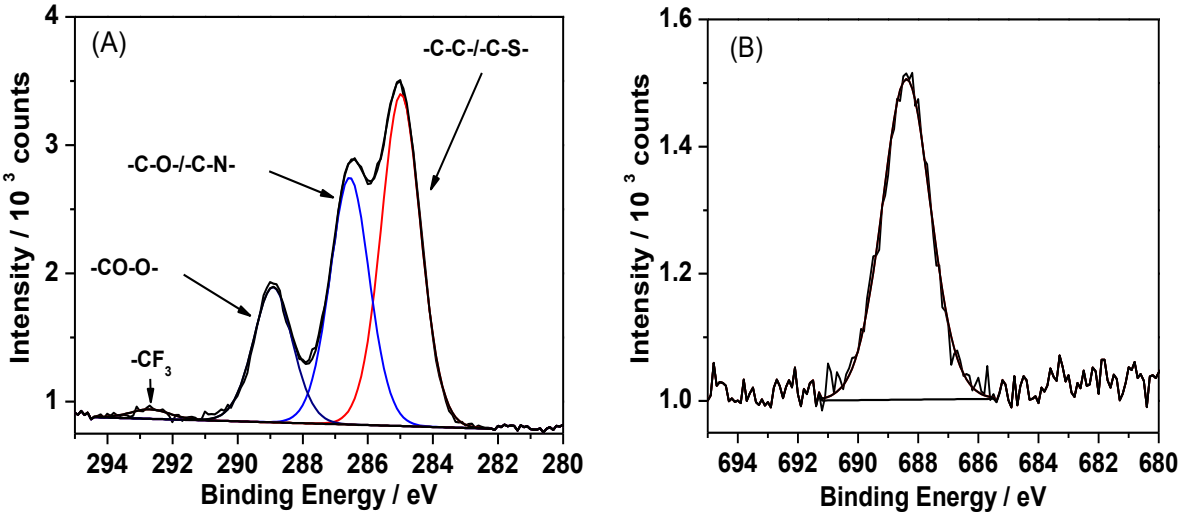

Figure 4.14 X-ray photoelectron spectra recorded for PCysMA brushes exposed to UV radiation (total dose = 14 J cm^{-2}) and subsequently immersed in an ethanolic solution of trifluoroethylamine: (a) C1s core-line spectrum, (b) F1s core-line spectrum.

A uniform PCysMA brush-functionalized silicon wafer was exposed to UV radiation using a photomask and subsequently imaged using AFM. Figure 4.15 shows the gradual change in brush height between the masked and exposed regions as a function of the UV dose. After a 48 J cm^{-2} UV dose, the extent of brush erosion in the exposed regions was approximately 12 nm, thus the mean erosion rate was estimated to be 0.25 nm J^{-1} cm^2.

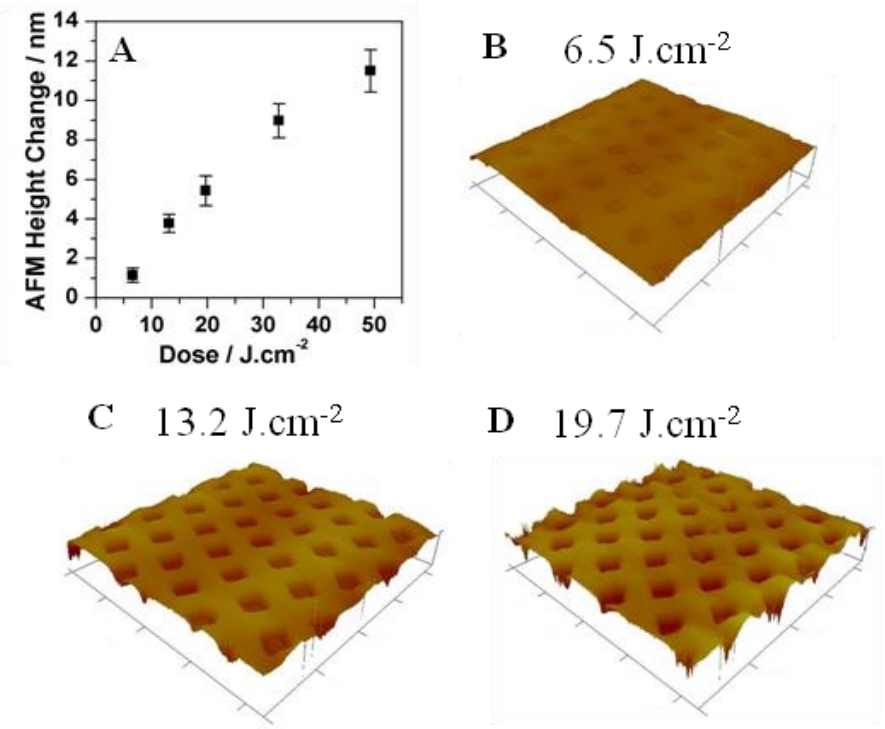

Figure 4.15 (A) Difference in height between masked and exposed areas as a function of dose for PCysMA brushes samples exposed to UV light through a mask (original dry thickness 18.0nm). Images (B) to (D) show 75X75 μm^2 AFM topographical images, with a common vertical range of 20 nm, as a function of UV exposure

4.3.9 Nano-fabrication of PCysMA film

Nano-scale lines were created by photodegradation of a PCysMA brush using the IL technique.[195,197] A dual beam interference set-up was used to generate the desired surface pattern. A coherent UV laser beam was directed towards a mirror and the PCysMA brush-coated silicon wafer was placed at an angular separation of 2θ. Half of the laser beam fell on the mirror, from where it was reflected onto the sample to interfere with the other half of the beam, forming a pattern with a sinusoidal intensity and a period of $\lambda/2\sin\theta$, where λ is the laser wavelength. The PCysMA brush was exposed to a UV dose of 13.2 J cm^{-2} at angles of 10^o, 20^o, 30^o and 45^o. Figure 4.16 (shows the AFM height images obtained for the resulting nano-patterned substrate. The dark bands correspond to regions of extensive surface modification, while the bright bands correspond to regions of minimal modification. The topographical images show nano-lines of the PCysMA brush with a line-width (full width at

half-maximum, FWHM) of 350 ± 5 nm, 245 ± 5 nm, 130 ± 5 nm and 100 ± 5 nm, and heights of 3 ± 1 nm, 3 ± 0.5 nm, 3 ± 0.5 nm and 2 ± 0.5 nm respectively.

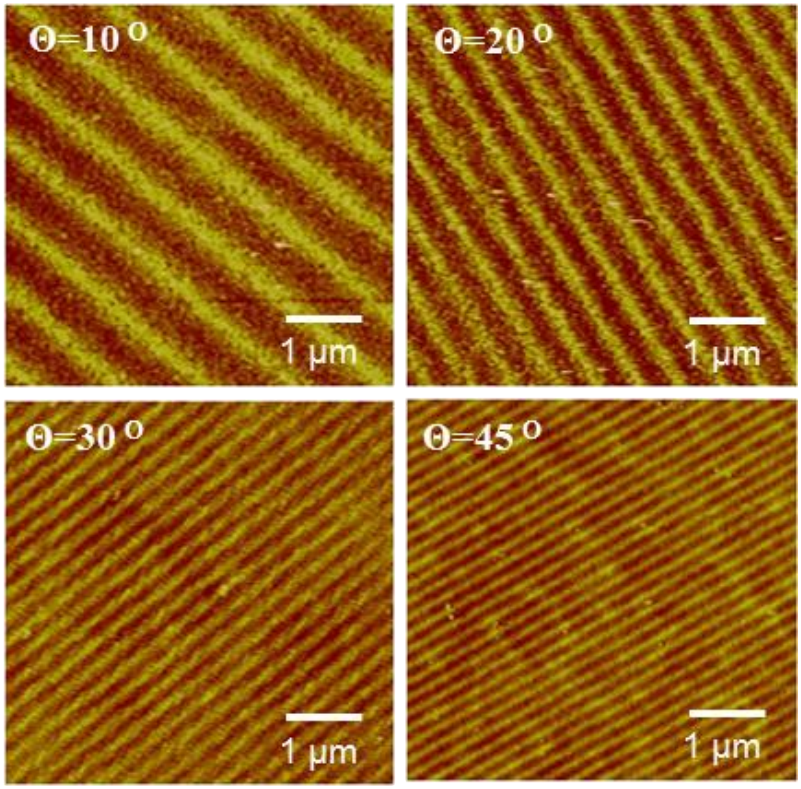

Figure 4.16 Height images of PCysMA brushes fabricated using 2 beam interference lithography exposed to a UV dose of 13.2 J.cm^{-2} . Image size: 5 μm × 5 μm. The *z*-range: 0-10 nm dark to bright in all cases.

Three-beam IL was utilized to create hole patterns with hexagonal symmetry. A standard two-beam Lloyd's mirror interferometer was converted into a three-beam interferometer by adding a second Lloyd's mirror, with the position of the mirrors selected so as to guarantee 120° symmetry of exposure. This arrangement simplifies the alignment by fixing the position of the mirrors with respect to the sample. Moreover, only a single exposure is required to generate hole patterns. The periodicity (p) of the patterns is given by $p = 2\lambda/3\sin\theta$. This three-beam IL set-up was used to fabricate nano-patterned PCysMA brushes using a fixed UV dose of 13.2 J.cm^{-2}. Figure 4.17 shows an AFM tapping mode height image obtained for a PCysMA brush using three-beam IL. The periodicity was 220 ± 10 nm and the holes produced within the PCysMA brushes had a mean diameter of 120 ± 10 nm. The average

hole depth was 4 ± 1 nm, as determined from a large number of cross-sections (10 section lines).

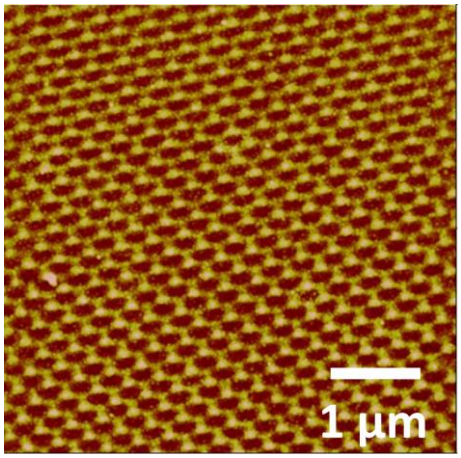

Figure 4.17 Height images of PCysMA brushes fabricated using 3 beam interference lithography exposed to a UV dose of 13.2 J cm^{-2}. Image size: 5 μm × 5 μm. The *z*-range: 0-8 nm dark to bright.

4.3.10 Protein Patterning

To demonstrate their anti-biofouling performance, PCysMA brushes were subjected to UV irradiation (λ = 244 nm) using a photomask. Such photodegradation introduces carbonyl groups into the brush surface, leading to a significant reduction in the protein resistance of the exposed regions. Indeed, the photogenerated carbonyl groups can be used to immobilize fluorescent proteins (GFP).[193,351-352]

Confocal fluorescence images were obtained for an unexposed PCysMA brush and a PCysMA brush exposed to a dose of 13.2 J cm^{-2} using a photomask after immersion of both samples into an aqueous PBS solution containing 10 µg mL^{-1} GFP, see Figure 4.18. No fluorescence can be detected in Figure 4.18A within the limits of sensitivity, which indicates that the pristine PCysMA brush strongly resists protein adsorption. In contrast, Figure 4.18B exhibits a strong green fluorescence from the square (UV-irradiated) regions, indicating specific GFP immobilization in these areas. These well-defined GFP patterns within a PCysMA brush with minimal background fluorescence suggests that this new anti-biofouling surface coating offers considerable potential for various biomedical applications.

Nano-patterned lines of GFP were fabricated by IL (see Figure 4.18C and Figure 4.18D). This PCysMA brush sample was exposed to a UV dose of 13.2 J cm^{-2} at an angle of 10^{o}, followed by immersion in an aqueous PBS solution containing 10 µg mL^{-1} YFP. The green lines indicate immobilized GFP conjugated to the chemically modified brush regions, whereas the unmodified brush regions sstrongly resist protein adsorption. Individual lines are well-resolved and the mean line width was estimated to be 350 nm.

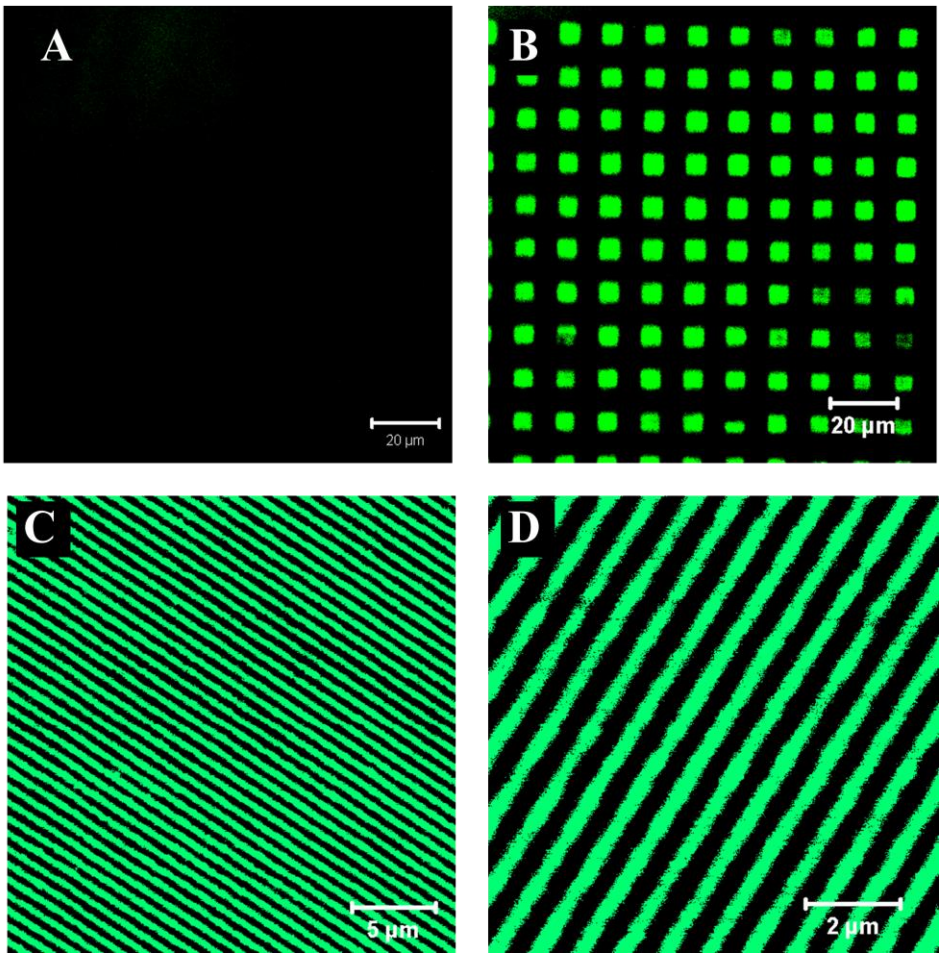

Figure 4.18 Confocal fluorescence images obtained for PCysMA brushes after conjugation to a green fluorescent protein (GFP). (A) No protein adsorption is detected for the pristine PCysMA brush; (B) GFP protein is immobilized within bright green squares after selective degradation of PCysMA using a photomask (dark areas represent the unexposed PCysMA brush); (C and D) GFP immobilized in nano-patterned lines after selective degradation of PCysMA using a two-beam interferometer with $\theta = 10^{o}$.

The same protocol above was utilized to pattern PCysMA brushes by two beam IL at 30^{o} and by three beam IL. These samples were imaged after immobilization of GFP using tapping mode AFM (Figure 4.19). In the height image, the height difference between modified and unmodified brushes was ca.2.5-3 nm before protein adsorption. However, there was a decrease in the height of lines after protein immobilization, to ca.0.5 nm. The widths of the protein lines were ca. 110±10 nm. The protein features exhibit bright contrast in the phase images because of the viscosity of the protein molecules.[353] Figure 4.20 shows representative height and phase images obtained for the patterned PCysMA brush using three beam IL, before and after GFP protein immobilization. In this case, the hole depth decreased from ca. 4.0 nm to 1.5±0.5 nm, after protein adsorption, which indicates the adsorption of the proteins in the holes.

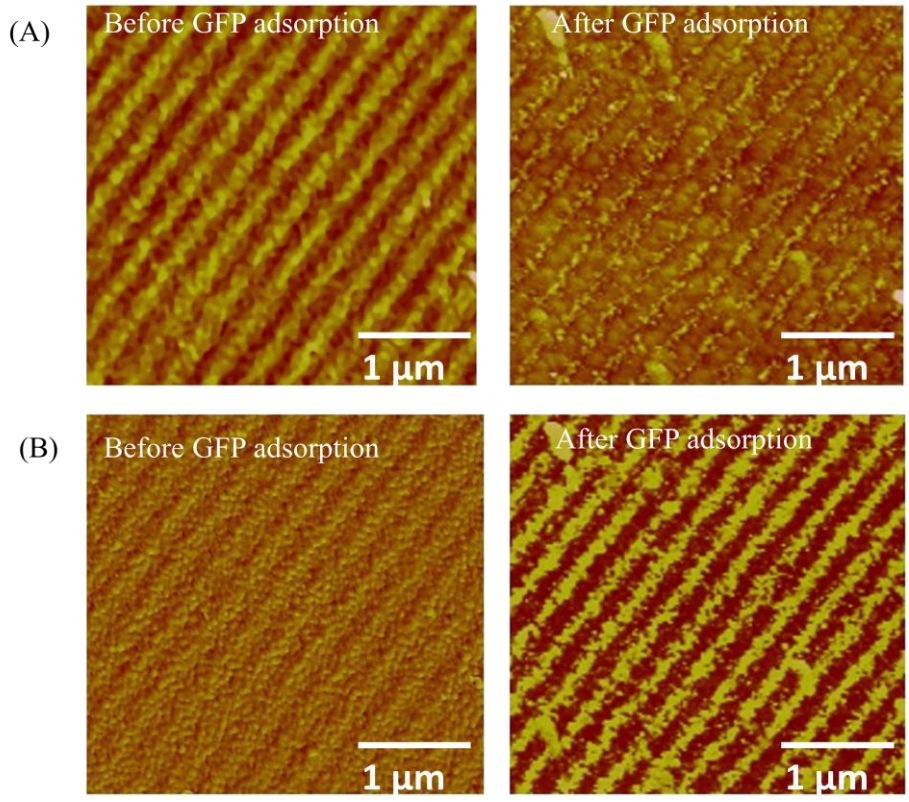

Figure 4.19 Tapping mode AFM images of IL patterned PCysMA brush at 30^{o}, before and after GFP immobilization. (A) Hieght images, 3.0 × 3.0 µm^{2}, z-range: 0 – 10 nm dark to bright in both images. (B) Phase images, 3.0 × 3.0 µm^{2}, z-range: 0- 50^{o} dark to bright in the left image and 0- 250^{o} dark to bright in the right image.

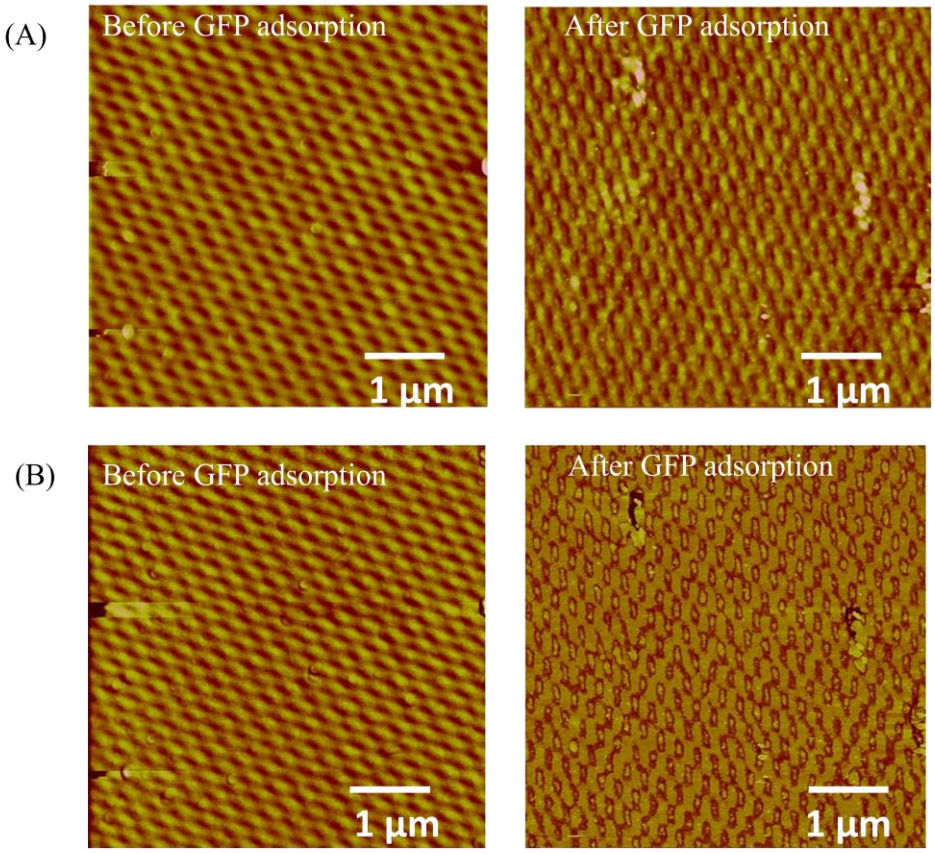

Figure 4.20 Tapping mode AFM images of patterned PCysMA brush using three beam IL, before and after GFP immobilization. (A) Hieght images, 5.0 × 5.0 μm^2, z-range: 0 – 10 nm dark to bright in both images. (B) Phase images, 5.0 × 5.0 μm^2, z-range: 0- 10^o dark to bright in both images.

4.3.11 PMPC brushes for comparative complement depletion assays

Kinetic study of PMPC brushes In previous works, the growth of PMPC brushes from planar surfaces has been studied.[164-165,354-356] Morse et al. reported the growth of PMPC on silicon using an amide based ATRP initiator group in a methanol/ water mixture, and the molar ratio of MPC : CuBr : $CuBr_2$: bipy was 60 : 1 : 0.3 : 2.8 at 20 ^{o}C and the maximum ellipsometric thickness was ca. 300 nm at ca. 21 h.[356] Iwata et al. reported the preparation of PMPC brushes on a silica surface using 3-(2-bromoisobutyryl)propyl dimethylchlorosilane (BDCS) as an initiator, and Cu(I)Br and bipyridine as a catalyst system in methanol/water mixture.[164] They reported a maximum ellipsometric thickness of ca.18 nm in 18 h. Edmondson et al. reported PMPC brush grown on silicon wafers at 20 ^{o}C using a polyelectrolytic macroinitiator and they studied the effect of changing the Cu^{I}/Cu^{II} on the brush growth rate, in mixed alcohol/water solvents.[165]

SAMs-coated Si substrates were derivatized with the initiators as described in chapter 3. Polymerization of MPC was achieved by surface-initiated ATRP. The mole ratio between the monomer and catalyst system was selected to be 60:1:0.5:3 for [MPC]:[Cu^{I}]:[Cu^{II}]:[bipy] respectively in a 1:1 mixture of water and methanol at 20 ^{o}C. In the first experiment, CuBr, $CuBr_2$ and bipy were used as the catalyst system. This reaction was extremely fast. A brush thickness of 6 nm was obtained in 5 min and almost 65 nm in 1 h (Figure. 4.21). The rate of growth of PMPC brushes was about 1.1 nm per min over this period of time. In a second experiment, CuBr and $CuBr_2$ were replaced by CuCl and $CuCl_2$, respectively. Figure 5.1 shows the variation in the dry brush thickness with polymerization time. At all times, the mean brushes thickness was significantly smaller than in the case for the copper bromide catalyst. After 10 min, the brush thickness was 5 nm. The thickness increased with time but after more than 3 h, it was only ca. 40 nm. The polymerization rate of PMPC was ca. 0.25 nm min^{-1}.

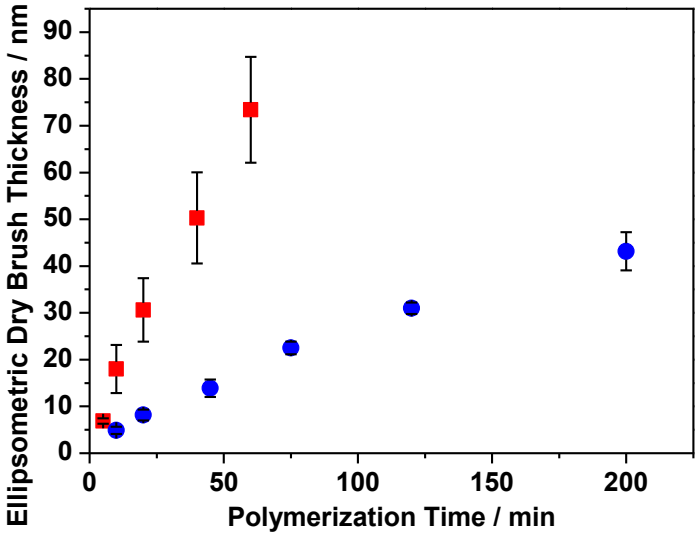

Figure 4.21. Variation in the dry PMPC brush thickness grown on Si wafer as a function of polymerization time at 20 ^{o}C, Conditions: (■) [MPC]: [CuBr]: [$CuBr_2$]: [Bipy] molar ratio = 60: 1.0 : 0.5 : 3, in 1:1 H_2O: methanol ratio. (●) [MPC]: [CuCl]: [$CuBr_2$]: [Bipy] molar ratio = 60: 1.0 : 0.5 : 3, in 1:1 H_2O: methanol ratio.

XPS characterization Wide scans were used to estimate the composition of the PMPC. The % contents of C, O, N and P were found to be 61.8, 27.2, 4.92 and 6, respectively, which are close to the calculated values (57.9, 31.5, 5.2 and 5.2). High resolution C1s, N1s and P2p XPS spectra were acquired for PMPC brushes (original thickness 20 nm) (Figure 4.22 (A-C)). XPS C1s spectra were fitted using three components at binding energies of 285.0, 286.3 and 288.5 eV, attributable to the C−C, C−O/C−N and O=C−O, respectively. The ratios of C−C, C−O/C−N and O=C−O obtained from the C1s spectrum were 3 : 5.7 : 1 which is close to the predicted ratio 3 : 6 : 1. The N1s core-line spectrum recorded for the PMPC film could be fitted in one components at a binding energy of 401.5 eV, which corresponds to the C−N^+− group. The P2p high resolution spectrum was fitted with two components with relative intensities of 1.9 : 1, corresponding to $P2p_{3/2}$ and $P2p_{1/2}$ with binding energies of ~133 and ~134 eV, respectively. The relative intensity of these components formed by the spin-orbit coupling which is defined by expression (2J+1).

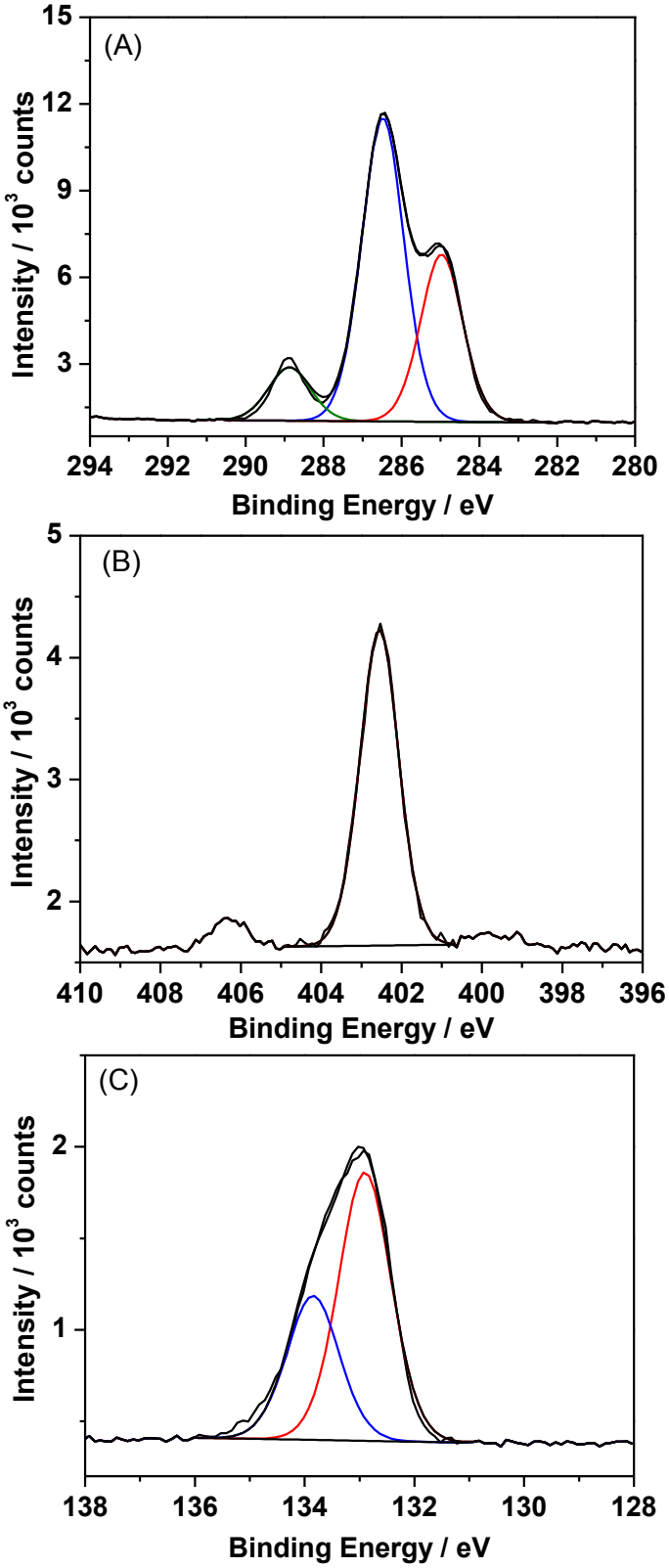

Figure 4.22. Curve-fitted XPS spectra recorded for PMPC brushes: (A) C1s core-line spectrum. (B) N1s core-line spectrum. (C) P2p core-line spectrum

4.3.12 POEGMA brushes for comparative complement depletion assays

Kinetic study of POEGMA brushes The polymerisation conditions were adapted from those described by Brown et al.[117] Poly(oligo(ethylene glycol)methyl ether methacrylate) (M'w 480 g/mol) was purified using a column containing alumina in order to remove the inhibitors. The growth of the polymer layer was characterized using ellipsometry.

The mole ratio between the monomer and catalyst system was 62:1:0.3:2.8 for [POEGMA]:[Cu ^{I}]:[Cu ^{II}]:[bipy] respectively in water at 20 ^{o}C. The rate of brush growth was fast (Figure 4.23). The brush thickness increased gradually over 3 h. The maximum thickness was obtained was 85 nm in 3 h.

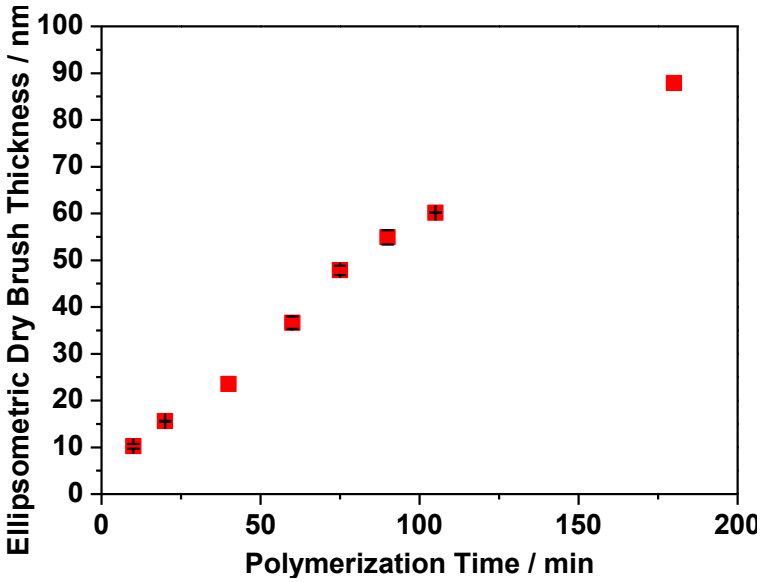

Figure 4.23 Variation in the dry POEGMA brush thickness grown on Si wafer as a function of polymerization time at 20 ^{o}C, Conditions: [POEGMA]: [CuBr]: [$CuBr_2$]: [Bipy] molar ratio = 62: 1.0 : 0.3 : 2.8, in H_2O.

XPS characterization High resolution C1s XPS spectra was obtained for POEGMA brush (Figure 4.24). XPS C1s spectra was fitted using three components at binding energies of 285.0, 286.3 and 288.5 eV, corresponding to the C−C, C−O and O=C−O, respectively. The ratios of C−C, C−O and O=C−O was 14 : 2 : 1, comparing to the calculated ratio 17 : 3 : 1.

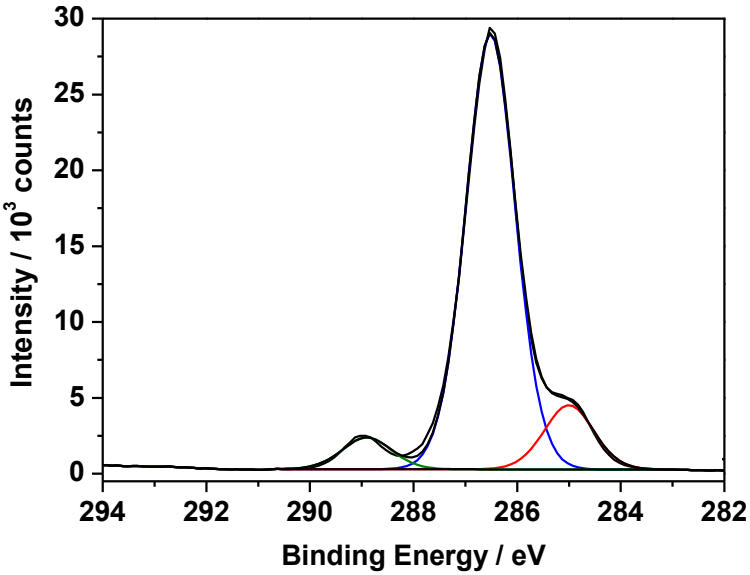

Figure 4.24 XPS high resolution C1s spectra of POEGMA brush.

4.3.13 Cell adhesion test and complement depletion assay

These experiments were done by Dr. Irene Canton. Human Dermal Fibroblasts (HDF) cell adhesion onto PCysMA brushes. PCysMA brushes were grown from identical 13 mm diameter circular glass slides to examine the extent of cellular adhesion on these substrates. Uncoated glass slides were used as controls. Both PCysMA-coated and uncoated glass slides were disinfected and placed at the bottom of 24-well plates. HDFs cells were then added (1 x 105 cells per well) and cells were incubated for 24 h at 37 ^{o}C.

In agreement with the previous section the resistance PCysMA brush of proteins, almost no cells were observed on the PCysMA modified glass surfaces and when they attached, cells presented a more round morphology whereas the control cells were adherent and fully stretched (Figure 4.25). This suggests that the surfaces remained non-fouling in the presence of normal culture media and cells over the 24h incubation period. Qualitative analysis of the images showed that very few cells were attached in either the short or medium thickness brushes, but no cells at all were observed in the long brushes (Figure 4.25). This suggests an improved non-fouling performance on the last ones.

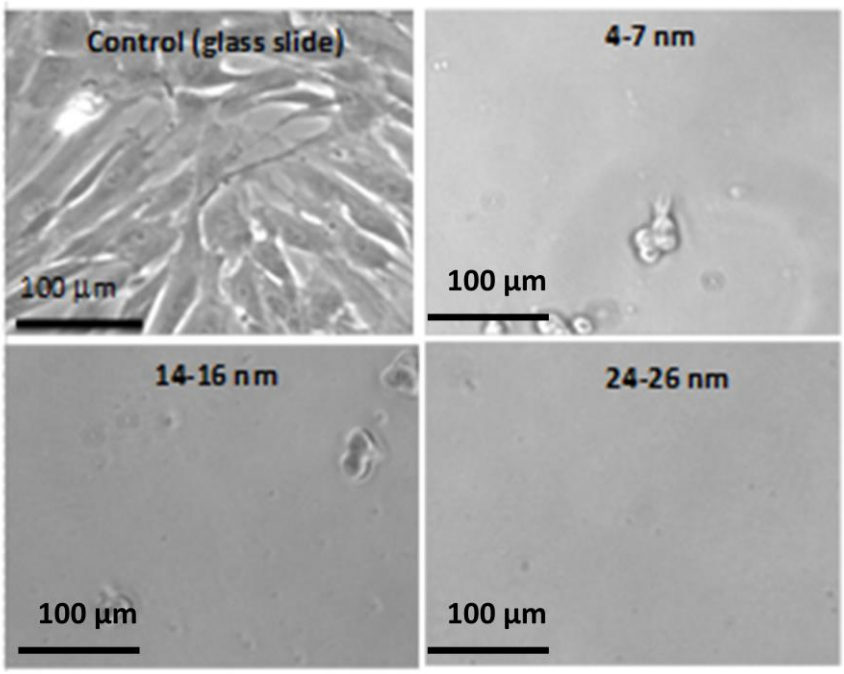

Figure 4.25 Shows optical micrographs obtained for HDF cells growing on the brush surfaces after 24 h incubation.

A complement depletion assay was utilized to further investigate the effect of varying the PCysMA brush thickness in the context of protein fouling (see Figure 4.26). On exposure of the PCysMA brush-coated glass slides to human serum, all brushes performed much better with regard to complement depletion than typical non-adherent surfaces. Shorter and intermediate PCysMA brushes (4-7 nm and 13-16 nm dry thicknesses, respectively) led to weak but detectable depletion compared to the zero depletion control. However, the relatively long PCysMA brushes (24-28 nm dry thickness) showed no statistically significant differences compared to the zero depletion control (see Figure 4.26). These results confirmed the qualitative observations reported in Figure 4.25, suggesting that a certain minimum brush thickness is required for optimum anti-biofouling performance.

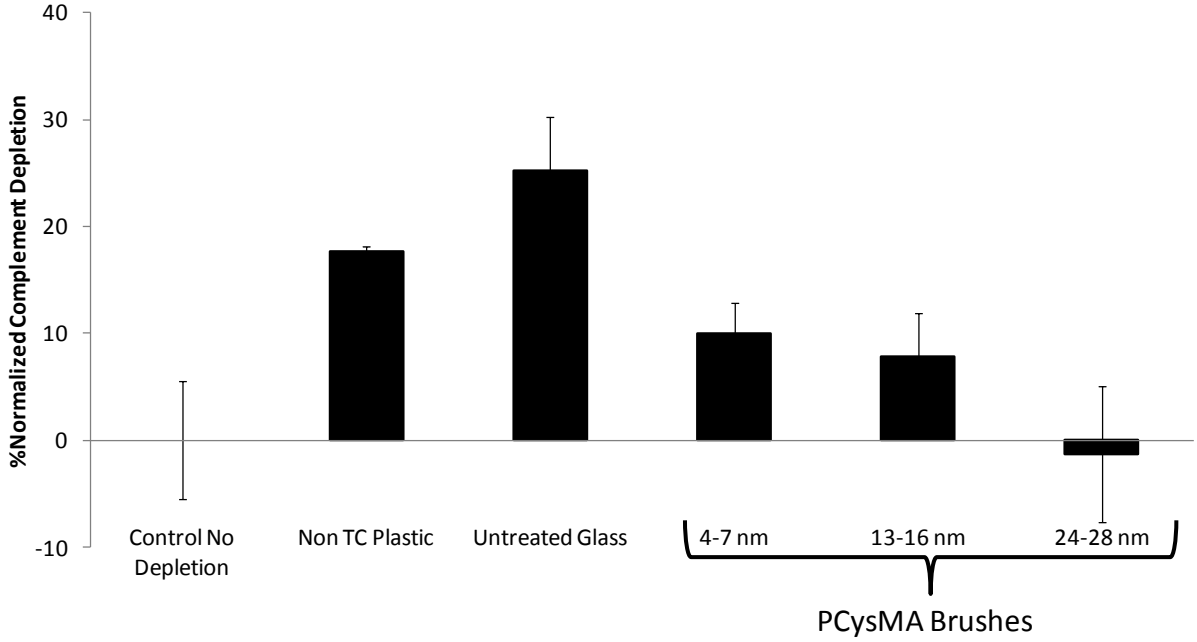

Figure 4.26 Complement depletion assays performed on PCysMA brushes of varying dry thickness (4-7 nm, 13-16 nm and 24-28 nm) and incubated with human serum (100 μL) for 1 h at 37^{o}C. Additional control surfaces were also used (e.g. non-tissue culture (TC) plastic and an untreated glass slide). N = 3 independent experiments were performed in duplicate wells.

Finally, the complement depletion performance of well-known anti-biofouling PMPC and POEGMA brushes was compared to PCysMA brushes of comparable dry thickness (approximately 25-30 nm in each case), see Figure 4.27. To maximize the assay sensitivity, complement depletion was monitored over a range of normal human serum concentrations ((NHS), 100%, 50% and 25%). PCysMA brushes proved to be slightly superior to the PMPC and POEGMA brushes in their anti-biofouling properties over the entire concentration range (Figure 4.27). The former brush exhibited no discernible difference compared to the zero depletion control, whereas the PMPC and POEGMA brushes each showed a small but significant increase in complement depletion.

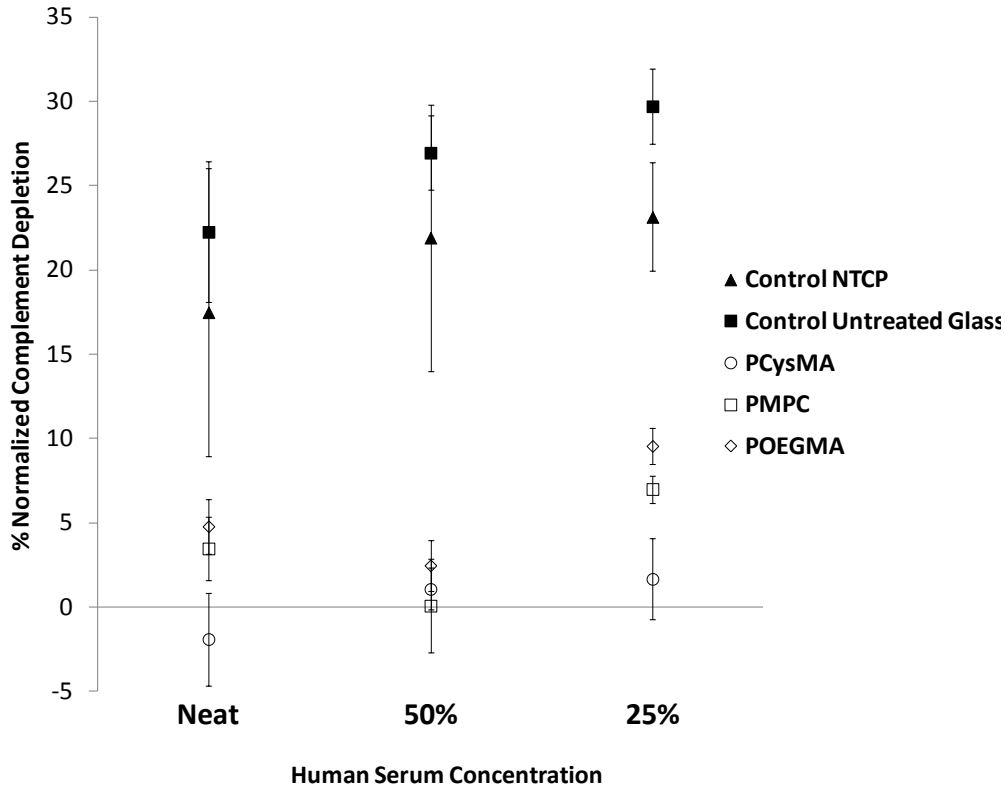

Figure 4.27 Comparative complement depletion assays for three types of anti-biofouling polymer brushes. PCysMA, PMPC and POEGMA brushes of equivalent thickness (approx. 25-30 nm) were tested for complement depletion and data were compared to both non-tissue culture (TC) plastic control (NTCP) and untreated glass. Anti-biofouling performance was monitored over a range of human serum concentrations (100%, 50% and 25% serum). N = 3 independent experiments in duplicate wells.

4.4 Conclusions

A new amino acid methacrylate monomer, cysteine methacrylate (CysMA), was prepared on a 40 gram scale via a facile thia-Michael addition reaction conducted in aqueous solution. This monomer was used to prepare novel zwitterionic PCysMA brushes via SI-ATRP technique with mean brush thicknesses ranging between 4 and 27 nm. Such brushes exhibit pH-responsive behavior. For example, the mean brush thickness increased significantly below pH 2 and above pH 9.5, as judged by ellipsometry and AFM studies. Surface zeta potential studies indicate that PCysMA brushes acquire cationic character below the former pH and anionic character above the latter pH, with zwitterionic character being observed at intermediate pH. Modest brush swelling occurs in the presence of added salt at pH 6, which is attributed to the well-known 'anti-polyelectrolyte effect' exhibited by polybetaines, and the brush collapse in the addition of salt at pH 1.5 and 9.8. XPS studies of photodegraded PCysMA brushes confirm that aldehyde groups are generated after prolonged UV irradiation at 244 nm. Both micro- and nano-structured PCysMA brushes can be conjugated to green fluorescent protein (GFP) via surface aldehyde groups generated during their photodegradation. PCysMA brushes proved to be highly resistant to adhesion when exposed to HDF cells, while complement consumption/depletion assays confirm that such brushes exhibit superior antibiofouling performance to that of well known PMPC and POEGMA brushes.

Chapter 5: The formation of polymer brushes for use as supports for lipid bilayers

5.1 Introduction

Solid-supported lipid bilayers were first studied by Tamm et al.[357] Lipid bilayers placed on planar substrates have been used in the fabrication of biosensors and in studies of biological phenomena in recent years.[358-361] Lipid bilayers can form on planar surfaces when vesicle suspensions are brought in contact with hydrophilic substrates.[362] Many substrates have been used as supported lipid bilayers such as glass, silica and oxidized silicon.[358] The interaction between the surface and bilayers can be through van der Waals, electrostatic, hydration, or steric forces.[358,363]

Hydrophilic surfaces can form ultrathin layers of water to act as a lubricant between the bilayer and the surface.[363-364] This lubricant enables the bilayers to exhibit their properties similar to those of free bilayers and leads to good fluid bilayer behaviour on the substrate.[361-362] The disadvantage of forming bilayers on the surfaces of solid materials is that transmembrane proteins can easily insert into the bilayer and interact with the surface; as a result they can lose their lateral mobility.[362] To overcome this limitation, it has been suggested that, bilayers can be separated from the surface by intercalating hydrophilic polymer layer between them.[362,365]

Several types of polymers have been studied as supports for lipid bilayers. Ideally, these polymers also prevent nonspecific protein adsorption to surfaces.[358,366] The brush roughness can affect the formation of lipid bilayers because, if the defects in the supported polymers are greater than the thickness of the bilayer then the lipid bilayer will contain defects.[358,365] Furthermore, the polymer film should provide a strongly hydrated cushion to decouple the membrane from the supported surface. The assembly of supported lipid bilayers onto the surface of polymers is often achieved through fusion of lipid vesicles.[367-368] Liposomes can be made to adsorb, unroll, and, fuse to form a homogeneous bilayer onto polymer surface, after carefully tanning the concentration and the size of the vesicles.[369-371] Lipid bilayers have been formed on polymer supports, including neutral polymer (e.g. PEG and polyacrylamide films),[358,362,364,372-373] stimuli responsive polymer (e.g. PAA),[374-376] and zwitterionic brushes (e.g. poly(sulfobetaine methacrylate) (PSBMA)).[154] The adsorption of lipid vesicles onto polymer supports can be achieved by using polymers with charged groups.[377] Zwitterionic

polymers exhibit varied properties, depending on the polymer association state in aqueous solutions and the density of the brushes due to the presence of dipole–dipole and charge–charge interactions among the zwitterionic groups.[152,378] The surface hydrophilic/hydrophobic properties of zwitterionic brushes can be controlled by varying the brush thickness.[378]

Recently, Piehler and co-workers have established a new approach for the spatial control of lipid phase separation using tethered polymer-supported membranes, obtained by vesicle fusion on a poly(ethylene glycol) brush functionalized with fatty acid moieties, which allowed functional reconstitution of transmembrane proteins.[379] The SI-ATRP technique has been used to grow homogeneous polymer brushes on substrates that can serve as supports for bilayers.[154,358] The formation of neutral lipid bilayers on polyacrylamide brushes grown on fused silica via ATRP has been studied by Smith et al.[358] Santonicola et al. reported that poly(sulfobetaine methacrylate) (PSBMA) brushes grafted onto glass substrates have been successfully used to support lipid bilayers under physiological conditions.[154]

Several polymers including neutral polymer brushes (poly(hydroxypropyl methacrylate) (PHPMA)), and polyelectrolyte polymers brushes (PTBAEMA, PDMAEMA, PMAA, PMPC, PKSPMA, PMETAC and PCysMA), have been suggested for use as supports lipid bilayers. However, in this chapter, we focused on the use of SI-ATRP to grow PMPC, PKSPMA, PMETAC and PCysMA brushes layers on glass surfaces as substrates for the formation of zwitterionic, negative and positive lipid bilayers, with the ultimate goal of incorporating transmembrane proteins (Scheme 5.1). The brush growth of these polymers was studied using ellipsometry, in order to grow a suitable brush thickness in which to form bilayers. XPS was used to characterize the surfaces. AFM was also used to study the roughness and the change in the thicknesses of these brushes in both the dry state and under PBS. The surface zeta potential was determined as a function of pH for both PMPC brushes. In cooperation with Prof. Steve Evans group in Leeds University, the formation and the diffusion coefficients of lipid bilayers on these brushes were characterized by fluorescence recovery after photobleaching (FRAP).

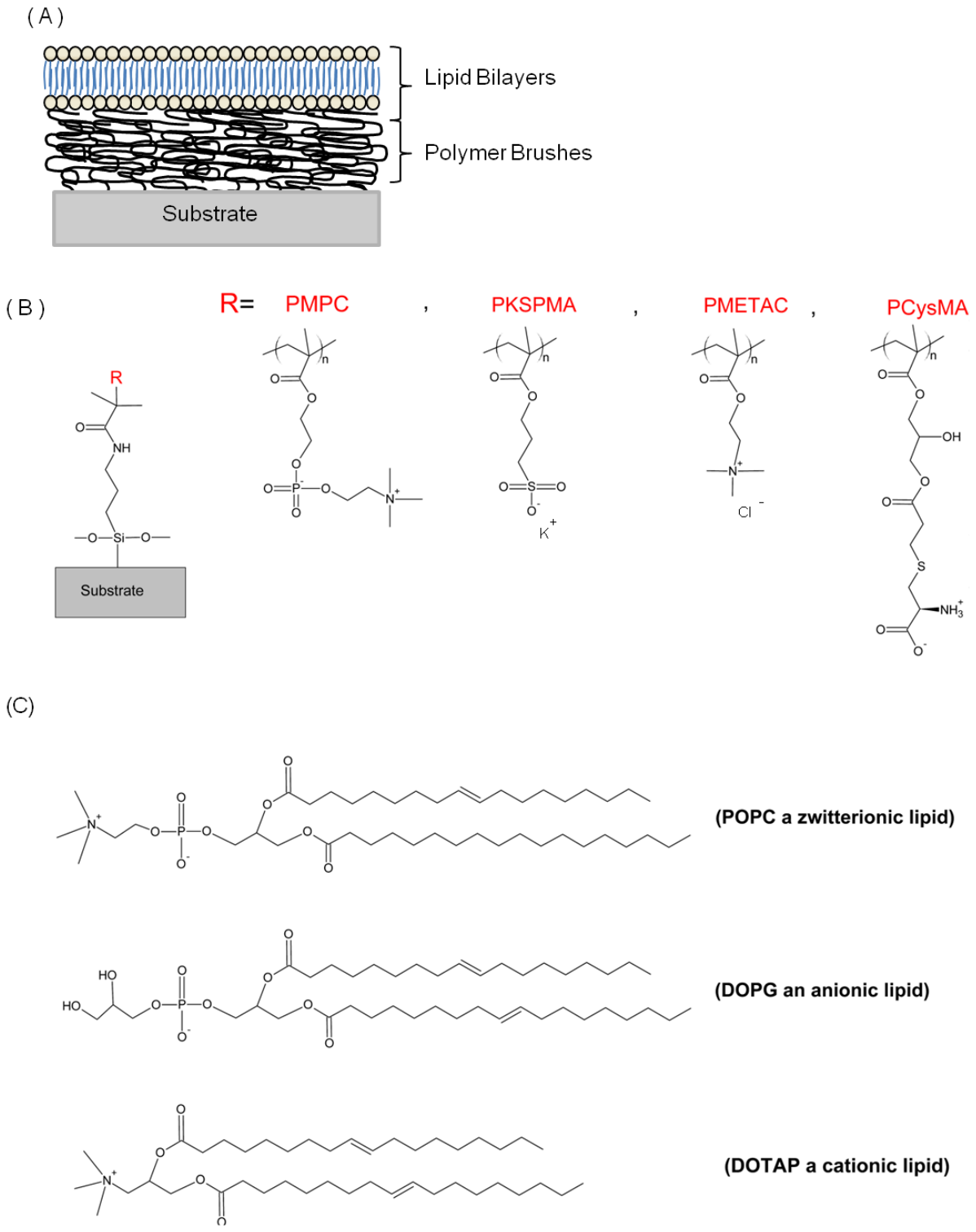

Scheme 5.1 (A) Schematic diagram showing the formation of a lipid bilayer supported on a polymer brushes. (B) The structures of the polymer brushes to be synthesised for use as support for lipid bilayers. (C) The structure of the lipids used here.

5.2 Experimental

5.2.1 Preparation and UV modification of bromo initiators

BIBB-APTES films on silicon wafers and glass cover slips (18 mm) were prepared as described in section 2.3.1. BIBB-APTES films on a silicon wafer were exposed to UV light through an copper electron microscope grid as a mask (2000 mesh). After an exposure of 2 J cm^{-2}, the samples were and washed with ethanol, and dried under N_2 (chapter 3).

5.2.2 Preparation of PMPC brushes

PMPC brushes were prepared as described in chapter 4. MPC (6.0 g, 20 mmol) was placed in a flask under a nitrogen atmosphere after four pump/refill cycles. Water and methanol were degassed separately by a stream of nitrogen (for at least 60 min). Water (5 mL) and methanol (5 mL) were added to the MPC by syringe at room temperature. CuBr (48.4 mg, 0.338 mmol), $CuBr_2$ (36.8 mg, 0.165 mmol), and 2,2'-bipyridine (157.5 mg, 1.014 mmol) were added, then the mixture was stirred under nitrogen for 10 min and then briefly immersed in an ultrasonic bath to aid catalyst dissolution. Initiator-functionalized glasses were sealed in Schlenk tubes, degassed, then filled with nitrogen. The polymerization solution (2 mL) was added to each tube from a syringe. After various times, individual tubes were opened and washed with water and methanol. The PMPC brush-coated glasses were briefly sonicated removed and then rinsed with water and methanol, and dried under a nitrogen stream.

5.2.3 Preparation of poly(3-sulfopropyl methacrylate potassium salt) (PKSPMA) brushes

3-Sulfopropylmethacrylate potassium salt monomer (5.0 g, 20 mmol) was dissolved by stirring in 6 mL of methanol and 3 mL of water at room temperature. Bipy (187 mg, 1.2 mmol) and $CuBr_2$ (32 mg, 0.14 mmol) were added to the solution. The mixture was stirred, degassed using nitrogen stream bubbling for 60 min then CuBr (47.5 mg, 0.386 mmol) was added. The mixture was stirred and degassed for 10 min. Initiator-functionalized wafers were sealed in a Schlenk tube and degassed (four vacuum pump/N_2 refill cycles). The reaction mixture was added to this Schlenk tube using a syringe by adding enough solution to cover the sample completely. After a range of suitable polymerization times, the samples were removed and washed with water and methanol. The samples were briefly sonicated and thoroughly rinsed with deionized water and methanol, followed by drying under a nitrogen

stream. The mean brush thickness on Si was measured by ellipsometry.[380-381] The contact angle of PKSPMS was θ_{AW} less than 7^{o}.

5.2.4 Preparation of poly(2-methacrylato)ethyl trimethylammonium chloride) (PMETAC) brushes

2-(Methacrylato)ethyl trimethylammonium chloride solution (METAC) is supplied as 80% solution in water. METAC (13.85 g, 67 mmol) was dissolved in 20 mL of a 1:4 mixture of water and isopropanol. Bipy (382 mg, 2.4 mmol) and $CuBr_2$ (11.2 mg, 0.05 mmol) were added. The mixture was stirred and degassed for 1 h and then CuBr (144 mg, 1.0 mmol) was added to the solution. Initiator-functionalized silicon wafers were sealed in Radley tubes, and degassed via repeated vacuum/refill cycles, and enough polymerization solution was added to each tube to submerge the substrate completely. After a range of polymerization times, the samples were removed and washed with water and methanol. The samples were briefly sonicated and thoroughly rinsed with deionized water and methanol, followed by drying under a nitrogen stream. The mean polymer brush thickness on silicon wafer was measured by ellipsometry.[382] The contact angle of PMETAC was measured to be less than 10^{o}.

5.2.5 Preparation of PCysMA brushes

PCysMA brushes were prepared as stated in chapter 4. Surface initiator-functionalized glass cover slips were placed in Schlenk tubes, degassed, then filled with N_2. CysMA (5.0 g, 15.0 mmol) was dissolved in dionized water (12.0 mL) at 20^{o}C and degassed for 30 min. Cu(I)Br (71.4 mg, 0.5 mmol), bipy (234 mg, 1.5 mmol) and Cu(II)Br_2 (55.6 mg, 0.25 mmol) were added to the solution. This reaction mixture was degassed for 10 min, and then briefly sonicated. Polymerization solution (2 mL) was transferred into each Schlenk tube. After 15 min, the substrates were removed, sonicated in water and rinsed with ethanol, and then dried with N_2. The contact angle of dried PCysMA brush was measured to be $43^{o}\pm2$.

5.2.6 Surface characterization

In this work, ellipsometry, AFM and XPS were used to characterize polymer brushes, as described in chapter 2. Contact angles were measured from three water droplets, across the surface and averaged to determine the change in polarity of the surface. The growth thickness of polymer brushes on silicon over the time was measured by ellipsometry. Wide scan and high resolution XPS spectra were analyzed to determine the surface structure of the surface.

AFM was used to study the mean roughness and the thickness of the polymer brushes immersed in PBS.

5.2.7 Polymer brushes supported lipid bilayer

Lipid bilayers were formed on polymer brushes by Anita Blakeston, Johannes Roth and Matthew Cheetham Leeds University. The lipids used for this study were POPC (1-palmitoyl-2-oleoyl-sn-glycero-3-phosphocholine), DOPG (1,2-di-(9Z-octadecenoyl)-sn-glycero-3-phospho-(1'-rac-glycerol)) and DOTAP (1,2-dioleoyl-3-trimethylammonium-propane). The phospholipid Texas Red®DHPE (1,2-dihexadecanoyl-sn-glycero-3-phosphoethanolamine, triethylammonium salt)-labeled on the head group with the bright, red-fluorescent Texas Red® dye (excitation/emission maxima ~595/615 nm) was used as a fluorescent probe. The dried lipids were dissolved in a mixture of chloroform and methanol (1:1). The lipids were prepared in glass vials, following molar ratios: 99.5:0.5 POPC:Texas Red (as POPC), 10:89.5:0.5 DOTAP:POPC:Texas Red (as 10% DOTAP), 24.9:74.6:0.5 DOTAP:POPC:Texas Red (as 25% DOTAP) and 49.75:49.75:0.5 DOTAP:POPC:Texas Red (as 50% DOTAP). Then, the lipids were dried under a flow of nitrogen gas. Vesicle solutions were prepared at concentrations of 1.0 mg mL^{-1}, using either a phosphate buffer or deionised water.

A polymer film was formed on a glass cover slip, which was sealed in a flow cell and the deionised water or buffer injected into it. After 15 min the lipid was injected and the cell stored in the dark at room temperature to incubate. Times for this are shown in the results section. After 2 h incubation the polymer surface in the flow cell was rinsed with deionised water or buffer as shown in the results and studied using fluorescence recovery after photobleaching (FRAP). A time sequence of images was taken in order to determine the diffusion coefficient of lipids. If no bilayer or diffusion was observed at this stage then incubation was extended, after injecting with more lipid. The flow cell was maintained at an elevated temperature of 55 ^{o}C for 1 h, followed by extended incubation at ambient room temperature for at least 48 h.

Three different lipid compositions were incubated onto polymer samples, using vesicle deposition (one mixture per polymer sample) in a flow cell, as follows:

- zwitterionic lipids (POPC)
- Positive lipids (DOTAP/POPC mixture)
- Negative lipids (DOPG/POPC mixture)

The proportion of charged lipid in the vesicles was varied to establish the lowest amount of charge that is required to form a bilayer. The lipids were prepared using a range of solutions including deionised water and PBS buffer.

The initial intensity of the fluorophore before bleaching was normalised to be 1.0 and subtracted from the reading each time. Zero intensity is determined in the bleached spot. The normalised intensity data were plotted versus time. The Axelrod method was used to determine the diffusion coefficient. The diffusion coefficient was calculated from the following equation:[362,383]

$$D = \frac{\omega^2}{4t_{1/2}}$$

ω is the radius of the bleached spot and $t_{1/2}$ is the time to recover half the intensity.

5.3 Result and discussion

5.3.1 PMPC brush

5.3.1.1 Characterization of PMPC brushes

Surface zeta potential Vo et al. reported the zeta potential of the neutral zwitterionic PMPC chains on silica to be ±5 mV over a wide pH range.[384] In these experiments, the surface zeta potential of PMPC brushes grown on a planar surface was determined over a wide range of solution pH, see Figure 5.1A. The PMPC brush exhibited a very low surface zeta potential (±10 mV). Figure 5.1B shows the change in surface zeta potential observed for a PMPC brush exposed to added salt (either $CaCl_2$ or KCl; 0.1 to 5.0 mM). The PMPC brush is zwitterionic character at relatively low levels of added electrolyte. From the surface zeta potential curves shown in Figure 5.1B, it is clear that the PMPC brush acquires greater negative surface character when immersed in $CaCl_2$ compared to KCl. The surface zeta potential increases from about -8 mV (0.1 mM $CaCl_2$) and reaches -20 mV above 5 mM $CaCl_2$. For KCl, the surface zeta potential becomes slightly negative (-10) at concentration above 2.5 mM KCl. The observed weakly anionic character may indicate preferential adsorption of Cl^- and/or OH^- from the bulk solution.

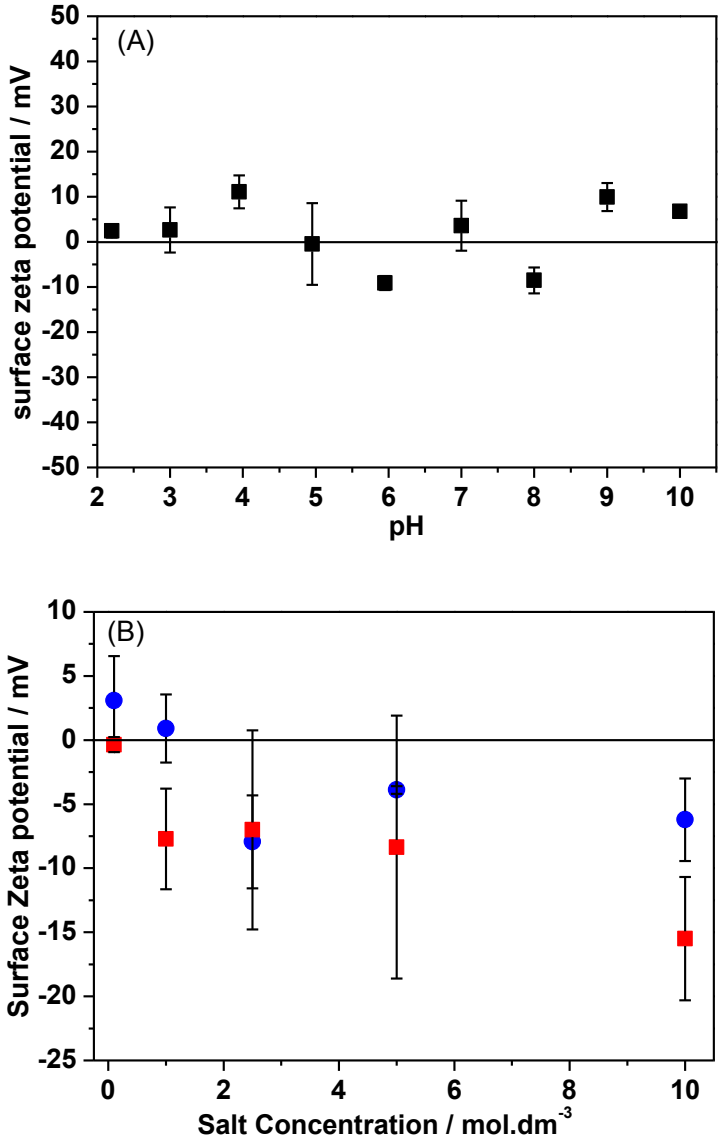

Figure 5.1 Surface zeta potential obtained for PMPC brushes (original dry brush thickness = 60 nm) using a Malvern dip cell. (A) PMPC brush immersed in (1 mM KCl) aqueous solutions of varying pH. (B) PMPC brush immersed in aqueous solution of varying salt concentration (using HPLC water), (●) in KCl and (■) $CaCl_2$.

AFM The topography of the brush surface was acquired using AFM in tapping mode. Figure 5.2 shows a height image of a PMPC brush grafted on to Si wafer with a mean thickness about 10 nm. The AFM root-mean-squared (rms) of this dry PMPC brush was between 0.2 and 0.4 nm. When imaged under PBS, the same surface yield a surface roughness less than 0.3 nm. These rms values were similar to previous studies,[354-355] indicating that the prepared brush were homogeneous and consisted of dense PMPC brushes.

The swelling of PMPC brushes in water was previously studied and it was found that the ellipsometric thickness increased from 32.5 nm in dry state to ca.153 nm under pure water.[165] PMPC brush swelling in aqueous solutions of NaCl with a range of concentrations was studied by Takahara and co-workers.[166] They observed that the swelling of PMPC brush independent of the salt concentration and the brush thickness increased from ca.25 nm in dry state to almost 150 nm in solutions. In this study, the swelling of PMPC under PBS was studied using AFM for patterned samples. Figure 5.3 shows the change in height between dry PMPC and PMPC under PBS. There is an increase of about a factor of three in the brush thickness from 10 nm under dry condition to ca. 35 nm under PBS.

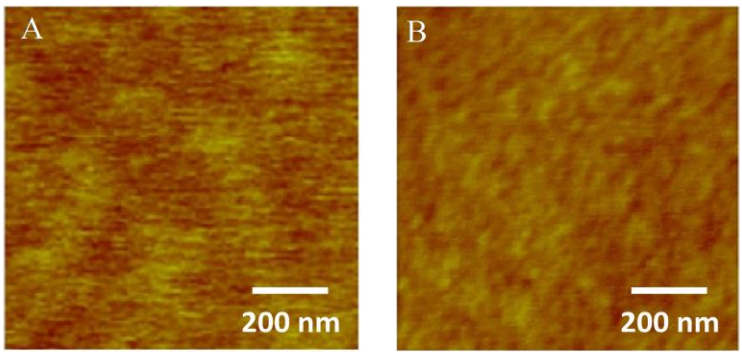

Figure. 5.2. AFM tapping mode image of PMPC brushes (image size 1 μm × 1 μm). (A) Dry PMPC brush. (B) Same PMPC brush under PBS. The *z*-range: 0- 10 nm dark to bright in both images.

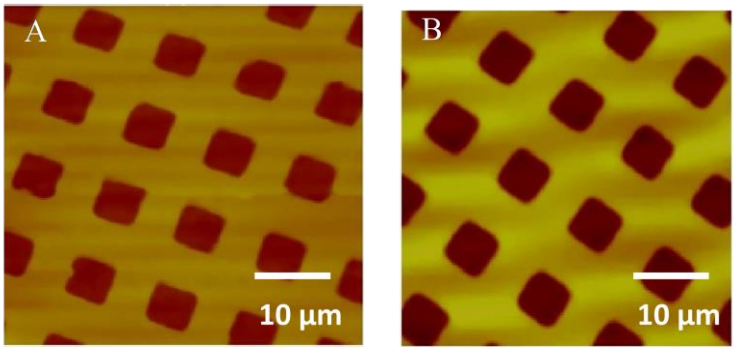

Figure. 5.3. AFM height image of PMPC brushes acquired by tapping mode (image size 50 μm × 50 μm). . (A) Dry PMPC brushes. (B) Same PMPC brush under PBS. The *z*-range: 0-100 nm dark to bright in both images.

5.3.1.2 PMPC brushes as supported lipid layers

PMPC brushes are known to have excellent biocompatibility and non-fouling properties; it would be an advantage to be able to form a fluid lipid bilayer. So far in the literature, no report shows the successful formation of lipid bilayers on PMPC brushes. On the contrary, PMPC brushes have been found to resist the adsorption of lipids, have been used to pattern lipid bilayers.[385]

In the present work, PMPC brushes were prepared on 18 mm glass cover slips with a range of lengths between 8 and 15 nm. Positive (DOTAP) and negative (DOPG) vesicles were used at high concentrations (ca. 70%) to attempt to overcome the resistance to lipid adsorption of PMPC layers by increasing the interaction between the head groups of the brushes and the lipid vesicles. After incubation, the surface showed significant amounts of vesicles absorbed on the PMPC surface. The flow cell was rinsed with 1 M solution of NaCl and Ca^{2+} ions to rupture the vesicles by removing water from their interiors.[386] However, little difference was observed in the surfaces formed with and without salt. In the subsequent FRAP experiment, no recovery was observed in the bleached area, evidence of vesicles adsorption without bilayer formation.

In other studies, the introduction of short chain lipids to the vesicles has been found to reduce the time needed for vesicle rupture.[387] The short chain lipids should perform as a detergent and increase the possibility of vesicle rupture. It was hypothesized that they may also aid lipid bilayer formation on the brush surfaces. After the introduction of 5 mol% of 1,2-hexyanoylsn-glycero-3-phosphocholine (DHPC-C6) into the lipid vesicles, islands of lipid bilayers were formed on PMPC surfaces, with diameters the range100 – 150 µm. Figure 5.4 shows the FRAP images of an island of bilayer formed on PMPC brushes using a mixture of DOTAP/POPC/DHPC C6 with molar ratio of 47.5:47.5:5, respectively. Diffusion coefficient was determined by fitting the normalized fluorescence recovery data and found to be 0.4 $\mu m^2 s^{-1}$.

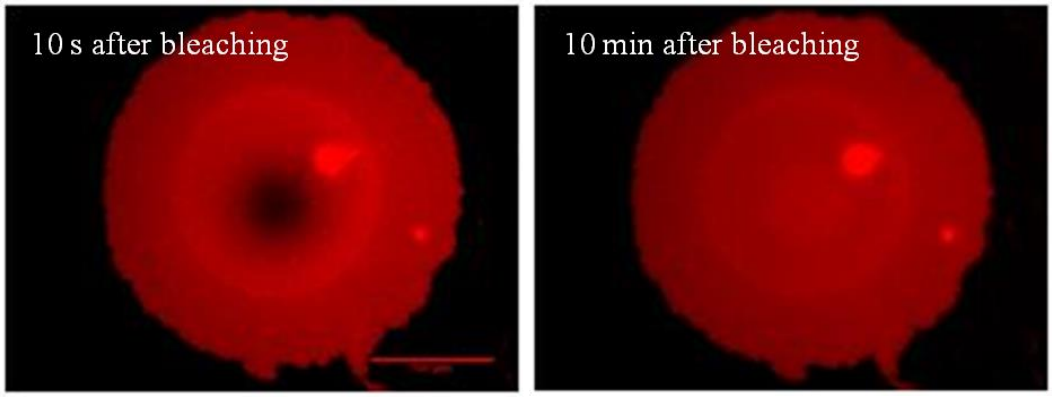

Figure 5.4. FRAP images showing the bleaching and subsequent recovery of lipid bilayers on PMPC produced using vesicle fusion of DOTAP:POPC:DHPC C6 with molar ratio of 47.5:47.5:5. Exposed spot is 25 μm diameter.

Spin-coating of lipid solutions has been used to obtain well defined lipid bilayers on a solid support, depending on spin speeds and lipid concentration.[388] This approach was also used to form bilayer on PMPC brushes. A mixture of DOTAP/POPC with a 1:1 molar ratio was spin-cast from isopropanol solution. It has been suggested that isopropanol is a good solvent for the lipid acid with hydrophilic surfaces.[389] It was observed lipid bilayers formed on PMPC brushes. Figure 5.5 shows FRAP images for the bleaching and recovery of lipid bilayers on PMPC produced by spin coating of POPC/DOTAP (50/50). A homogeneous bilayer was formed with diffusion coefficient of ca. 0.1 $\mu m^2\ s^{-1}$, as determined by fitting the normalized fluorescence recovery data. The diffusion coefficients was lower than the one formed from the DHPC C6 vesicle incubation, but a fluid lipid bilayers was observed instead islands adsorbed into the surface.

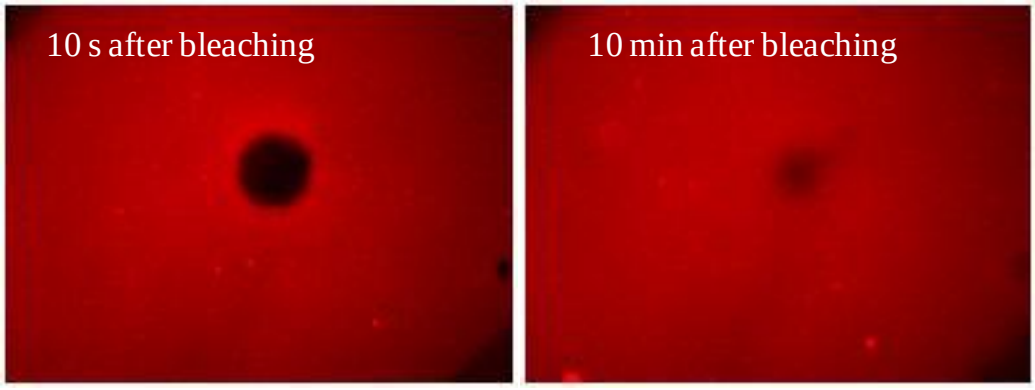

Figure 5.5. The images showing the bleaching and recovery of lipid bilayers on PMPC produced by spin-coating of POPC:DOTAP with a molar ratio with 1:1 from isopropanol. Exposed spot is 25 μm diameter

5.3.2 PKSPMA brush

5.3.2.1 Preparation of PKSPMA

Anionic polyelectrolyte brushes were prepared from aqueous solutions of 3-sulfopropylmethacrylate and were grown on gold, Si and/or glass substrates by SI-ATRP.[390-391] Masci et al. described the synthesis of PKSPMA brush by ATRP in water/DMF mixed solvent using a $CuCl/CuCl_2$ ratio and bipyridine as a catalyst at 20 °C.[390] Huck and co-workers described the synthesis of PKSPMA brushes onto gold and Si surfaces. The effect of $CuCl/CuCl_2$ ratio was examined in methanol/water mixture and the synthesized PKSPMA brushes displayed a thickness up to few hundred nm.[391]

To control brush growth (and hence thickness), two different experimental formulations were examined to grow PKSPMA brushes on initiated silicon wafers by SI-ATRP. The composition of the reagent mixture was selected to be 50: 1 for [M]: [CuBr] for a 1:1 water: methanol ratio at 20°C. The $CuBr/CuBr_2$ molar ratio was selected to be 1/0.05 or 1/0.35. The ellipsometric thickness of these PKSPMA brushes was measured and plotted in Figure 5.6.

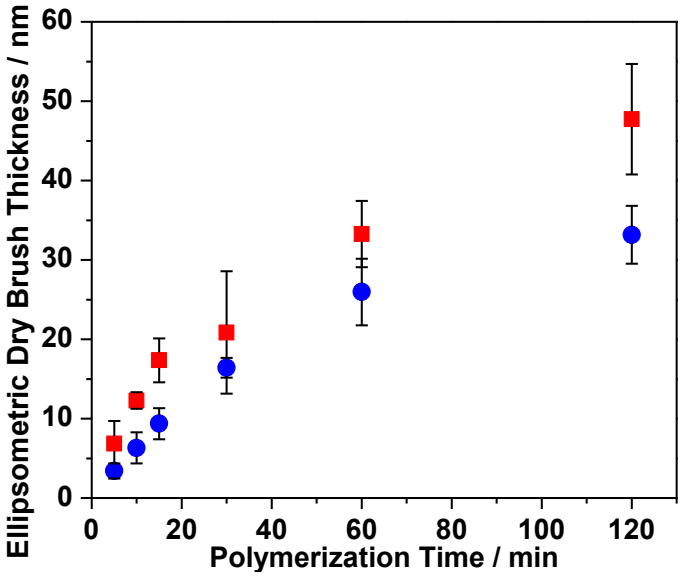

Figure 5.6. Change in thickness of PKSPMA brushes as a function of $CuBr/CuBr_2$ molar ratio and polymerization time at 20 °C, Conditions: (■) [KSPMA]: [CuBr]: [$CuBr_2$]: [Bipy] molar ratio = 50: 1.0 : 0.05 : 2.5, in 1:1 H_2O: methanol ratio. (●) [KSPMA]: [CuBr]: [$CuBr_2$]: [Bipy] molar ratio = 50: 1.0 : 0.35 : 2.5, in 1:1 H_2O: methanol ratio.

There is a dramatic increase in the brush thickness over 120 min for a $CuBr/CuBr_2$ molar ratio of 1/0.05. For a 1/0.35 $CuBr/CuBr_2$ molar ratio, the thickness of the film increased linearly from 2.5 nm to ca. 25 nm in 60 min; for longer times there was a small increase in the brush thickness to ca, 22 nm after 120 min, which could be because of termination of the chains or/and loss of the catalyst activity.

5.3.2.2 Characterization of PKSPMA brush

XPS High resolution C1s and S2p XPS spectra were acquired for 15 nm thick PKSPMA brushes, as shown in Figure 5.7. The C1s core level spectrum was fitted with three peak components at binding energies of 285.0, 286.4 and 288.8 eV, attributable to the C−C/C−S, C−O and O=C−O, respectively. The areas of the C−C/C−S, C−O and O=C−O components were in the ratio 5.6 : 1.4 : 1 which is close to the calculated ratio 6 : 1 : 1. The S2p core level spectrum was fitted into two components at binding energies of ~167.5 and ~169 eV, due to the $C-SO_3^-$.[392]

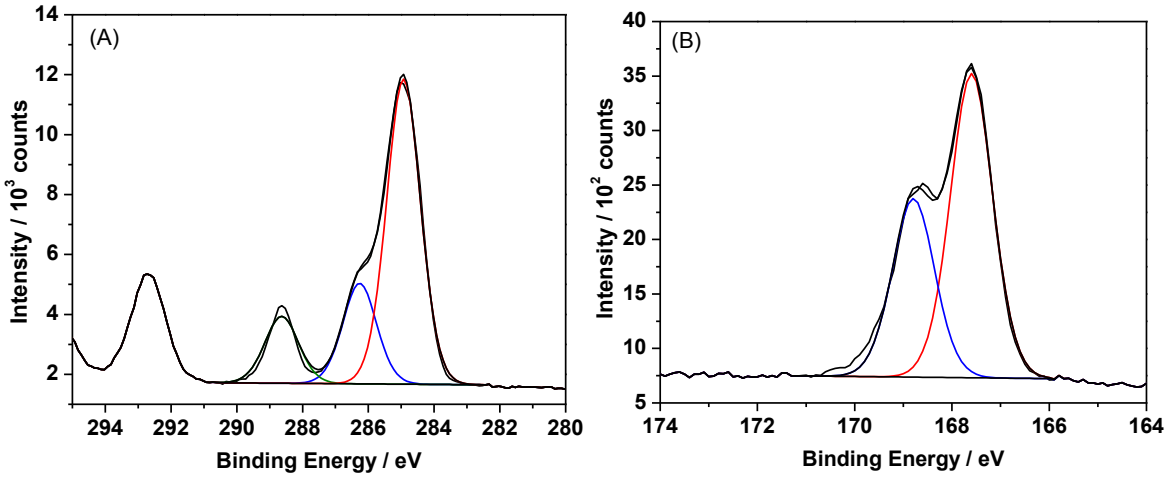

Figure 5.7. Curve-fitted XPS spectra recorded for PKSPMA brushes: (A) C1s core-line spectrum. (B) S2p core-line spectrum.

AFM In previous studies, the roughness of 210 nm thick dry PKSPMA brushes grown on a Au substrate was reported to be 1.45 nm measured over a scan size corresponding to 5x5 μm^2.[391] The PKSPMA surface topography was examined by AFM using tapping mode. Figure 5.8 shows the height image of a PKSPMA brush of ca.15 nm thickness. PKSPMA

brushes both dry and immersed in PBS exhibited a relatively smooth topography with mean roughnesses varying between 0.2 and 0.5 nm. The height image of a patterned PKSPMA brush shows that its thickness immersed in PBS was twice that of the dry brush and the mean brush height increased ca. 30 nm to ca. 65 nm (Figure 5.9).

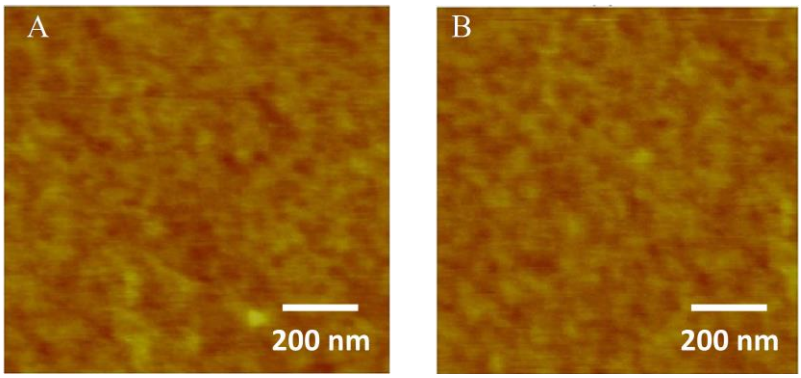

Figure 5.8. Tapping mode AFM images of ca. 15 nm thick PKSPMA brushes. (A) Dry PKSPMA brushes. (B) The same PKSPMA brushes under PBS. Image size 1 × 1 μm^2. The *z*-range: 0- 10 nm dark to bright in both images.

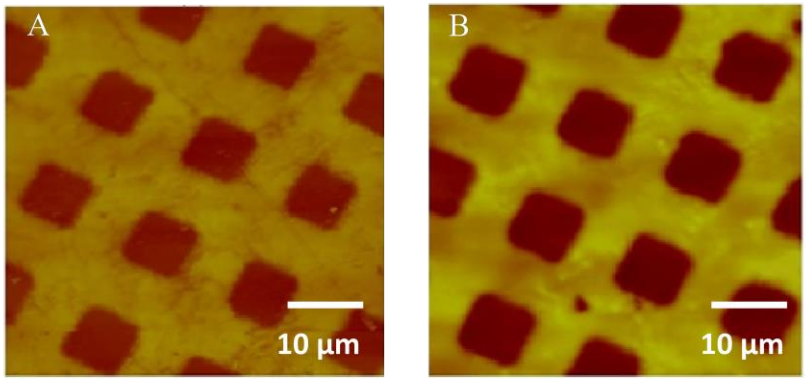

Figure 5.9. AFM tapping mode height images of PKSPMA brushes. (A) Dry PKSPMA brushes. (B) PKSPMA brushes under PBS. Image size 50 × 50 μm^2. The *z*-range: 0- 150 nm dark to bright in both images.

5.3.2.3 Lipid bilayers on PKSPMA brushes

PKSPMA brushes were prepared with thicknesses between 10 and 17 nm on 18 mm glass slides. It was attempted to form lipid bilayers, and the membrane fluidity was evaluated as a

function of the conditions used. Liposomes were used with a lipid mixture in the ratio 30:70 POPC: DOTAP, with 0.1% ATTO590-DOPE fluorophore. DOTAP is a positively charged lipid, so the direct interaction between the vesicles and the surface involves attraction between opposite charges. PBS at pH 7.4 was chosen for incubation, and has been used commonly for formation of bilayers on glass by vesicle fusion. After incubation, the lipid bilayer was rinsed with deionized water. Figure 5.10 shows the FRAP images of PKSPMA brushes at 10 s and 5 min after bleaching. The images show significant vesicle adsorption on the surface, and an evidence of a fluid bilayer beneath. The recovery after photobleaching was slow and the diffusion coefficient was found to be 0.5 $\mu m^2/s$. The surface was then rinsed with PBS in a range of pH 3.0-10.0, and also with $CaCl_2$ to detach adsorbed vesicles but did not seem to work.

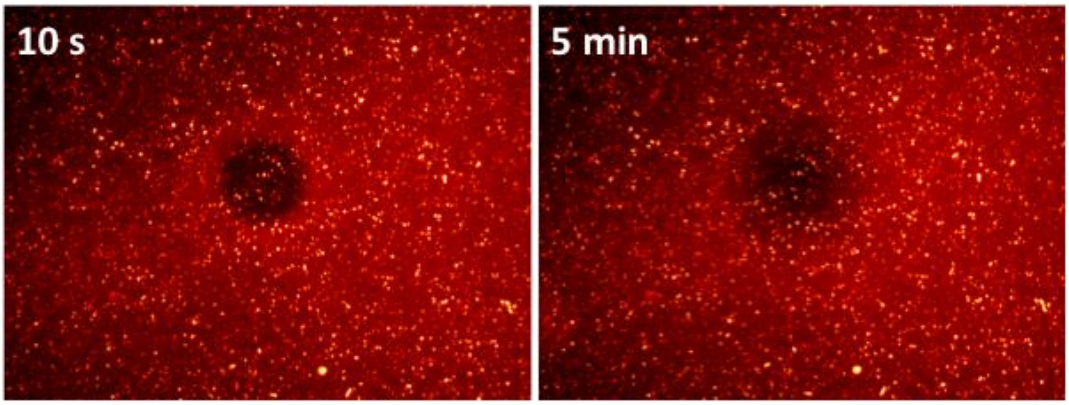

Figure 5.10. Showing FRAP images of PKSPMA brushes at 10 s and 5 min after bleaching, using 30:70 of POPC/DOTAP mixture in PBS at 20 ^oC. Exposed spot is 25 μm diameter.

The formation of zwitterionic POPC lipids on PKSPMS brushes was also attempted. POPC was used with 0.1% ATTO590-DOPE fluorophore in 140 mM NaCl and 5 mM $CaCl_2$ at pH 4.0. After incubation, the surface seemed to consist of intact vesicles, without appearance of lipid layer beneath. No significant change was observed in the surface after cycling the pH range between 2.5 and 10. However, a large quantity of the adsorbed vesicles were detached from the surface after soaking overnight at pH 10 and the result showed that no evidence of a lipid layer remained. Finally, POPC with 0.5% TR-DHPE fluorophore was tested at pH 10. The surface seemed to have less vesicles adsorbed, however, no evidence of forming an underlying lipid layer was observed. There was no success on forming zwitterionic lipids on PKSPMA surfaces.

5.3.3 PMETAC brushes

5.3.3.1 Synthesis of PMETAC brushes

Many groups have investigated the preparation of PMETAC brushes from planar substrates.[393-395] A well-defined PMETAC brush was prepared by copper catalyzed SI-ATRP of METAC monomer in 2,2,2-trifluoroethanol (TFE) at 60 ^{o}C using [((2-bromo-2-methylpropionyl)oxy)hexyl]triethoxysilane (BHE) immobilized on silicon wafer.[393] Dong et al. prepared PMETAC brushes with thicknesses of ca. 60 nm on silicon using CuBr, $CuBr_2$ and bipy as a catalyst system in protic media at room temperature.[394]

Here, CuBr, $CuBr_2$ and bipy ligand were used as a catalyst system to polymerize METAC by SI- ATRP. The mole ratio between the monomer and catalyst was selected to be 67:1:0.05:2.4 for [M]:[CuBr]:[$CuBr_2$]:[bipy] respectively in 1:4 water:isopropanol at 20 ^{o}C. The dry thickness of the PMETAC brush was measured by ellipsometry as shown in Figure 5.11. The brush thickness increased gradually over time from ca. 2 nm in 5 min to almost 65 nm in 300 min. The rate of growth of PMETAC brushes was about 0.25 nm per min over this period.

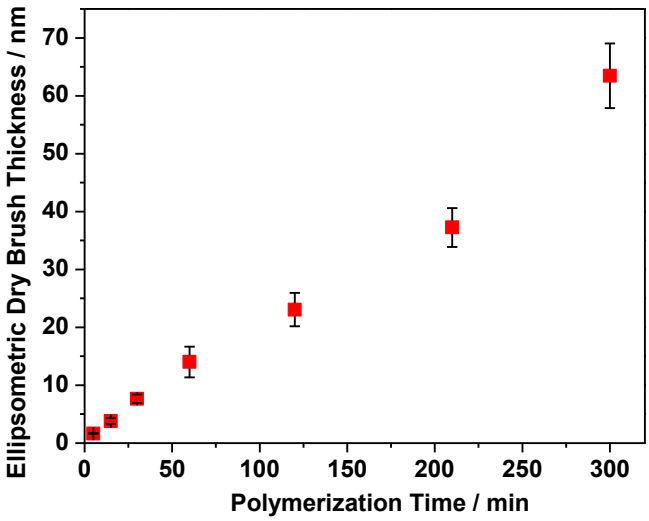

Figure 5.11. Growth of PMETAC brushes thickness over time. Brush growth conditions were 67 : 1 : 0.05 : 2.4 for [METAC] : [CuBr] : [$CuBr_2$] : [bipy].

5.3.3.2 Characterization of PMETAC brush

XPS High resolution C1s and N1s spectra were obtained for PMETAC brushes with original thicknesses of 12 nm (Figure 5.12 (A and B)). The C1s spectrum was fitted using three components at binding energies of 285.0, 286.3 and 289.0 eV, corresponding to the C−C, C−O/C−N and O=C−O, respectively. The ratios of C−C, C−O/C−N and O=C−O obtained from the C1s spectrum were 3.4 : 4.6 : 1 which is close to expected ratio 3 : 5 : 1. The N1s core-line spectrum was resolved into a C−N^+− peak component with binding energy 402.7 eV.

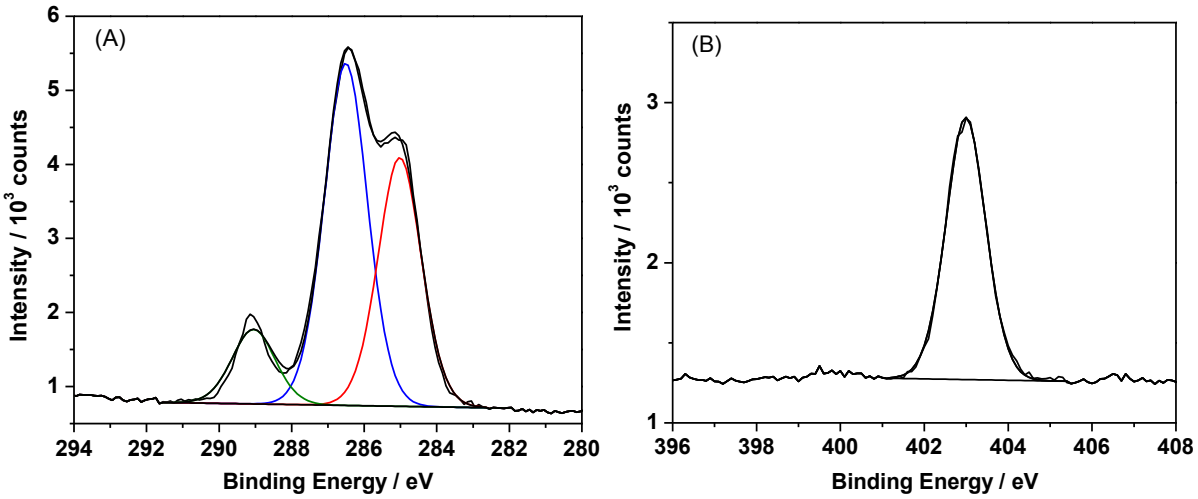

Figure 5.12. High resolution XPS spectra of PKSPMA brushes: (A) C1s core-line spectrum. (B) N1s core-line spectrum

AFM To study the brush topography, 10 nm PMETAC brushes were imaged by AFM using tapping mode (Figure 5.13). The dry surface roughness over size 1 μm × 1 μm was determined to be between 0.2 and 0.4 nm. The PMETAC brush surface roughness under PBS was reduced to between 0.15 and 0.3 nm which indicated that PMETAC brushes were homogeneous with high grafting density.

The swelling of PMETAC brushes was also studied by AFM (Figure 5.14). There was an increase in the mean PMETAC brush thickness under PBS. The brush thickness increased from about 17 to 35 nm, ca. twice the dry brush thickness, in agreement with a pervious study by Huck and co-workers.[396]

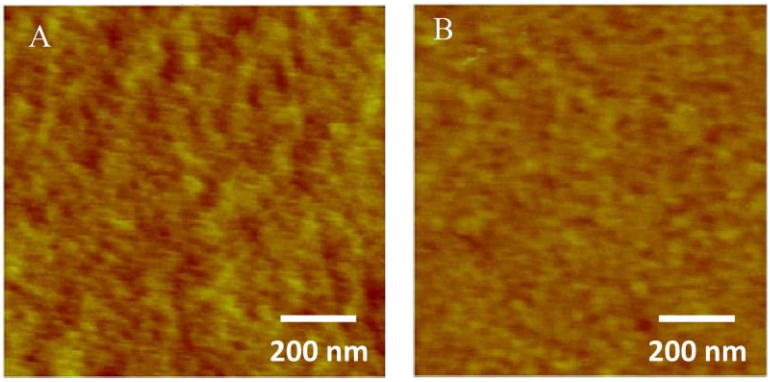

Figure 5.13. AFM tapping mode images of ca. 10 nm PMETAC brushes. (A) Dry PMETAC brushes. (B) The same PMETAC brushes under PBS. Image size 1 × 1 μm^2. The *z*-range: 0-10 nm dark to bright in both images.

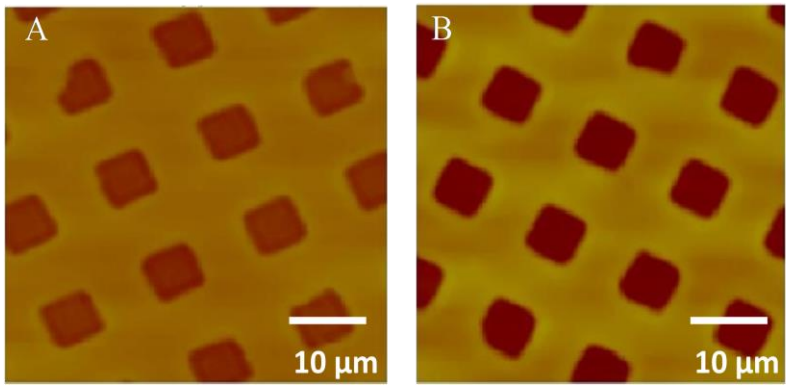

Figure 5.14. AFM height images of PMETAC brushes. (A) Dry PMETAC brushes. (B) The same PMETAC brushes under PBS. Image size 50 × 50 μm^2. The *z*-range: 0- 100 nm dark to bright in both images.

5.3.3.3 Bilayer formation on PMETAC brushes

PMETAC brushes were prepared on glass substrates with ellipsometric dry thickness in the range 8-14 nm. As was found previously for the anionic brushes, the use of a high proportion of oppositely charged lipid in the vesicles seems to have a fluid lipid layer. Vesicle adsorption is driven by interaction between opposite charges, increasing the concentration of negative charge lipids may increase the interaction between the vesicles and the PMETAC surface. A mixture of anionic DOPG and zwitterionic POPC liposomes was tested with different proportions (25, 50 and 70 mol % of DOPG in POPC) in PBS. After incubation, a

fluid lipid layer was formed on PMETACE surface. The diffusion coefficient was fairly slow between 0.01 and 0.02 $\mu m^2 s^{-1}$, as determined by fitting the normalized fluorescence recovery data. It was observed that increasing the concentration of anionic DOPG appeared to have little effect in the diffusion coefficients of bilayers. Little difference was observed in the diffusion coefficients when deionised water was used, instead of PBS. Figure 5.15 shows the FRAP images of lipid bilayers POPC:DOPG with molar ratio with 1:1 using deionised water. The images show that uniform lipids bilayers was formed with very little vesicle adsorption on the surface. The recovery after photobleaching was very slow and the diffusion coefficient was found to be 0.024 $\mu m^2/s$. It is worth to clarify that no lipids biylayer was formed on PMETAC brushes when zwitterionic POPC liposomes was used under the same conditions.

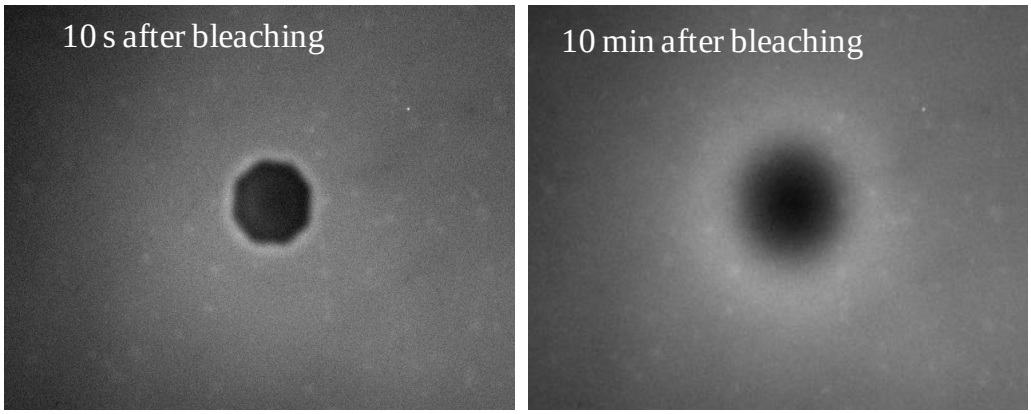

Figure 5.15. FRAP images showing a fluid bilayer on PMETAC brushes at 10 s and 10 min after bleaching, using 1:1 molar ratio of DOPG/POPC mixture in deionised water at 20 ^oC. Exposed spot is 25 μm diameter.

5.3.4 PCysMA brush

5.3.4.1 PCysMA brush as supported lipid layers

PCysMA brushes were prepared with dry thicknesses of 5 to10 nm on 18 mm glass slides. Zwitterionic POPC vesicles were used in both deionised water and PBS. After incubation, some vesicles remained intact on the surface with a density too low to cause bilayer formation on the PCysMA brushes. In a subsequent FRAP experiment, no recovery was observed in the bleached area, evidence of vesicle adsorption on the surface without bilayer

formation, (Figure 5.16). The introduction of DHPC-C6 into the lipid vesicles seemed to form small good islands of lipid bilayer on PCysMA surface. However, the diffusion coefficient was very slow.

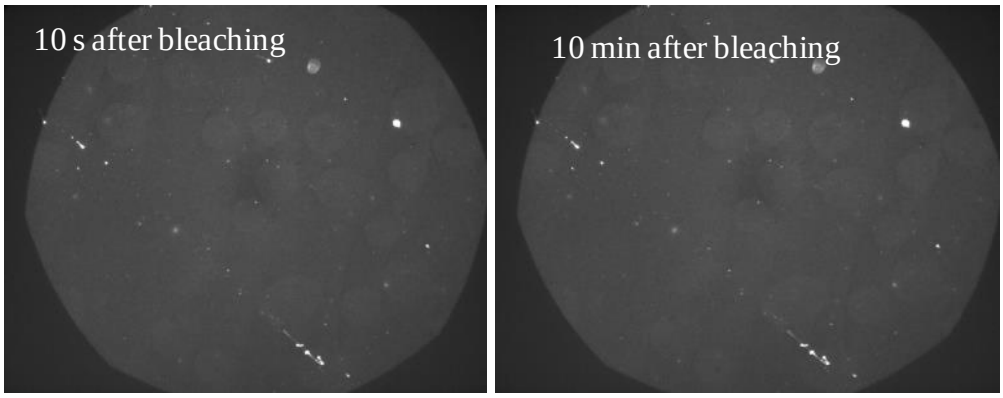

Figure 5.16. Showing FRAB images of POPC lipids on PCysMA brushes in deionised water at 10 s and 10 minutes after bleaching at 20 ^{o}C. Exposed spot is 25 μm diameter.

Liposomes formed from a mixture of POPC and DOTAP were also examined at different concentration in 10 mM phosphate buffer at pH 7.1 in the absence of NaCl. It was observed that the introduction of positively charge lipids increased the density of the vesicles adsorbed into the surface. When a mixture of DOTAP/POPC with 1:9 molar ratio was used, there was an increase in the adsorbed vesicles but insufficient to form a bilayer. However, when 25% mol DOTAP vesicles were used, a dense layer of vesicles was absorbed into the surface. After incubation for 2 h, lipids bilayer was rinsed with deionized water and imaged. The images showed significant vesicle adsorption on the surface, but no evidence of a fluid bilayer formation. When the sample was incubated overnight, no evidence of a fluid bilayer was observed. The formation of double bilayer was observed when the sample incubated for 48 h. Figure 5.17A shows FRAP images of PCysMA brushes at 10 s and 5 min after bleaching. The images show that the outer bilayer was in-complete on the surface, and an evidence of a fluid bilayer. The recovery after photobleaching was relatively high and the diffusion coefficient was found to be 0.7 μm^2/s. A homogeneous lipid layer was formed on the surface, with reduction in the size of the top bilayer, after further incubation time. In FRAP experiment, a recovery in bleached area was observed, with a diffusion coefficient of ca. 1.0 μm^2 s^{-1}, as determined by fitting the normalized fluorescence recovery data (Figure 5.17B). The use of liposomes mixture of DOTAP/POPC with 1:1 molar ratio was also

examined using the same protocol. The FRAP experiments suggested that lipid bilayers were formed on PCysMA brushes. However, there was a reduction in diffusion coefficient ca. 0.4 $\mu m^2 s^{-1}$

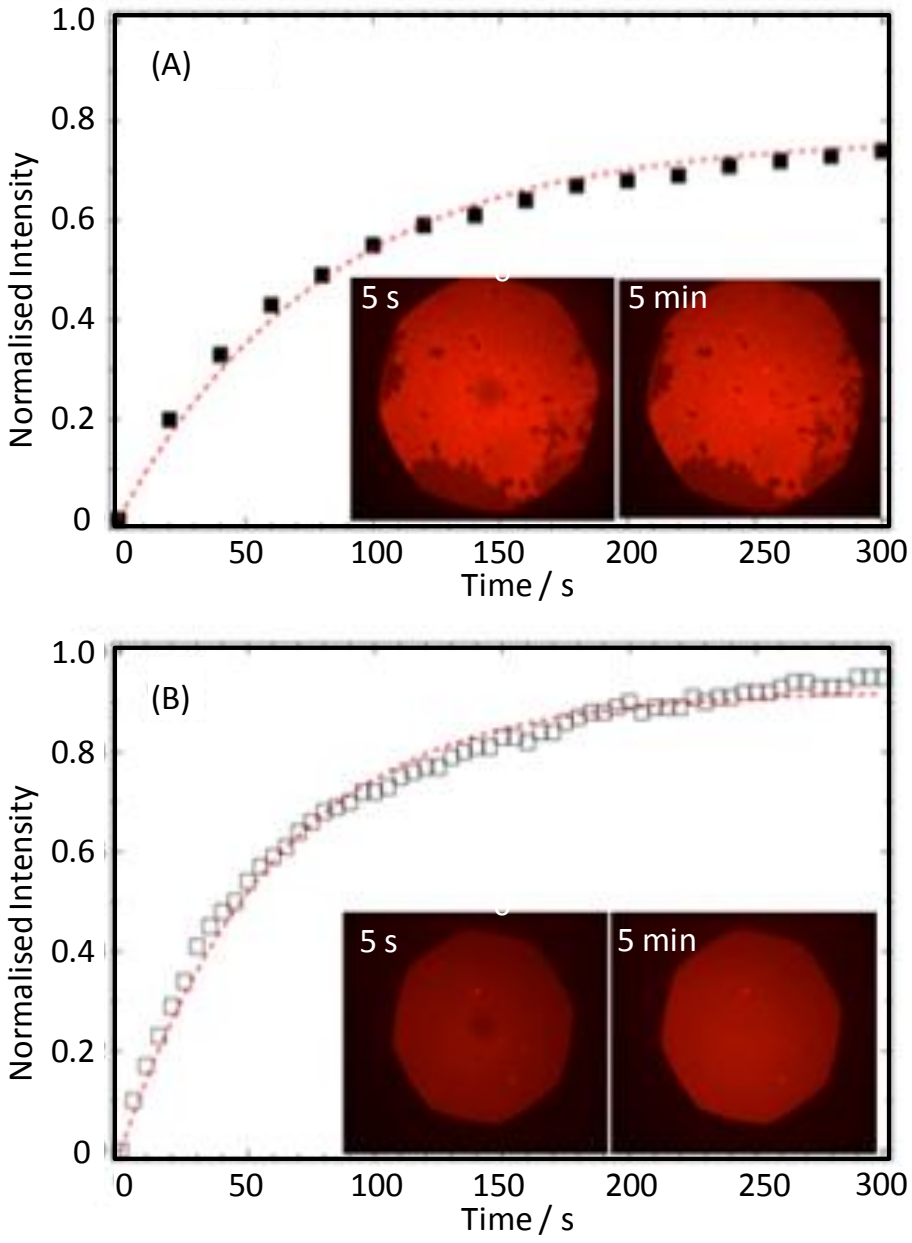

Figure 5.17. FRAP diffusion plots and images recorded 5 s and 5 min after bleaching, a mixture of DOTAP/POPC with 25:75 mol % in 10 mM phosphate buffer at pH 7.1 in the absence of NaCl. (A) PCysMA brushes incubated for 48 h. (B) The same sample incubated for a further 48 h. Exposed spot is 25 μm diameter.

5.4 Conclusion

The growth of PKSPMA and PMETAC brushes on Si substrates has been investigated at variety of conditions. The surface charge of PMPC brush was ca. ±10 mV. The thickness of PKSPMA and PMETAC brushes were also controlled. All these brushes were fully characterized using AFM and XPS.

No lipids were formed on PMPC brushes when using positive and negative vesicles. However, the introduction of chain lipids (C6) in the positive charge lipids can rupture the vesicle, therefore islands of lipid bilayers were formed on PMPC brushes, with diffusion coefficient of 0.4 $\mu m^2\ s^{-1}$. Also, a homogeneous bilayer was formed on PMPC surface with diffusion coefficient of ca. 0.1 $\mu m^2\ s^{-1}$, when using spin-coating approach. There was no success on forming zwitterionic lipids on PKSPMA brushes. When positive vesicles used, the brushes show significant vesicle absorbed on the surface, and a fluid bilayer underneath with diffusion coefficient ca. 0.5 $\mu m^2/s$. A fluid lipid layer was formed on PMETAC surface, with very slow diffusion coefficient ca. 0.01 to 0.02 $\mu m^2\ s^{-1}$; depending on the proportions of the negative lipids. In FRAP experiment, no evidence of the zwitterionic POPC vesicle adsorption on the PCysMA brushes was observed. The introduction of positively charge lipids increased the density of the vesicles adsorbed into the surface. The vesicles slowly fused and required several days to form a fluid bilayer on the PCysMA brushes. A homogeneous lipid layer was formed on the PCysMA surface, after 48 h incubation time when used 25% mol DOTAP vesicles. In FRAP experiment, the diffusion coefficient of lipids on PCysMA was ca. 1.0 $\mu m^2\ s^{-1}$, comparable to that observed for supported lipids bilayers on glass.

Chapter 6: The preparation of binary patterned gold / PCysMA brush using a combination of photolithography and SI-ATRP techniques

6.1 Introduction

Thin organic films have been applied widely in nanotechnology. Self-assembled monolayers have been used as resist materials for etching of metallic surfaces.[13,397-399] Micro-contact printing has been used to pattern alkylthiolate SAMs on the surfaces of gold, silver and copper, prior to etching in $S_2O_3^{2-}$/ferri/ferrocyanide-based solutions to generate microstructure of gold, silver and copper microstructures.[13] Long-chain thiols have been patterned on gold surfaces to mask them for wet etching using CN^-/O_2 solutions to yield high resolution patterns in gold.[398] Polymer films have also been used as resists for wet chemical etchants to transfer patterns into underlying substrates.[400-401] A range of polymer brushes, including PMMA and PDMAEMA on gold surface have been used as robust barriers to wet chemical etchants, including KI/I_2, $KCN/K_3Fe(CN)_6$, and aqua regia (a mixture of HNO_3 and HCl).[400] Polymer multilayers on patterned SAMs have also been used as resists for the wet chemical etching of KI-based commercial gold etchants, to generate patterns with very small numbers of defects.[401] The fabrication of nanostructures with high resolution has been achieved using several techniques such as electron beam lithography,[402-404] scanning near-field photolithography (SNOM),[188,405] and interference lithography (IL).[406-408] Nanostructures with widths 5-7 nm have been fabricated in Si using films of PMMA as a resist.[404] Organothiol SAMs on gold and organosilane SAMs on Si have been patterned by UHV-STM, and the patterns subsequently transferred into the substrate by wet etching using a solution of KCN and KOH for gold and HF for Si to give sub 55 nm wide lines.[397] Alkanthiolate SAMs on gold have been patterned by SNOM, and subsequently immersed into a ferri/ferrocyanide etching solution to transfer the patterns into the underlying gold surface yielding 55 nm wide features.[405] Gold nanostructures were also been prepared by near field photopatterning of thiol SAMs on Au followed by immersion in an etching solution consisting of mercaptoethylamine in ethanol to give patterns with a FWHM of 30 nm.[188]

IL is a powerful technique for the fabrication on nanopatterns over large area. It has been reported that a layer of photoresist on Si wafer was photopatterned by two perpendicular exposures using a Lloyd's-mirror interferometer and light with a wavelength of 325 nm. The patterns were transferred into the substrate by etching in a solution of H_2O, HF, and H_2O_2, to

from arrays of Si nanowires over a very large area (1cm^2).[408] A photoresist film on a gold surface was exposed by IL (325 nm) then the pattern was transferred into gold surface by dry etching (ion beam etching) to generate Au nanolines with a width of 115 nm and a period of 395 nm in an area as large as 5 mm^2.[407] Hedberg-Dirk and Martinez have reported the fabrication of arrays of holes in a gold film with a diameter of 140–350 nm and depth of 33 nm in an area over 4 cm^2.[406]

Titanium is a biocompatible material that has been widely used in medical applications, such as dental implants, pacemakers and heart-valves,[103,409-411] whereas chromium is considered to be high toxic material.[412-413] Many studies have described the formation of silane films on titania surfaces.[103,409,414-415] However, there has been very little work focused on the formation SAMs on chromia surfaces.[105,397] Silanization of titania with 3-aminopropyltriethoxylsilane (APTES) has been presented by many groups.[409,414-415] 11-(2-Bromo-2-methyl)propionyloxy)undecenyldimethylchlorosilane has been successfully immobilized on titania surfaces to yield an initiator-functionalised surface.[103,416] Hild et al. reported the formation of close-packed octadecyltrimethoxysilane (OTMS) on chromium oxide.[105]

Polymer brushes immobilized onto Ti surfaces have been broadly studied.[103,410,417] Collard and co-workers have reported the functionalisation of poly(OEGMA) brushes with peptides on Ti surfaces, to control the cell adhesion to the surface.[103] Peptide-modified poly(2-gluconamidoethyl) methacrylate (GAMA) brush immobilized on Ti surface have been investigated by Raynor et al.[416] Gao et al. have investigated the biocompatibility and biofilm resistance of copolymer brushes containing N,N-dimethylacrylamide (DMA) and aminopropyl methacrylamide hydrochloride prepared from a titanium deposited silicon wafer, using SI-ATRP.[414] Kang et al. have reported the growth of poly(ethyleneglycol)methacrylate (PEGMA) from modified Ti surface with a catechol-based ATRP initiator.[410] Patterns of POEGMA brushes on Ti surface formed using a combination of SI-ATRP and photolithography have been reported by Messersmith and co-workers.[411] A photoresist on Ti surface was first patterned, then a catecholic initiator was adsorbed in exposed regions. POEGMA was then grown from initiator-functionalised sites after removal of the photoresist film.

The control of protein immobilization has been studied using a variety of methods and surfaces.[418-421] Oligo(ethylene glycol) (OEG)-terminated SAMs of alkylthiols and siloxane

have been photo-patterned using SNOM to introduce aldehyde groups that covalently anchor proteins.[418,422-423] A Lloyd's mirror interferometer has been used to photodegrade OEG-terminated SAMs of alkylthiols on gold to immobilize proteins to form nanolines.[353] Photo-sensitive aminosilanes modified with 2- nitrophenylethoxycarbonyl (NPEOC) have been used to yield patterns of amine groups with high efficiency after deprotection. Proteins were selectively immobilized into nanopatterned, photodeprotected areas.[424] Streptavidin was specifically immobilized, after activation of the hydroxyl groups of PEGMA brushes with N,N'-disuccinimidyl carbonate to generate micropatterns of protein in the Ti surface.[410] A combination of photo- and pH-sensitivity have been utilized by Doh and Irvine to pattern multicomponent proteins using photogenerated polyelectrolyte bilayers.[425]

Figure 6.1 shows schematically the fabrication process attempted here. A thin film of gold is prepared on glass coated with titanium and chromium as adhesive layers. The gold is functionalised with a SAMs of octadecanethiol (ODT) which is patterned by exposing the samples either through a mask or using a Lloyd's mirror two-beam interferometer. The exposed SAM is etched using mercaptoethylamine in ethanol. The bare oxide regions exposed between the resulting gold structures are functionalised by attachment of BIBB-APTES. PCysMA brushes are grown from the initiator-functionalised regions in both mico- and nano-patterned gold surfaces. Patterned samples prepared according to this scheme were characterised by AFM and XPS, and used for the immobilisation of proteins.

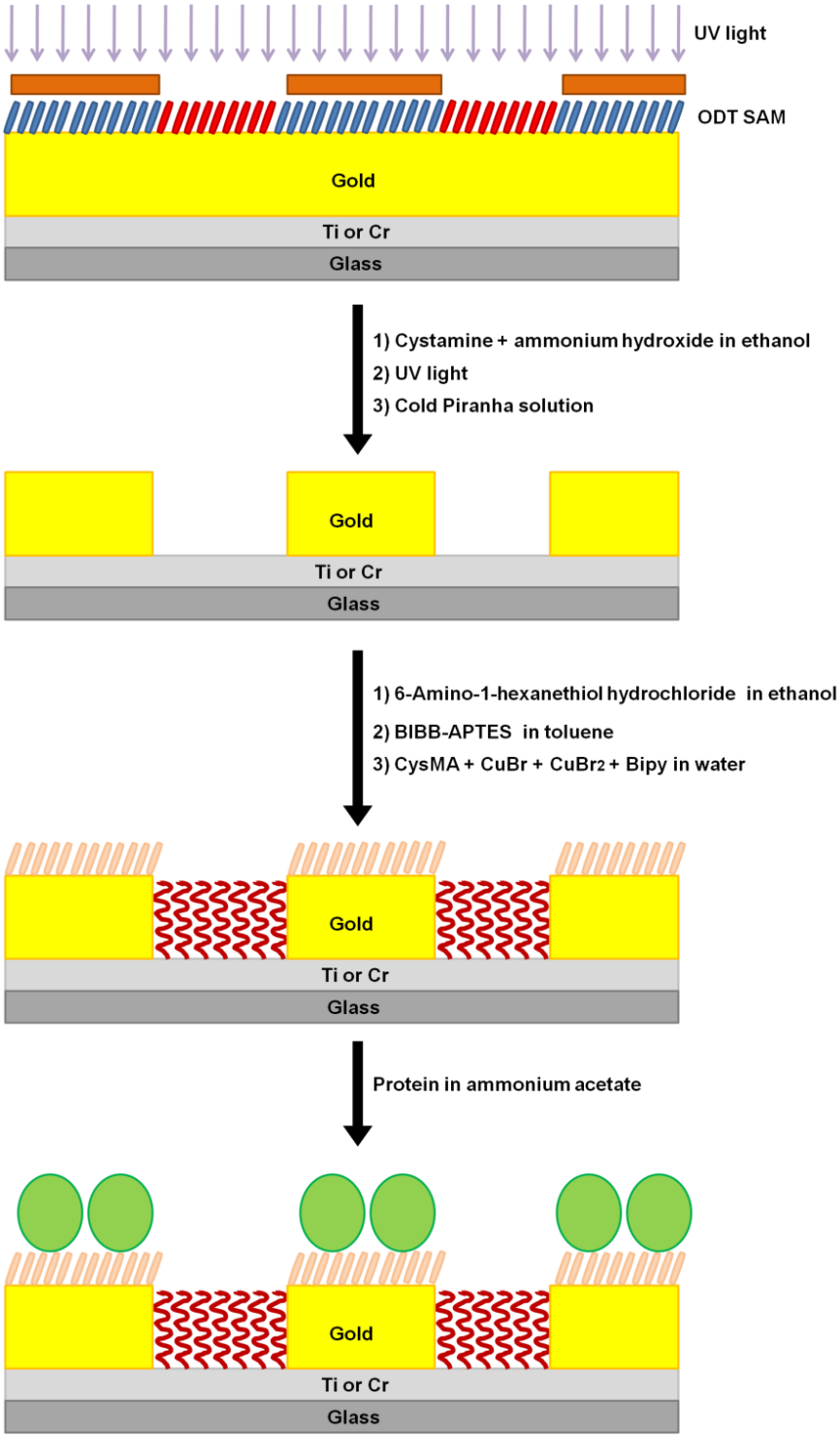

Scheme 6.1 Schematic diagram showing the preparation of binary surfaces consisting of protein-coated gold structures separated by PCysMA brushes.

6.2 Experimental

6.2.1 Synthesis of 2-Bromo-2-methyl-N-(3-triethoxysilyl-propyl)-propionamide (BIBB-APTES)

2-Bromo-2-methyl-N-(3-triethoxysilyl-propyl)-propionamide (BIBB-APTES) was synthesized according to previously reported method.[161,426] To a solution of 4.00 mL (3.8 g, 17.1 mmol) (3-aminopropyl)triethoxysilane and 3.60 mL of triethylamine (2.62 g, 25.8 mmol) in 100 mL dry THF, 1.50 mL (2.79 g, 12.1 mmol) 2- Bromo-2-methyl-propionyl bromide was added drop-wise. The reaction mixture was stirred for 12 hours under N_2. The precipitate was filtered off and the solvent was removed. The product was redissolved in 20 mL of DCM and washed twice with 0.01N of HCl and twice with deionised water. The organic phase was dried with magnesium sulphate and filtered. The product was purified by column chromatography on silica gel using a combination of n-hexane and ethyl acetate with ratio 2:1. The fragments were combined and the solvent was removed to produce a colourless oil with a yield of 84.3% (5.3g). ^{1}H NMR (250 MHz, $CDCl_3$): δ 6.9 (s, 1H, NH), 3.82 (q, 6H, $SiOCH_2$), 3.28 (t, 2H, CH_2N), 1.95 (s, 6H, CH3,), 1.68 (m, 2H, CH_2), 1.22 (t, 9H OCH_2CH_3), 0.65 (t, 2H, $SiCH_2$). ^{13}C NMR (250 MHz, $CDCl_3$): δ 171.86, 63.24, 54.92, 42.56, 32.59, 22.68, 7.56.

6.2.2 Sample preparation

The preparation of gold film and 1-octadecanethiol (ODT) SAMs were described in section 2.3. Cleaned glass microscope slides were first coated with ca. 5 nm of titanium/chromium, followed by ca. 20 nm of gold under pressure ca. 1.0 x 10^{-6} mbar, and the deposition rate less was ca. 0.1 nm s^{-1} for Cr/Ti and ca. 0.4 nm s^{-1} for Au. Then, the samples were immersed in 2 mM solution of ODT in degassed ethanol for at least 18 h to form SAMs. Prior to use, the samples was washed with ethanol and dried under N_2.

6.2.3 UV irradiation and patterning

SAMs of ODT on gold were patterned using a frequency-doubled argon ion laser (244 nm) as described in section 2.6. The power was ca. 15 mW, and the exposed area was ca. 0.2 cm^2. SAMs of ODT on gold were exposed to UV light.

Micro-patterned ODT SAMs on gold were obtained by exposing the samples to UV light through a copper electron microscope grid as mask. Interference lithography (IL) was also

used to pattern ODT SAMs. After photopatterning of the ODT monolayers, gold films were etched by immersion in a 0.2 M solution of mercaptoethylamine hydrochloride in 8% v/v of 35 % of ammonia in ethanol. After etching, the samples were exposed again to UV light to photo-oxidize the remaining ODT SAMs, and then they were washed with ethanol, and dried under N_2.

To re-functionalized the gold surface, the samples were exposed to UV light and immersed in 2 mM solutions of 6-amino-1-hexanethiol hydrochloride (AHT) in degassed ethanol, for 24 h at 20 ^{o}C. Subsequently, they were rinsed with ethanol and dried under N_2. The samples were submerged in a 0.5 M aqueous solution of glutaraldehyde for 1 h, then washed with water and dried under nitrogen.

6.2.4 Preparation of initiator functionalised silane films

The preparation of BIBB-APTES film on Ti was prepared following previously published procedures.[103,427] The samples were cleaned by treatment with cooled piranha solution (20^{o}C) for 5 min, followed by washing with copious amounts of deionized water. The samples were dried at 100 °C for 2 h and then immersed in a 5 mM initiator solution (BIBB-APTES) in toluene for 24 h to form a SAM on TiO_2 surface. The samples were washed and sonicated in toluene and ethanol, and dried under N_2.

BIBB-APTES SAMs on Cr was formed using a previously published methodology for silane preparation on Cr surface.[105] The samples were first oxidized by immersion into a cooled piranha solution for 5 min. Afterward the samples were washed with deionized water then rinsed an alkaline water-ethanol solution (a solution of ethanol (10 mL) and 1mM of NaOH solution (1 mL)) under reflux condition for 30 min. Subsequently the samples were immersed into a 5 mM of BIBB-APTES solution in toluene at least 24 h. Finally the samples were rinsed and sonicated in toluene and ethanol, and then dried under steam of N_2.

6.2.5 Preparation of PCysMA brushes

PCysMA brushes were prepared as stated in chapter 4. Surface initiator-functionalized Ti and Cr were placed in Schlenk tubes, degassed, and then filled with N_2. CysMA (5.0 g, 15.0 mmol) was dissolved in dionized water (12.0 mL) at 20 ^{o}C and degassed for 30 min. Cu(I)Br (71.4 mg, 0.5 mmol), bipy (234 mg, 1.5 mmol) and Cu(II)Br_2 (55.6 mg, 0.25 mmol) were added to the solution. This reaction mixture was degassed for 10 min, and then briefly

sonicated. Polymerization solution (2 mL) was transferred into each Schlenk tube. After 30 min, the substrates were removed, sonicated in water and rinsed with ethanol, and then dried with N_2.

5.2.6 Protein Immobilization

Protein immobilization on patterned surfaces was studied using FluoSphere NeutrAvidin microspheres (0.04 µm, yellow-green fluorescence). The samples were immersed in a solution of ammonium acetate (0.1M) containing NeutrAvidin-functionalised nanoparticles (1 µg mL^{-1}) for 15 min, then rinsed with ammonium acetate solution and deionized water, and gently dried under N_2.

5.2.7 Surface characterization

Contact angles, AFM, XPS and confocal microscopy were used to characterize surfaces, as described in Chapter 2. Contact angles were measured from three water droplets, across the surface and averaged to determine the change in polarity of the surface. AFM was used to study the topography of the surface. Wide scan and high resolution XPS spectra were analyzed to determine the surface compositions. Confocal microscopy were used to image proteins on binary patterned gold/PCysMA brush surface.

6.3 Result and discussion

6.3.1 UV modification and patterning

The samples were exposed to different UV exposures to determine the dose that is required to complete the photo-oxidation of the ODT SAM. After exposure, all samples were rinsed in ethanol and dried with nitrogen. Figure 6.1 shows the variation in the of water contact angle with the UV exposure. The contact angle of ODT SAMs decreased gradually from ~105° to 85° following to exposure to UV irradiation. A limiting contact angle of ca. 86º was obtained at dose of ca. 30 $J.cm^{-2}$. No significant reduction in the contact angle was observed after 8 min exposure which corresponded to a dose of 30 $J.cm^{-2}$. This indicates the completion of photo-oxidation reaction

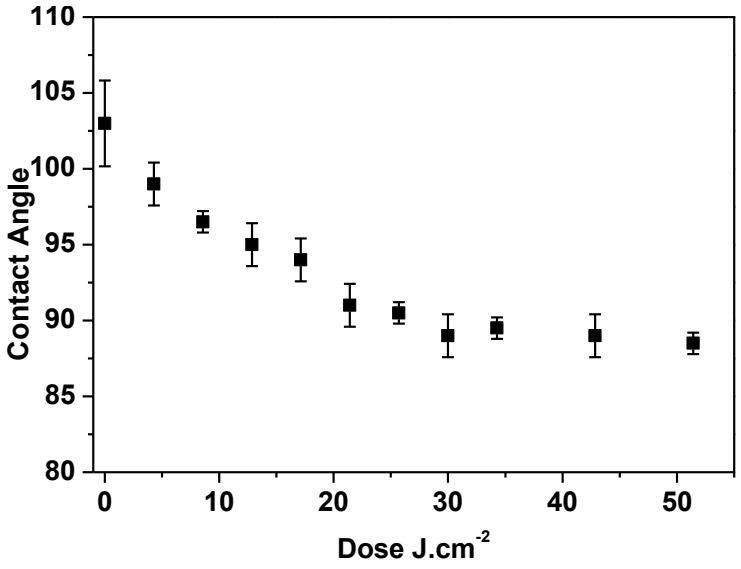

Figure 6.1 Graph illustrating variation in contact angles for octadecyl thiol (ODT) as a function of irradiation dose.

The photo-oxidation of ODT causes the conversion of alkylthiolates into alkylsulfonates, due to the formation of hot electrons at gold surface (see equation below).[249] The alkylsulfonates are weakly bonded to gold surface and can be removed easily or displaced by other adsorbate molecules.

$$AuSR + 3/2\ O_2 + e^- \longrightarrow Au + RSO_3^-$$

In previous studies, the SAM thiol was masked during photopatterning so that the oxidation occurred only in exposed regions. The photopatterned sample was immersed in a solution of a contrasting thiol to displace the oxidized products in exposed areas on the surface.[200,216-217] In the present study, ODT SAMs on gold surfaces were exposed to 50 J cm^{-2} UV irradiation to fully oxidize the ODT SAMs, and then the samples were immersed in cooled Piranha solution (20 ^oC) for 5 min to oxidize the residual organic materials. After washing, the samples were dipped into 2 mM solutions of AHT in degassed ethanol, for 24 h at 20 ^oC to form close packed self-assembled monolayers. The contact angle dropped from ca. 83±3^o for cleaned gold to ca 35±7^o for amine functionalized surface. No significant change occurred in the contact angle after the samples had been reacted with glutaraldehyde to yield the aldehyde functionalized surface.

High resolution C1s spectra were acquired for surfaces after adsorption of AHT and after reaction with gluataraldehyde (Figure 6.2 (A and B). For AHT SAMs, the C1s spectrum was fitted using two components, corresponding to the hydrocarbon peak -C-C-/ -C-S- at 285.0 eV and -C-NH group at 286.5 eV. The predicted experimental ratio of -C-C-/-C-S- : -C-NH- is 6.2 : 1, which close to the predicted ratio (5 : 1), see Figure 6.2A. Significant changes were observed in the C1s region after coupling with gluataraldehyde (Figure 6.2B). The spectra was fitted into three components at binding energies of 285.0, 286.3 and 288.3 eV, attributable to the -C-C-/-C-S-, -C=N/-C-N and -C=O, respectively. The ratio of the -C-C-/-C-S-, -C=N-/-C-N- and -C=O was found to be similar to the expected ratio (8:2:1).

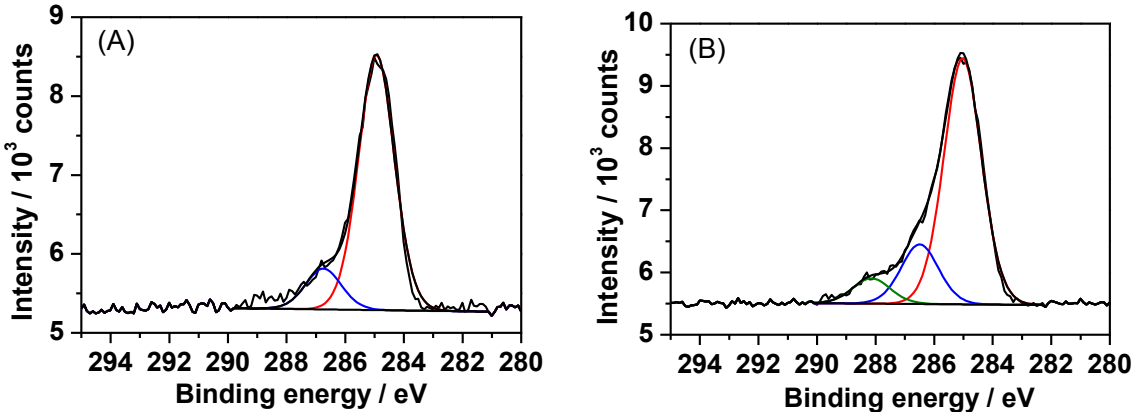

Figure 6.2 XPS spectra of 6-amino-1-hexanethiol (AHT) on gold film. (A) High-resolution of C1s spectrum of 6-amino-1-hexanethiol (AHT) on Au. (B) High-resolution of C1s spectrum 6-amino-1-hexanethiol after coupling with gluataraldehyde on Au.

Micron- and nano-scale patterns were prepared by exposing SAMs of ODT to a UV dose of 35 J cm^{-2} and 25 J cm^{-2}, respectively, using an electron microscope grid as mask, and a Lloyd's mirror interferometer. Subsequently, the samples were etched using a solution consisting of 0.2 mM of MEA and 8 % v/v of 35 % ammonia in ethanol. MEA acts as a bidentate ligand by coordination to gold atoms in both the thiol and amine groups, and as a result gold dissolves in the exposed areas in the presence of ammonia as a catalyst.[188] Samples of micro-patterned ODT monolayers on ca. 20 nm thick gold were etched by immersion in MEA solution at different times. AFM topographical images of micro-patterned gold were used to determine the optimum etching time, as shown in Figure 6.3. In the masked areas (bars) the gold was expected to remain intact, while in the exposed areas (squares) it would be removed. The etch depth could thus be determined from the height difference

measured from a line section. Figure 6.4 shows the change in the height of samples exposed to MEA solution for 2.5, 7.5, 15, 20, 25 and 30 min. It can be seen that at less than 15 min etching time, was not removed completely from the exposed area. Exposing the patterned samples to the etch solution for 20 min yielded a height difference equal to expected thickness. It was observed that after exposing the samples to the etch solution for 25 min or more, the unoxidized areas began to be etched, although these areas were fully covered by ODT SAMs. This is possibly due to undercutting of the ODT SAMs in unoxidized areas.

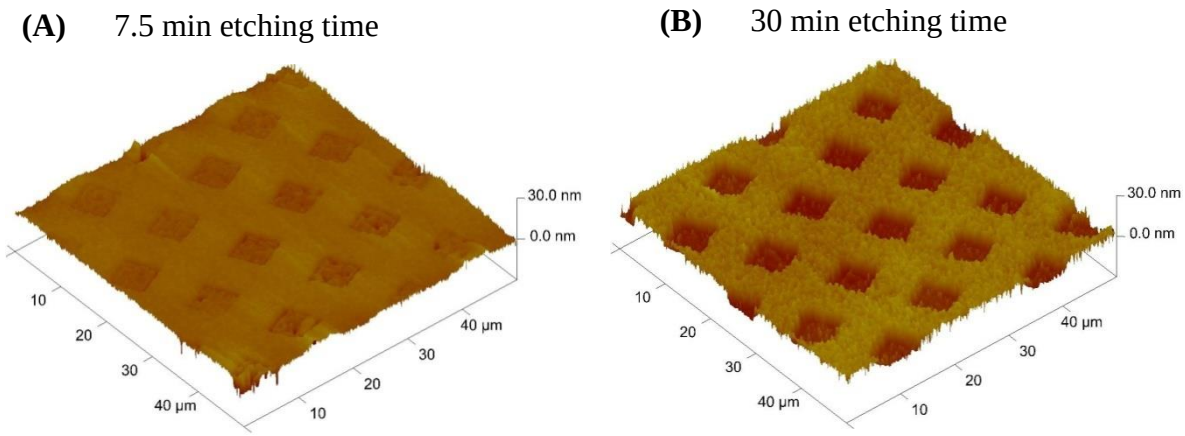

Figure 6.3 Images (A) and (B) show 50x50 µm^2 AFM tapping height images, with a common vertical range of 30 nm, at different etching time.

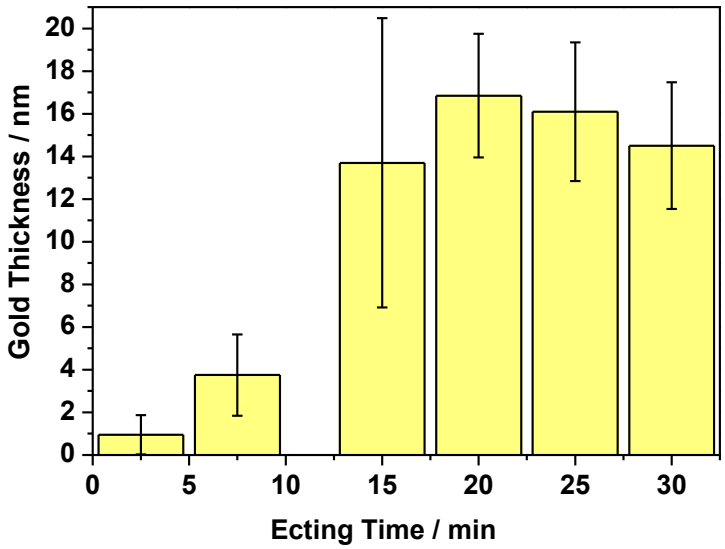

Figure 6.4 Graph showing variation in gold thickness as a function of etching time.

Nanolines pattern of gold were prepared by patterning ODT SAMs on gold surfaces using a Lloyd's mirror interferometer with the angle between the sample and mirror set at 10^{o}. Patterned ODT SMAs were exposed to the etch solution for 15 and 20 min. The height difference between areas exposed to maxima and minima in the interferogram was measured for AFM images. It was observed that immersion of the samples in the etching solution for 15 min yielded a height difference similar to the gold thickness (16±1 nm), sugesting removel of gold from areas exposed to interference maxima without effect on the regions exposed to minima in the interference pattern (Figure 6.5). In some cases, longer etching times (20 min) were found to cause removal of gold from regions exposed to minima, leading to reduce in height difference.

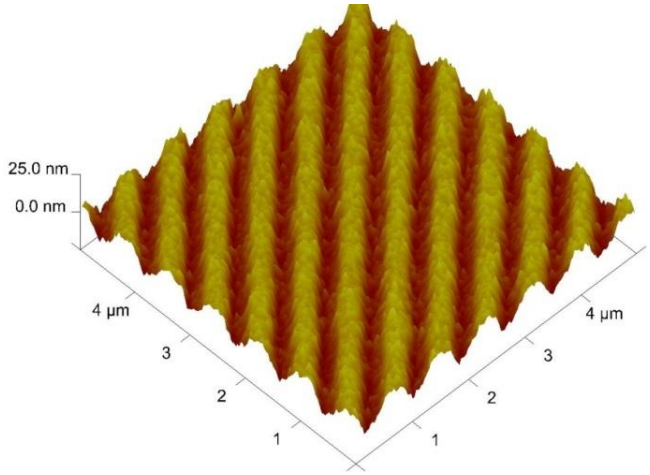

Figure 6.5 AFM tapping height image 5.0x5.0 μm^2 of gold nano-structured prepared by IL at 10^{o}, with a common vertical range of 25 nm, at 15 min etching time.

Interference lithography was used to fabricate gold nanodots by using two orthogonal exposures of ODT SAMs on gold. Figure 6.6 shows a schematic diagram of the technique that used to fabricate nanodots. The sample was placed on the stage, close to the mirror, and exposed to UV light. The sample was subsequently rotated by 90 degrees on the stage and exposed for a second time to UV light. The two bands of alternating constructive and destructive interference in the overlapping interferograms intersected to give dots on the sample surface.

Figure 6.7 shows AFM topographical images of gold nanodots that were fabricated using two orthogonal exposures. An ODT monolayer on gold was exposed twice to a dose of 25 J cm^{-2}

at 244 nm. After photopatterning, the sample was immersed in the etching solution for 15 min. Arrays of gold nanodots were obtained after etching the sample. The AFM image shows that the height difference between the tops of the nanodots and the troughs between them was ca. 17.5±2 nm. These data suggest that complete removal of the gold from has occurred between the dots.

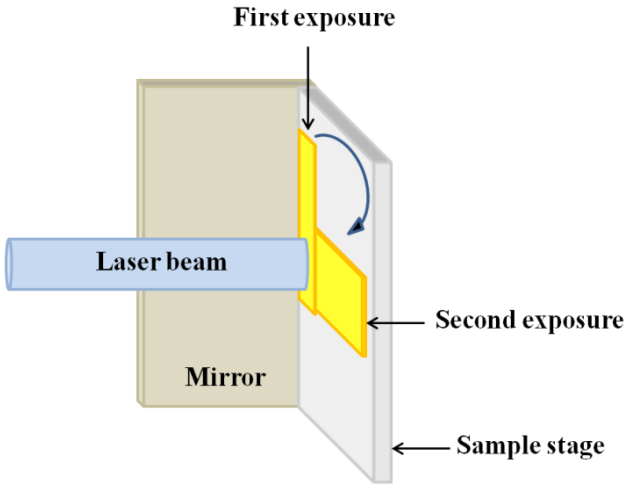

Figure 6.6 Schematic representation of the method used for orthogonal repeated exposures of sample surface.

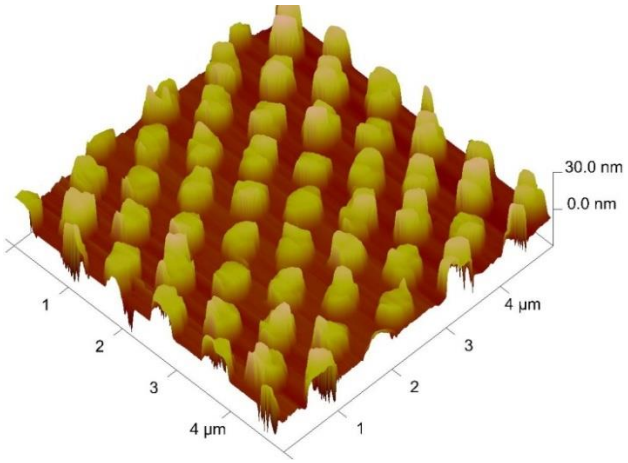

Figure 6.7 A 5.0x5.0 µm^2 tapping mode AFM height image of gold nanodots formed following orthogonal exposures a dual beam interferometer 10^o, after 15 min etching time.

6.3.2 Initiator silane-coated surfaces

SAMs of ODT on gold surfaces with Ti and Cr adhesive layers, were exposed to 35 J cm^{-2} at 244 nm UV light, the same dose that used for patterning to oxidized the ODT SAMs. Gold films were etched by dipping the samples into etching solution for 20 min, to yield films of Ti and Cr. Figure 6.8 shows AFM topographical images of gold before and after etching. It is clear that the roughness of the surface decreased after etching. The gold roughness (rms) was within the range 1.3 to 2.2 nm, depending on the film preparation conditions. The roughness of Ti and Cr surfaces resulting from etched samples, was measured to be 0.8±0.4 nm.

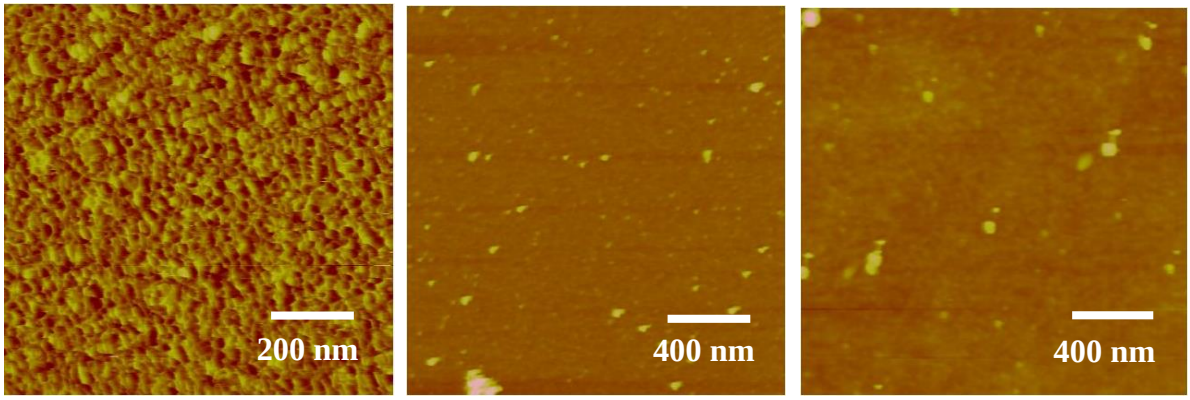

Figure 6.8 AFM height images of gold film before and after etching. (A) Gold surface resulted from the evaporation, 1.0 × 1.0 μm^2. (B) Ti surface after etching gold, 2.0 × 2.0 μm^2. (C) Cr surface after etching gold. 2.0 × 2.0 μm^2. z-range 0 – 10 nm dark to bright in all cases.

XPS was performed to determine the chemical compositions of surfaces before and after gold etching. Figure 6.9 shows the variation of the Au4f, Ti2p and Cr2p spectra for samples before and after etching. Figure 6.9A and 6.9B show that significant decrease in the components of Au was observed after etching, suggesting the removal of gold from the surface. The spectrum showed an indication of the presence of Au after a 20 min etching time. The similar trend goes for Ti2p and Cr2p spectra (Figure 6.9C and 6.9D). High resolution spectra showed no indication of the presence of both Ti and Cr before etching. Both spectra appeared with high intensity, after the surface had been etched.

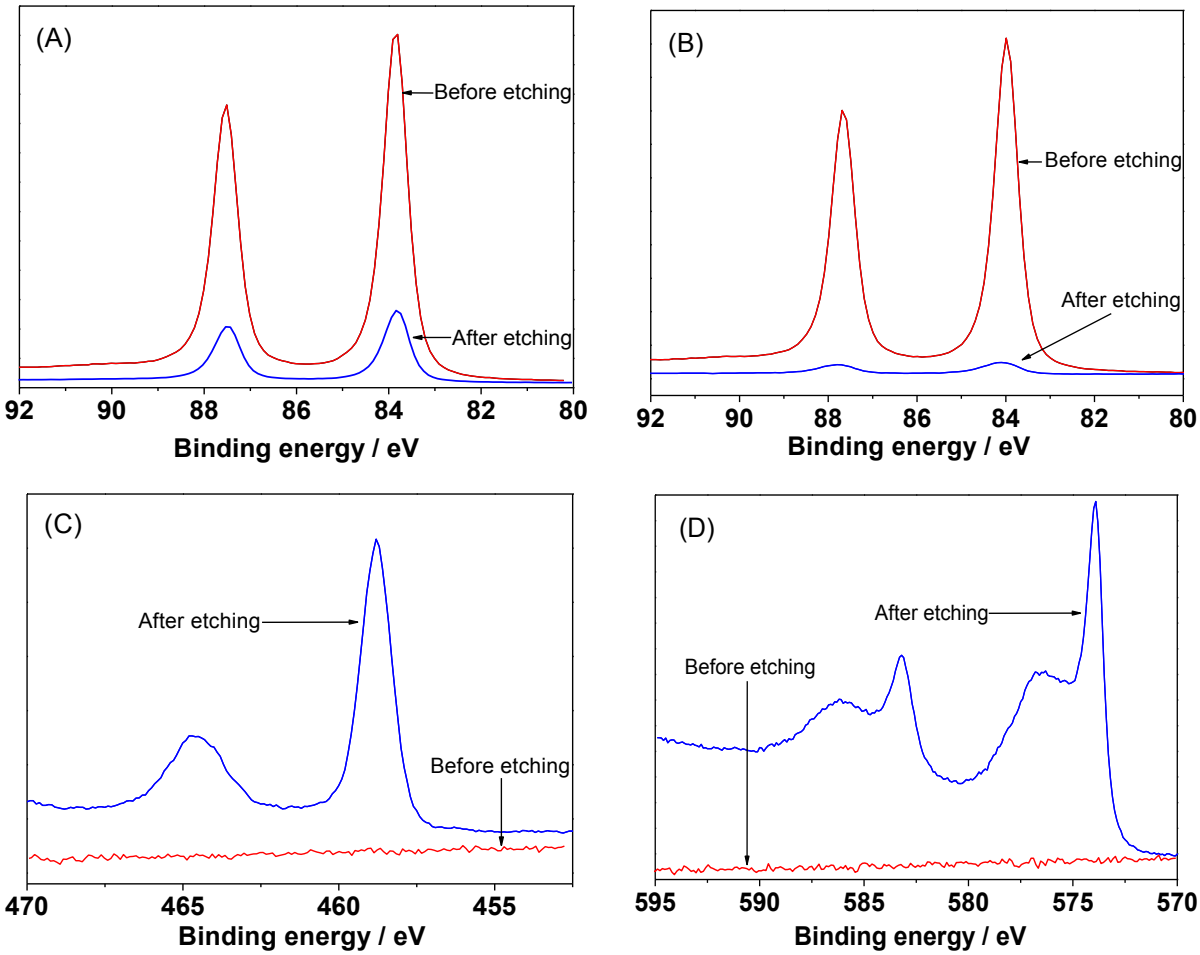

Figure 6.9 XPS spectra of gold film prepared on Ti and Cr layers, before and after etching. (A) High-resolution of Au4f spectrum for samples of Au on Ti. (B) High-resolution of Au4f spectrum for samples of Au on Cr. (C) Ti2p spectrum for samples of Au on Ti (D) Cr2p spectrum for samples of Au on Cr.

The contact angle in both Ti and Cr films obtained after gold etching was measured to be 18±4^{o}. The samples with Ti films were cleaned by treatment with cooled piranha solution (20 ^{o}C) for 5 min to remove the organic contamination from the surface, followed by washing several times with deionized water to remove the acid residue, and dried at 100 °C. The contact angle was found to be 17±3^{o}. The samples were immersed in a 5 mM BIBB-APTES in toluene for 24 h to form a SAM on TiO_2 surface, with contact angle of 71±4^{o}.

The samples with Cr layers were first oxidized by immersion into a cooled piranha solution for 5 min to create a film of Cr^{III} oxide. Hild et al found that the formation of silane SAMs depended on the reflux time and NaOH concentration in the ethanolic solution.[105] They

suggested that the silane SAMs reacted with CrO^- that generated from NaOH in the reflux solution. The samples were immersed into a 5 mM of BIBB-APTES solution in toluene for 2 days to yield silane SAMs initiator with contact angle of 62±4°. Figure 6.10 summarizes the change in the contact angle of both Ti and Cr after each step.

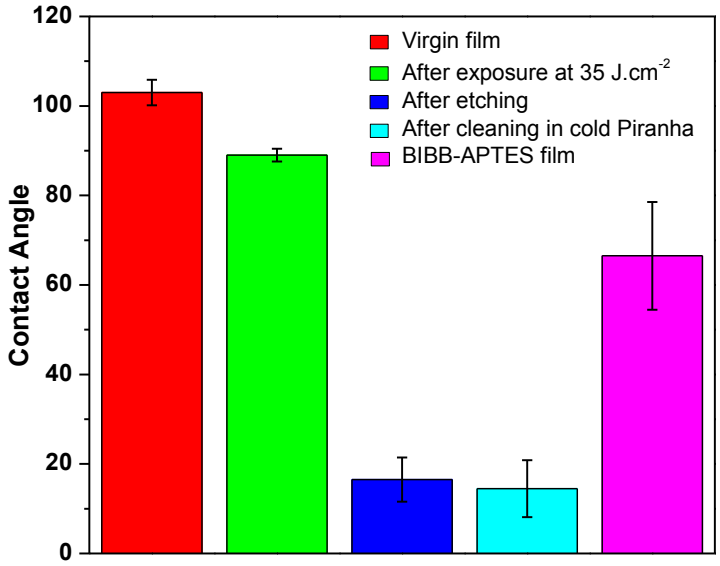

Figure 6.10 shows the change in the contact angle measurements during the initiation process of Ti and Cr surfaces.

High resolution C1s and Br3d spectra were acquired for Ti and Cr after etching and attachment of BIBB-APTES (Figure 6.11). The C1s core level spectra (Figure 6.11 (A) and (B)) were fitted using three components at binding energies of 285.0, 286.3 and 288.4 eV, corresponding to C-C, C-Br/C-NCO and O=C-N, respectively. The theoretical ratio of C-C: C-Br/C-NCO: O=C-N is 4:2:1 and the ratios obtained from the C1s spectrum were found to be 4.6:2:1 for the titania surface, and 4.9:2:1for a BIBB-APTES film on chromia. The Br3d spectra shown in Figure 6.11 (C and D) were resolved into two components at 70.3 and 71.3 eV, with relative intensities of 1.4:1, corresponding to $Br3d_{5/2}$ and $Br3d_{3/2}$, respectively. In B3d region for initiated Cr, a single peak in was observed at binding energy of 74.2 eV which is corresponding to Cr3s, see Figure 6.11 D.[392] From these results, it can be concluded that the BIBB-APTES initiator has been successfully immobilized on both Ti and Cr surfaces, after gold film had been etched. This is important for the effective polymerization of PCysMA.

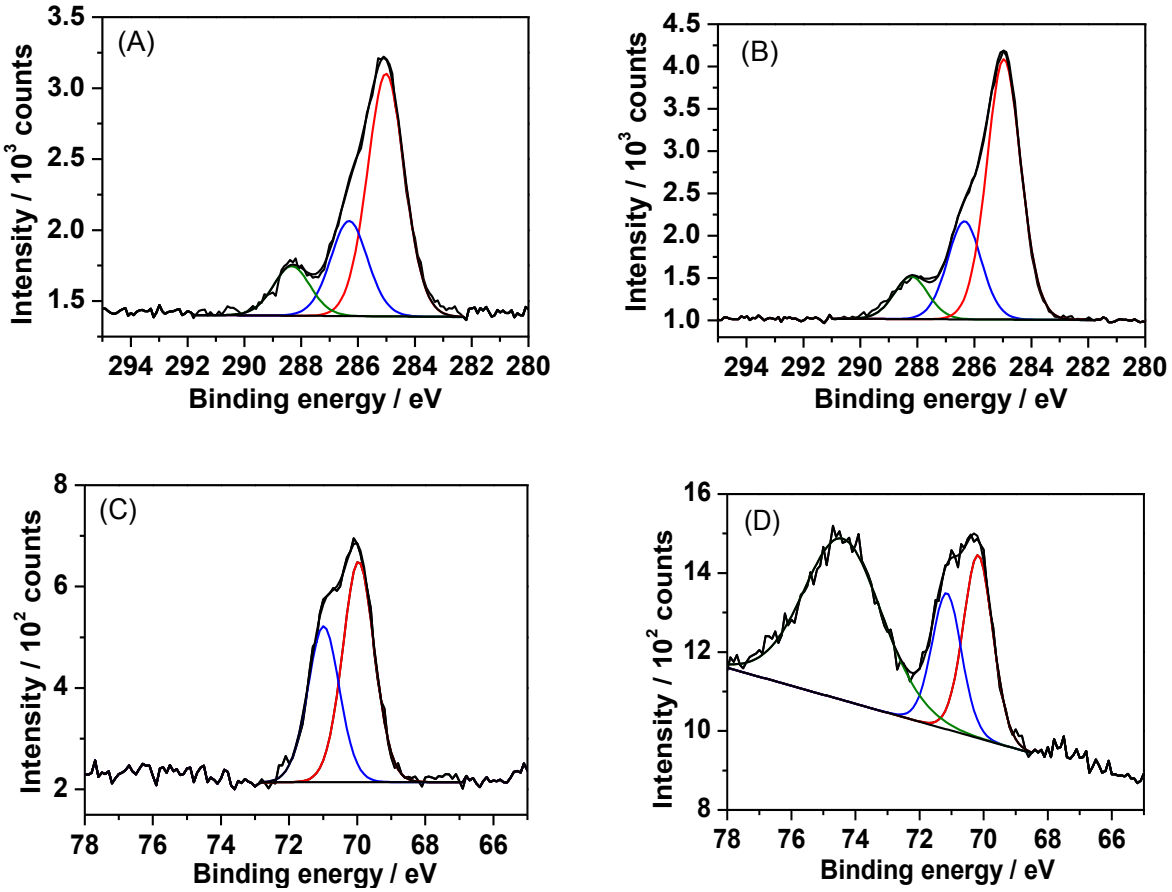

Figure 6.11 Narrow scan of XPS spectra of 2-bromo-2-methyl-N-(3-(triethoxysilyl) propyl) propanamide (BIBB-APTES) functionalized Ti and Cr surfaces. (A) C1s of BIBB-APETS on Ti , (B) C1s of BIBB-APETS on Cr, (C) Br3d of Ti functionalized with BIBB-APETS, and (D) Br3d of BIBB-APETS on Cr.

6.3.3 Growth of PCysMA brush from Ti and Cr surfaces

BIBB-APTES films on Ti and Cr obtained from etched samples were immersed in a polymerization solution, as described in section 4.2.3. XPS analysis was used to confirm the growth of PCysMA brushes on both surfaces. XPS data of PCysMA prepared on Ti and Cr was found to be consistent with the previous results in chapter 4. Figure 6.12 shows the C1s, N1s and S2p regions of the XPS spectra of PCysMA brush at high resolution. XPS C1s spectra were fitted using three components with binding energies of 285.0, 286.3 and 288.5 eV, which attributed to C−C, C−O/C−N and O=C−O, respectively. The C−C, C−O/C−N and O=C−O atomic ratios calculated were found to be close to the theoretical ratio of 2 : 1.3 : 1. The high resolution N1s spectrum recorded for these PCysMA brushes were fitted with two

components at binding energy of 399.0 eV and 401.5 eV, which correspond to C-NH_2 and C-NH_3^+ species. The S2p peak was fitted with two components with binding energies of 163.5 and 164.5 eV, were attributed to $S2p_{3/2}$ and $S2p_{1/2}$, respectively. The relative intensities of these components were 1.9 : 1.

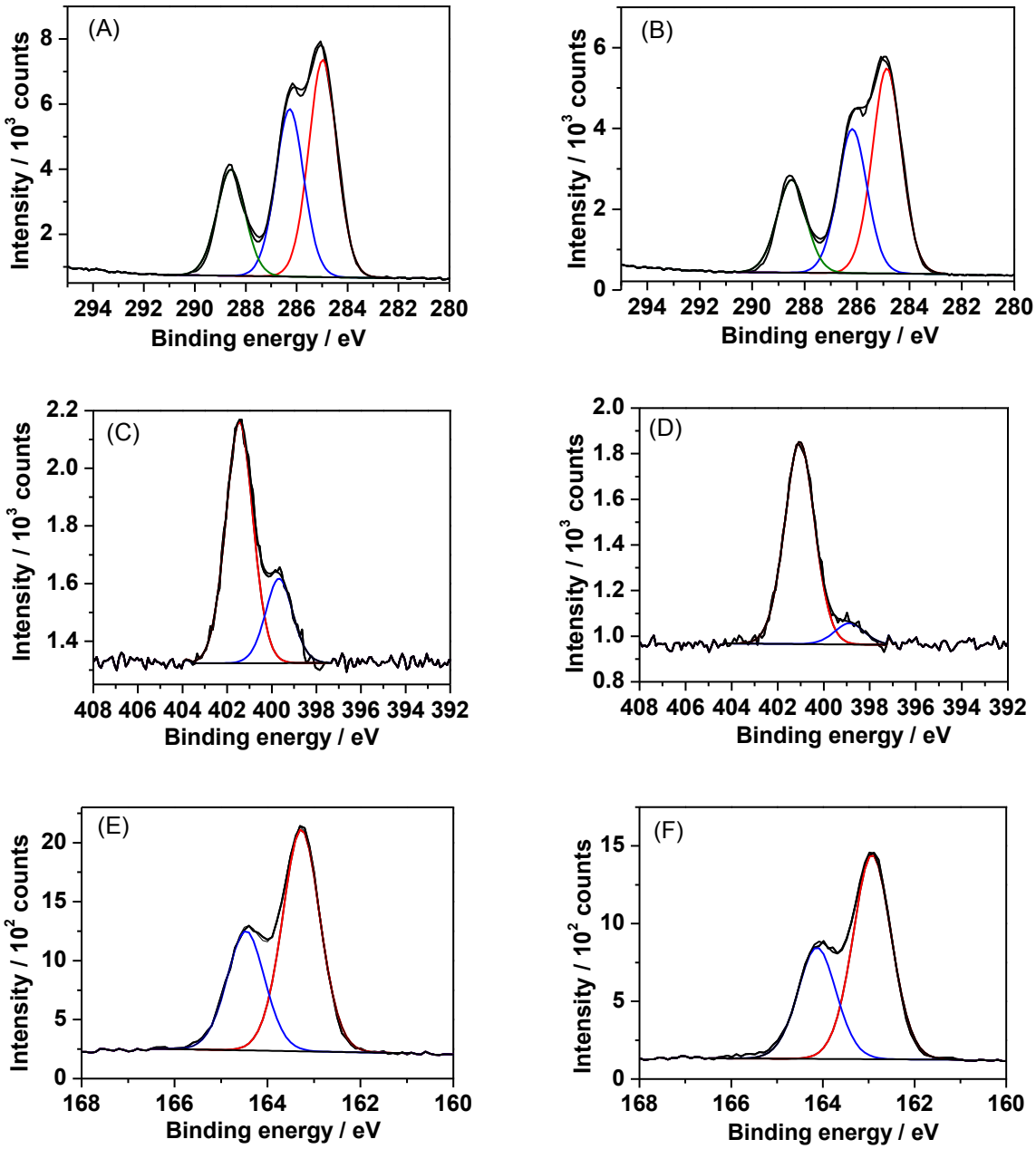

Figure 6.12 XPS high resolution spectra of PCysMA brush grown from Ti and Cr surfaces. (A) C1s of PCysMA on Ti, (B) C1s of PCysMA on Cr, (C) N1s of Ti modified PCysMA, (D) N1s of PCysMA on Cr, (E) S2p of Ti functionalized with PCysMA, and (F) S2p of PCysMA on Cr.

6.3.4 Synthesis of binary patterned gold / PCysMA brush

The preparation of binary patterned gold / PCysMA brush was achieved on both the micro- and the nano-scale. ODT monolayers on ca. 20 nm thick gold were patterned, through a mask or using IL, respectively, by exposing the samples to 35 J cm^{-2} or 25 J cm^{-2}, followed by dipping the samples into the etching solution for 20 min in micro-patterning or for 15 min in nano-patterning. After etching the samples were exposed again to UV light at 50 J cm^{-2} to oxidize unexposed ODT monolayers, then cleaned with cold Piranha solution to remove any contamination from the surface. Samples with adhesive layers of chromium were immersed in mixture of 10 mL ethanol and 1 mL of 1 mM NaOH at 60-70^{o}C. All samples were immersed into 2 mM solution of AHT for 18 h, to form gold functionalized with amine groups. The immobilization of BIBB-APTES initiators on both Ti and Cr regions have been achieved by immersing patterned samples into 5 mM of BIBB-APTES solution in toluene for 24 h. PCysMA brush were then grown from initiated regions to have a combination of gold and PCysMA brush surface.

Figure 6.13 shows AFM topographical images of a sample that had been etched for 20 min after exposing for 35 J.cm^{-2}, then PCysMA were grown from Ti initiated regions. The cross section of these images suggested that the difference in depth between etching area (squares) and the gold (bars) was measured to be ca. 16 nm. It is clear that the height difference between PCysMA brush grown from etched regions and gold surface was found between 3 nm and 5 nm. A similar experiment has been done using a sample with Cr as adhesive layer, as shown in Figure 6.14. The reduction in the height difference the squares and the bars proved the successful growth on PCysMA brush in fabricated regions.

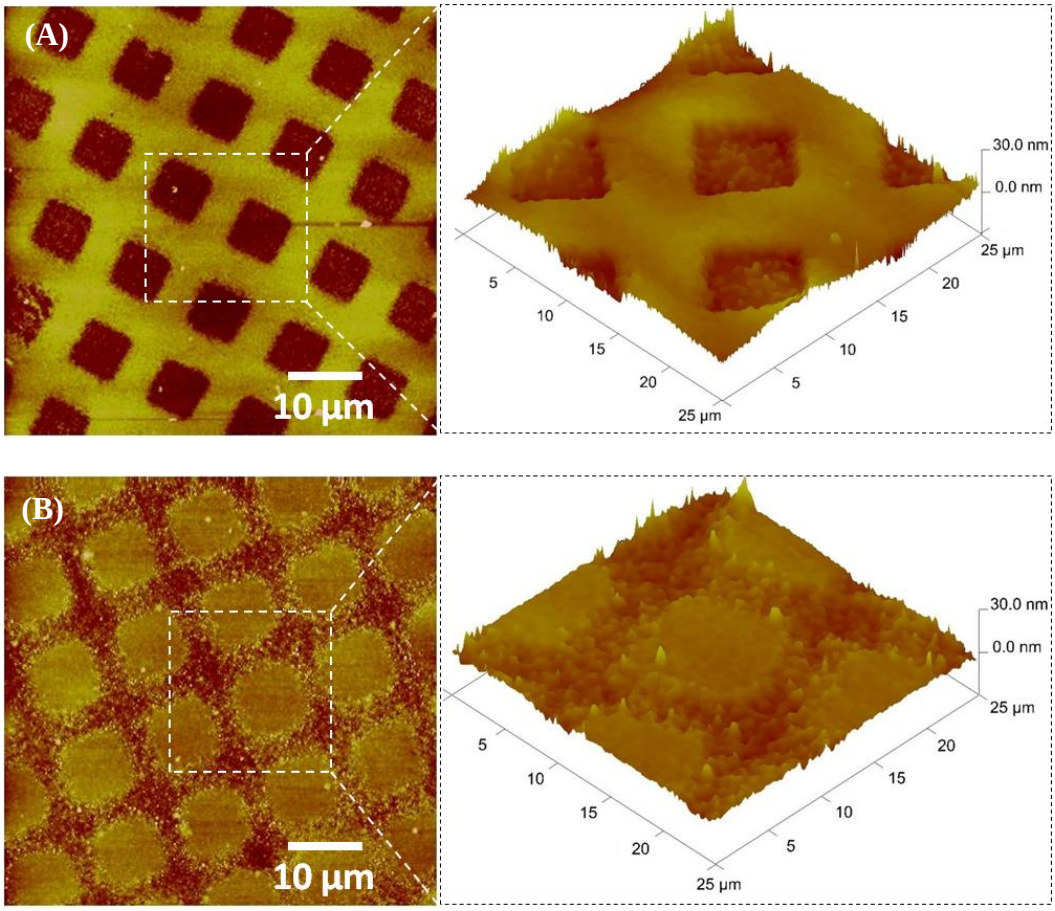

Figure 6.13 AFM tapping mode height images: (A) micro-structure of gold on Ti layer after etching for 20 min, (B) the same sample after immersion in PCysMA polymerization solution for 30 min. Images size 60x60µm^2, z-range 0 – 30 nm dark to bright.

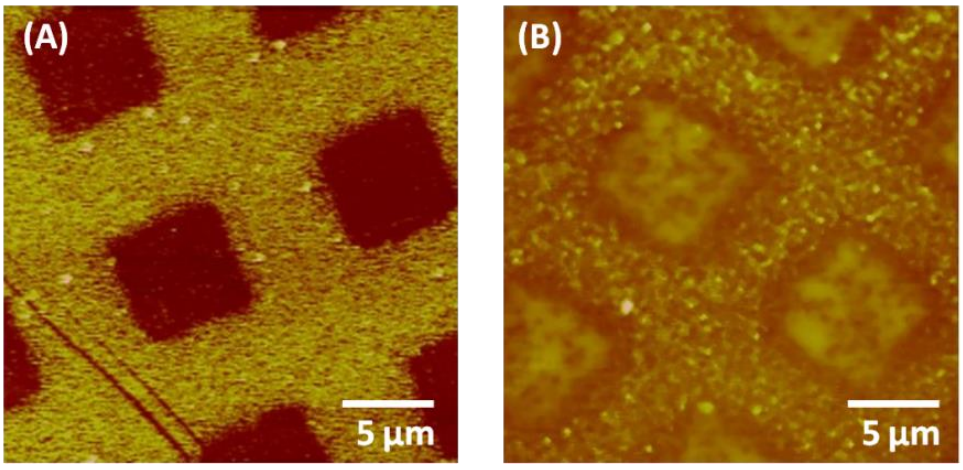

Figure 6.14 AFM height images: (A) micro-structure of gold on Cr layer after etching for 20 min, (B) similar sample after growth of PCysMA brush. Images size 25x25 µm^2, z-range 0 – 30 nm dark to bright.

The feasibility of fabricating nanopatterned gold/ PCysMA structures was examined. Figure 6.15 shows an ODT monolayer on gold film that has been patterned by IL at 10^{o} and etched for 15 min, before and after the growth of PCysMA brush. The cross section shows parallel lines with period 595 nm and the height of the lines were ca. 14.0 nm with FWHM of 310 nm , for the sample without PCysMA brush. There was a change in the height after the sample had been immersed in polymerization solution for 30 min. The height was ca. 2±1 nm with FWHM of 390±10 nm, which indicated the successful growth of PCysMA brush from etched areas.

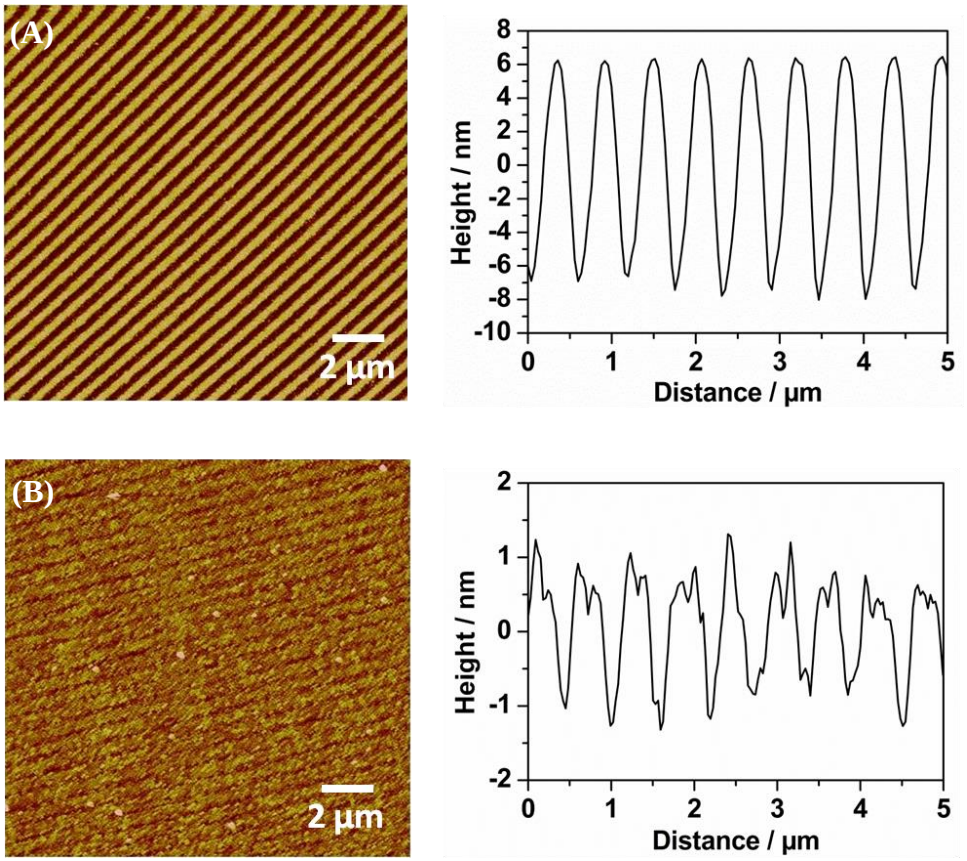

Figure 6.15 AFM topographical images and the cross section: (A) Au lines that were fabricated using IL at 10^{o} after immersing in the solution of MEA for 15 min. (B) The sample after exposing to PCysMA polymerization solution for min. Images size 15x15µm^2, z-range 0 – 30 nm dark to bright.

To further demonstrate the growth of PCysMA brush over nanodots, ODT SAMs were patterned using IL ($2\theta = 10^{o}$) and an angle of 90^{o} between the first and second exposures. The sample was etched and PCysMA brushes were grown from the areas between the dots, as

shown in Figure 6.16. The height of the gold nanodots was found to be ca. 19±2 nm and the FWHM was 300±20 nm with a period of 560±10 nm. After polymerization, the result was that the height difference between the tops of the nanodots and the troughs between them (PCysMA brush) was significantly reduced and measured to be less than 5 nm.

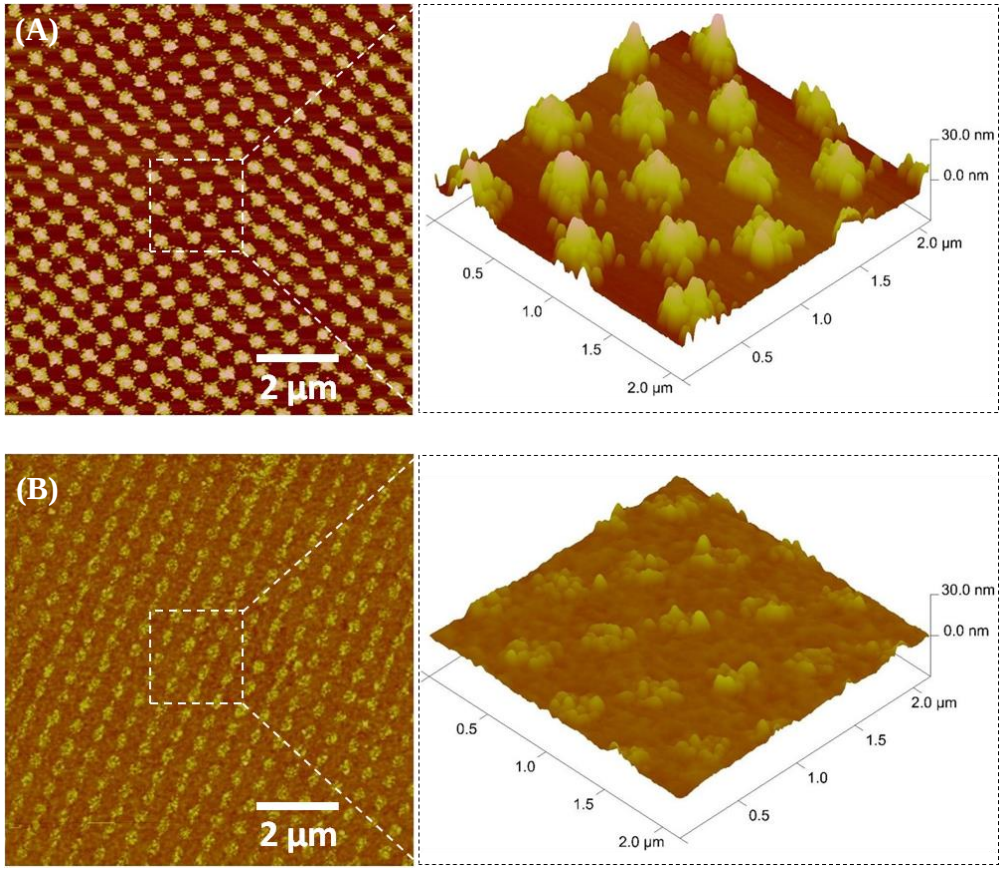

Figure 6.16 AFM height images recorded: (A) gold nanodots were fabricated orthogonal exposures using IL at 10^{o}, after immersing in the etching solution for 15 min. (B) Similar sample were exposed to PCysMA polymerization solution for min. Images size 10x10µm^2, z-range 0 – 30 nm dark to bright.

6.3.5 Formation of lipid bilayers on a binary patterned gold/PCysMA brushes

Micro-patterned binary gold/PCysMA brushes were prepared by photo-patterning ODT SAMs through a mask (1000 mesh grad), followed by etching the samples. The samples were exposed again to UV light at 50 J.cm^{-2}, then cleaned with cold Piranha solution, as described in section 6.3.4. All samples were immersed into 1 mM solution of ODT for 24 h. BIBB-APTES film was formed on Ti regions by immersing the substrates into 5 mM of BIBB-

APTES in toluene for 24 hours. PCysMA brushes were grown from initiated regions by submersion the samples into polymerization solution at conditions [CysMA]: [CuBr]: [$CuBr_2$]: [Bipy] with molar ratio of 30: 1.0 : 0.5 : 3, respectively, for 2h to yield 5-8 nm polymer thick.

The experiments of lipid bilayers formation was carried out in co-operation of Leeds University. The formation of lipids was studied using positively charged lipids of 25 mol % of DOTAP lipid in POPC in PBS, as discussed in Chapter 5. The sample was incubated in this mixture for 4 days. Figure 6.17 shows the FRAP images of binary micro-patterned gold/PCysMA brush before and after bleaching at 30 seconds and 15 min. These results illustrate that smooth lipid bilayers were formed on PCysMA brushes regions (squares) with no mobility, and no lipids attached to ODT SAMs (bars) were detected. However, no evidence of lipid diffusion was observed.

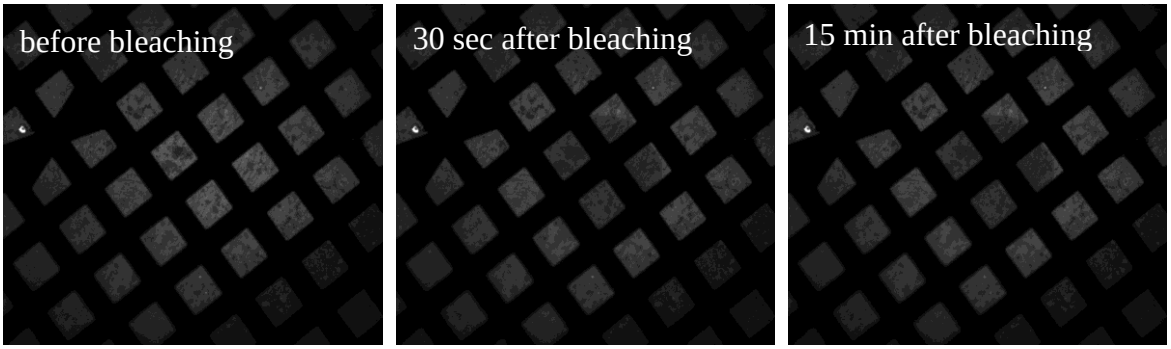

Figure 6.17 Shows FRAP images of binary patterned gold/PCysMA brushes before bleaching and at 30 seconds and 15 min after bleaching, using , DOTAP/POPC mixture with 1:4 molar ratio at 20 ^{o}C.

6.3.6 Protein attachment to patterned surfaces

Binary patterned gold / PCysMA brush was prepared as described in previous section 6.3.5. AHT was used instead of ODT to functionalise gold surface with amine groups. Then the samples immersed in FluoSphere NeutrAvidin-labeled microspheres 0.04 μm, yellow-green fluorescent (505/515), 1% solids solution to allow the protein to attach into gold surface, while the PCysMA resists the protein attachment. Microspheres are spherical latex particles in the colloidal size range of 40 nm that are formed from an amorphous polymer. FluoSpheres beads are made using high-quality, ultraclean polystyrene and are loaded with a

variety of dyes to create fluorescent beads. NeutrAvidin biotin-binding protein is a form of avidin, prepared to remove carbohydrates and lower the isoelectric point. Neutral protein is produced with less nonspecific binding than conventional avidin. Figure 6.18 shows the AFM height image of the sample after immersion into a 0.1M aqueous ammonium acetate solution containing 1 µg mL^{-1} NeutrAvidin nanoparticles. In the gold (bars), NeutrAvidin nanoparticles was expected to attach, while in the PCysMA brushes (squares) it would resist the attachment. The height of nanoparticles could thus be determined from the height difference measured from a line section. The data analysis suggested that the height of the nanoparticles attached to gold surface was between 30-50 nm heights, which is close to the size of the NeutrAvidin nanoparticles, which is 40 nm. As expected, the PCysMA brush in squares resisted the attachment of protein.

Confocal fluorescence images were obtained for patterned gold/PCysMA brush after attachment of NeutrAvidin nanoparticles, see Figure 6.19. Green fluorescence was observed from the bars regions, indicating that protein-coated nanoparticles were adsorbed in these areas. No fluorescence was detected from squares which suggest that PCysMA brush resists the protein adsorption.

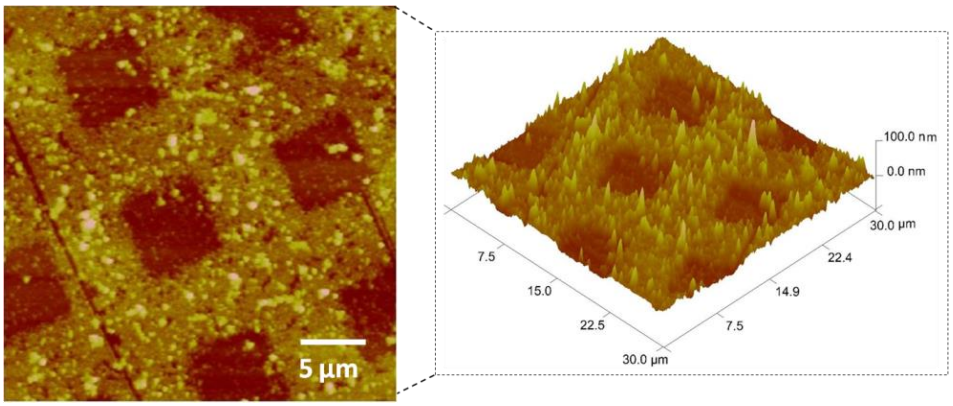

Figure 6.18 AFM height images of microstructure binary gold/PCysMA brushes after attachment of NeutrAvidin nanoparticles to the surface. Images size 30x30µm^2, z-range 0 – 100 nm dark to bright.

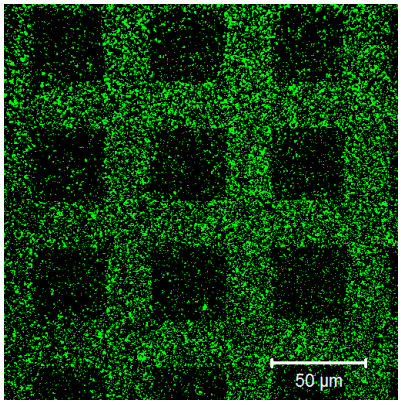

Figure 6.19 Confocal fluorescence images obtained for microstructure binary gold/PCysMA brushes after absorption of NeutrAvidin nanoparticles to the surface.

6.4 Conclusion

Thin films of gold have been prepared on titanium and chromium as adhesive layers. ODT SAMs were fully photo-oxidized at ca. 30 $J.cm^{-2}$, as judged by contact angle measurements. ODT monolayers on gold surface have been patterned by exposing the samples at ca. 35 $J.cm^{-2}$ through a photoresist mask and ca. 25 $J.cm^{-2}$ by a Lloyd's mirror two-beam interferometer. The etching process has been studied in both micro- and nanopatterned. Gold micro-structures were obtained after immersion of the samples into etching solution for 20 min, and gold nano-structures were obtained after 15 min etching time. XPS suggested that not all gold had been removed from the surface at these etching conditions. Silane films derivatised with a ATRP initiator (BIBB-APTES) have been formed on both titania and chromia surfaces, after the gold film had been etched, as confirmed by contact angle measurements and XPS. PCysMA brushes have been grown from BIBB-APTES functionalised Ti and Cr surfaces. The AFM height images showed the growth of PCysMA brushes from the oxide regions to yield patterned binary gold/PCysMA brush structures at both mico- and nanometre length scales. These structures were used for immobilization of NeutrAvidin nanoparticles on gold surface, and characterized with AFM and confocal microscopy.

Chapter 7: Conclusion and Future Work

In the present study, SI-ATRP has been used to grow variety of polymer brushes. The physical characterization of these brushes has been determined by various surface science techniques. Photolithography technique has been utilized to pattern the surfaces.

In chapter 3, the linear growth of ~ 28 nm PTBAEMA brushes has been achieved using surface-initiated ATRP, at 20^{o}C. Both micropatterned and nanopatterned PTBAEMA brushes have been prepared using either selected area UV laser irradiation or interferometric lithography, respectively. These pH-responsive weak polybase brushes can be crosslinked via their secondary amine groups using a commercially available polymeric diisocyanate crosslinker. If this reaction is conducted in a good solvent (THF), then relatively uniform crosslinking is achieved throughout the brush layer. On the other hand, if crosslinking is conducted using a bad solvent (*n*-hexane), then it is confined to the upper surface of the brush layer. The spatial location of the crosslinking profoundly affects the pH-responsive behavior of the PTBAEMA brush layer when immersed in acidic solution. The swollen protonated linear brush is four times thicker than the dry brush layer. In contrast, the THF-crosslinked brush can only swell to around 2.5 times the dry brush thickness, with the n-hexane-crosslinked brush exhibiting intermediate behavior. The difference between the pKa ^{bulk} and the pKa ^{surf} of PTBAEMA brush grown from planner surface was proved, although such behavior has been reported previously in several theoretical simulations and experimental results. The pKa ^{surf} of PTBAEMA brush was assessed to be ca. 7.7, comparing to what has been reported for pKa ^{bulk} (8.0). At this degree of cross-linking, the cross-linking process has not affect the pKa ^{surf}.

In chapter 4, cysteine methacrylate (CysMA), a new amino acid methacrylate monomer, was prepared via a facile thia-Michael addition reaction in aqueous solution. Novel zwitterionic PCysMA brushes were prepared using this monomer via SI-ATRP. The maximum brush thickness was found to be 27 nm. These brushes exhibit pH-responsive behavior, due to the presence of amino- and carboxylic groups. At low pH (pH < 1.7), the carboxylic and amino groups are protonated and the brushes become cationic and stretch away from the surface due to the strong electrostatic repulsion between adjacent chains. In contrast, at pH > 9.7 the brushes became anionic due to the de-protonation of both carboxylic and amino groups. At pH between 1.7 and 9.7, the brushes are zwitterionic and are not pH responsive. Surface zeta potential measurements indicate that at lower pH the PCysMA brushes acquire cationic

character, and at pH above 9, anionic character was observed, with zwitterionic character at intermediate pH. Modest brush swelling was observed in the addition of salt at pH 6. In contrast, the brush collapsed on salt addition at either pH 1.5 or pH 9.8. The UV photo-degradation of PCysMA brushes was also studied using XPS and AFM. XPS data showed that the exposure to light with a wavelength of 244 nm created aldehyde groups that could be derivatized with amines. Exposure of PCysMA brushes through a photomask yielded sharp, well-defined micro-patterns. Physical removal of material occurred during UV photo-degradation as revealed by AFM topographical images, with rate of removal of material of 0.8 nm cm^{-2}. Nano-structured PCysMA brushes were obtained using IL. It was found that non-exposed PCysMA brushes resisted the adsorption of protein whereas the exposed, photodegraded reigns exhibited extensive adsorption because protein molecules adsorption can covalently bind to the surface via aldehyde groups. Micro- and nano-scale protein patterns were fabricated and characterized using fluorescence microscopy. Excellent contrast was observed between modified and unmodified regions.

In chapter 5, a variety of conditions were used to control the growth of PKSPMA and PMETAC brushes. The change in the thickness of these brushes under PBS solutions was studied. The surface zeta potential of PMPC brushes at different pH was found to be ca. 0 ± 10 mV. The formation of lipid bilayers on PMPC, PKSPMA, PMETAC and PCysMA was studied using FRAP. Negative lipids formed bilayers on PMPC and PMETAC brushes, but the lipids exhibited very low mobility. Positive lipid bilayers formed on PKSPMA brushes, but exhibited very low mobility. On PCysMA brushes, however, a very good bilayers formed that exhibited relatively high mobility, comparable to that observed for supported lipids bilayers on glass.

In the final experiment chapter, SAMs of ODT on gold prepared on Ti and Cr have been photo-oxidized using UV light. The surfaces were successfully re-functionalized with AHT. ODT monolayers were patterned by exposing the sample through a mask and using a Lloyd's mirror two-beam interferometer, followed by etching to obtain, respectively, micro- and nanopatterned surfaces. It has been found that the optimum etching time was 20 min for micro-structure formation and 15 min for nano-structures. In the oxide regions formed by removal of gold, silane initiators have been successfully immobilized on both Ti and Cr surfaces. PCysMA brush has been grown from the functionalised oxide regions in both mico- and nano-patterned gold surfaces. AFM and confocal microscopy were used to characterize binary patterned gold/PCysMA brush after NeutrAvidin nanoparticles had been immobilized.

In future work, control of spatial location in surface derivatisation can be achieved through sequential chemical reactions via careful selection of the solvents. For example, amino-groups in polymer chains can be quaternised when they react with alkyl halides. When a good solvent for the polymer is used, the quantization reaction should occur throughout the swollen brush layer. In a poor solvent the reaction leads to quaternisation of just the upper surface of the collapsed brush.

The pH-responsivity of the new PCysMA brush may be useful for certain applications. One possible application is the modification of mesoporous materials with PCysMA brushes to modulate ionic transport, depending on the pH, as described by Azzaroni and co-workers.[336-337] A second potential application for such brushes is the reversible adsorption and desorption of nanoparticles or proteins via pH modulation, as described by Jiang and co-workers.[428]

The effects of the binary patterned gold nanodots/PCysMA brush on their optical properties could be monitored by spectrophotometry. The binary patterned surfaces consisting of gold nanodots and PCysMA brushes may be utilized as label-free LSPR biosensors for proteins. Also, these structures may be suitable for surface enhanced Raman spectroscopy. The formation of lipid bilayers on these structures can also be investigated, and feasibility of attaching two light harvesting proteins (LH1 and LH2) in order to make spectroscopic measurements may be tested.

References

(1) Love, J. C.; Estroff, L. A.; Kriebel, J. K.; Nuzzo, R. G.; Whitesides, G. M. *Chemical reviews* **2005**, *105*, 1103.
(2) Ulman, A. *Chemical reviews* **1996**, *96*, 1533.
(3) Senaratne, W.; Andruzzi, L.; Ober, C. K. *Biomacromolecules* **2005**, *6*, 2427.
(4) Ferretti, S.; Paynter, S.; Russell, D. A.; Sapsford, K. E.; Richardson, D. J. *TrAC Trends in Analytical Chemistry* **2000**, *19*, 530.
(5) Laibinis, P. E.; Whitesides, G. M.; Allara, D. L.; Tao, Y. T.; Parikh, A. N.; Nuzzo, R. G. *Journal of the American Chemical Society* **1991**, *113*, 7152.
(6) Nuzzo, R. G.; Allara, D. L. *Journal of the American Chemical Society* **1983**, *105*, 4481.
(7) Vuillaume, D.; Boulas, C.; Collet, J.; Davidovits, J.; Rondelez, F. *Applied physics letters* **1996**, *69*, 1646.
(8) Faucheux, N.; Schweiss, R.; Lützow, K.; Werner, C.; Groth, T. *Biomaterials* **2004**, *25*, 2721.
(9) Ostuni, E.; Chapman, R. G.; Liang, M. N.; Meluleni, G.; Pier, G.; Ingber, D. E.; Whitesides, G. M. *Langmuir* **2001**, *17*, 6336.
(10) Li, Y.-S.; Wang, Y.; Tran, T.; Perkins, A. *Spectrochimica Acta Part A: Molecular and Biomolecular Spectroscopy* **2005**, *61*, 3032.
(11) Bain, C. D.; Whitesides, G. M. *Journal of the American Chemical Society* **1988**, *110*, 3665.
(12) Kapur, R.; Rudolph, A. S. *Experimental cell research* **1998**, *244*, 275.
(13) Xia, Y.; Zhao, X.-M.; Kim, E.; Whitesides, G. M. *Chemistry of materials* **1995**, *7*, 2332.
(14) Xia, Y.; Rogers, J. A.; Paul, K. E.; Whitesides, G. M. *Chemical Reviews* **1999**, *99*, 1823.
(15) Krämer, S.; Fuierer, R. R.; Gorman, C. B. *Chemical reviews* **2003**, *103*, 4367.
(16) Bain, C. D.; Whitesides, G. M. *Journal of the American Chemical Society* **1988**, *110*, 6560.
(17) Sellers, H.; Ulman, A.; Shnidman, Y.; Eilers, J. E. *Journal of the American Chemical Society* **1993**, *115*, 9389.
(18) Laibinis, P. E.; Whitesides, G. M. *Journal of the American Chemical Society* **1992**, *114*, 9022.
(19) Love, J. C.; Wolfe, D. B.; Haasch, R.; Chabinyc, M. L.; Paul, K. E.; Whitesides, G. M.; Nuzzo, R. G. *Journal of the American Chemical Society* **2003**, *125*, 2597.
(20) Manolova, M.; Ivanova, V.; Kolb, D.; Boyen, H.-G.; Ziemann, P.; Büttner, M.; Romanyuk, A.; Oelhafen, P. *Surface science* **2005**, *590*, 146.
(21) Mekhalif, Z.; Laffineur, F.; Couturier, N.; Delhalle, J. *Langmuir* **2003**, *19*, 637.
(22) Schlesinger, M.; Paunovic, M. *Modern electroplating*; John Wiley & Sons, 2011; Vol. 55.
(23) Dubois, L. H.; Zegarski, B. R.; Nuzzo, R. G. *The Journal of chemical physics* **1993**, *98*, 678.
(24) Bain, C. D.; Troughton, E. B.; Tao, Y. T.; Evall, J.; Whitesides, G. M.; Nuzzo, R. G. *Journal of the American Chemical Society* **1989**, *111*, 321.
(25) Lee, N.-S.; Kang, H.; Ito, E.; Hara, M.; Noh, J. *Bulletin of the Korean Chemical Society* **2010**, *31*, 2137.
(26) Schwartz, D. K. *Annual Review of Physical Chemistry* **2001**, *52*, 107.
(27) Yamada, R.; Wano, H.; Uosaki, K. *Langmuir* **2000**, *16*, 5523.
(28) Bensebaa, F.; Voicu, R.; Huron, L.; Ellis, T. H.; Kruus, E. *Langmuir* **1997**, *13*, 5335.
(29) Kawasaki, M.; Sato, T.; Tanaka, T.; Takao, K. *Langmuir* **2000**, *16*, 1719.
(30) Haensch, C.; Hoeppener, S.; Schubert, U. S. *Chemical Society Reviews* **2010**, *39*, 2323.
(31) Waddell, T. G.; Leyden, D. E.; DeBello, M. T. *Journal of the American Chemical Society* **1981**, *103*, 5303.
(32) Wang, Y.; Lieberman, M. *Langmuir* **2003**, *19*, 1159.
(33) Wang, M.; Liechti, K. M.; Wang, Q.; White, J. *Langmuir* **2005**, *21*, 1848.
(34) Fiorilli, S.; Rivolo, P.; Descrovi, E.; Ricciardi, C.; Pasquardini, L.; Lunelli, L.; Vanzetti, L.; Pederzolli, C.; Onida, B.; Garrone, E. *Journal of colloid and interface science* **2008**, *321*, 235.
(35) Silberzan, P.; Leger, L.; Ausserre, D.; Benattar, J. *Langmuir* **1991**, *7*, 1647.

(36) Cras, J.; Rowe-Taitt, C.; Nivens, D.; Ligler, F. *Biosensors and Bioelectronics* **1999**, *14*, 683.
(37) Vandenberg, E. T.; Bertilsson, L.; Liedberg, B.; Uvdal, K.; Erlandsson, R.; Elwing, H.; Lundström, I. *Journal of colloid and interface science* **1991**, *147*, 103.
(38) Zhang, F.; Srinivasan, M. *Langmuir* **2004**, *20*, 2309.
(39) Angst, D. L.; Simmons, G. W. *Langmuir* **1991**, *7*, 2236.
(40) Le Grange, J.; Markham, J.; Kurkjian, C. *Langmuir* **1993**, *9*, 1749.
(41) McGovern, M. E.; Kallury, K. M.; Thompson, M. *Langmuir* **1994**, *10*, 3607.
(42) Rozlosnik, N.; Gerstenberg, M. C.; Larsen, N. B. *Langmuir* **2003**, *19*, 1182.
(43) Brzoska, J.; Azouz, I. B.; Rondelez, F. *Langmuir* **1994**, *10*, 4367.
(44) Ohtake, T.; Mino, N.; Ogawa, K. *Langmuir* **1992**, *8*, 2081.
(45) Almeida, A.; Salvadori, M.; Petri, D. *Langmuir* **2002**, *18*, 6914.
(46) Sugimura, H.; Nakagiri, N. *Journal of the American Chemical Society* **1997**, *119*, 9226.
(47) Zhu, M.; Lerum, M. Z.; Chen, W. *Langmuir* **2011**, *28*, 416.
(48) Asenath Smith, E.; Chen, W. *Langmuir* **2008**, *24*, 12405.
(49) Aissaoui, N.; Bergaoui, L.; Landoulsi, J.; Lambert, J.-F.; Boujday, S. *Langmuir* **2011**, *28*, 656.
(50) Fadeev, A. Y.; McCarthy, T. J. *Langmuir* **2000**, *16*, 7268.
(51) Siqueira Petri, D. F.; Wenz, G.; Schunk, P.; Schimmel, T. *Langmuir* **1999**, *15*, 4520.
(52) Zhang, Z.; Hu, R.; Liu, Z. *Langmuir* **2000**, *16*, 1158.
(53) Heid, S.; Effenberger, F.; Bierbaum, K.; Grunze, M. *Langmuir* **1996**, *12*, 2118.
(54) White, L.; Tripp, C. *Journal of colloid and interface science* **2000**, *232*, 400.
(55) Schick, G. A.; Sun, Z. *Langmuir* **1994**, *10*, 3105.
(56) Advincula, R. C.; Brittain, W. J.; Caster, K. C.; Rühe, J. *Polymer brushes*; Wiley Online Library, 2004.
(57) Barbey, R.; Lavanant, L.; Paripovic, D.; Schüwer, N.; Sugnaux, C.; Tugulu, S.; Klok, H. A. *Chemical Reviews* **2009**, *109*, 5437.
(58) Ayres, N. *Polymer Chemistry* **2010**, *1*, 769.
(59) Orski, S. V.; Fries, K. H.; Sontag, S. K.; Locklin, J. *Journal of Materials Chemistry* **2011**, *21*, 14135.
(60) Yu, B.; Zheng, Z. J.; Li, Y.; Zhou, F. *Journal of Fiber Bioengineering and Informatics* **2009**, *1*, 249.
(61) Zhou, X.; Liu, X.; Xie, Z.; Zheng, Z. *Nanoscale* **2011**, *3*, 4929.
(62) Chen, T.; Ferris, R.; Zhang, J.; Ducker, R.; Zauscher, S. *Progress in Polymer Science* **2010**, *35*, 94.
(63) Lee, H.; Pietrasik, J.; Sheiko, S. S.; Matyjaszewski, K. *Progress in Polymer Science* **2010**, *35*, 24.
(64) Zhao, B.; Brittain, W. J. *Progress in Polymer Science* **2000**, *25*, 677.
(65) Minko, S. *Journal of Macromolecular Science, Part C: Polymer Reviews* **2006**, *46*, 397.
(66) Tran, Y.; Auroy, P. *Journal of the American Chemical Society* **2001**, *123*, 3644.
(67) Sumerlin, B. S.; Lowe, A. B.; Stroud, P. A.; Zhang, P.; Marek, W.; McCormick, C. L. *Langmuir* **2003**, *19*, 5559.
(68) Papra, A.; Gadegaard, N.; Larsen, N. B. *Langmuir* **2001**, *17*, 1457.
(69) Luzinov, I.; Julthongpiput, D.; Malz, H.; Pionteck, J.; Tsukruk, V. V. *Macromolecules* **2000**, *33*, 1043.
(70) Edmondson, S.; Osborne, V. L.; Huck, W. T. *Chemical society reviews* **2004**, *33*, 14.
(71) Bünsow, J.; Kelby, T. S.; Huck, W. T. S. *Accounts of chemical research* **2009**, *43*, 466.
(72) Wang, Y. P.; Pei, X. W.; He, X. Y.; Lei, Z. Q. *European polymer journal* **2005**, *41*, 737.
(73) Fristrup, C. J.; Jankova, K.; Hvilsted, S. *Soft Matter* **2009**, *5*, 4623.
(74) Pyun, J.; Kowalewski, T.; Matyjaszewski, K. *Macromolecular Rapid Communications* **2003**, *24*, 1043.
(75) Hawker, C. J. *Accounts of chemical research* **1997**, *30*, 373.
(76) Hawker, C. J.; Bosman, A. W.; Harth, E. *Chemical Reviews* **2001**, *101*, 3661.
(77) Jordan, R.; Ulman, A.; Kang, J. F.; Rafailovich, M. H.; Sokolov, J. *Journal of the American Chemical Society* **1999**, *121*, 1016.

(78) Baum, M.; Brittain, W. J. *Macromolecules* **2002**, *35*, 610.
(79) Husseman, M.; Malmström, E. E.; McNamara, M.; Mate, M.; Mecerreyes, D.; Benoit, D. G.; Hedrick, J. L.; Mansky, P.; Huang, E.; Russell, T. P. *Macromolecules* **1999**, *32*, 1424.
(80) Wang, J. S.; Matyjaszewski, K. *Journal of the American Chemical Society* **1995**, *117*, 5614.
(81) Matyjaszewski, K.; Xia, J. *Chemical Reviews* **2001**, *101*, 2921.
(82) Tsarevsky, N. V.; Braunecker, W. A.; Matyjaszewski, K. *Journal of organometallic chemistry* **2007**, *692*, 3212.
(83) Zhao, Y.; Wang, L.; Xiao, A.; Yu, H. *Progress in Polymer Science* **2010**, *35*, 1195.
(84) Braunecker, W. A.; Matyjaszewski, K. *Journal of Molecular Catalysis A: Chemical* **2006**, *254*, 155.
(85) Xiao, D.; Wirth, M. J. *Macromolecules* **2002**, *35*, 2919.
(86) Matyjaszewski, K. *Current Opinion in Solid State and Materials Science* **1996**, *1*, 769.
(87) Patten, T. E.; Matyjaszewski, K. *Accounts of chemical research* **1999**, *32*, 895.
(88) Wang, J. S.; Matyjaszewski, K. *Macromolecules* **1995**, *28*, 7901.
(89) Matyjaszewski, K.; Shipp, D. A.; Wang, J. L.; Grimaud, T.; Patten, T. E. *Macromolecules* **1998**, *31*, 6836.
(90) Patten, T. E.; Matyjaszewski, K. *Advanced Materials* **1998**, *10*, 901.
(91) Pintauer, T.; Matyjaszewski, K. *Coordination chemistry reviews* **2005**, *249*, 1155.
(92) Xu, F.; Neoh, K.; Kang, E. *Progress in Polymer Science* **2009**, *34*, 719.
(93) Edmondson, S.; Osborne, V. L.; Huck, W. T. S. *Chemcal Society Reviews* **2003**, *33*, 14.
(94) Ma, H.; Textor, M.; Clark, R. L.; Chilkoti, A. *Biointerphases* **2006**, *1*, 35.
(95) Ayres, N.; Boyes, S. G.; Brittain, W. J. *Langmuir* **2007**, *23*, 182.
(96) Matyjaszewski, K.; Miller, P. J.; Shukla, N.; Immaraporn, B.; Gelman, A.; Luokala, B. B.; Siclovan, T. M.; Kickelbick, G.; Vallant, T.; Hoffmann, H. *Macromolecules* **1999**, *32*, 8716.
(97) Topham, P. D.; Howse, J. R.; Crook, C. J.; Parnell, A. J.; Geoghegan, M.; Jones, R. A.; Ryan, A. J. *Polymer International* **2006**, *55*, 808.
(98) Kitano, H.; Kondo, T.; Suzuki, H.; Ohno, K. *Journal of colloid and interface science* **2010**, *345*, 325.
(99) Ell, J. R.; Mulder, D. E.; Faller, R.; Patten, T. E.; Kuhl, T. L. *Macromolecules* **2009**, *42*, 9523.
(100) Edmondson, S.; Armes, S. P. *Polymer International* **2009**, *58*, 307.
(101) Marsh, A.; Khan, A.; Garcia, M.; Haddleton, D. M. *Chem. Commun.* **2000**, 2083.
(102) Ma, H.; Li, D.; Sheng, X.; Zhao, B.; Chilkoti, A. *Langmuir* **2006**, *22*, 3751.
(103) Raynor, J. E.; Petrie, T. A.; García, A. J.; Collard, D. M. *Advanced Materials* **2007**, *19*, 1724.
(104) Kang, S. M.; Kong, B.; Oh, E.; Choi, J. S.; Choi, I. S. *Colloids and Surfaces B: Biointerfaces* **2010**, *75*, 385.
(105) Hild, R.; David, C.; Müller, H.; Völkel, B.; Kayser, D.; Grunze, M. *Langmuir* **1998**, *14*, 342.
(106) Zhao, C.; Li, L.; Zheng, J. *Langmuir* **2010**, *26*, 17375.
(107) Zhao, C.; Li, L.; Wang, Q.; Yu, Q.; Zheng, J. *Langmuir* **2011**, *27*, 4906.
(108) Li, G.; Xue, H.; Cheng, G.; Chen, S.; Zhang, F.; Jiang, S. *The Journal of Physical Chemistry B* **2008**, *112*, 15269.
(109) Adams, D. J.; Young, I. *Journal of Polymer Science Part A: Polymer Chemistry* **2008**, *46*, 6082.
(110) Adams, D. J.; Butler, M. F.; Weaver, A. C. *Langmuir* **2006**, *22*, 4534.
(111) Broyer, R. M.; Quaker, G. M.; Maynard, H. D. *Journal of the American Chemical Society* **2008**, *130*, 1041.
(112) Couet, J.; Biesalski, M. *Soft Matter* **2006**, *2*, 1005.
(113) Teodorescu, M.; Matyjaszewski, K. *Macromolecules* **1999**, *32*, 4826.
(114) Limer, A.; Haddleton, D. M. *Macromolecules* **2006**, *39*, 1353.
(115) Li, Y.; Tang, Y.; Narain, R.; Lewis, A. L.; Armes, S. P. *Langmuir* **2005**, *21*, 9946.
(116) Teodorescu, M. *Macromolecular rapid communications* **2000**, *21*, 190.
(117) Brown, A. A.; Khan, N. S.; Steinbock, L.; Huck, W. T. *European polymer journal* **2005**, *41*, 1757.
(118) Ejaz, M.; Yamamoto, S.; Ohno, K.; Tsujii, Y.; Fukuda, T. *Macromolecules* **1998**, *31*, 5934.

(119) Wang, X.-S.; Jackson, R.; Armes, S. *Macromolecules* **2000**, *33*, 255.
(120) Perruchot, C.; Khan, M.; Kamitsi, A.; Armes, S. v.; Von Werne, T.; Patten, T. *Langmuir* **2001**, *17*, 4479.
(121) Wang, X.-S.; Armes, S. *Macromolecules* **2000**, *33*, 6640.
(122) Robinson, K.; Khan, M.; de Paz Banez, M.; Wang, X.; Armes, S. *Macromolecules* **2001**, *34*, 3155.
(123) Jones, D. M.; Huck, W. T. *Advanced Materials* **2001**, *13*, 1256.
(124) Huang, W.; Kim, J.-B.; Bruening, M. L.; Baker, G. L. *Macromolecules* **2002**, *35*, 1175.
(125) Kim, J.-B.; Bruening, M. L.; Baker, G. L. *Journal of the American Chemical Society* **2000**, *122*, 7616.
(126) Feng, W.; Chen, R.; Brash, J. L.; Zhu, S. *Macromolecular rapid communications* **2005**, *26*, 1383.
(127) Feng, W.; Nieh, M.-P.; Zhu, S.; Harroun, T. A.; Katsaras, J.; Brash, J. L. *Biointerphases* **2007**, *2*, 34.
(128) Lego, B.; François, M.; Skene, W.; Giasson, S. *Langmuir* **2009**, *25*, 5313.
(129) Yamamoto, K.; Miwa, Y.; Tanaka, H.; Sakaguchi, M.; Shimada, S. *Journal of Polymer Science Part A: Polymer Chemistry* **2002**, *40*, 3350.
(130) Wu, T.; Efimenko, K.; Genzer, J. *Journal of the American Chemical Society* **2002**, *124*, 9394.
(131) Jones, D. M.; Brown, A. A.; Huck, W. T. *Langmuir* **2002**, *18*, 1265.
(132) Halperin, A.; Tirrell, M.; Lodge, T. *Macromolecules: Synthesis, Order and Advanced Properties* **1992**, 31.
(133) Chen, J. K.; Hsieh, C. Y.; Huang, C. F.; Li, P. M.; Kuo, S. W.; Chang, F. C. *Macromolecules* **2008**, *41*, 8729.
(134) Aoki, H.; Kitamura, M.; Ito, S. *Macromolecules* **2008**, *41*, 285.
(135) Rowe, M. D.; Hammer, B. A. G.; Boyes, S. G. *Macromolecules* **2008**, *41*, 4147.
(136) Huang, W.; Kim, J.-B.; Baker, G. L.; Bruening, M. L. *Nanotechnology* **2003**, *14*, 1075.
(137) Yu, K.; Wang, H.; Han, Y. *Langmuir* **2007**, *23*, 8957.
(138) Dai, S.; Ravi, P.; Tam, K. C. *Soft Matter* **2008**, *4*, 435.
(139) Cheng, N.; Brown, A. A.; Azzaroni, O.; Huck, W. T. *Macromolecules* **2008**, *41*, 6317.
(140) Currie, E.; Sieval, A.; Fleer, G.; Stuart, M. C. *Langmuir* **2000**, *16*, 8324.
(141) Treat, N. D.; Ayres, N.; Boyes, S. G.; Brittain, W. J. *Macromolecules* **2006**, *39*, 26.
(142) Sanjuan, S.; Perrin, P.; Pantoustier, N.; Tran, Y. *Langmuir* **2007**, *23*, 5769.
(143) Neil, D.; Ayres, N.; Boyes, S. G.; Brittain, W. J. *Macromolecules* **2006**, *39*, 26.
(144) Wu, T.; Genzer, J.; Gong, P.; Szleifer, I.; Vlček, P.; Šubr, V. *Polymer Brushes* **2004**, 287.
(145) Jia, H.; Wildes, A.; Titmuss, S. *Macromolecules* **2011**, *45*, 305.
(146) Moglianetti, M.; Webster, J. R.; Edmondson, S.; Armes, S. P.; Titmuss, S. *Langmuir* **2010**, *26*, 12684.
(147) Geoghegan, M.; Ruiz-Pérez, L.; Dang, C. C.; Parnell, A. J.; Martin, S. J.; Howse, J. R.; Jones, R. A.; Golestanian, R.; Topham, P. D.; Crook, C. J. *Soft Matter* **2006**, *2*, 1076.
(148) Xu, Y.; Bolisetty, S.; Drechsler, M.; Fang, B.; Yuan, J.; Ballauff, M.; Müller, A. H. *Polymer* **2008**, *49*, 3957.
(149) Biesalski, M.; Johannsmann, D.; Rühe, J. *The Journal of chemical physics* **2004**, *120*, 8807.
(150) Azzaroni, O.; Moya, S.; Farhan, T.; Brown, A. A.; Huck, W. T. *Macromolecules* **2005**, *38*, 10192.
(151) Azzaroni, O.; Moya, S. E.; Brown, A. A.; Zheng, Z.; Donath, E.; Huck, W. T. *Advanced Functional Materials* **2006**, *16*, 1037.
(152) Lowe, A. B.; McCormick, C. L. *Chemical reviews* **2002**, *102*, 4177.
(153) Ladd, J.; Zhang, Z.; Chen, S.; Hower, J. C.; Jiang, S. *Biomacromolecules* **2008**, *9*, 1357.
(154) Santonicola, M. G.; Memesa, M.; Meszyńska, A.; Ma, Y.; Vancso, G. J. *Soft Matter* **2012**, *8*, 1556.
(155) Liu, Q.; Singh, A.; Liu, L. *Biomacromolecules* **2012**, *14*, 226.
(156) Feng, W.; Zhu, S.; Ishihara, K.; Brash, J. L. *Langmuir* **2005**, *21*, 5980.

(157) Feng, W.; Brash, J. L.; Zhu, S. *Biomaterials* **2006**, *27*, 847.
(158) Wu, J.; Lin, W.; Wang, Z.; Chen, S.; Chang, Y. *Langmuir* **2012**, *28*, 7436.
(159) Lalani, R.; Liu, L. *Biomacromolecules* **2012**, *13*, 1853.
(160) Jiang, S.; Cao, Z. *Advanced Materials* **2010**, *22*, 920.
(161) Zhang, Z.; Chao, T.; Chen, S.; Jiang, S. *Langmuir* **2006**, *22*, 10072.
(162) Yang, W.; Zhang, L.; Wang, S.; White, A. D.; Jiang, S. *Biomaterials* **2009**, *30*, 5617.
(163) Chen, M.; Briscoe, W. H.; Armes, S. P.; Klein, J. *Science* **2009**, *323*, 1698.
(164) Iwata, R.; Suk-In, P.; Hoven, V. P.; Takahara, A.; Akiyoshi, K.; Iwasaki, Y. *Biomacromolecules* **2004**, *5*, 2308.
(165) Edmondson, S.; Nguyen, N. T.; Lewis, A. L.; Armes, S. P. *Langmuir* **2010**, *26*, 7216.
(166) Kobayashi, M.; Terayama, Y.; Kikuchi, M.; Takahara, A. *Soft Matter* **2013**, *9*, 5138.
(167) Salaita, K.; Wang, Y.; Mirkin, C. A. *Nature Nanotechnology* **2007**, *2*, 145.
(168) Ginger, D. S.; Zhang, H.; Mirkin, C. A. *Angewandte Chemie International Edition* **2004**, *43*, 30.
(169) Mijatovic, D.; Eijkel, J.; Van Den Berg, A. *Lab Chip* **2005**, *5*, 492.
(170) Wachulak, P.; Capeluto, M.; Menoni, C.; Rocca, J.; Marconi, M. *Opto-Electronics Review* **2008**, *16*, 444.
(171) Wouters, D.; Schubert, U. S. *Angewandte Chemie International Edition* **2004**, *43*, 2480.
(172) Kumar, A.; Whitesides, G. M. *Applied Physics Letters* **1993**, *63*, 2002.
(173) Nie, Z.; Kumacheva, E. *Nature Materials* **2008**, *7*, 277.
(174) Ruiz, S. A.; Chen, C. S. *Soft Matter* **2006**, *3*, 168.
(175) Bernard, A.; Renault, J. P.; Michel, B.; Bosshard, H. R.; Delamarche, E. *Advanced Materials* **2000**, *12*, 1067.
(176) Mrksich, M.; Dike, L. E.; Tien, J.; Ingber, D. E.; Whitesides, G. M. *Experimental cell research* **1997**, *235*, 305.
(177) Holdcroft, S. *Advanced Materials* **2001**, *13*, 1753.
(178) Quist, A. P.; Pavlovic, E.; Oscarsson, S. *Analytical and bioanalytical chemistry* **2005**, *381*, 591.
(179) Wilbur, J. L.; Kumar, A.; Kim, E.; Whitesides, G. M. *Advanced Materials* **1994**, *6*, 600.
(180) Jackman, R. J.; Wilbur, J. L.; Whitesides, G. M. *Science* **1995**, *269*, 664.
(181) Zhou, F.; Zheng, Z.; Yu, B.; Liu, W.; Huck, W. T. S. *Journal of the American Chemical Society* **2006**, *128*, 16253.
(182) Hammond, P. T.; Whitesides, G. M. *Macromolecules* **1995**, *28*, 7569.
(183) Grunwald, C.; Eck, W.; Opitz, N.; Kuhlmann, J.; Wöll, C. *Physical Chemistry Chemical Physics* **2004**, *6*, 4358.
(184) Husemann, M.; Mecerreyes, D.; Hawker, C. J.; Hedrick, J. L.; Shah, R.; Abbott, N. L. *Angewandte Chemie International Edition* **1999**, *38*, 647.
(185) Zou, Y.; Yeh, P. Y. J.; Rossi, N. A. A.; Brooks, D. E.; Kizhakkedathu, J. N. *Biomacromolecules* **2009**, *11*, 284.
(186) Leggett, G. J. *Chemcal Society Reviews* **2006**, *35*, 1150.
(187) Sun, S.; Chong, K. S.; Leggett, G. J. *Nanotechnology* **2005**, *16*, 1798.
(188) Ducker, R. E.; Leggett, G. J. *Journal of the American Chemical Society* **2006**, *128*, 392.
(189) Alang Ahmad, S. A.; Wong, L. S.; ul-Haq, E.; Hobbs, J. K.; Leggett, G. J.; Micklefield, J. *Journal of the American Chemical Society* **2009**, *131*, 1513.
(190) Kamitani, R.; Niikura, K.; Onodera, T.; Iwasaki, N.; Shimaoka, H.; Ijiro, K. *Bulletin of the Chemical Society of Japan* **2007**, *80*, 1808.
(191) Ahmad, S. A.; Leggett, G. J.; Hucknall, A.; Chilkoti, A. *Biointerphases* **2011**, *6*, 8.
(192) Zhou, F.; Liu, W.; Hao, J.; Xu, T.; Chen, M.; Xue, Q. *Advanced Functional Materials* **2003**, *13*, 938.
(193) Alang Ahmad, S.; Hucknall, A.; Chilkoti, A.; Leggett, G. J. *Langmuir* **2010**, *26*, 9937.
(194) Moon, J. H.; Ford, J.; Yang, S. *Polymers for advanced technologies* **2006**, *17*, 83.
(195) Lu, C.; Lipson, R. *Laser & Photonics Reviews* **2010**, *4*, 568.
(196) Jang, J. H.; Ullal, C. K.; Maldovan, M.; Gorishnyy, T.; Kooi, S.; Koh, C.; Thomas, E. L. *Advanced Functional Materials* **2007**, *17*, 3027.

(197) Brueck, S. *Proceedings of the IEEE* **2005**, *93*, 1704.
(198) Xia, D.; Ku, Z.; Lee, S.; Brueck, S. *Advanced Materials* **2011**, *23*, 147.
(199) Solak, H. H.; He, D.; Li, W.; Singh-Gasson, S.; Cerrina, F.; Sohn, B.-H.; Yang, X.; Nealey, P. *Applied Physics Letters* **1999**, *75*, 2328.
(200) Friebel, S.; Aizenberg, J.; Abad, S.; Wiltzius, P. *Applied Physics Letters* **2000**, *77*, 2406.
(201) Turchanin, A.; Schnietz, M.; El-Desawy, M.; Solak, H. H.; David, C.; Gölzhäuser, A. *Small* **2007**, *3*, 2114.
(202) Steven, R. *Nanoscale* **2011**, *3*, 2511.
(203) Solak, H. H.; David, C.; Gobrecht, J.; Golovkina, V.; Cerrina, F.; Kim, S.; Nealey, P. *Microelectronic engineering* **2003**, *67*, 56.
(204) Schuh, C.; Santer, S.; Prucker, O.; Rühe, J. *Advanced Materials* **2009**, *21*, 4706.
(205) Tseng, A. A.; Chen, K.; Chen, C. D.; Ma, K. J. *Electronics Packaging Manufacturing, IEEE Transactions on* **2003**, *26*, 141.
(206) Pallandre, A.; Glinel, K.; Jonas, A. M.; Nysten, B. *Nano letters* **2004**, *4*, 365.
(207) Gölzhäuser, A.; Eck, W.; Geyer, W.; Stadler, V.; Weimann, T.; Hinze, P.; Grunze, M. *Advanced Materials* **2001**, *13*, 803.
(208) Gadegaard, N.; Chen, X.; Rutten, F. J.; Alexander, M. R. *Langmuir* **2008**, *24*, 2057.
(209) Lercel, M.; Whelan, C.; Craighead, H.; Seshadri, K.; Allara, D. *Journal of Vacuum Science & Technology B* **1996**, *14*, 4085.
(210) Rastogi, A.; Paik, M. Y.; Tanaka, M.; Ober, C. K. *ACS nano* **2010**, *4*, 771.
(211) Paik, M. Y.; Xu, Y.; Rastogi, A.; Tanaka, M.; Yi, Y.; Ober, C. K. *Nano letters* **2010**.
(212) Mirkin, C. A.; Hong, S.; Demers, L. *ChemPhysChem* **2001**, *2*, 37.
(213) Tseng, A. A.; Notargiacomo, A.; Chen, T. *Journal of Vacuum Science & Technology B: Microelectronics and Nanometer Structures* **2005**, *23*, 877.
(214) Heinzelmann, H.; Pohl, D. *Applied Physics A: Materials Science & Processing* **1994**, *59*, 89.
(215) Leggett, G. J. *NanoBioTechnology* **2007**, *3*, 223.
(216) Sun, S.; Chong, K. S. L.; Leggett, G. J. *Journal of the American Chemical Society* **2002**, *124*, 2414.
(217) Sun, S.; Leggett, G. J. *Nano letters* **2004**, *4*, 1381.
(218) Piner, R. D.; Zhu, J.; Xu, F.; Hong, S.; Mirkin, C. A. *Science* **1999**, *283*, 661.
(219) Zhou, X.; Wang, X.; Shen, Y.; Xie, Z.; Zheng, Z. *Angewandte Chemie International Edition* **2011**, *50*, 6506.
(220) Zhou, X.; Liu, Z.; Xie, Z.; Liu, X.; Zheng, Z. *Small* **2012**, *8*, 3568.
(221) Garcia, R.; Martinez, R. V.; Martinez, J. *Chemcal Society Reviews* **2005**, *35*, 29.
(222) Xie, X.; Chung, H.; Sow, C.; Wee, A. *Materials Science and Engineering: R: Reports* **2006**, *54*, 1.
(223) Chowdhury, D. *Current Science* **2009**, *96*, 923.
(224) Rolandi, M.; Quate, C. F.; Dai, H. *Advanced Materials* **2002**, *14*, 191.
(225) Zheng, Z.; Yang, M.; Zhang, B. *The Journal of Physical Chemistry C* **2010**, *114*, 19220.
(226) Qin, G.; Gu, J.; Liu, K.; Xiao, Z.; Yam, C. M.; Cai, C. *Langmuir* **2011**, *27*, 6987.
(227) Shedd, G. M.; Russell, P. *Nanotechnology* **1990**, *1*, 67.
(228) El Zubir, O.; Barlow, I.; Leggett, G. J.; Williams, N. H. *Nanoscale* **2013**, *5*, 11125.
(229) Kaholek, M.; Lee, W.-K.; LaMattina, B.; Caster, K. C.; Zauscher, S. *Nano letters* **2004**, *4*, 373.
(230) Janssen, D.; De Palma, R.; Verlaak, S.; Heremans, P.; Dehaen, W. *Thin Solid Films* **2006**, *515*, 1433.
(231) Brown, A. A.; Khan, N. S.; Steinbock, L.; Huck, W. T. S. *European polymer journal* **2005**, *41*, 1757.
(232) Kato, K.; Uchida, E.; Kang, E.-T.; Uyama, Y.; Ikada, Y. *Progress in Polymer Science* **2003**, *28*, 209.
(233) Decker, E.; Frank, B.; Suo, Y.; Garoff, S. *Colloids and Surfaces A: Physicochemical and Engineering Aspects* **1999**, *156*, 177.
(234) Tadmor, R. *Langmuir* **2004**, *20*, 7659.

(235) Good, R. J. *Journal of adhesion science and technology* **1992**, 12, 1269.
(236) Zisman, W. A. *Advances in Chemistry Series* **1964**, *43*.
(237) Binnig, G.; Quate, C. F.; Gerber, C. *Physical review letters* **1986**, *56*, 930.
(238) Noy, A.; Vezenov, D. V.; Lieber, C. M. *Annual Review of Materials Science* **1997**, *27*, 381.
(239) Carpick, R. W.; Salmeron, M. *Chemical Reviews* **1997**, *97*, 1163.
(240) Meyer, G.; Amer, N. M. *Applied Physics Letters* **1988**, *53*, 1045.
(241) Giessibl, F. J. *Reviews of modern physics* **2003**, *75*, 949.
(242) Leggett, G. J. *Analytica chimica acta* **2003**, *479*, 17.
(243) M Salapaka, S.; De, T.; Sebastian, A. *International Journal of Robust and Nonlinear Control* **2005**, *15*, 821.
(244) Zhong, Q.; Inniss, D.; Kjoller, K.; Elings, V. *Surface Science Letters* **1993**, *290*, L688.
(245) Binggeli, M.; Mate, C. *Applied Physics Letters* **1994**, *65*, 415.
(246) Junno, T.; Anand, S.; Deppert, K.; Montelius, L.; Samuelson, L. *Applied Physics Letters* **1995**, *66*, 3295.
(247) Hansma, P.; Cleveland, J.; Radmacher, M.; Walters, D.; Hillner, P.; Bezanilla, M.; Fritz, M.; Vie, D.; Hansma, H.; Prater, C. *Applied Physics Letters* **1994**, *64*, 1738.
(248) Drake, B.; Prater, C.; Weisenhorn, A.; Gould, S.; Albrecht, T.; Quate, C.; Cannell, D.; Hansma, H.; Hansma, P. *Science* **1989**, *243*, 1586.
(249) Leggett, G. J.; Brewer, N. J.; Chong, K. S. *Physical Chemistry Chemical Physics* **2005**, *7*, 1107.
(250) Colburn, T. J.; Leggett, G. J. *Langmuir* **2007**, *23*, 4959.
(251) Hurley, C. R.; Leggett, G. J. *Langmuir* **2006**, *22*, 4179.
(252) Brewer, N. J.; Beake, B. D.; Leggett, G. J. *Langmuir* **2001**, *17*, 1970.
(253) Ohring, M. *Materials science of thin films*; Academic press, 2001.
(254) Jellison, G. E. *Thin Solid Films* **1993**, *234*, 416.
(255) Jellison Jr, G. *Thin Solid Films* **1998**, *313*, 33.
(256) Tompkins, H.; Irene, E. A. *Handbook of ellipsometry*; William Andrew, 2005.
(257) Hauge, P. *Surface science* **1980**, *96*, 108.
(258) Edmondson, S.; Vo, C.-D.; Armes, S. P.; Unali, G.-F. *Macromolecules* **2007**, *40*, 5271.
(259) Fielding, L. A.; Edmondson, S.; Armes, S. P. *Journal of Materials Chemistry* **2011**, *21*, 11773.
(260) Briggs, D. *Surface analysis of polymers by XPS and static SIMS*; Cambridge University Press, 1998.
(261) Vickerman, J. C.; Gilmore, I. S. *Surface analysis: the principal techniques*; Wiley Online Library, 2009; Vol. 2.
(262) Alexander, M.; Short, R.; Jones, F.; Michaeli, W.; Blomfield, C. *Applied surface science* **1999**, *137*, 179.
(263) Seah, M. *Surface and Interface Analysis* **1980**, *2*, 222.
(264) Minsky, M. *Scanning* **1988**, *10*, 128.
(265) Amos, W.; White, J. *Biology of the Cell* **2003**, *95*, 335.
(266) Tata, B.; Raj, B. *Bulletin of Materials Science* **1998**, *21*, 263.
(267) Goddard, J. M.; Hotchkiss, J. *Progress in Polymer Science* **2007**, *32*, 698.
(268) Kirby, B. J.; Hasselbrink, E. F. *Electrophoresis* **2004**, *25*, 187.
(269) Kirby, B. J.; Hasselbrink, E. F. *Electrophoresis* **2004**, *25*, 203.
(270) Mela, P.; van den Berg, A.; Fintschenko, Y.; Cummings, E. B.; Simmons, B. A.; Kirby, B. J. *Electrophoresis* **2005**, *26*, 1792.
(271) Zimmermann, R.; Birkert, O.; Gauglitz, G.; Werner, C. *ChemPhysChem* **2003**, *4*, 509.
(272) Corbett, J. C. W.; McNeil-Watson, F.; Jack, R. O.; Howarth, M. *Colloids and Surfaces A: Physicochemical and Engineering Aspects* **2012**, *396*, 169.
(273) Xie, Q.; Hong, M.; Tan, H.; Chen, G.; Shi, L.; Chong, T. *Journal of alloys and compounds* **2008**, *449*, 261.
(274) de Boor, J.; Geyer, N.; Gösele, U.; Schmidt, V. *Optics letters* **2009**, *34*, 1783.
(275) Solak, H.; David, C.; Gobrecht, J.; Wang, L.; Cerrina, F. *Journal of Vacuum Science & Technology B* **2002**, *20*, 2844.

(276) Lee, H. S.; Eckmann, D. M.; Lee, D.; Hickok, N. J.; Composto, R. J. *Langmuir* **2011**.
(277) Dai, X.; Zhou, F.; Khan, N.; Huck, W. T. S.; Kaminski, C. F. *Langmuir* **2008**, *24*, 13182.
(278) Connal, L. A.; Li, Q.; Quinn, J. F.; Tjipto, E.; Caruso, F.; Qiao, G. G. *Macromolecules* **2008**, *41*, 2620.
(279) Li, G.; Song, S.; Guo, L.; Ma, S. *Journal of Polymer Science Part A: Polymer Chemistry* **2008**, *46*, 5028.
(280) Binks, B. P.; Murakami, R.; Armes, S. P.; Fujii, S.; Schmid, A. *Langmuir* **2007**, *23*, 8691.
(281) He, E.; Yue, C. Y.; Tam, K. C. *Langmuir* **2009**, *25*, 4892.
(282) Ravi, P.; Dai, S.; Tan, C. H.; Tam, K. C. *Macromolecules* **2005**, *38*, 933.
(283) Munoz-Bonilla, A.; Fernandez-Garcia, M.; Haddleton, D. M. *Soft Matter* **2007**, *3*, 725.
(284) Hu, L.; Chu, L.-Y.; Yang, M.; Wang, H.-D.; Niu, C. H. *Journal of Colloid and Interface Science* **2007**, *311*, 110.
(285) Liu, F.; Urban, M. W. *Macromolecules* **2008**, *41*, 6531.
(286) McParlane, J.; Dupin, D.; Saunders, J. M.; Lally, S.; Armes, S. P.; Saunders, B. R. *Soft Matter* **2012**, *8*, 6239.
(287) Li, D.; He, Q.; Cui, Y.; Li, J. *Chemistry of Materials* **2007**, *19*, 412.
(288) Witte, K. N.; Kim, S.; Won, Y.-Y. *The Journal of Physical Chemistry B* **2009**, *113*, 11076.
(289) Huang, W.; Baker, G. L.; Bruening, M. L. *Angewandte Chemie* **2001**, *113*, 1558.
(290) Moglianetti, M.; Webster, J. R.; Edmondson, S.; Armes, S. P.; Titmuss, S. *Langmuir* **2011**, *27*, 4489.
(291) Morse, A. J.; Dupin, D.; Thompson, K. L.; Armes, S. P.; Ouzineb, K.; Mills, P.; Swart, R. *Langmuir* **2012**, *28*, 11742.
(292) Lenoir, S.; Pagnoulle, C.; Galleni, M.; Compere, P.; Jerome, R.; Detrembleur, C. *Biomacromolecules* **2006**, *7*, 2291.
(293) Thomassin, J.-M.; Lenoir, S.; Riga, J.; Jerome, R.; Detrembleur, C. *Biomacromolecules* **2007**, *8*, 1171.
(294) Alswieleh, A. M.; Cheng, N.; Leggett, G. J.; Armes, S. P. *Langmuir* **2014**.
(295) Oren, R.; Liang, Z.; Barnard, J. S.; Warren, S. C.; Wiesner, U.; Huck, W. T. S. *Journal of the American Chemical Society* **2009**, *131*, 1670.
(296) Basu, R.; Kinser, C.; Tovar, J.; Hersam, M. *Chemical physics* **2006**, *326*, 144.
(297) van der Maaden, K.; Sliedregt, K.; Kros, A.; Jiskoot, W.; Bouwstra, J. *Langmuir* **2012**, *28*, 3403.
(298) Zhang, H.; He, H.-X.; Wang, J.; Mu, T.; Liu, Z.-F. *Applied Physics A* **1998**, *66*, S269.
(299) Wu, Z.; Xiang, H.; Kim, T.; Chun, M.-S.; Lee, K. *Journal of colloid and interface science* **2006**, *304*, 119.
(300) Matyjaszewski, K.; Miller, P. J.; Shukla, N.; Immaraporn, B.; Gelman, A.; Luokala, B. B.; Siclovan, T. M.; Kickelbick, G.; Vallant, T.; Hoffmann, H.; Pakula, T. *Macromolecules* **1999**, *32*, 8716.
(301) Kim, J.-B.; Bruening, M. L.; Baker, G. L. *Journal of the American Chemical Society* **2000**, *122*, 7616.
(302) Matyjaszewski, K.; Xia, J. *Chemical Reviews* **2001**, *101*, 2921.
(303) Ding, S.; Floyd, J. A.; Walters, K. B. *Journal of Polymer Science Part A: Polymer Chemistry* **2009**, *47*, 6552.
(304) Kaholek, M.; Lee, W.-K.; Feng, J.; LaMattina, B.; Dyer, D. J.; Zauscher, S. *Chemistry of materials* **2006**, *18*, 3660.
(305) Walsh, A.; Thompson, K.; Armes, S.; York, D. *Langmuir* **2010**, *26*, 18039.
(306) Thompson, K. L.; Armes, S. P. *Chemical Communications* **2010**, *46*, 5274.
(307) Jia, H.; Grillo, I.; Titmuss, S. *Langmuir* **2010**, *26*, 7482.
(308) Meyers, S. R.; Grinstaff, M. W. *Chemical Reviews* **2011**, *112*, 1615.
(309) Langer, R.; Tirrell, D. A. *Nature* **2004**, *428*, 487.
(310) Castner, D. G.; Ratner, B. D. *Surface science* **2002**, *500*, 28.
(311) Lewis, A.; Tolhurst, L.; Stratford, P. *Biomaterials* **2002**, *23*, 1697.
(312) Vlastarakos, P. V.; Nikolopoulos, T. P.; Korres, S.; Tavoulari, E.; Tzagaroulakis, A.; Ferekidis, E. *European journal of pediatrics* **2007**, *166*, 385.

(313) Chan, M. Y.; Weitz, J. I.; Merhi, Y.; Harrington, R. A.; Becker, R. C. *Journal of thrombosis and thrombolysis* **2009**, *28*, 366.
(314) Lee, J. H.; Lee, H. B.; Andrade, J. D. *Progress in Polymer Science* **1995**, *20*, 1043.
(315) Harris, J. M. *Poly (ethylene glycol) chemistry: biotechnical and biomedical applications*; Springer, 1992.
(316) Feldman, K.; Hähner, G.; Spencer, N.; Harder, P.; Grunze, M. *Journal of the American Chemical Society* **1999**, *121*, 10134.
(317) Webster, R.; Didier, E.; Harris, P.; Siegel, N.; Stadler, J.; Tilbury, L.; Smith, D. *Drug Metabolism and Disposition* **2007**, *35*, 9.
(318) Chen, S.; Li, L.; Zhao, C.; Zheng, J. *Polymer* **2010**, *51*, 5283.
(319) Arima, Y.; Toda, M.; Iwata, H. *Biomaterials* **2008**, *29*, 551.
(320) Zhang, Z.; Zhang, M.; Chen, S.; Horbett, T. A.; Ratner, B. D.; Jiang, S. *Biomaterials* **2008**, *29*, 4285.
(321) Ham, H. O.; Park, S. H.; Kurutz, J. W.; Szleifer, I. G.; Messersmith, P. B. *Journal of the American Chemical Society* **2013**, *135*, 13015.
(322) Lavanant, L.; Pullin, B.; Hubbell, J. A.; Klok, H. A. *Macromolecular bioscience* **2010**, *10*, 101.
(323) Chen, S.; Zheng, J.; Li, L.; Jiang, S. *Journal of the American Chemical Society* **2005**, *127*, 14473.
(324) Yang, W.; Chen, S.; Cheng, G.; Vaisocherová, H.; Xue, H.; Li, W.; Zhang, J.; Jiang, S. *Langmuir* **2008**, *24*, 9211.
(325) Feng, W.; Brash, J.; Zhu, S. *Journal of Polymer Science Part A: Polymer Chemistry* **2004**, *42*, 2931.
(326) Zhang, Z.; Chen, S.; Jiang, S. *Biomacromolecules* **2006**, *7*, 3311.
(327) Rühe, J.; Ballauff, M.; Biesalski, M.; Dziezok, P.; Gröhn, F.; Johannsmann, D.; Houbenov, N.; Hugenberg, N.; Konradi, R.; Minko, S. In *Polyelectrolytes with Defined Molecular Architecture I*; Springer: 2004, p 79.
(328) Stuart, M. A. C.; Huck, W. T.; Genzer, J.; Müller, M.; Ober, C.; Stamm, M.; Sukhorukov, G. B.; Szleifer, I.; Tsukruk, V. V.; Urban, M. *Nature materials* **2010**, *9*, 101.
(329) de las Heras Alarcón, C.; Pennadam, S.; Alexander, C. *Chemical society reviews* **2005**, *34*, 276.
(330) Wu, T.; Gong, P.; Szleifer, I.; Vlcˇek, P.; Šubr, V.; Genzer, J. *Macromolecules* **2007**, *40*, 8756.
(331) Parnell, A. J.; Martin, S. J.; Jones, R. A.; Vasilev, C.; Crook, C. J.; Ryan, A. J. *Soft Matter* **2009**, *5*, 296.
(332) Santonicola, M. G.; de Groot, G. W.; Memesa, M.; Meszyńska, A.; Vancso, G. J. *Langmuir* **2010**, *26*, 17513.
(333) Schepelina, O.; Zharov, I. *Langmuir* **2008**, *24*, 14188.
(334) Rosen, J. E.; Gu, F. X. *Langmuir* **2011**, *27*, 10507.
(335) Monson, C. F.; Cong, X.; Robison, A. D.; Pace, H. P.; Liu, C.; Poyton, M. F.; Cremer, P. S. *Journal of the American Chemical Society* **2012**, *134*, 7773.
(336) Yameen, B.; Ali, M.; Neumann, R.; Ensinger, W.; Knoll, W.; Azzaroni, O. *Journal of the American Chemical Society* **2009**, *131*, 2070.
(337) Calvo, A.; Yameen, B.; Williams, F. J.; Soler-Illia, G. J.; Azzaroni, O. *Journal of the American Chemical Society* **2009**, *131*, 10866.
(338) Alswieleh, A. M.; Cheng, N.; Canton, I.; Ustbas, B.; Xue, X.; Ladmiral, V.; Xia, S.; Ducker, R. E.; El Zubir, O.; Cartron, M. L. *Journal of the American Chemical Society* **2014**.
(339) Zhang, Z.; Morse, A. J.; Armes, S. P.; Lewis, A. L.; Geoghegan, M.; Leggett, G. J. *Langmuir* **2011**.
(340) Frisch, S. M.; Ruoslahti, E. *Current opinion in cell biology* **1997**, *9*, 701.
(341) Meerasa, A.; G Huang, J.; X Gu, F. *Current Drug Delivery* **2011**, *8*, 290.
(342) Chan, J. W.; Hoyle, C. E.; Lowe, A. B.; Bowman, M. *Macromolecules* **2010**, *43*, 6381.
(343) Dodero, G.; De Michieli, L.; Cavalleri, O.; Rolandi, R.; Oliveri, L.; Dacca, A.; Parodi, R. *Colloids and Surfaces A: Physicochemical and Engineering Aspects* **2000**, *175*, 121.
(344) Cavalleri, O.; Gonella, G.; Terreni, S.; Vignolo, M.; Floreano, L.; Morgante, A.; Canepa, M.; Rolandi, R. *Physical Chemistry Chemical Physics* **2004**, *6*, 4042.

(345) Dewick, P. M. *Essentials of organic chemistry: for students of pharmacy, medicinal chemistry and biological chemistry*; Wiley. com, 2006.
(346) Dong, R.; Lindau, M.; Ober, C. K. *Langmuir* **2009**, *25*, 4774.
(347) Biesalski, M.; Johannsmann, D.; Rühe, J. *The Journal of chemical physics* **2002**, *117*, 4988.
(348) Zhang, H.; Rühe, J. *Macromolecules* **2005**, *38*, 4855.
(349) Willott, J. D.; Murdoch, T. J.; Humphreys, B. A.; Edmondson, S.; Webber, G. B.; Wanless, E. J. *Langmuir* **2014**, *30*, 1827.
(350) Thompson, K. L.; Read, E. S.; Armes, S. P. *Polymer Degradation and Stability* **2008**, *93*, 1460.
(351) Ganesan, R.; Yoo, S. Y.; Choi, J.-H.; Lee, S. Y.; Kim, J.-B. *Journal of Materials Chemistry* **2008**, *18*, 703.
(352) Yun, J.-M.; Jung, C.-H.; Kim, D.-K.; Hwang, I.-T.; Choi, J.-H.; Ganesan, R.; Kim, J.-B. *Journal of Materials Chemistry.* **2010**, *20*, 2007.
(353) Adams, J.; Tizazu, G.; Janusz, S.; Brueck, S.; Lopez, G.; Leggett, G. *Langmuir* **2010**, *26*, 13600.
(354) Chen, M.; Briscoe, W. H.; Armes, S. P.; Cohen, H.; Klein, J. *ChemPhysChem* **2007**, *8*, 1303.
(355) Kitano, K.; Inoue, Y.; Matsuno, R.; Takai, M.; Ishihara, K. *Colloids and Surfaces B: Biointerfaces* **2009**, *74*, 350.
(356) Morse, A. J.; Edmondson, S.; Dupin, D.; Armes, S. P.; Zhang, Z.; Leggett, G.; Thompson, R. L.; Lewis, A. *Soft Matter* **2010**, *6*, 1571.
(357) Tamm, L. K.; McConnell, H. M. *Biophysical journal* **1985**, *47*, 105.
(358) Smith, E. A.; Coym, J. W.; Cowell, S. M.; Tokimoto, T.; Hruby, V. J.; Yamamura, H. I.; Wirth, M. J. *Langmuir* **2005**, *21*, 9644.
(359) Zhang, L.; Longo, M. L.; Stroeve, P. *Langmuir* **2000**, *16*, 5093.
(360) Sackmann, E. *Science* **1996**, *271*, 43.
(361) Naumann, C. A.; Prucker, O.; Lehmann, T.; Rühe, J.; Knoll, W.; Frank, C. W. *Biomacromolecules* **2002**, *3*, 27.
(362) Munro, J. C.; Frank, C. W. *Langmuir* **2004**, *20*, 10567.
(363) Albertorio, F.; Diaz, A. J.; Yang, T.; Chapa, V. A.; Kataoka, S.; Castellana, E. T.; Cremer, P. S. *Langmuir* **2005**, *21*, 7476.
(364) Ye, Q.; Konradi, R.; Textor, M.; Reimhult, E. *Langmuir* **2009**, *25*, 13534.
(365) Sackmann, E.; Tanaka, M. *Trends in biotechnology* **2000**, *18*, 58.
(366) Tanaka, M.; Sackmann, E. *Nature* **2005**, *437*, 656.
(367) Brian, A. A.; McConnell, H. M. *Proceedings of the National Academy of Sciences* **1984**, *81*, 6159.
(368) Keller, C.; Glasmästar, K.; Zhdanov, V.; Kasemo, B. *Physical Review Letters* **2000**, *84*, 5443.
(369) Cremer, P. S.; Boxer, S. G. *The Journal of Physical Chemistry B* **1999**, *103*, 2554.
(370) Richter, R. P.; Bérat, R.; Brisson, A. R. *Langmuir* **2006**, *22*, 3497.
(371) Reimhult, E.; Höök, F.; Kasemo, B. *Langmuir* **2003**, *19*, 1681.
(372) Wagner, M. L.; Tamm, L. K. *Biophysical journal* **2000**, *79*, 1400.
(373) Kühner, M.; Tampe, R.; Sackmann, E. *Biophysical journal* **1994**, *67*, 217.
(374) Fang, N.; Tan, W. J.; Leong, K. W.; Mao, H.-Q.; Chan, V. *Colloids and Surfaces B: Biointerfaces* **2005**, *42*, 245.
(375) Renner, L.; Osaki, T.; Chiantia, S.; Schwille, P.; Pompe, T.; Werner, C. *The Journal of Physical Chemistry B* **2008**, *112*, 6373.
(376) El-Khouri, R. J.; Bricarello, D. A.; Watkins, E. B.; Kim, C. Y.; Miller, C. E.; Patten, T. E.; Parikh, A. N.; Kuhl, T. L. *Nano letters* **2011**, *11*, 2169.
(377) Théato, P.; Zentel, R. *Langmuir* **2000**, *16*, 1801.
(378) Azzaroni, O.; Brown, A. A.; Huck, W. T. *Angewandte Chemie* **2006**, *118*, 1802.
(379) Roder, F.; Birkholz, O.; Beutel, O.; Paterok, D.; Piehler, J. *Journal of the American Chemical Society* **2013**, *135*, 1189.
(380) Döbbelin, M.; Arias, G.; Loinaz, I.; Llarena, I.; Mecerreyes, D.; Moya, S. *Macromolecular Rapid Communications* **2008**, *29*, 871.

(381) Ramstedt, M.; Cheng, N.; Azzaroni, O.; Mossialos, D.; Mathieu, H. J.; Huck, W. T. S. *Langmuir* **2007**, *23*, 3314.
(382) Kelby, T. S.; Huck, W. T. S. *Macromolecules* **2010**, *43*, 5382.
(383) Axelrod, D.; Koppel, D.; Schlessinger, J.; Elson, E.; Webb, W. *Biophysical journal* **1976**, *16*, 1055.
(384) Vo, C.-D.; Schmid, A.; Armes, S. P.; Sakai, K.; Biggs, S. *Langmuir* **2007**, *23*, 408.
(385) Nakai, K.; Morigaki, K.; Iwasaki, Y. *Soft Matter* **2010**, *6*, 5937.
(386) Papahadjopoulos, D.; Vail, W.; Pangborn, W.; Poste, G. *Biochimica et Biophysica Acta (BBA)-Biomembranes* **1976**, *448*, 265.
(387) Morigaki, K.; Kimura, S.; Okada, K.; Kawasaki, T.; Kawasaki, K. *Langmuir* **2012**, *28*, 9649.
(388) Mennicke, U.; Salditt, T. *Langmuir* **2002**, *18*, 8172.
(389) Yamada, N. L. *Langmuir* **2012**, *28*, 17381.
(390) Masci, G.; Bontempo, D.; Tiso, N.; Diociaiuti, M.; Mannina, L.; Capitani, D.; Crescenzi, V. *Macromolecules* **2004**, *37*, 4464.
(391) Ramstedt, M.; Cheng, N.; Azzaroni, O.; Mossialos, D.; Mathieu, H. J.; Huck, W. T. *Langmuir* **2007**, *23*, 3314.
(392) Wagner, C. D.; Muilenberg, G. E. *Handbook of x-ray photoelectron spectroscopy: a reference book of standard data for use in x-ray photoelectron spectroscopy*; Physical Electronics Division, Perkin-Elmer Corp., 1979.
(393) Kobayashi, M.; Terada, M.; Terayama, Y.; Kikuchi, M.; Takahara, A. *Macromolecules* **2010**, *43*, 8409.
(394) Dong, R.; Molloy, R. P.; Lindau, M.; Ober, C. K. *Biomacromolecules* **2010**, *11*, 2027.
(395) Kelby, T. S.; Huck, W. T. *Macromolecules* **2010**, *43*, 5382.
(396) Azzaroni, O.; Brown, A. A.; Cheng, N.; Wei, A.; Jonas, A. M.; Huck, W. T. *Journal of Materials Chemistry* **2007**, *17*, 3433.
(397) Kleineberg, U.; Brechling, A.; Sundermann, M.; Heinzmann, U. *Advanced Functional Materials* **2001**, *11*, 208.
(398) Kumar, A.; Biebuyck, H. A.; Abbott, N. L.; Whitesides, G. M. *Journal of the American Chemical Society* **1992**, *114*, 9188.
(399) Kim, J.-H.; Kang, T.; Yoo, S. M.; Lee, S. Y.; Kim, B.; Choi, Y.-K. *Nanotechnology* **2009**, *20*, 235302.
(400) Shah, R. R.; Merreceyes, D.; Husemann, M.; Rees, I.; Abbott, N. L.; Hawker, C. J.; Hedrick, J. L. *Macromolecules* **2000**, *33*, 597.
(401) Huck, W. T.; Yan, L.; Stroock, A.; Haag, R.; Whitesides, G. M. *Langmuir* **1999**, *15*, 6862.
(402) Sondag-Huethorst, J.; Van Helleputte, H.; Fokkink, L. *Applied Physics Letters* **1994**, *64*, 285.
(403) Lercel, M.; Redinbo, G.; Pardo, F.; Rooks, M.; Tiberio, R.; Simpson, P.; Craighead, H.; Sheen, C.; Parikh, A.; Allara, D. *Journal of Vacuum Science & Technology B* **1994**, *12*, 3663.
(404) Chen, W.; Ahmed, H. *Applied Physics Letters* **1993**, *62*, 1499.
(405) Sun, S.; Leggett, G. J. *Nano letters* **2002**, *2*, 1223.
(406) Hedberg-Dirk, E. L.; Martinez, U. A. *Journal of Nanomaterials* **2010**, *2010*, 13.
(407) Guo, H.; Nau, D.; Radke, A.; Zhang, X.; Stodolka, J.; Yang, X.; Tikhodeev, S.; Gippius, N.; Giessen, H. *Applied Physics B* **2005**, *81*, 271.
(408) Choi, W.; Liew, T.; Dawood, M.; Smith, H. I.; Thompson, C.; Hong, M. *Nano letters* **2008**, *8*, 3799.
(409) Xiao, S.; Textor, M.; D SPENCER, N.; Wieland, M.; Keller, B.; Sigrist, H. *Journal of materials science: Materials in Medicine* **1997**, *8*, 867.
(410) Kang, S. M.; Lee, B. S.; Kim, W.-J.; Choi, I. S.; Kil, M.; Jung, H.-j.; Oh, E. *Macromolecular Research* **2009**, *17*, 174.
(411) Fan, X.; Lin, L.; Dalsin, J. L.; Messersmith, P. B. *Journal of the American Chemical Society* **2005**, *127*, 15843.
(412) Levina, A.; Codd, R.; Dillon, C. T.; Lay, P. A. *Progress in Inorganic Chemistry, Volume 51* **2003**, 145.

(413) Zayed, A. M.; Terry, N. *Plant and soil* **2003**, *249*, 139.
(414) Gao, G.; Lange, D.; Hilpert, K.; Kindrachuk, J.; Zou, Y.; Cheng, J. T.; Kazemzadeh-Narbat, M.; Yu, K.; Wang, R.; Straus, S. K. *Biomaterials* **2011**, *32*, 3899.
(415) Gabriel, M.; Nazmi, K.; Veerman, E. C.; Nieuw Amerongen, A. V.; Zentner, A. *Bioconjugate chemistry* **2006**, *17*, 548.
(416) Raynor, J. E.; Petrie, T. A.; Fears, K. P.; Latour, R. A.; García, A. J.; Collard, D. M. *Biomacromolecules* **2009**, *10*, 748.
(417) Fan, X.; Lin, L.; Messersmith, P. B. *Biomacromolecules* **2006**, *7*, 2443.
(418) Ducker, R. E.; Janusz, S.; Sun, S.; Leggett, G. J. *Journal of the American Chemical Society* **2007**, *129*, 14842.
(419) Mrksich, M.; Sigal, G. B.; Whitesides, G. M. *Langmuir* **1995**, *11*, 4383.
(420) Harder, P.; Grunze, M.; Dahint, R.; Whitesides, G.; Laibinis, P. *The Journal of Physical Chemistry B* **1998**, *102*, 426.
(421) Luk, Y.-Y.; Kato, M.; Mrksich, M. *Langmuir* **2000**, *16*, 9604.
(422) Montague, M.; Ducker, R. E.; Chong, K. S.; Manning, R. J.; Rutten, F. J.; Davies, M. C.; Leggett, G. J. *Langmuir* **2007**, *23*, 7328.
(423) Reynolds, N. P.; Tucker, J. D.; Davison, P. A.; Timney, J. A.; Hunter, C. N.; Leggett, G. J. *Journal of the American Chemical Society* **2009**, *131*, 896.
(424) Alang Ahmad, S. A.; Wong, L. S.; ul-Haq, E.; Hobbs, J. K.; Leggett, G. J.; Micklefield, J. *Journal of the American Chemical Society* **2011**, *133*, 2749.
(425) Doh, J.; Irvine, D. J. *Journal of the American Chemical Society* **2004**, *126*, 9170.
(426) Mulvihill, M. J.; Rupert, B. L.; He, R.; Hochbaum, A.; Arnold, J.; Yang, P. *Journal of the American Chemical Society* **2005**, *127*, 16040.
(427) Lee, J. P.; Jang, Y. J.; Sung, M. M. *Advanced Functional Materials* **2003**, *13*, 873.
(428) Sundaram, H. S.; Ella-Menye, J.-R.; Brault, N. D.; Shao, Q.; Jiang, S. *Chemical Science* **2014**, *5*, 200.